CARDIFF SCHOOL OF BIOSCIENCES

THESIS PRESENTED TO CARDIFF UNIVERSITY FOR THE DEGREE OF DOCTOR OF PHILOSOPHY

Optical extinction and coherent multiphoton micro-spectroscopy of single nanoparticles

Author:

LUKAS PAYNE

Supervisors:

Prof. P. BORRI

Prof. W.W. LANGBEIN

December 3, 2015

Declaration and Statements

DECLARATION

This work has not been submitted in substance for any other degree or award at this or any other university or place of learning, nor is being submitted concurrently in candidature for any degree or other award.

Signed .....Lukas Payne.....(candidate) Date .....03/12/2015.....

STATEMENT 1

This thesis is being submitted in partial fulfillment of the requirements for the degree of Doctor of Philosophy.

Signed .....Lukas Payne.....(candidate) Date .....03/12/2015.....

STATEMENT 2

This thesis is the result of my own independent work/investigation, except where otherwise stated. Other sources are acknowledged by explicit references. The views expressed are my own.

Signed .....Lukas Payne.....(candidate) Date .....03/12/2015.....

STATEMENT 3

I hereby give consent for my thesis, if accepted, to be available for photocopying and for inter-library loan, and for the title and summary to be made available to outside organisations.

Signed .....Lukas Payne.....(candidate) Date .....03/12/2015.....

Abstract

Nanoparticles of many varieties are increasingly studied for use in the physical, chemical, and biological sciences. Metallic nanoparticles exhibit morphology-dependent localised surface plasmon resonances (LSPR), which couple to propagating light, and manifest as a resonant particle polarisability at the LSPR frequency. These resonances can be harnessed for a variety of applications. Many of these applications require characterisation of NP properties, such as their optical response, summarised by the absorption and scattering cross sections. Quantitative measurement of individual NPs is technically difficult, and ensemble measurement techniques, such as absorption spectroscopy, are frequently employed. However, individual NP properties can vary significantly, within the ensemble. In this work, we present a novel, and easy to implement, wide-field extinction microscopy technique, capable of analysing hundreds of nanoparticles simultaneously. Using this technique, we are able to characterise individual gold nanoparticles down to 5 nm diameter, and collate the data to produce ensemble statistics. Furthermore, we developed a program for the rapid analysis of the acquired image, enabling implementation by others in a cost-effective and efficient manner. Using the wide-field extinction technique, we have studied several sizes of gold, platinum, silver, and diamond nanoparticles. We used gold nanoparticles to provide a proof of concept, and found good agreement with the literature. We also present an experimental investigation towards an in-vitro plasmon ruler. Coupled metallic NPs exhibit a LSPR, which is dependent on interparticle distance. The four-wave mixing technique we employ is phase-sensitive, allowing measurement of the shift of the resonance frequency of gold NPs. To provide proof-of-principle of the plasmon ruler, we correlatively studied gold nanoparticle dimers, with transmission electron microscopy, and four-wave mixing microscopy. In this way, we obtained a direct measure of the interparticle distance, and could relate it to the measured phase shift in four-wave mixing.

Acknowledgements

The research carried out during this PhD was part of a larger cooperative effort, which I'm proud to have been a part of. I benefited from a great deal of assistance, during my time in the Cardiff Biophotonics group, and I would like to take this chance to thank all those who helped along the way.

I would like to first thank my supervisors, Professors Paola Borri and Wolfgang Langbein, without whom this project would not exist. I truly appreciate their willingness to lend their time, extensive knowledge, and interest towards making my PhD a very fruitful piece of work. I have learned a great deal during my time here. Furthermore, I thank them for their general capacity for understanding and kindness.

I would also like to acknowledge the EPSRC for funding this studentship and the Ettore nanoscopy project (Grant Code: EP/I005072/1).

Thanks in advance to my examiners, for their time and energy.

Thanks to Dr. Peter Watson, who acted as my internal assessor, and who provided me advice, a great deal of laughs, and quite a few pints, throughout the last 4 years.

Thanks to all members of the Biophotonics group. In particular thanks to: Dr. George Zoriniants, for our many discussions, for your help with any questions I had, for your contribution of the modeling of coupled nanoparticle cross-sections, and for teaching me how to use the FWM microscope, and to Dr. Iestyn Pope for his help with various mechanisms on the microscope, teaching me how to use MultiCARS, nearly always taking the first meeting on Tuesdays, our chats, and anything else I may have forgotten! Thanks also to Craig McPhee, who established the Piranha cleaning procedure, and generally for our discussions and various cooperations throughout the years. Thanks to Dr. Richard Perrins who helped with some early chemistry, which was vital to devel-

opment of our glass functionalisation technique. Also, a general thank you to all of the folks in the office who have always been friendly and helpful. A final internal thanks to Kez Cleal, who provided some much needed chemistry insight, and who let me borrow chemicals whenever I needed.

I would like to thank our external collaborators: BBI Solutions, and our direct contact there, Darren Rowles, who provided all of the metallic nanoparticles in this research, and Dr. Paul Verkade, and Dr. Kenton Arkill, at the Wolfson Bioimaging Facility in Bristol University, for their efforts using transmission electron microscopy to image our nanoparticle dimers.

Thanks to the country of Wales, who has hosted me. You're an under-appreciated little place, full of great secrets for those willing to explore a bit, and find them. I've really enjoyed my time here.

Personal thanks to my friends here in Cardiff, who have made it a great time: in no particular order, Kez, Salah, Josie, Mairi, and Toby. Thanks to Laura for taking the long road with me, as best we could.

Last, but not least, thanks to my mother and my father, for all they have done for me, which has lead me to this opportunity. Without them, this would not be possible. I hope always to make you proud. To my parents, my brother, my sister, and Laura, sorry I keep wandering off to other countries! I hope to spend some much needed time with you all soon!

Publications and Conferences

Publications

Some of the content contained in this thesis has been published in the following articles:

1. L. Payne, G. Zoriniants, F. Masia, K. Arkill, P. Verkade, D. Rowles, W. Langbein, and P. Borri. Optical micro-spectroscopy of single metallic nanoparticles: quantitative extinction and transient resonant four-wave mixing. *Faraday Discuss.*, 2015. DOI: 10.1039/C5FD00079C

2. I. Pope, L. Payne, G. Zoriniants, E. Thomas, O. Williams, P. Watson, W. Langbein, and P. Borri. Coherent anti-Stokes Raman scattering microscopy of single nanodiamonds. *Nat Nano*, 9(11):940-946, 2014. DOI: 10.1038/nnano.2014.210

3. L. Payne, W. Langbein, and P. Borri. Polarization-resolved extinction and scattering cross-sections of individual gold nanoparticles measured by wide-field microscopy on a large ensemble. *Applied Physics Letters*, 102(13), 2013. DOI: 10.1063/1.4800564

Conferences

Some of the content contained in this thesis has been presented during oral or poster sessions at the following conferences:

1. L. Payne, G. Zoriniants, F. Masia, W. Langbein, and P. Borri. Optical micro-spectroscopy of single metallic nanoparticles: Polarzation-resolved extinction

and transient Four-Wave Mixing. *Oral Presentation.* Photon14, Imperial College London, UK, 1-4 September, 2014.

2. I. Pope, L. Payne, G. Zoriniants, E. Thomas, O. Williams, P. Watson, W. Langbein, and P. Borri. Coherent anti-Stokes Raman scattering microscopy of single nanodiamonds. *Oral Presentation.* NaNaX6 - Nanoscience with nanocrystal, Bad Hofgastein, Austria, 18-23 May, 2014.

3. L. Payne, G. Zoriniants, F. Masia, W. Langbein, and P. Borri. Optical microspectroscopy of single metallic nanoparticles: Polarzation-resolved extinction and transient Four-Wave Mixing. *Poster Presentation.* NaNaX6 - Nanoscience with nanocrystal, Bad Hofgastein, Austria, 18-23 May, 2014.

4. L. Payne, W. Langbein, and P. Borri. Polarization-resolved extinction and scattering cross-sections of individual gold, silver, and diamond nanoparticles measured by wide-field microscopy on large ensemble. *Poster Presentation.* Bio-Nano-Photonics 2013, Cardiff University, Cardiff, UK, 16-17 Sept. 2013.

5. Polarization-resolved extinction and scattering cross-sections of individual gold, and silver, nanoparticles via wide-field microscopy on a large ensemble. *Poster Presentation.* ECONOS13, University of Exeter, Exeter, UK, 22-24 April, 2013.

Contents

Introduction

Nanoparticles of many varieties are becoming increasingly important in physical, chemical, and biological research, both for fundamental science, and for various applications. Metallic nanoparticles (NPs) exhibit morphology-dependent localized surface plasmon resonances (LSPR) which couple to propagating light and manifest as a resonant particle polarisability at the LSPR frequency. These local optical resonances can be exploited to image metallic NPs with high sensitivity and to probe nanoscale regions in the NP vicinity, via the local field enhancement effect, as well as to enhance the spontaneous emission of quantum emitters nearby (Purcell enhancement, antenna effect). Possible applications range from sub-wavelength optical devices [1], catalysis[2] and photovoltaics [3] to biomedical imaging [4,5] and sensing [6–8]. Furthermore, non-metallic nanoparticles, such as nanodiamonds, have shown promising potential in, for example, non-toxic drug/molecular delivery into live cells[9]. These particles could potentially be used for imaging[10], to study cellular localisation/mobilisation of biologically labeled materials.

Generally, fluorescence-based techniques dominate optical bioimaging. They offer an impressive resource for the imaging and measurement of cellular and molecular function. Some fluorescence techniques can achieve super-resolution, beyond the diffraction limit, which for optical wavelengths limits the resolution to around 200 nm. The super-resolution of these microscopes is achieved with the assistance of a fluorescent label, which can photobleach causing unwanted chemical side-effects, leading to cytotoxicity. Additionally, signal can be weak requiring long exposure times. Thus, imaging techniques capable of detecting single non-fluorescing NP-labels, under live-cell imaging conditions, and with similar resolution, would be relevant tools for optical bioimaging. Non-fluorescing NPs can sidestep problems, such as photobleaching, etc.,

but could also provide an enhanced platform for correlative studies with electron microscopy (EM). Various forms of EM are used for observing cellular structures at resolutions on the order of a nanometer or smaller[11], but live-cell imaging is not feasible. Often, correlative light-EM is performed in several steps, commencing with live-cell fluorescence imaging, after which the cell is flash frozen, and then imaged with EM. However, fluorophores are not typically visible with EM, unless equipped for cathodoluminescence, hence decreasing the direct correlative capabilities. In contrast, sufficiently large NPs would remain visible in EM. Use of non-fluorescing NPs as bioimaging labels has not been as thoroughly investigated as the use of fluorphores, though. Many current techniques for imaging single non-fluorescing NPs are less amenable to bioimaging. For example, differential interference contrast (DIC) microscopy[12], and Raman scattering[13], have been used to study non-fluorescing nanodiamonds. DIC is a wide-field, phase contrast technique, and hence is not label-specific. Raman scattering is chemically specific, but too slow to be useful in live-cell imaging. Metallic NPs, can be imaged in-situ, with a technique called photothermal imaging (PTI)[14]. In PTI a NP is periodically heated, in turn heating its environment. The induced change in the surrounding refractive index is then probed. It can be very sensitive, capable of detecting NPs down to 1.4 nm diameter[15]. However, PTI suffers from a background due to absorption by cellular structures, even in the absence of NPs[14,16]. Coherent anti-Stokes Raman scattering (CARS) microscopy and four-wave mixing imaging (FWM) of metallic NPs are two *nonlinear* imaging techniques, which are developed and applied in the Cardiff Biophotonics group. CARS is a reasonably established method in the nonlinear optical community. Using CARS, we recently demonstrated quantitative imaging of single non-fluorescing nanodiamonds, down to 60 nm diameter, in live cells[17]. FWM has been developed within the group, and has been used for *background-free* imaging of gold NPs, down to 10 nm, in HepG2 cells[5,18]. Since, both techniques are nonlinear, they are intrinsically sectioning, and offering a resolution beyond the standard diffraction limit. Furthermore, FWM lends itself to correlation with EM, as the large electron density of gold and silver NPs makes them commonly used, EM markers.

In order to understand and optimise the nonlinear imaging techniques of non-fluorescing NPs, we must first characterise the NP morphologies and linear optical

properties. The linear optical properties are summarised by the absorption, scattering, and extinction cross-sections. Since NPs useful in bioimaging are much smaller than visible wavelengths, their shapes and sizes are typically examined with scanning or transmission EM (SEM, TEM). NP samples are often provided by manufacturers in suspension, hence optical cross-sections are generally studied in an ensemble, via absorption spectroscopy. However, individual NP optical properties, in the ensemble, can differ significantly due to size, shape, and environmental variability. It is therefore important to study them at the single NP level. Several, techniques are currently used for single NP studies, including dark-field microscopy[19], photothermal imaging[4], and spatial modulation micro-spectroscopy[20]. These techniques can be sensitive and effective, but can be disadvantageous for reasons including lack of absolute units, measurement of only absorption *or* scattering, costly setups, and complex implementation. A simple and effective method, providing a rapid, sample-wide characterisation of the absorption and scattering optical cross-sections at the single NP level, would therefore be a significant progress in the field.

The research vision of this PhD project was to aid in the development of an optical "nanoscope", based on a combination of FWM imaging of metallic NPs, and CARS microscopy. As a basis of this development, it was necessary to develop a reproducible, robust method for the preparation and characterisation of metallic NPs, both individually, and in an ensemble. Specifically, we developed a wide-field optical extinction microscopy method to rapidly and quantitatively characterize the optical properties of NP samples. This thesis will explore the wide-field technique, and its results, in detail. Furthermore, covalent binding of NPs either to glass, or to each other to form NP dimers has been investigated. Development and characterisation of these samples, with wide-field optical extinction and FWM microscopy, will be discussed. Beyond linear optical studies, we present of FWM imaging to outline development of an in-situ imaging modality, based on metallic NP dimers acting as "plasmon rulers."

This thesis is structured as follows: Chapter 1 introduces the relevant physical and mathematical background, necessary for the description of the experimental techniques, and the discussion of the results obtained during this research. Chapter 2 explores the instruments, materials, experimental setups, and more standard meth-

ods, like glass cleaning, sample preparation, etc., used during this work. Chapter 3 describes the unique preparation of NP samples, via covalent binding of NPs to glass, or to each other for dimerisation studies. Chapter 4 presents the wide-field extinction microscopy, and extinction spectroscopy techniques developed within this PhD. Furthermore, it shows results obtained with these techniques on NPs of various sizes, shapes and materials. Chapter 5 describes the results of correlative FWM/TEM imaging of gold NP-dimers. It serves as a proof-of-concept for the use of FWM to measure nanometric distances, in-situ, via the interparticle distance dependence of the dimer LSPR peak position. The main topics and achievements, covered in the body of the thesis, are summarised in the conclusion.

CHAPTER 1

Background concepts

In this chapter, physical background relevant to the methods and analysis in this work is reviewed. We begin with basic considerations of the interaction of EM fields and matter in the linear field regime, moving through a discussion of the polarisability, electric susceptibility, and the optical properties of nanoparticles. The dielectric function and its importance in determining the optical properties of metals are then considered as precursor to a discussion of the optical properties of metallic particles. Finally, the discussion of EM fields and matter is then extended to include effects in the non-linear field regime.

1.1 Interaction of light with nanoparticles

1.1.1 Polarisability and optical cross-sections

An important aspect of the NPs, with regards to the research presented in this work, is their optical response. Light interaction with spherical objects has been studied for quite some time, with significant work from Lord Rayleigh (1842 – 1919) and Gustav Mie (1869 – 1957), after whom Rayleigh and Mie scattering are named. Rayleigh scattering approximates the interaction of light with particles whose diameter are much smaller than the incident wavelength. This regime allows use of the dipole approximation, i.e. the particle is small enough with respect to the wavelength of incident light, that it can be regarded as a point-like oscillating electric dipole. Mie scattering, on

the other hand, uses the exact solution to Maxwell's equations for *spherical* particles. Therefore, generally, it describes light interaction with a sphere, regardless of the relation between the size of the sphere and the wavelength of incident radiation. A core concept distinguishing the two theoretical approaches is that, when a particle is much smaller than the wavelength, the phase of the field is assumed to be homogenous over the particle region. For larger particles, the varying phase of the field over the particle is a consequence of electromagnetic (EM) retardation effects. For the purposes of NP research at optical wavelengths, the Rayleigh regime is suited for particle diameters below $\sim 60\,\text{nm}$.

We will use the complex formalism to describe an incident field, **E**. A plane wave propagating in the z-direction, and linearly polarised in the x-direction, is given by

$$\underline{\mathbf{E}} = \Re\left\{E_0 \mathrm{e}^{i(kz-\omega t+\phi)}\right\}\hat{x} = \Re\left\{\mathbf{A}\mathrm{e}^{i(kz-\omega t)}\right\} \tag{1.1.1}$$

$$\underline{\mathbf{E}} = \frac{1}{2}\left(\mathbf{A}\mathrm{e}^{i(kz-\omega t)} + \text{c.c.}\right), \tag{1.1.2}$$

where $\Re$ is the real part, c.c. is the complex conjugate of the terms on its left side, **A** is the complex amplitude, ω is the frequency, ϕ is the phase, $k = n\omega/c$ is the wavevector with vacuum wavelength, $\lambda_0 = 2\pi c/\omega$, in a medium of refractive index, n, and $\hat{\mathbf{x}}$ is the unit vector pointing in the x-direction. The complex amplitude is given by $\mathbf{A} = \hat{\mathbf{x}}E_0\mathrm{e}^{i\phi}$. In our notation convention, the underline indicates a real amplitude, bold lettering indicates a vector quantity, and * indicates the conjugate of a complex amplitude.

We begin by looking at the effect of an incident EM field on a material. All materials undergo an induced polarisation when in the presence of an EM field. In simple terms we can say there is a displacement of the electrons in the media, with respect to the corresponding nuclei. This is treated, microscopically, in terms of the atomic polarisability, α_P, by[21]

$$\mathbf{p} = q\mathbf{d} = \alpha_\text{P}\mathbf{E}_\text{i}, \tag{1.1.3}$$

with, **p**, the dipole moment associated with the charge, q, and the separation distance, **d**, of the electron cloud from the ionic centre, due to an incident field, $\mathbf{E}_\text{i}$. Note, **p**, by convention, points in the direction of the movement of the positive charge. However, in the zero frequency case, the field generated by the charge separation points in the opposite direction, counteracting the incident field. The polarisability is in general a

tensor, however, it is a scalar in the simple case of an atom. We can see why, by considering a small molecule, like carbon dioxide (CO_2). The structure of CO_2 is symmetric in one direction with an oxygen on either side of the carbon, with O=C=O. The orientation of this molecule, with respect to the field is important, because the molecule appears different when approached from different directions. Thus, the polarisability must also be different, for the different axes of the molecule.

The single atom, or molecule, in the presence of a field are special cases. In most situations, e.g. in media, an atom or molecule, is surrounded by other charges. As a result, $\mathbf{E}_\mathrm{i}$ cannot be considered to be due only to the incident field, but also to any charges, other induced dipoles, etc. in the surrounding medium. Simply put, $\mathbf{E}_\mathrm{i}$ is the field due to everything, *except* the dipole in question[21].

In an extended structure, we use the dipole moment per unit volume, also called the polarisation, $\mathbf{P}$, such that $\mathbf{p} = \mathbf{P}\mathrm{d}V$, with $\mathrm{d}V$ an infinitesimal volume element. Macroscopically, the field in the medium, due to the polarisation, is given by the sum of all of the fields due to each of the infinitesimal dipolar elements, $\mathbf{P}\mathrm{d}V$. In the linear response regime, i.e. for small fields (and excluding spontaneous polarization like ferroelectricity), the polarisation is[21]

$$\mathbf{P} = \epsilon_0 \chi \mathbf{E}, \tag{1.1.4}$$

with the electric permittivity of free space given by ϵ_0, the electric susceptibility by χ, and the *total* field including incident field, contributions from the polarisation, etc., by $\mathbf{E}$. χ is a unit-less measure of how easily a substance can be polarised, and is material-dependent. In general χ is a tensor, the off-diagonal elements of which describe the coupling between different vector components of the induced polarisation in a material. Let us consider glass, an amorphous solid, where, on average over the optical mode volume, $(\lambda/2)^3$, no significant distinction can be made as different directions are traversed in the material. This is an example of an homogeneous isotropic medium. In this case, χ is a scalar. However, some crystals are anisotropic, and in these cases χ cannot be reduced to a scalar. In the isotropic and linear case, the polarisation is given by Eq. 1.1.4. The susceptibility tensor will be discussed further in Sec. 1.2. The superposition of the total field and induced polarisation result in the electric displacement,

given by[21]

$$\mathbf{D} = \epsilon_0 \mathbf{E} + \mathbf{P} = \epsilon_0 (1 + \chi)\mathbf{E} = \epsilon_0 \epsilon_\mathrm{r} \mathbf{E} = \epsilon \mathbf{E}, \tag{1.1.5}$$

where ϵ_r is the relative electric permittivity, also known as the dielectric constant. It is given relative to ϵ_0, such that $\epsilon = \epsilon_0 \epsilon_\mathrm{r}$[21,22]. ϵ_r is related to the refractive index, n, by $\epsilon_\mathrm{r} = n^2$. In general, a material may be absorbing, so that n is complex, and given by $\tilde{n} = n + i\kappa$, with n the refractive index, and κ the absorption index. n is related to the phase velocity of the EM wave in the medium, while κ is a measure of attenuation of the field. This can be seen by inserting $\tilde{n}$ into Eq. 1.1.1, giving[22]

$$\mathbf{E}(z) = \mathbf{A}\mathrm{e}^{i(2\pi(n+i\kappa)z/\lambda_0 - \omega t)} = \mathrm{e}^{-2\pi\kappa z/\lambda_0}\mathbf{A}\mathrm{e}^{i(kz-\omega t)}. \tag{1.1.6}$$

We can see that κ leads to an exponential decay of the field along the propagation distance, z, in the material. Since, the intensity is proportional to the square modulus of the field, we have

$$I(z) = I_0 \mathrm{e}^{-4\pi\kappa z/\lambda_0} = \mathrm{I}_0 \mathrm{e}^{-\alpha_\mathrm{ac} z}, \tag{1.1.7}$$

where α_ac is the absorption coefficient. The Beer-Lambert law relates the absorption of light to the properties of a material through which it is traveling, by[23]

$$A(\lambda) = -\log\left(\frac{T}{T_0}\right) = \epsilon_\mathrm{mol} c_\mathrm{m} l, \tag{1.1.8}$$

with T the intensity of light transmitted through a distance, l, of a medium, with a concentration of absorbing material, c_m, and molar extinction coefficient, ϵ_mol, and T_0 the initial intensity. The molar extinction coefficient is related to the attenuation coefficient by $\epsilon_\mathrm{mol} = \alpha_\mathrm{ac}/c_\mathrm{m}$. The Beer-Lambert law can also be expressed as[23]

$$A(\lambda) = -\ln\left(\frac{T}{T_0}\right) = \sigma_\mathrm{abs} n_\mathrm{p} l, \tag{1.1.9}$$

where σ_abs is the absorption cross-section, and n_p is the number density of absorbers in the medium. We can relate σ_abs to α_ac with $\sigma_\mathrm{abs} = \alpha_\mathrm{ac} \log_{10}(\mathrm{e})/n_\mathrm{p}$. Note, in general, χ, ϵ_r and n, are functions of the frequency, ω, of the incident field. Since the fields are a function of time, it must be noted that the induced polarisation does not occur instantaneously. Rather, the polarisation is induced as a result of the exciting field at some time previously. Hence, in general, $\mathbf{P}(t)$ is related to $\mathbf{E}(t - t_\mathrm{r})$, with the time retardation given by $t_\mathrm{r} > 0$[21].

We can treat a small particle, with a size much smaller than the wavelength of the incident light, as a point dipole. The field due to the particle, and thus the polarisability, is effectively extracted by relation of Eq. 1.1.3 to Eq. 1.1.4[21], i.e. the field inside the NP is related to the field outside the NP, taking into account the susceptibilities of the surrounding medium, and of the particle. For a spherical particle, in the Rayleigh regime, it can be shown that the polarisability is given by[24–28]

$$\alpha_{\mathrm{P}} = 4\pi\epsilon_0 R^3 \frac{\epsilon_{\mathrm{p}} - \epsilon_{\mathrm{m}}}{\epsilon_{\mathrm{p}} + 2\epsilon_{\mathrm{m}}}, \tag{1.1.10}$$

where ϵ_{p} is the dielectric function inside the particle, ϵ_{m} is the dielectric function of the surrounding medium, and R is the radius of the particle. Eq. 1.1.10 is known as the Claussius-Mossotti homogenization[21,24]. Fig. 1.1 illustrates the effects of an incident field on a metallic nanoparticle.

The description of polarisability for particles within the dipole regime, can be extended to ellipsoidal particles, via Gans theory[29,30]. The geometry of the ellipsoid is characterised by three semi-axes, of lengths a_1, a_2, and a_3. Analytical integral equations are available in the general case of a particle of 3 semi-axes with different lengths. However, a closed form solution is only known if two of the lengths are the same[31]. In this work, we choose a_1 to be the long axis, and assume $a_2 = a_3$ to be the short axes, i.e. a prolate particle, such that the polarisability tensor, $\widehat{\alpha}$, is given in the main axis coordinate system by

$$\widehat{\alpha} = \begin{pmatrix} \alpha_1 & 0 & 0 \\ 0 & \alpha_2 & 0 \\ 0 & 0 & \alpha_2 \end{pmatrix}, \tag{1.1.11}$$

where α_1 and α_2 are the polarisabilities of the long and short axes, respectively. The polarisabilities are determined by,

$$\alpha_{\mathrm{i}} = V \frac{\epsilon_{\mathrm{p}} - \epsilon_{\mathrm{m}}}{\epsilon_{\mathrm{m}} + L_{\mathrm{i}}(\epsilon_{\mathrm{p}} - \epsilon_{\mathrm{m}})}, \tag{1.1.12}$$

with V the volume, and the index i indicating the major ($i = 1$) or minor ($i = 2$) semi-axis of the ellipsoid. The depolarisation factors, L_{i}, are given by

$$L_1 = \left(1 - \frac{1}{e^2}\right)\left(1 - \frac{1}{2e}\ln\left(\frac{1+e}{1-e}\right)\right), \quad L_2 = \frac{1 - L_1}{2}, \tag{1.1.13}$$

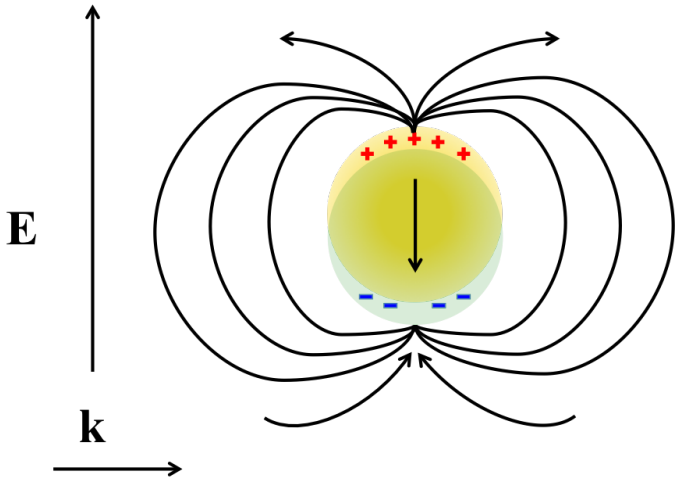

Fig. 1.1: Illustration of the effect of an incident electromagnetic field, as in Eq. 1.1.1, on conduction electrons, and the resulting dipolar polarisation, within the metallic nanoparticle.

with $e = \sqrt{1 - a_2^2/a_1^2}$, the eccentricity of the ellipsoid. If the particle is spherical, $L_1 = L_2 = L_3 = 1/3$, and Eq. 1.1.10 is reproduced.

Polarisabilities result in the scattering and absorption cross sections, σ_{sca} and σ_{abs}, respectively, whose sum is called the extinction cross-section, σ_{ext}. The extinction cross-section is the effective area of interaction, between the NP and an incident plane-wave EM field. σ_{ext} is defined as

$$\sigma_{\text{ext}} = \frac{P_{\text{ext}}}{I_{\text{i}}}, \tag{1.1.14}$$

with I_{i} the incident intensity, and P_{ext} the power loss in the forward direction, induced by both absorption and scattering. σ_{sca} and σ_{abs} are each similarly defined[32]. The absorption and scattering cross-sections, in the dipole approximation, are expressed as[30,31]

$$\sigma_{\text{abs}} = \sum_{\text{i}=1}^{3} \frac{k}{\epsilon_0} \Im[\alpha_{\text{i}}] \qquad \sigma_{\text{scat}} = \sum_{\text{i}=1}^{3} \frac{k^4}{6\pi\epsilon_0^2} |\alpha_{\text{i}}|^2, \tag{1.1.15}$$

where $\Im$ denotes the imaginary part, and i indicates the semi-axis. If the particle is spherical, Eq. 1.1.15 reduces to

$$\sigma_{\text{abs}} = \frac{k}{\epsilon_0} \Im[\alpha_{\text{P}}] \qquad \sigma_{\text{scat}} = \frac{k^4}{6\pi\epsilon_0^2} |\alpha_{\text{P}}|^2, \tag{1.1.16}$$

We will discuss the particular case of metallic NPs after introducing the free-electron models for description of the dielectric function of metals.

1.1.2 Drude and Drude-Sommerfeld free-electron models

Metals are highly conductive, because a fraction of the electrons in the bulk material are not bound to single atoms, but can move freely around the material. This is very important in metallic NPs, because it leads to coherent oscillations of these conduction electrons in the presence of a time-dependent electric field. While bound electrons are still shifted from their natural atomic orbits, the more significant effect here is the coherent shift of the conduction electron cloud about the entire particle. This concept is pictured in Fig. 1.1. The simplest theory describing the motion, and hence conductivity, of electrons in a metal is the Drude model, or free electron model[27,29,33]. The electrons are treated as a free electron gas, amidst static nuclei. The only interactions are assumed to be collisions, between the freely moving electrons and other electrons, lattice ions, phonons, etc., which occur at an effective rate, $\gamma_b = 1/\tau_\mathrm{r}$, with γ_b the bulk damping constant, τ_r the relaxation time. The magnitude and direction of the electrons will be changed upon collision. Note, the electrons will move collectively with an average drift velocity, v_d, in the direction of the field. v_d is used to determine the conductivity, $\sigma_\mathrm{c} = ne_-^2\tau_\mathrm{r}/m$, with n_e the number density of electrons, e_- the electron charge, and m the mass of an electron. The Fermi velocity, v_f is the group velocity of the electrons at the Fermi edge of the band structure. It is v_f, and τ_r, which determine the mean free path, with $l_\mathrm{f} = v_\mathrm{f}\tau_\mathrm{r}$, i.e. the path length between collisions. The conductivity can be used to determine the dielectric function of the metal, leading to[27,29,33]

$$\epsilon(\omega) = 1 - \frac{\omega_\mathrm{p}^2}{\omega(\omega + i\gamma_\mathrm{b})}, \tag{1.1.17}$$

with the plasma frequency, $\omega_\mathrm{p} = \sqrt{n_e e_-^2/\epsilon_0 m\omega^2}$. However, as mentioned only a certain fraction of the electrons in the metal are actually conduction electrons. The Sommerfeld free electron model takes the Pauli-exclusion principle into account. Only electrons near the Fermi level can contribute to the conductivity, since the core electrons cannot change their electronic state[27,29,33]. In this case, v_r becomes v_f, the Fermi velocity, and the mass becomes the effective mass. The latter is derived from considerations of band structure[27,29,33]. Neither the classical Drude model, nor the Drude-Sommerfeld model, take into consideration excitation of deeper lying electrons into the conduction band. A term can be added to Eq. 1.1.17 to account for bound elec-

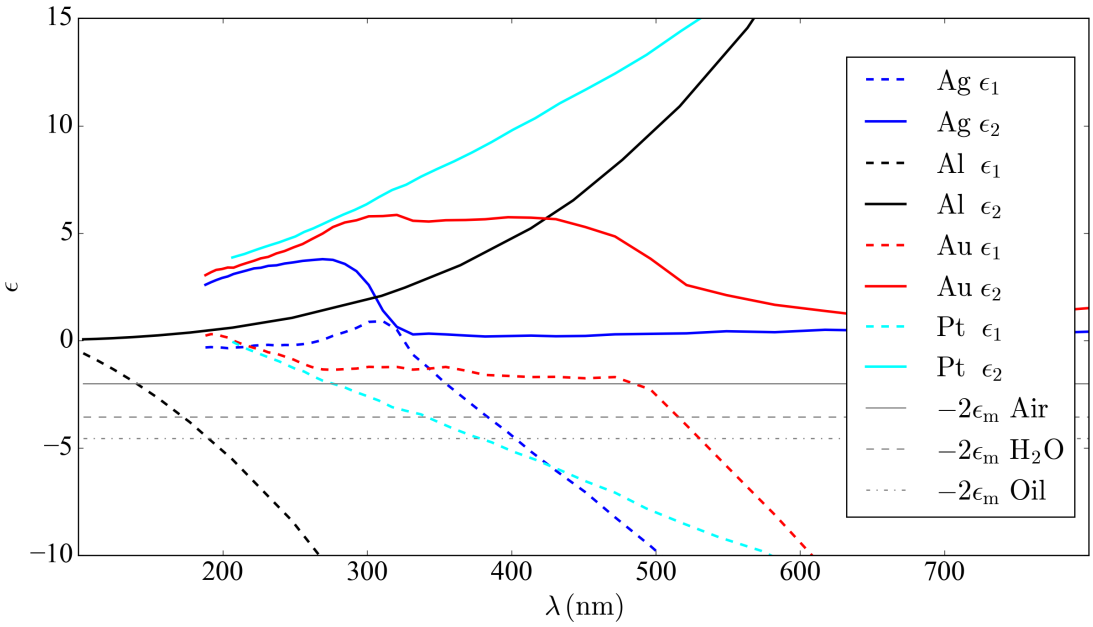

Fig. 1.2: Complex dielectric function ϵ_1 (dotted lines) and ϵ_2 (solid lines), for four different metals; Ag, Al, Au, and Pt, with data for Au and Ag from Ref. 35, for Pt from Ref. 36, and for Al from Ref. 37. Data was not available below $\lambda \approx 200\,\text{nm}$ for Ag, Au, or Pt. Note, -2ϵ_m is shown for air, H_2O, and oil for ease of reference.

trons associated with the interband transitions[29,33,34], giving

$$\epsilon(\omega) = \epsilon^{\text{ib}}(\omega) + 1 - \frac{\omega_\text{p}^2}{\omega(\omega + i\gamma_\text{b})}, \tag{1.1.18}$$

with $\epsilon^{\text{ib}}(\omega)$ the interband contribution. From Eq. 1.1.17 and Eq. 1.1.18, we see that the dielectric function of a metal has real and complex parts. So, we express the complex dielectric function, as $\epsilon_\text{r} = \epsilon_1 + i\epsilon_2$. The complex part is related to damping, which is significantly increased by the interband absorption. The real and imaginary parts of the dielectric functions of gold (Au), silver (Ag), aluminium (Al), and platinum (Pt), measured by reflectance and transmission measurements on thin films, can be seen in Fig. 1.2. In metals, the Fermi energy lies within a band. Au, Ag, and Al have full 5d, 4d, and 3s shells, respectively. This leads to Fermi energies 5.53 eV, 5.49 eV, and 11.7 eV[33], in the next highest and partially filled bands, 6s, 5s, and 3p, respectively. Pt, on the other hand, has a configuration, whereby the 5d band is left unfilled. The final electron sits in the 6s shell, since it has a lower energy than the last remaining 5d state. Thus, the Fermi energy of Pt, at 9.74 eV, is in the d-band, resulting in conduction electrons

from two bands, namely 5d and 6s. Looking at ϵ_2 in Fig. 1.2 we can see the onset of the interband absorption, i.e. the difference in energy between the top of the d-band and the Fermi energy, for Au and Ag, around 516 nm (2.4 eV) and 318 nm (3.9 eV)[29]. In the case of Pt, ϵ_2 is very large across the range. This can be attributed to the large density of states and increased electron-electron scattering, due to the position of the Fermi surface within the d-band. Al, on the other hand, exhibits comparatively small ϵ_2, within the presented domain, with no significant features. These effects have important implications for the magnitude of the optical cross-sections, as well as LSPR peak position and linewidth, as will be discussed in Sec. 1.1.3.

1.1.3 Optical cross-sections of metallic NPs

The largest extinction cross section occurs at what is known as the localized surface plasmon resonance (LSPR). The LSPR is defined to be the frequency at which the polarizability is maximum, hence approximately when the denominator of Eq. 1.1.10, and thus Eq. 1.1.19, is minimized, i.e. when $\epsilon_1 = -2\epsilon_\mathrm{m}$. Metals exhibit the important characteristic that the real part of the dielectric function can be negative, making this requirement possible. The size of the extinction cross-section, depends on the frequency of the incident radiation, particle size and shape, and NP and host materials. To see the effect of the NP material on the LSPR position, linewidth, and magnitude of the cross-sections, we can put Eq. 1.1.16 into a more explicit form, by writing σ_abs and σ_sca in terms of the real and imaginary parts of ϵ_r, given by[30]

$$\sigma_\mathrm{abs} = \frac{18\pi V \epsilon_0 \epsilon_\mathrm{m}^{\frac{3}{2}}}{\lambda_0} \frac{\epsilon_2}{(\epsilon_1 + 2\epsilon_\mathrm{m})^2 + \epsilon_2^2} \qquad \sigma_\mathrm{scat} = \frac{24\pi^3 V^2 \epsilon_0 \epsilon_\mathrm{m}^2}{\lambda_0^4} \frac{(\epsilon_1 - \epsilon_\mathrm{m})^2 + \epsilon_2^2}{(\epsilon_1 + 2\epsilon_\mathrm{m})^2 + \epsilon_2^2} \tag{1.1.19}$$

Upon examination of Eq. 1.1.19, we see a resemblance to the Cauchy, or Lorentz, distribution, described by

$$f(x; x_0, \Gamma) = \frac{1}{\pi} \frac{\Gamma}{\Gamma^2 + (x - x_0)^2}, \tag{1.1.20}$$

where x_0 and Γ are the mode and half-width at half-maximum (HWHM), respectively. Hence, inspecting Eq. 1.1.19, we can infer that ϵ_1, and ϵ_2, (corresponding to x_0 and Γ), determine the LSPR position and resonance linewidth, respectively. We can see from Fig. 1.2, that for Ag with $\lambda \in (350, 410)$ nm and for Au with $\lambda \in (490, 550)$ nm,

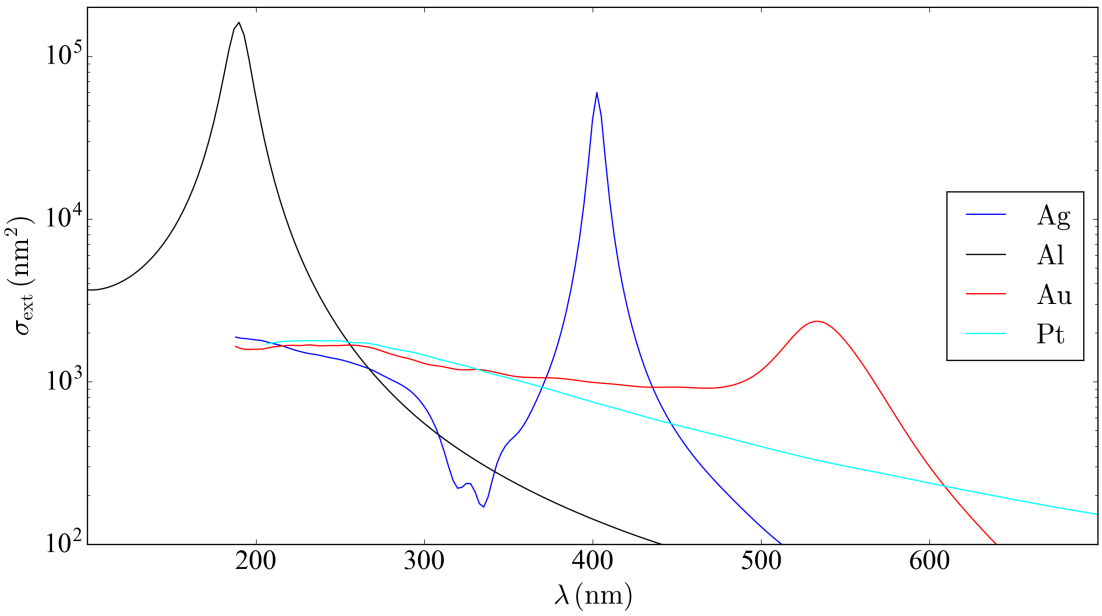

Fig. 1.3: Calculated σ_{ext} for a 30 diameter particle in oil, with $n = 1.51$, for a particle made of Ag, Al, Au, or Pt, as labeled. Data for the dielectric function are as in Fig. 1.2

$\epsilon_1 \in (-5,-2)$, coincident with $-2\epsilon_{\mathrm{m}}$ of common immersion media, e.g. air, water, oil, etc. Al and Pt display this behavior in the ultraviolet, at about 190 nm and 350 nm, respectively. Fig. 1.3 shows the extinction cross-section for the metals in Fig. 1.2, in the case of a particle of 30 nm diameter, in a medium of refractive index $n = 1.51$. The difference in the imaginary part of ϵ amongst the different metals, as well as the k and k^4 scaling of absorption and scattering, leads to very different magnitudes of σ_{ext}. Al displays a small ϵ_2 at the LSPR, leading to a narrow linewidth, and a large cross-section ($2 \times 10^5\,\mathrm{nm}^2$). The onset of interband transitions from the d-band to the conduction band in gold is close to the LSPR frequency. This leads to a plateau, visible on the blue side of the extinction spectrum. Furthermore, the increased damping due to this interband absorption leads to a comparatively small cross-section and broad linewidth. The onset of interband absorption is blue-shifted from the LSPR for Ag, allowing for a narrow linewidth and large cross-section ($10^4\,\mathrm{nm}^2$). The minimum in σ_{ext}, on the short wavelength side of the Ag LSPR, is due to the change of sign of the real part of epsilon, around 320 nm, at the onset of the d-band absorption. ϵ_1 quickly becomes negative again, around $\lambda = 300$ nm, at which point we see a similar plateau to that of gold. Note,

in practice, the large values of σ_{ext} for Al and Ag are not easily observed, due to rapid surface oxidation by atmospheric oxygen, or sulphur, respectively. Unlike, the other three metals, Pt does not exhibit a clear resonance. While there is an increase in σ_{ext} around 275 nm, corresponding to $\epsilon_1 = -2\epsilon_{\text{m}}$, ϵ_2 dominates the extinction spectrum, leading to a broad absorption.

We now consider the effect of the host material refractive index on Ag and Au. From air ($n \approx 1$) to oil ($n = 1.51$), ϵ_{m} varies from 1 to 2.28. Hence, inspecting Fig. 1.2, the LSPR is red-shifted by nearly 50 nm for an NP in oil, compared one in air. In Au, this leads to significantly decreased damping, due to interband absorption. The red-shift can be understood as the result of increased charge screening for increased refractive index in the surrounding medium. The more highly polarisable the host material, the more the field at the NP will be mitigated, slowing the oscillation of the conduction electrons, and leading to the red-shift in the LSPR.

At this point it is pertinent to introduce some qualitative discussions regarding the effect of size, shape, and environment on the LSPR, in terms of resonance position, width, and strength, as well as on the relative strengths of absorption and scattering. For spherical particles in the Rayleigh limit, the polarisability, and hence, the magnitudes of the cross-sections, are functions of particle size, and of the frequency. Taking into account retardation, the LSPR frequency gains a size dependence, displayed by Mie theory. From experimentation and Mie theory, it is evident that the peak red-shifts with increasing particle size[25,27,38,39]. As particle size increases, the inhomogeneous phase leads to electromagnetic retardation effects, which in turn leads to increased radiative damping and the characteristic red-shift[25,27,31,32,40]. For very small particles, e.g. <10nm, where particle size and the mean free path of electrons become comparable, the effective medium description by the bulk ϵ is modified. In this case, there is also a theoretically predicted red-shift caused by increased electron-surface scattering[39,41,42]. Blue-shifts have also been reported, and attributed to quantum confinement[39,43]. Fig. 1.4, 1.5, & 1.6 show the effects of particle size, and host medium refractive index, on the optical cross-sections and LSPR peak positions. Other important effects relating to particle size/environment, are the relative contributions of scattering and absorption to the extinction, and the width of the resonance. In order to under-

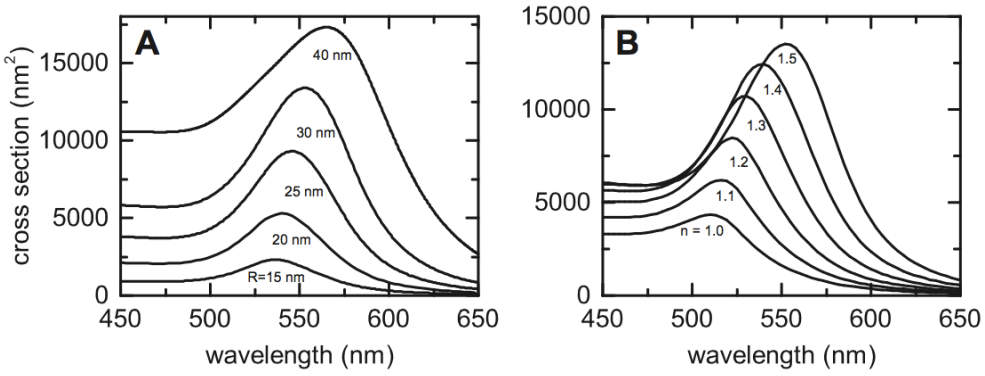

Fig. 1.4: Absorption spectra of AuNP with (A) various radii as given for $n_{\mathrm{m}} = 1.5$, and (B) for increasing refractive index, n_{m}, with a diameter, $D = 60\,\mathrm{nm}$. Figure reproduced from Ref. 32 with permission.

stand these effects, we discuss the decay, or damping, of the LSPR, which can be radiative or non-radiative. The radiative decay converts the plasmon into a photon and creates scattering. The non-radiative decay converts the plasmon into a single electron excitation, given by interband or intraband electronic transitions. For any metal, the conduction electrons can be excited, via intraband transitions, within the conduction band. These transitions are weak, since they do not respect k-conservation within the band. Additional interband transitions are present from lower-lying bands, such as the d-bands in Au. The non-radiative decay creates absorption, the end result of which, is the relaxation of the electron excitation, via electron electron scattering (within the first few 100 fs), and via electron phonon scattering in the first few picoseconds, and the dissipation of the excess energy as heat[27,29,34].

The various decay mechanisms discussed determine the width of the resonance. In Au, and to a lesser extent, in Ag, interband absorption plays a role in broadening the resonance, particularly on the high energy (short wavelength) side of the spectrum. This can be seen clearly in Fig. 1.3 , 1.4, and 1.6, where the resonance is asymmetrical, with a plateau appearing in the blue part of the spectrum. The interband damping can be avoided, by shifting the resonance to the red. Hence, importantly, increasing particle size, or host medium refractive index, can lead to a decrease in interband damping at the LSPR, which decreases the width of the resonance. However, as the particle size becomes much larger, radiative damping increases, and multipole modes become more

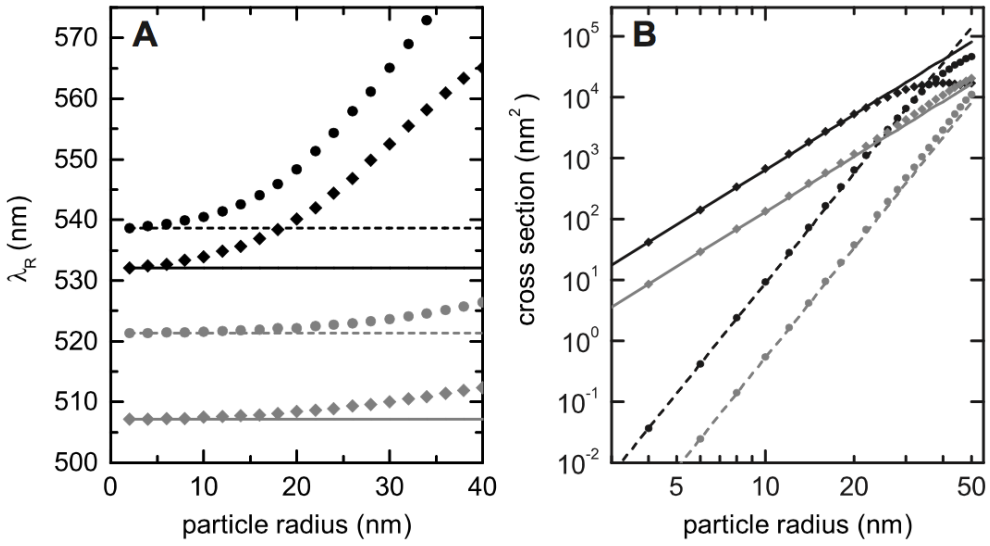

Fig. 1.5: (A) Comparison of the LSPR wavelength of AuNPs in the dipole approximation and for Mie theory, for $n_m = 1.0$ (grey) and $n_m = 1.5$ (black). The circles (Mie) and dashed lines (dipole) represent scattering, the diamonds (Mie) and solid lines (dipole) represent absorption. (B) Comparison of the absorption and scattering cross sections at the resonance wavelength in the dipole approximation and for Mie theory, for $n_m = 1.0$ (grey) and $n_m = 1.5$ (black). The symbol coding is the same as in (A), note the log-log scale. Figure reproduced from Ref. 32 with permission.

prominent[24,25,27,44]. This leads to a broadening of the resonance, even as non-radiative damping is reduced by the red-shift of the frequency. The dominance of scattering or absorption in the extinction, is an interplay, between the damping mechanisms in the decay of the plasmon. The size-dependent effects on broadening of the resonance, and increase of the σ_{sca} relative to σ_{abs} and σ_{ext}[25,27,32,45], can be seen in Fig. 1.6.

Elongated particles can also be manufactured, such that they exhibit red-shifted resonances, due to the high aspect ratio. This can be seen directly from Eq. 1.1.12, and 1.1.13. For a rod of high aspect ratio, L_1 decreases, leading to a minimal denominator for $\epsilon_1 = -\epsilon_m(1-L_1)/L_1$. In the case of an aspect ratio of 2:1, we have $L_1 = 0.174$, and $L_2 = 0.413$. For the long axis, the new LSPR occurs, in oil, for $\epsilon_1 = -10.8$. Referring to Fig. 1.2, this leads to a red-shift of the LSPR of nearly 100 nm. Significantly, for Au, this means the LSPR position is sufficiently red-shifted to be far below the frequency threshold of the interband absorption. Furthermore, $\sigma_{sca}/\sigma_{abs} \propto V$, hence, by keep-

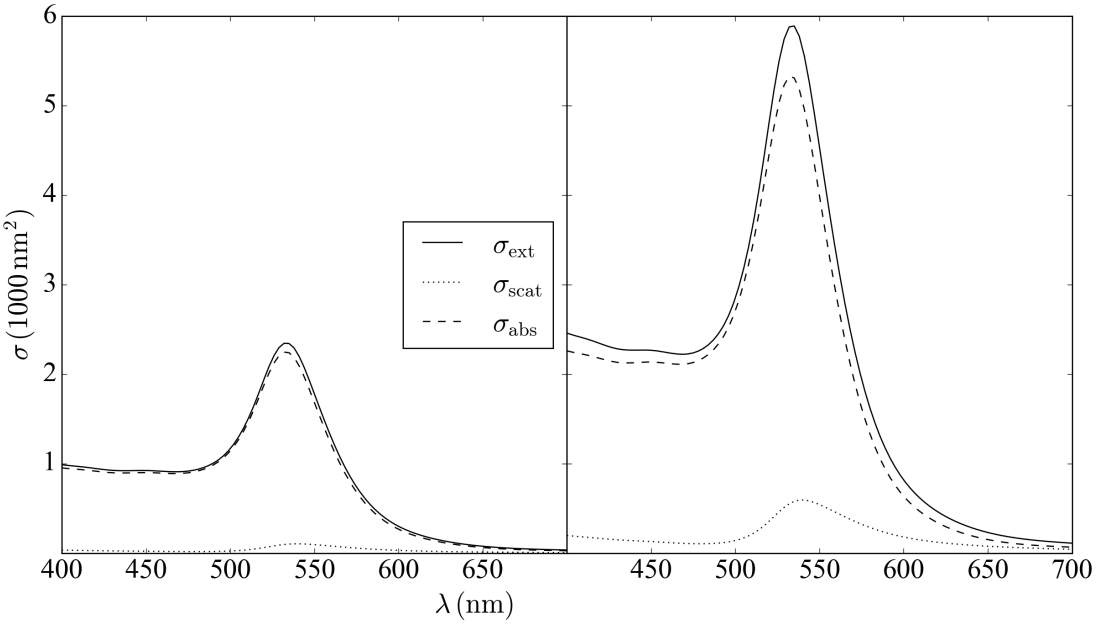

Fig. 1.6: Calculated σ_{ext}, σ_{abs}, and σ_{sca} spectra of an AuNP of 30 nm diameter (left) and 40 nm diameter (right). Calculations were made using Eq. 1.1.16, with dielectric function data from Ref. 35. The refractive index of the environment is $n_m = 1.51$.

ing the overall size (volume) of the particles small, the radiative damping can be controlled. As a result the rods exhibit an almost Lorentzian-lineshaped, and spectrally narrow, LSPR. This has been shown with gold nanorods of high aspect ratio[27,38].

Unique NP geometries represent an increasingly investigated field. For instance, nanodisks[46], oblate spheroids, or rod-like particles[25,38], NP dimers and aggregates[8,47,48], exhibit interesting effects on LSPR linewidth, peak position tunability, and field enhancements. Nanorods have been shown to yield very large fields at the tips relative to spherical NPs of similar material and size. NP dimers, i.e. coupled single NPs, display increased field strengths in the gap. These special shapes/formations have been proposed as potentially improved models for signal enhancement in fluorescence[49,50] and surface enhanced Raman studies[48,51], compared to their spherical counterparts. Furthermore, dimers exhibit an LSPR along the dimer axis, whose peak position is dependent upon the interparticle distance[8,41,47,52]. The detection of the shift of the LSPR as a result of changing interparticle distance has been suggested as a nanometric sensor, also called a "plasmon ruler"[8,41,47,53]. The symmetric longitudinal mode of NP dimers

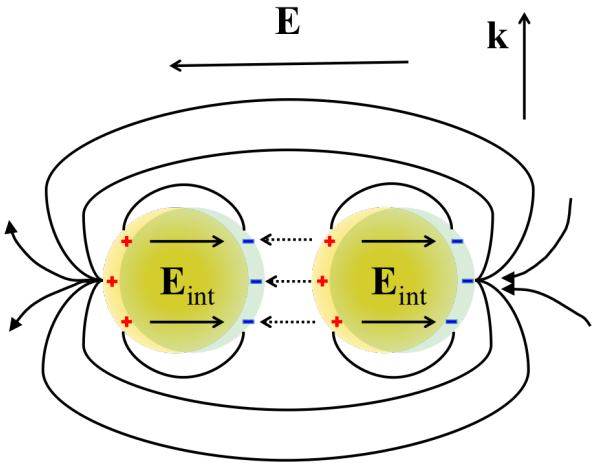

Fig. 1.7: Illustration of the effects of coupling two NPs. The gold circles represent the metallic NPs, and the green transparent circles represents the NP electron clouds.

displays a red-shift for decreasing interparticle distance. The coupling between the particles acts to decrease the restoring force of the individual particle nuclei, resulting in the red-shift. This is drawn schematically in Fig. 1.7. The dependence of the LSPR peak position on gap size is presented versus the gap size to particle diameter ratio, G/D, which is correct in the Rayleigh regime where λ does not constitute an additional scaling parameter. The G/D dependence is frequently fitted, in literature, with an exponential decay function of the form[48,53],

$$\frac{\Delta\lambda}{\lambda_0} = f\mathrm{e}^{-\frac{G}{D\tau}}, \tag{1.1.21}$$

with $\Delta\lambda/\lambda_0$ the fractional change in the wavelength from the LSPR peak position of the single particle, and f and τ fit parameters. We note that this fit does not have the correct limiting behaviour, both for small and for large distances. The dipole-dipole interaction is more appropriately described[48] by $(G/D)^{-3}$. This equation relates the potential due to the interparticle coupling, which is proportional to G^{-3} to that of the single NP restoring potential[48], proportional to $1/V = 1/D^3$.

1.2 Nonlinear optics

1.2.1 Introductory concepts

The linear response, described in the previous section, is valid if the susceptibility is not influenced by the EM field. With increasing field strength, significant changes of the susceptibility occur, so that the material response has to complemented by nonlinear terms in the field. This section gives a brief introduction to nonlinear optical phenomena, relevant to the FWM experimental section of this work. It is based Ref. 54.

In linear media, $\mathbf{P}$ is given by Eq. 1.1.4, with a complex amplitude, $\mathbf{P} = \epsilon_0 \chi \mathbf{A}$. In the presence of intense EM fields, $\mathbf{P}$ becomes nonlinearly dependent on the magnitude of $\mathbf{E}$. To describe this dependence, $\mathbf{P}$ can be expanded in a power series with

$$\mathbf{P} = \epsilon_0 \chi^{(1)} \mathbf{A} + \epsilon_0 \chi^{(2)} \mathbf{A}^2 + \epsilon_0 \chi^{(3)} \mathbf{A}^3 + ... + \epsilon_0 \chi^{(\mathrm{m})} \mathbf{A}^{\mathrm{m}}, \tag{1.2.1}$$

where m represents a given order of the susceptibility. Here, $\chi^{(1)}$ is called the linear susceptibility. $\chi^{(2)}$ and $\chi^{(3)}$ are the second- and third-order nonlinear susceptibilities, respectively. Typically, $\chi^{(\mathrm{m})}$ is a rank $m++1$ tensor[54]. That is, for an incident field with three vector components, χ has 3^{m+1} terms. In most cases increasing orders of χ correspond to higher order terms in $\mathbf{P}$, which are decreasing in magnitude. In Sec. 1.1.1, we considered a linear and isotropic material, where χ is a scalar. In the linear and anisotropic case, χ becomes the second rank tensor, $\chi^{(1)}$. As an example, the x-component of $\mathbf{P}$, can be represented as

$$P_{\mathrm{x}} = \epsilon_0 \left(\chi_{\mathrm{xx}} A_{\mathrm{x}} + \chi_{\mathrm{xy}} A_{\mathrm{y}} + \chi_{\mathrm{xz}} A_{\mathrm{z}} \right), \tag{1.2.2}$$

where, χ_{xx}, χ_{xy}, and χ_{xz} refer to the xx, xy, and xz correlative components of $\chi^{(1)}$. The polarization per unit volume can then be represented in a condensed form as

$$P_{\mathrm{i}} = \epsilon_0 \chi^{(1)}_{\mathrm{ij}} A_{\mathrm{j}}, \tag{1.2.3}$$

where we sum over repeating indices. Thus, $\chi^{(1)}$ has 9 terms. With the second-order nonlinear susceptibility, $\mathbf{P}$ becomes

$$P_{\mathrm{i}} = \epsilon_0 \chi^{(2)}_{\mathrm{ijk}} A_{\mathrm{j}} A_{\mathrm{k}}. \tag{1.2.4}$$

$\chi^{(2)}$ has 27 terms and is now dependent on two incident field vectors. Increasing orders of χ are treated with the same approach, resulting in large numbers of independent components.

We can now consider the resulting radiation when a field is applied to an anisotropic, nonlinear medium. The form of Eq. 1.1.2 will be used in the following so we can clearly observe the contribution of different frequencies in the nonlinear polarization. Furthermore, this form allows us to explicitly see the contribution of the complex conjugates in the nonlinear generated fields, i.e. ω and $-\omega$ are distinct. In this section we will treat both χ and the applied field E as scalars to simplify notation. Take the polarization, up to second order, in the case of two applied fields, with

$$\underline{E} = \frac{1}{2}\left(A_1 \mathrm{e}^{i(k_1 z-\omega_1 t)} + \mathrm{A}_2 \mathrm{e}^{i(k_2 z-\omega_2 t)}\right) + \text{c.c.}, \tag{1.2.5}$$

as

$$\underline{P} = \epsilon_0 \chi^{(1)} \underline{E} + \epsilon_0 \chi^{(2)} \underline{E}^2. \tag{1.2.6}$$

We can separate this into two parts, namely linear and nonlinear terms, such that,

$$\underline{P} = \underline{P}^{\mathrm{L}} + \underline{P}^{\mathrm{NL}}. \tag{1.2.7}$$

So we have

$$\underline{P}^{\mathrm{L}} = \frac{\epsilon_0 \chi^{(1)}}{2}\left(A_1 \mathrm{e}^{i(k_1 z-\omega_1 t)} + \mathrm{A}_2 \mathrm{e}^{i(k_2 z-\omega_2 t)}\right) + \text{c.c.} \tag{1.2.8}$$

Now for $\underline{P}^{\mathrm{NL}}$, we need to look at $\underline{E}^2$, which is given by,

$$\begin{aligned}\underline{E}^2 = \frac{A_1 A_1^* + A_2 A_2^*}{2} + \frac{A_1^2}{4}\mathrm{e}^{2i(k_1 z-\omega_1 t)} + \frac{\mathrm{A}_2^2}{4}\mathrm{e}^{2i(k_2 z-\omega_2 t)} \\ + \frac{A_1 A_2}{2}\mathrm{e}^{-i((\omega_1+\omega_2)t-(k_1+k_2)z)} + \frac{\mathrm{A}_1\mathrm{A}_2^*}{2}\mathrm{e}^{i((k_1-k_2)z+(\omega_2-\omega_1)t)} + \text{c.c.}\end{aligned} \tag{1.2.9}$$

Hence,

$$\begin{aligned}\underline{P}^{\mathrm{NL}} = \epsilon_0 \chi^{(2)}\Bigg(\frac{E_1^2 + E_2^2}{2} + \frac{E_1^2}{4}\mathrm{e}^{2i(k_1 z-\omega_1 t+\phi_1)} + \frac{\mathrm{E}_2^2}{4}\mathrm{e}^{2i(k_2 z-\omega_2 t+\phi_2)} \\ + \frac{E_1 E_2}{2}\mathrm{e}^{-i\left((\omega_1+\omega_2)t-(k_1+k_2)z-(\phi_1+\phi_2)\right)} + \frac{\mathrm{E}_1\mathrm{E}_2}{2}\mathrm{e}^{i\left((k_1-k_2)z+(\omega_2-\omega_1)t+(\phi_1-\phi_2)\right)}\Bigg) + \text{c.c.}\end{aligned} \tag{1.2.10}$$

From Eq. 1.2.8, we see that the linear response of the material does not generate different frequencies. However, the second-order nonlinear polarisation in Eq. 1.2.10

presents terms, which are nonlinear combinations of the original fields, namely a non-oscillating term describing a static induced polarization,

$$\epsilon_0 \chi^{(2)} \frac{E_1^2 + E_2^2}{2},$$

components oscillating at twice the original frequencies

$$\frac{\epsilon_0 \chi^{(2)} E_1^2}{4} \mathrm{e}^{2i(k_1 z - \omega_1 t + \phi_1)} + \text{c.c.} \quad \& \quad \frac{\epsilon_0 \chi^{(2)} \mathrm{E}_2^2}{4} \mathrm{e}^{2i(k_2 z - \omega_2 t + \phi_2)} + \text{c.c.},$$

and components oscillating at sum and difference frequencies,

$$\frac{\epsilon_0 \chi^{(2)} E_1 E_2}{2} \mathrm{e}^{-i((\omega_1+\omega_2)t - (k_1+k_2)z - (\phi_1+\phi_2))} + \text{c.c.} \quad \& \quad \frac{\epsilon_0 \chi^{(2)} \mathrm{E}_1 \mathrm{E}_2}{2} \mathrm{e}^{i((k_1+k_2)z + (\omega_2-\omega_1)t + (\phi_1-\phi_2))} + \text{c.c.}$$

The components at $\pm 2\omega_1$ and $\pm 2\omega_2$ are proportional to the square of the input field at each frequency, and are called the second harmonic frequencies of the input fields. The components at the sum and difference frequencies are proportional to the product of the two input field amplitudes. These processes are examples of three-wave mixing, since two input fields lead to generation of a third at a new frequency. The creation of sum frequencies, and difference frequencies, is termed sum-frequency generation (SFG) and difference-frequency generation (DFG), respectively. The case where $\omega_1 = \omega_2$, is a special case of SFG, called second harmonic generation (SHG). Also, note the phase offsets, namely $2\phi_1$, $2\phi_2$, $\phi_1 + \phi_2$, and $\phi_1 - \phi_2$, which appear in the generated fields. The phases of the generated fields are different from each other and from the input fields.

1.2.2 $\chi^{(3)}$ effects and four-wave mixing

In this thesis, the nonlinear experiments focus on the effects of $\chi^{(3)}$ nonlinearities. In a general sense, FWM processes are analogous to the three-wave mixing processes resulting from excitation of the $\chi^{(2)}$ response. Since, we have more coupling terms in $\chi^{(3)}$, we can generate more frequencies. We have

$$\underline{P}(\omega; \omega_1, \omega_2, \omega_3) = \epsilon_0 \underline{\chi}^{(3)} \underline{E}(\omega_1) \underline{E}(\omega_2) \underline{E}(\omega_3), \tag{1.2.11}$$

with ω on the left side of the semi-colon indicating a generated frequency, and terms on the right side of the semi-colon indicating input frequencies. Note, in the special

case of $\omega = \omega_1 = \omega_2 = \omega_3$, the analogous process to SHG in $\chi^{(3)}$ is called third-harmonic generation (THG), and it results in a fourth wave at frequency $\omega_4 = 3\omega$.

Most importantly for this work, specific $\chi^{(3)}$ nonlinearities act as a modification of the refractive index. If we let $\omega_1 = \omega_2 = \omega_3$, then one part of the third-order polarisation is

$$P(\omega) = \epsilon_0 \chi^{(3)} E(\omega) E^*(\omega) E(\omega) \tag{1.2.12}$$

$$= \epsilon_0 \left(\chi^{(3)} E E^*\right) E(\omega) \tag{1.2.13}$$

$$= \frac{2}{cn} \left(\chi^{(3)} I\right) E(\omega). \tag{1.2.14}$$

The interference of the first two fields induces a change in the nonlinear susceptibility. That change modifies the refractive index by the addition of a nonlinear term proportional to $\chi^{(3)}$ and I, the intensity of the applied field. These effects are material-dependent. This is a key concept of the FWM technique, since we can choose to tune the frequency of the FWM to be resonant with the LSPR of a metallic NP. Further discussion on this topic is reserved for Sec. 5.2, and will serve as preparation for the experimental work in Sec. 5.3.

CHAPTER 2

Setups, materials, and methods

In this chapter, we explore the various devices and setups used to perform the experiments described in Chapters 3, 4, and 5. We begin by examining the microscope stand, optics, and cameras, which are the basis of the majority of experimental techniques in this work. Two spectrometers, namely a cuvette-based modular absorption spectrometer, and a Czerny-Turner type imaging spectrometer and associated detectors, are then investigated. Next, the optical and lock-in amplifier schemes of the FWM mixing setup are described in detail. Miscellaneous items are listed at the end of the chapter.

2.1 Microscopy setup

The experimental set-up consists of an inverted microscope (Nikon Ti-U) equipped with an 100 W halogen white-light illumination of adjustable intensity, a Nikon neutral color balance (NCB) filter or Hoya light balancing optical blue filter (LB200), an oil condenser of 1.4 numerical aperture (NA) with a removable home-built dark-field illumination of 1.1-1.4 NA, a choice between a 40x 0.95 NA dry objective and a 100x 1.45 NA oil objective, and 1x or 1.5x intermediate magnification. The LB200 and NCB filter transmission spectra are given in Appendix A.1 and Appendix A.2, respectively. The sample position is finely controlled, by a xyz-piezoelectric stage (nanostage). The nanostage is Mad City Laboratory model NanoLP200, with $\sim$ 0.4 nm accuracy and 200 μm range. A consumer Canon EOS 40D color camera (in the following abbreviated

Fig. 2.1: Photograph of the left side of the Ti-U microscope. The 40D is attached to the left port of the microscope. The PCO is attached to the eye-piece side port.

as 40D), with a 14-bit CMOS detector, containing 2592 x 3888 pixels (10.1 megapixel), of 5.7 μm pixel pitch, and full-well capacity, $N_{\mathrm{fw}} = 4 \times 10^4$, is attached to the left port of the microscope. A PCO Edge 5.5 (abbreviated as PCO), low noise (1.1 electron read noise), capable of 100 frames per second (FPS) for full sensor, grayscale (b/w), water-cooled, scientific-CMOS camera (sCMOS), with 2560 x 2160 pixels (5.5 megapixel), of 6.5 μm pixel pitch, and $N_{\mathrm{fw}} = 3 \times 10^4$ is attached to the eye-piece side port. A view of the left side of the microscope, with the cameras can be seen in Fig. 2.1. The microscope can be seen in profile with objective turret, nanopositioning stage, condenser mount and lamp housing/filter sliders in Fig. 2.2. The right port of the microscope (not shown) couples light either from/to the FWM setup, described in Sec. 2.5, or to the imaging spectrometer setup, described in Sec. 2.2.1. Setup selection is controlled by a flip mirror. When in place, the microscope image is reflected towards a Horiba Jobin-Yvon iHR 550 imaging spectrometer. The flip mirror and FWM beam paths can be seen in Fig. 2.10.

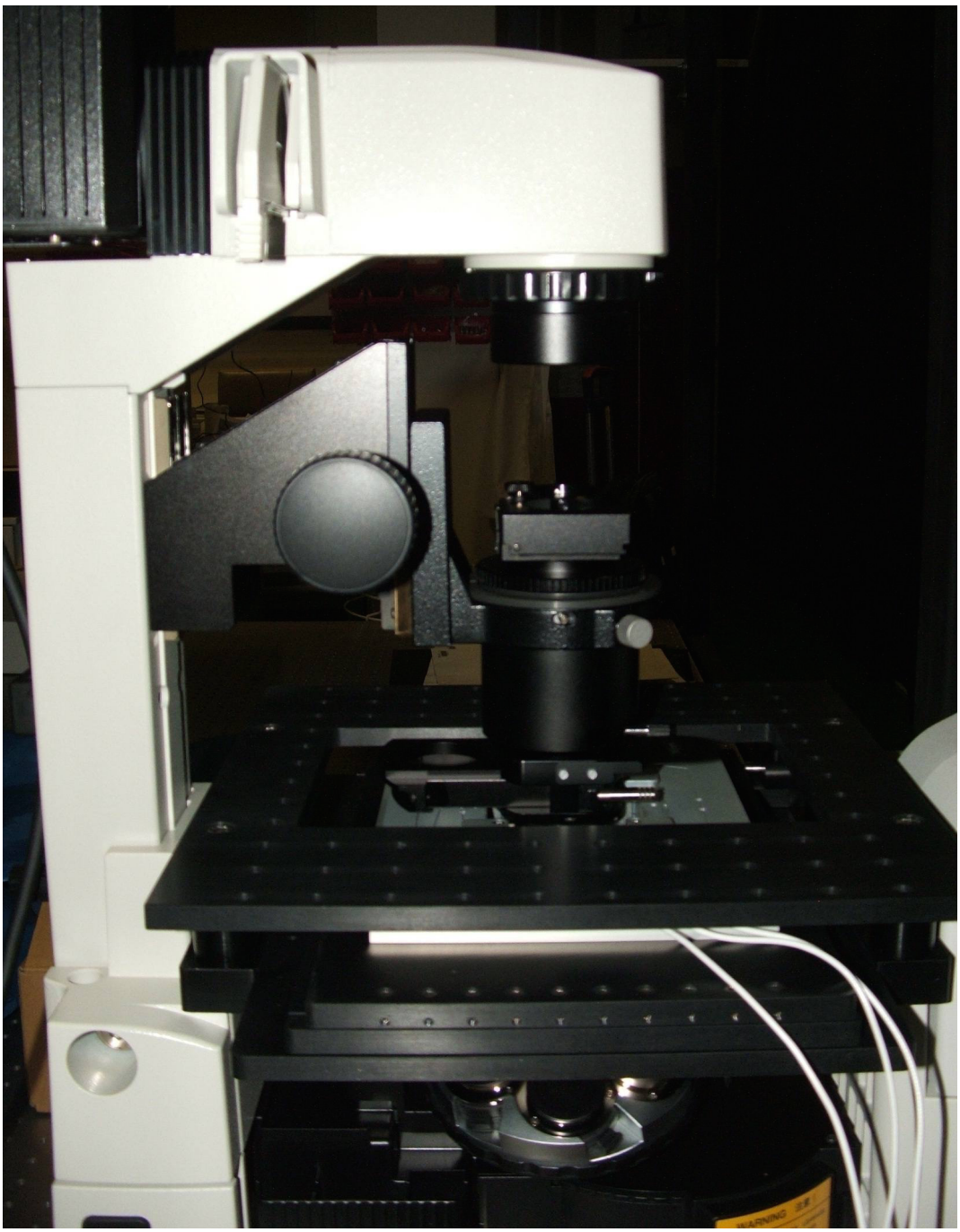

Fig. 2.2: A profile image of the microscope body, objective turret (below stage), nanopositioning stage, condenser mount, and lamp housing/filter sliders.

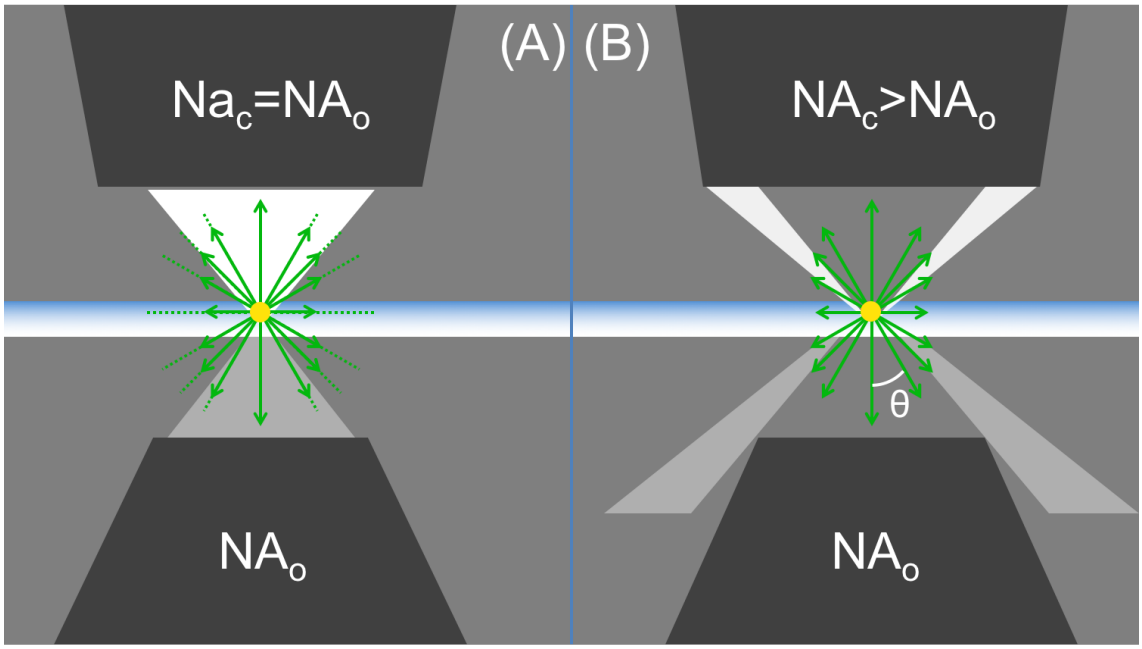

Fig. 2.3: A drawing of the brightfield (A) and darkfield (B) schemes, depicting the excitation geometries in both cases, and the resulting collection by the objective. The solid (dotted) green rays indicate dipolar (isotropic) scattering. The illumination is represented by white triangles on the excitation side of the sample, and by gray triangles on the collection side. The grayscale color difference portrays the power lost from the incident light due to absorption (A) and scattering (A & B) by the particle. In (B) θ indicates the angle between the forward direction ($\theta = 0$) and a scattered ray.

2.1.1 Brightfield and darkfield configurations

In brightfield microscopy, the condenser numerical aperture (NA_c) is matched to the objective NA (NA_o). This is the transmission configuration we employ in the wide-field extinction technique (see Sec. 4.2.1). In a transmission setup, a NP in the field of view will absorb and scatter light, resulting in a loss of power in the transmitted field. We measure this power loss as the extinction. We also use darkfield microscopy to observe scattering of NPs. In a darkfield setup, NA_c must not be overlapping NA_o. This is typically achieved by blocking the excitation at $NA_c \leq NA_o$, using a darkfield ring, leaving only excitation for $NA_c > NA_o$, which the objective does not transmit. On an ideally clean substrate, there would be no light reaching the observer, in darkfield geometry. However, if anything is present on the substrate, e.g. a NP, a piece of debris, a cell, etc.,

it will scatter light in all directions. The objective can collect a fraction of this scattering. The two schemes are schematically shown in Fig. 2.3. In our setup, the 1.4 NA oil condenser is used for all experiments. The 0.95 NA objective can be used for darkfield and transmission microscopies. For the latter, the aperture iris of the condenser is closed down to limit the condenser NA to that of the objective. This is performed by removing the eyepiece, and closing the iris until the edge just becomes visible. The 1.45 NA objective is restricted to brightfield transmission microscopy, and the aperture iris is left fully open in this case. As part of this setup, a linear polariser was also put into place in the illumination of the Ti-U, above the condenser. The polariser can be rotated to achieve polarisations in steps of 15° from 0° – 180°. A cut was made in the polariser sheet to allow selection of unpolarised excitation. Polariser angle was controlled, using a servo, by the MultiCARS software (see Sec. 2.5).

2.1.2 Consumer camera Canon 40D

The 40D produces images in 14-bit .CR2 (Canon proprietary) raw format with 10.1 megapixel resolution. The images were converted using the DCRAW plugin in ImageJ, providing 16bit RGB images with a linear response to intensity and no color balancing (see Sec. 4.2.4.2 for a more detailed description of the image-handling). The color camera enables a coarse spectroscopic detection separating the three wavelength ranges of red (R) 570-650 nm, green (G) 480-580 nm, and blue (B) 420-510 nm. The 10.1 megapixel sensor is made up of $2.52 \cdot 10^6$ Bayer pixels, which are each constructed of 4 color pixels in the pattern $1B:2G:1R$ (see Sec. 4.2.4.2 for more details). Quantum efficiency (QE) can be measured across the visible spectrum for each of the color pixels, but the effective, or geometric, quantum efficiency (GQE) takes the Bayer pattern into account. A factor, f, is determined by the number of pixels of a given color divided by the 4 color pixels of the Bayer pixel, so $GQE = f \times QE$, with f given by, 0.25 for the B and R pixels, and 0.5 for the G pixels. The GQE for the 40D is shown in Fig. 2.4. The 40D has a range of shutter speeds from 30 s to 1/4000 s, as well as a range of light sensitivities, with ISO from 100 to 3200, with ~ 1/3 intermediate stops available. Use of shutter speeds faster than ~ 1/500 s produces images exhibiting intensity gradients due to the lag of the mechanical shutter. We use shutter speeds on the order 1/100 s for

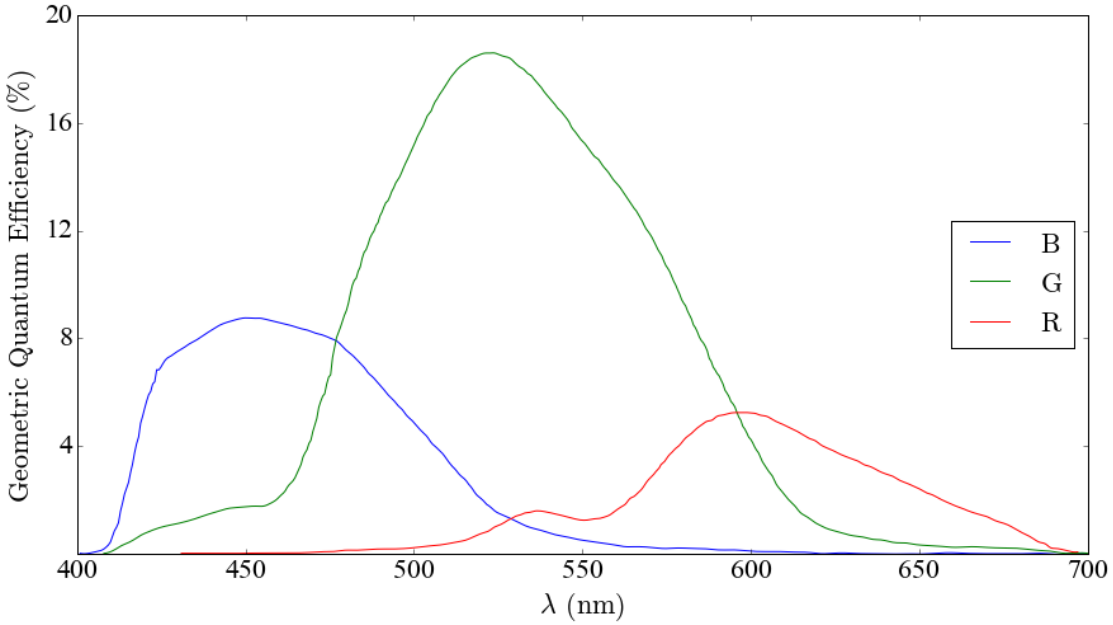

Fig. 2.4: The GQE for Bayer pixels of the Canon 40D taken from Ref. 55.

experiments. For all measurements in this work, we use ISO 100 for lowest shot noise. A detailed analysis of the 40D noise, saturation, and gain is provided in Appendix B.2. The camera is used in remote connection mode, via USB to a PC, with mirror lock-up. This provides the convenience of remote live-view, which outputs the live image to the computer screen. A subject imaged by a digital single lens reflex (DSLR) camera can be viewed through the eyepiece, or by the built-in LCD monitor, available on many models. In order for the subject to be viewed through the eyepiece, light entering the lens is reflected up by a mirror. When the shutter release is pressed to capture an image, the mirror flips up, allowing the light to pass straight to the sensor, where the shutter then controls exposure time. For some situations, a user may wish to keep the mirror locked in the “up" position, e.g. digital live-view, so only the shutter is involved in the capture process. We noted that mirror lock-up is a requirement for sensitive measurements, since the mechanical action of the mirror vibrates the microscope sufficiently to blur the image of NPs. The Canon EOS Utility software, which remotely controls the 40D, does not allow for timed capture of image sequences, when the mirror is locked up, meaning images must be captured manually by the user in remote live view. This is performed by clicking the trigger release icon in the EOS utility program. Further-

more, framerates are limited by the transfer rate of the USB to ~ 2 frames per second (FPS) depending on the speed and regularity of the user's mouse clicks. This leads to practical limitations in terms of the number of images possible to capture in a single experiment with the 40D.

2.1.3 Scientific CMOS camera PCO.edge 5.5

A distinct advantage of the PCO is the fast framerate of 100 FPS at full sensor size. In addition, the region of interest (ROI) is adjustable allowing decreased storage size, and increased framerates, e.g. 397 FPS for 400 x 400 pixel ROI. Maximum framerates are also determined by: (1) available memory and/or write-speeds of the harddisk, (2) the connection to the PC. In our setup the connection is provided by cameralink cables, mediated by the Microenable IV cameralink framegrabber PCIe card, enabling 790 MB/s transfer rate. PCO integration times range from 1ms to 2 s for 286 MHz readout speed. The PCO also features online averaging up to 256 frames per (saved) image. Output images can be saved as 16-bit Tiff image type. Spectroscopic detection was achieved with the PCO using bandpass filters (Semrock) in the excitation beam path, in the wavelength ranges of 470 ± 11 nm for blue, 530 ± 20 nm for green and 607 ± 18 nm for red. Filter transmission spectra are given in Appendix A.3. Analysis of the noise, saturation, and gain of the PCO is given in Appendix B.1.

2.1.4 Ti-U transmission illumination settings and filters

Most of the widefield extinction measurements described in Sec. 4.2.1 were performed using the 30 W lamp setting, which has a visibly red hue, compared to the blue-white color of the 100 W setting. We use the 30 W setting, because it provides more spectrally even illumination, *in combination with the blue LB200 filter*. By increasing the relative strength of the blue part of the lamp spectrum with the LB200, we can more evenly approach saturation across the three color channels of the Canon 40D. The effect of the LB200 on the output spectrum of the 7 W HL2000 lamp of the Ocean Optics (OO) setup (discussed in Sec. 2.2.2), can be seen in Fig. 2.5. With any configuration we can approach saturation ($\sim 2^{13.5}$ counts of the 2^{14} count range) of the Canon camera at fast

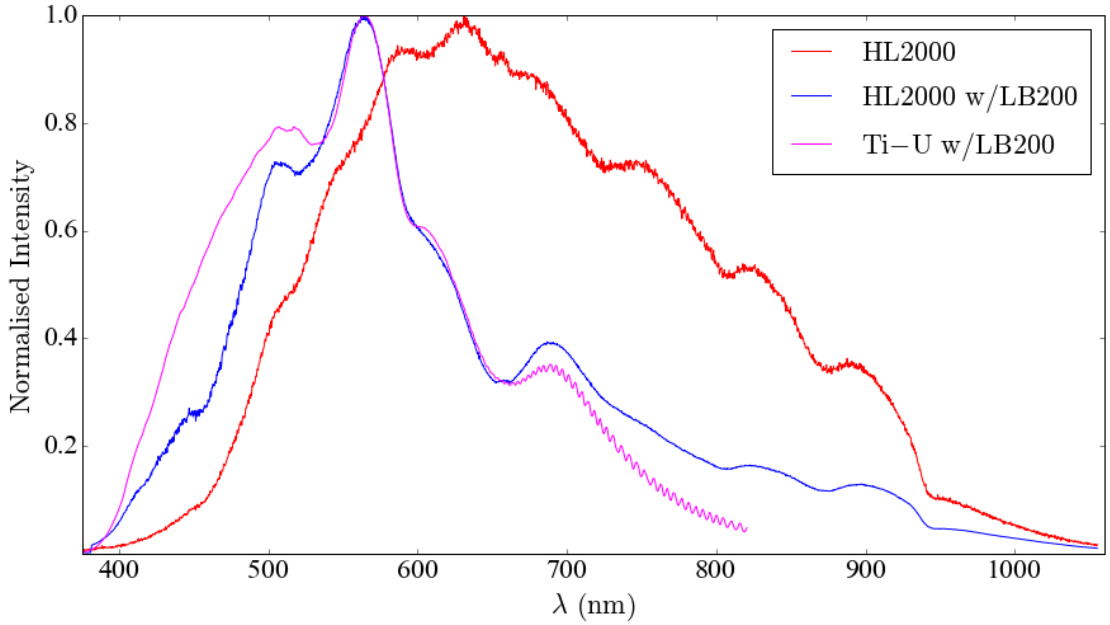

Fig. 2.5: Normalised intensity spectra of the Ti-U (100 W) and HL2000 (7 W) lamps. The two HL2000 spectra are differentiated by the effect of the LB200 filter. The Ti-U spectrum, measured with the iHR550 spectrometer discussed in Sec. 2.2.1, is shown only for the case where the LB200 was used.

exposure times (e.g. 1/100 s), hence the excitation intensity is not a concern. This is not the case for the extinction spectroscopy experiments, discussed in Sec. 4.8. The 100 W input power setting is needed to provide sufficient light to the spectrometer, keeping intensity counts high ($\sim 2^{15.5}$ of the 2^{16} count range), integration times lower (typically 0.1 s), and hence improving noise, and decreasing overall measurement time. The output spectrum of the 100 W lamp setting of the Ti-U, with LB200 filter, is shown in Fig. 2.5.

In order to assess the effect of lamp wattage on the excitation spectrum, we modeled the lamp filament as a blackbody radiator. Planck's Law describes the spectral radiance per unit solid angle per unit area of the radiating surface per unit wavelength, and is given by[56]

$$B_\lambda(\lambda, T) = \frac{2hc^2}{\lambda^5} \frac{1}{e^{\frac{hc}{\lambda k_b T}} - 1}, \tag{2.1.1}$$

where $h = 4.136 \times 10^{-15}$ eVs is Planck's constant, and $k_b = 8.617 \times 10^{-5}$ eVK^{-1} is the Boltzmann constant, and T is the temperature. To find the total power emitted by the

radiator per unit wavelength, we integrate Eq. 2.1.1 over the surface area of the radiator, S, and the solid angle, Ω, constituted by the hemisphere above the surface, which we will denote with, he, using

$$P_\lambda = \int_h \int_S B_\lambda(\lambda, T)\, \mathrm{d}A\, \mathrm{d}\Omega \tag{2.1.2}$$

To evaluate the integral of the solid angle, we assume the radiator satisfies Lambert's cosine law, such that the intensity of radiation making an angle, θ, with the surface normal is proportional to $\cos(\theta)$. In spherical coordinates, $\mathrm{d}\Omega$ is given by

$$\mathrm{d}\Omega = \sin\theta\, \mathrm{d}\theta\, \mathrm{d}\phi, \tag{2.1.3}$$

with θ the polar angle, and ϕ the azimuth angle. Thus, we find

$$P_\lambda = A \cdot \int_0^{\pi/2} \int_0^{2\pi} B_\lambda(\lambda, T) \cos\theta\, \sin\theta\, \mathrm{d}\theta\, \mathrm{d}\phi. \tag{2.1.4}$$

This leads to

$$P_\lambda = \pi\, A\, B_\lambda(\lambda, T). \tag{2.1.5}$$

We use the Stefan-Boltzmann law to relate the power and surface area of the filament to temperature, with[57]

$$T = \left(\frac{P}{A \varepsilon \sigma_{\mathrm{sb}}} \right)^{1/4}, \tag{2.1.6}$$

where T is the temperature in Kelvin, P_{in} is the lamp wattage, A the surface area of the filament, ε is the emissivitty, and σ_{sb} is the Stefan-Boltzmann constant. For an ideal blackbody, $\varepsilon = 1$. A was deduced from the filament dimensions $(4.8 \times 3.0)\,\mathrm{mm}^2$, given by the company specifications (bulb model Philips 77241 100W GY6.35 12V 1CT). We assume the filament has no depth, but two surfaces so that, $A = (2 \times 4.8 \times 3.0)\mathrm{mm}^2 = 2.88 \times 10^{-5}\,\mathrm{m}^2$. The 30 W and 100 W inputs then result in temperatures, $T = 2070\,\mathrm{K}$, and $T = 2797\,\mathrm{K}$, respectively. P_λ is shown in Fig. 2.6, for input powers, $P_{\mathrm{in}} = 30\,\mathrm{W}$ and $P_{\mathrm{in}} = 100\,\mathrm{W}$. An area of interest for us is the short wavelength portion of the spectrum, corresponding to expected position of the AgNP LSPR peak, so we present a zoom over the region (390-450) nm. To find the total power radiated in a given spectral range (λ_1, λ_2), we can integrate Eq. 2.1.5,

$$P_{\mathrm{em}} = \pi\, A \int_{\lambda 1}^{\lambda 2} B_\lambda(\lambda, T)\, \mathrm{d}\lambda. \tag{2.1.7}$$

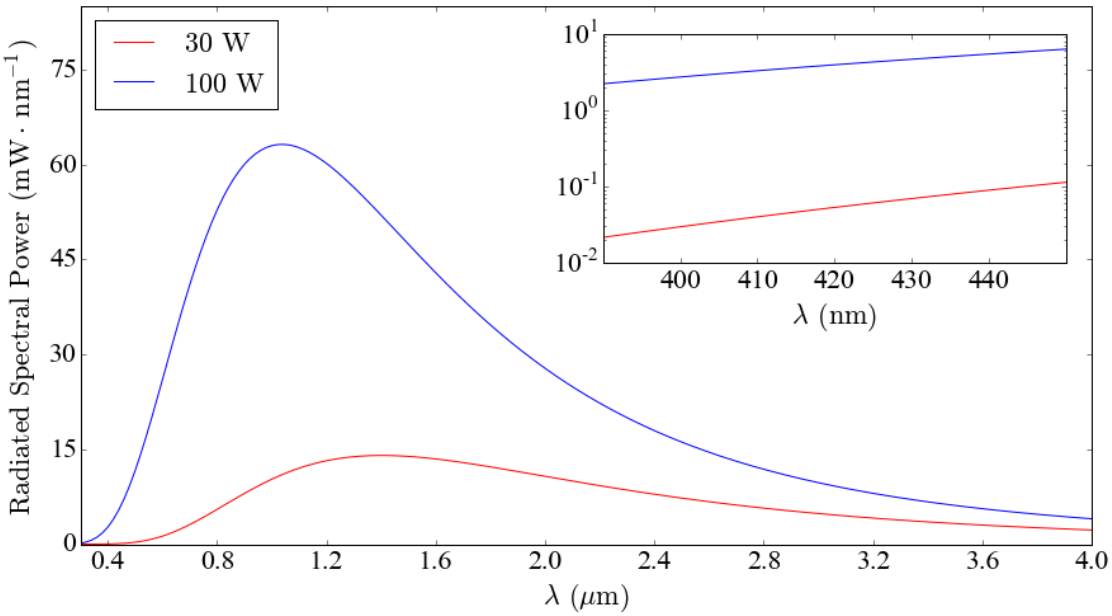

Fig. 2.6: The spectral power radiated by a blackbody at temperatures, 2070 K ad 2797 K, corresponding to P_{in}=30 W and P_{in}=100 W, respectively. The inset shows a zoom over the range (390-450) nm, with log-scale y-axis.

In the range (390-450) nm, we find that for 30 W input power the blackbody radiates ~ 3.5 mW, compared to ~ 241 mW for 100 W input, corresponding to a factor ~ 70 difference.

2.2 Spectroscopy setups

2.2.1 Extinction spectroscopy with imaging spectrometer

The Jobin-Yvon iHR550 spectrometer is an imaging spectrometer of the Czerny-Turner type. In this type of spectrometer, the light enters through a slight, is collimated and reflected by a concave mirror onto a diffraction grating, which disperses the light onto another mirror. The second mirror refocuses the spectrally dispersed images of the entrance slit, onto an exit slit of approximately the same width. This mirror is toroidal, compensating for the off-axis astigmatism and allowing for imaging on both directions of the output. In our setup, an Andor Newton DU-971N CCD camera, with a 1600 x 400

pixel sensor, of pixel pitch $W_p = 16\,\mu$m, is attached to the exit port of the microscope. The vertical pixels of the sensor allow spatial imaging of the sample, while the horizontal pixels are used for spectroscopy. The input slit opening, W_s, is adjustable. In this work we use $W_s = 60\,\mu$m. The iHR550 was equipped with a 100 lines/mm grating, providing a spectral range, $\Delta\lambda \sim 450$ nm over the detector, as measured. The optical coupling between the microscope and spectrometer is such that the intermediate image plane of the objective is imaged onto the slit of the spectrometer, and the back focal plane of the objective onto the grating. The grating is 76 x 76 mm^2, and the images size on the grating is 17.4 mm for the 40x 0.95 NA objective with 1.5x multiplier, or 16 mm for the 100x 1.45 NA objective. The slit has 1:1 magnification with the intermediate image plane, so we find that the size of the slit at the sample is W_s/M, with M the objective magnification. Hence, for the 100x objective, a 60 μm slit corresponds to 600 nm at the sample. This will be discussed further in Sec. 4.8.

We can determine the diffraction-limited spectral resolution, using[22]

$$\delta\lambda = \frac{\lambda}{mN}, \tag{2.2.1}$$

with $\delta\lambda$ the minimum resolvable wavelength difference, λ the mean wavelength, m the diffraction order, and N the total number of grooves. With spot sizes on the grating of 17.4 mm or 16 mm, for the 40x or 100x objectives, this leads to resolutions at order, $m = 1$ of $\delta\lambda = 0.345$ nm and $\delta\lambda = 0.375$ nm, respectively. Ocean optics, Horiba Jobin Yvon, and BWTEK, Inc. all specify the following[58,59] for determination of the full width at half maximum (FWHM) resolution, accounting for pixel and slit width, number of pixels, and the grating (via the spectral range),

$$\delta\lambda = \frac{RF\,\Delta\lambda\,W_s}{n\,W_p}, \tag{2.2.2}$$

with RF the resolving factor, and n the number of pixels in the horizontal direction. RF is a constant of the spectrometer related to the ratio W_s/W_p, and in this case is 1.643. Using Eq. 2.2.2, we find $\delta\lambda = 1.73$ nm, which is sufficient considering FWHM linewidths of single AuNP extinction spectra are larger than 25 nm. The spectrometer settings are controlled by Horiba proprietary software, USBSpectrometer V3. Relevant settings are wavelength position, grating selection, and slit-width. Imaging mode is performed with wavelength setting at 0, corresponding to zero order diffraction. The

grating rotation is set to a wavelength setting of 600nm, which aligns the direction of $\lambda = 600$ nm of the first order diffraction, approximately with the center horizontal pixel of the detector. The Andor Solis software was used to observe the live image and spectra, and record the data. When obtaining spectra, we typically work in "spectroscopy mode," which provides a line plot of spectra from different vertical bins or pixels. Spectra were averaged over 200 readouts,with exposure time 0.1s, obtaining typical intensity counts around 4×10^4. With these settings, noise in the normalised spectra is on the order of 0.01%.

2.2.2 Modular absorption spectroscopy

This modular spectroscopy setup is designed to measure absorption (or fluorescence with appropriate optics), typically in liquid samples contained in cuvettes. The setup consists of a 7 W lamp, cuvette holder, and USB spectrometer, all of which are fibre-coupled. All devices, components and software are from OO. The spectrometer is model USB2000-FLG, with fixed slit-width $W_s = 200\mu$m, a 600 lines/mm grating, $\Delta\lambda \sim 683$ nm, built-in Sony ILX511 linear 12-bit CCD array detector with 2048 pixels of pitch $W_p = 14\mu$m. The spectrometer is connected to a PC by USB. The spectral resolution with this configuration is specified by OO to be $\delta\lambda \sim 7.15$ nm, which is approximately 3 times smaller than single AuNP FWHM linewidths. The cuvette holder is the Qpod, with temperature-controllable range from $-30°$C to $105°$C, and a magnetic stirrer. Cuvettes used were standard plastic cuvettes of 1cm x 1cm base area. The lamp is the model HL2000-FHSA with fixed power setting, manual attenuator, controllable shutter, and wavelength range (360-2400)nm. The setup can be seen in Fig. 2.7. An opening for filters is available in the lamp housing, and typically the LB200 filter is used for nanoparticle absorption experiments. The resulting spectrum can be seen in Fig. 2.5. [t] The optical fibres are model QP400-1-UV-VIS with 400 μm core diameter, and relative transmission around 95% over the range (350-900)nm. Data is collected and analysed with the SpectraSuite software. Integration time for all work in this report is 3 ms, the minimum for this spectrometer. The lamp provides sufficient power to keep the counts near 4000, i.e. close to the saturation of the sensor. The fast integration time means, in principle, that we can average 1000 measurements in 3 s. However, in prac-

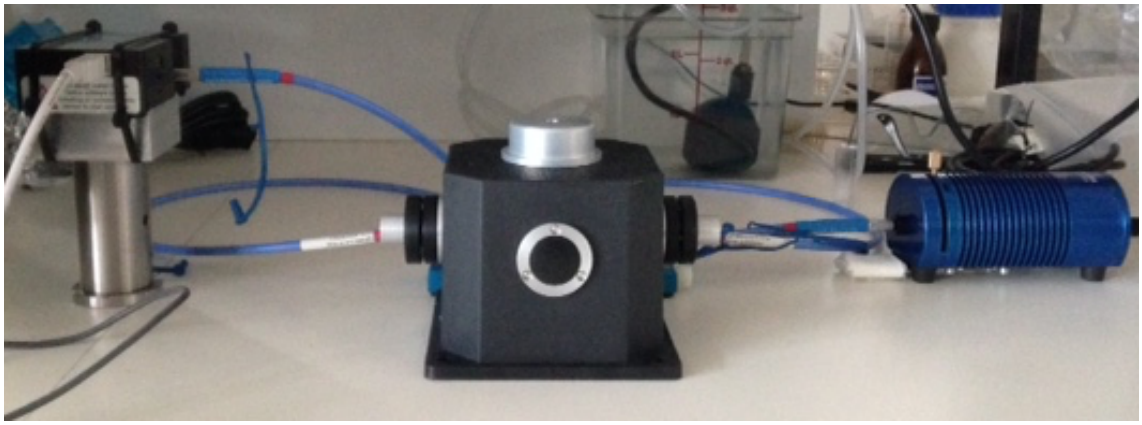

Fig. 2.7: A view of the absorption spectroscopy setup. The HL2000 lamp can be seen on the right, the Qpod at the center, and the USB2000 on the left, supported by a post.

tice, the averaged measurement is generated in about 13 s due to the processing, transfer, and save times. Shot noise in the normalised spectra is around 0.05% using these settings.

2.3 Glass cleaning

Glass cleaning was performed using the Piranha etch, also known as Caro's etch, in combination with light mechanical scrubbing. It is a common cleanroom technique for chemically removing organic debris from the surfaces of e.g., silicon wafers, glass, etc. It is often cited as a 3:1 or 4:1 mixture of neat sulphuric acid with 30% hydrogen peroxide (H_2O_2)[60]. It is highly dangerous, and requires strict safety precautions. We perform piranha treatments in a hood, with a running tap, and ice bath nearby, in case of spills. The piranha cleaning procedure can be found in Appendix C.1. Prior to using the piranha etch, glass slides and coverslips, are rubbed with high-grade cleanroom wipes and acetone. This step helps remove inorganic debris, which may need physical agitation for removal. The slides and coverslips are then placed in a small beaker containing the piranha solution, where they are left for ~ 10 minutes. They are subsequently removed from the beaker, one at a time and washed in three separate beakers of Millipore, 18 MΩ, distilled water. The triple beaker setup provides sequential dilution of the hazardous mixture. Once washed, the slides are dried with N_2 before being

stored in 50 ml falcon tubes, ready for functionalisation.

Miscellaneous glassware, such as, beakers, petri dishes, and graduated cylinders are cleaned with neat sulphuric acid, not piranha etch, again in a fume hood. Beakers are scrubbed mildly with cleanroom wipes and acetone, then rinsed with distilled water a few times. Next, enough acid is poured into any beakers, petri dishes, and petri dish lids, to coat the bottom of each of the containers. The containers are individually tilted and rotated so the acid can coat the sidewalls. They are then left to stand for ten minutes. Graduated cylinders of 10 ml or less are filled completely, and left to stand for 10 minutes. The sulphuric acid is poured down the sink, with tap running. All containers are filled with distilled water, and emptied into the sink. This is repeated up to five times. Not all miscellaneous glassware needs to be cleaned before every binding experiment, or before every piranha etching. Beakers are usually only cleaned once, and then designated for a particular chemical, e.g. distilled water, methanol, acetone, toluene, etc. If contamination is suspected, beakers should be cleaned again. Petri dishes and graduated cylinders, however, should be cleaned each time, to prevent cross-contamination by different NP solutions.

2.4 Drop-cast samples

For certain experiments, e.g. those with mild illumination conditions seen in Sec. 4, covalent binding was unnecessary. In these cases drop-cast samples were made instead. Glass slides, coverslips, and miscellaneous glassware are cleaned as in Sec. 2.3. A dilution of NP samples was prepared, for a concentration based on areal density of NPs needed for imaging (see Sec. 4.2.1), the area of the coverslip, and the volume to be applied. For drop-casting, the total volume of the dilution was determined by the number of coverslips needed for samples. Typically, 250 μl of the NP dilution was applied to a coverslip, resting on a piece of high-grade cleanroom paper, on a hot plate at 50 C. The coverslip was left until the solution is evaporated. During this time the coverslip was covered with a clean box, to help prevent dust and debris from landing on the exposed surface. The box should have a few small air holes, to allow any water vapor to escape. Once dry, the coverslip is ready for mounting onto a glass slide. Typically, 18 μl

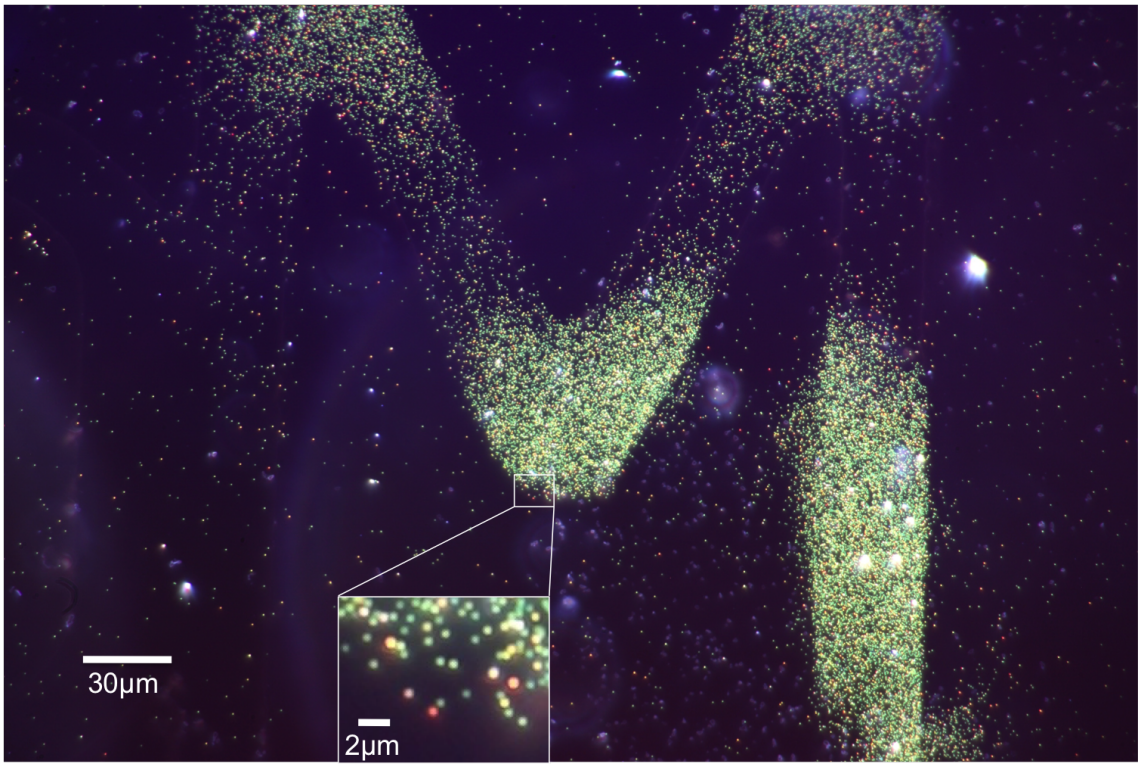

Fig. 2.8: Darkfield image of 60 nm AuNPs drop cast onto glass coverslip and immersed in silicone oil, taken with 0.95 NA 40x objective, 1.5 x tube multiplier, and 1.4 NA condenser equipped with a darkfield ring allowing NA~ (1.1−1.4). The image is a single capture of 3 s exposure, using the 40D. The AuNPs have collected into an "M," etched into a gridded coverslip.

of silicon oil was placed on a glass slide. The coverslip was added with functional-side down, so that the NPs were immersed. The sample was sealed with clear nail varnish. After the varnish dried, the sample was ready for imaging. Homogeneity of particle distribution in these drop-cast samples is not easily controlled, and generally determined by the evaporation. This leads to high density rings and a very dense central region. Nonetheless, selected areas of the sample are suitable for the imaging needs of the linear optical techniques described in Sec. 4. Examples of 60 nm Au- and AgNPs in silicone oil can be seen in Fig. 2.8, and Fig. 2.9, respectively. Notice the dominant green (blue) color of the AuNPs(AgNPs), due to the peak of the scattering cross-sections occurring in the G (B) channel of the 40D. Furthermore, the colors seen in Fig. 2.8 range from green to red, and in Fig. 2.9 from blue to red. As discussed in Sec. 1.1.3, a spherical AuNP (AgNP) of 60nm diameter has a LSPR of ~ 560 nm (~ 460 nm) in a medium with

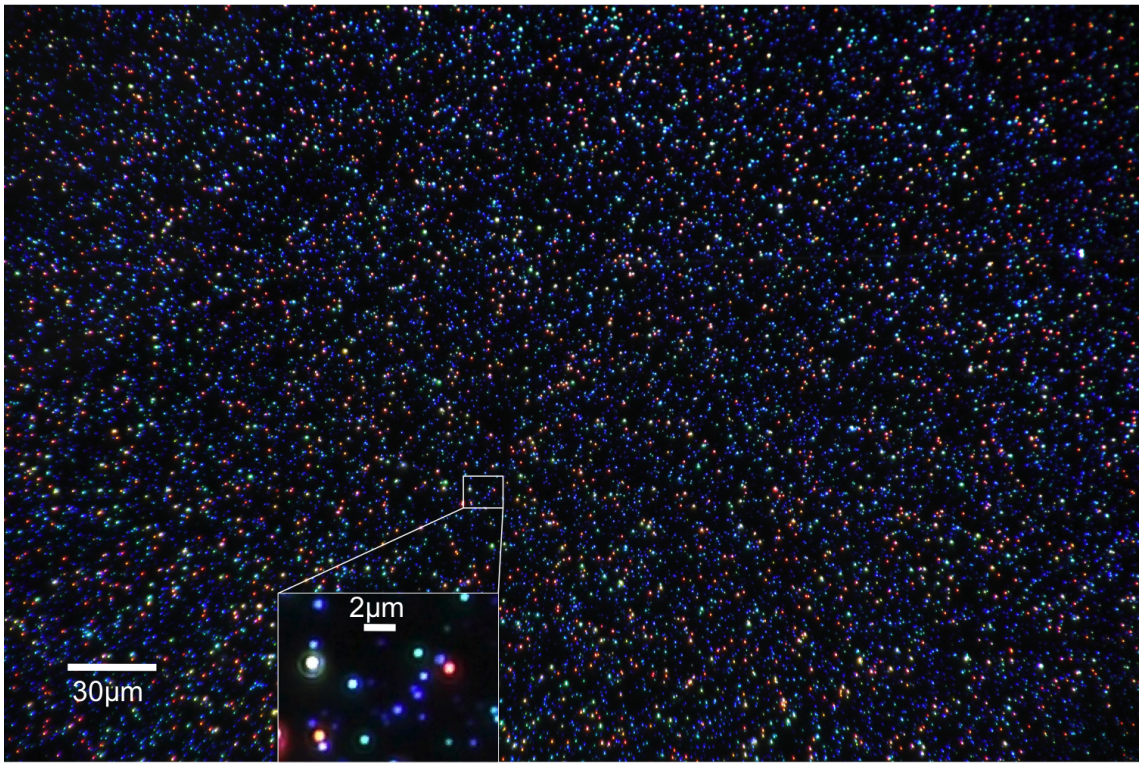

Fig. 2.9: As in Fig. 2.8 with 60 nm AgNPs.

refractive index 1.5. Red shifts from this resonance are due to aggregation, or particle asymmetry. Any "white" objects in the images are debris.

2.5 Four-wave mixing setup

The FWM setup is shown schematically in Fig. 2.10. Note, the FWM beam paths are coupled to the Ti-U when the flip mirror (FM) is down. Laser pulses of ~ 150 fs duration, centered at $\lambda = 550$ nm, are emitted at repetition rate, $\Omega_L/2\pi = 80$ MHz, by the signal output of a Newport/Spectra-Physics (NSP) Inspire optical parametric oscillator (OPO), pumped by the frequency-doubled output of a femtosecond NSP MaiTai Titanium:Sapphire (Ti:Sa) laser. The 550 nm signal output is approximately resonant to the LSPR for gold NPs. The output first passes through a $\lambda/2$ plate ($\lambda/2-1$ in Fig. 2.10), converting the vertically polarised output of the OPO to horizontally polarised light, with respect to the lab reference. This prepares the beam for entrance into the pulse compressor, with minimised reflection due to the Brewster angle. While the beams

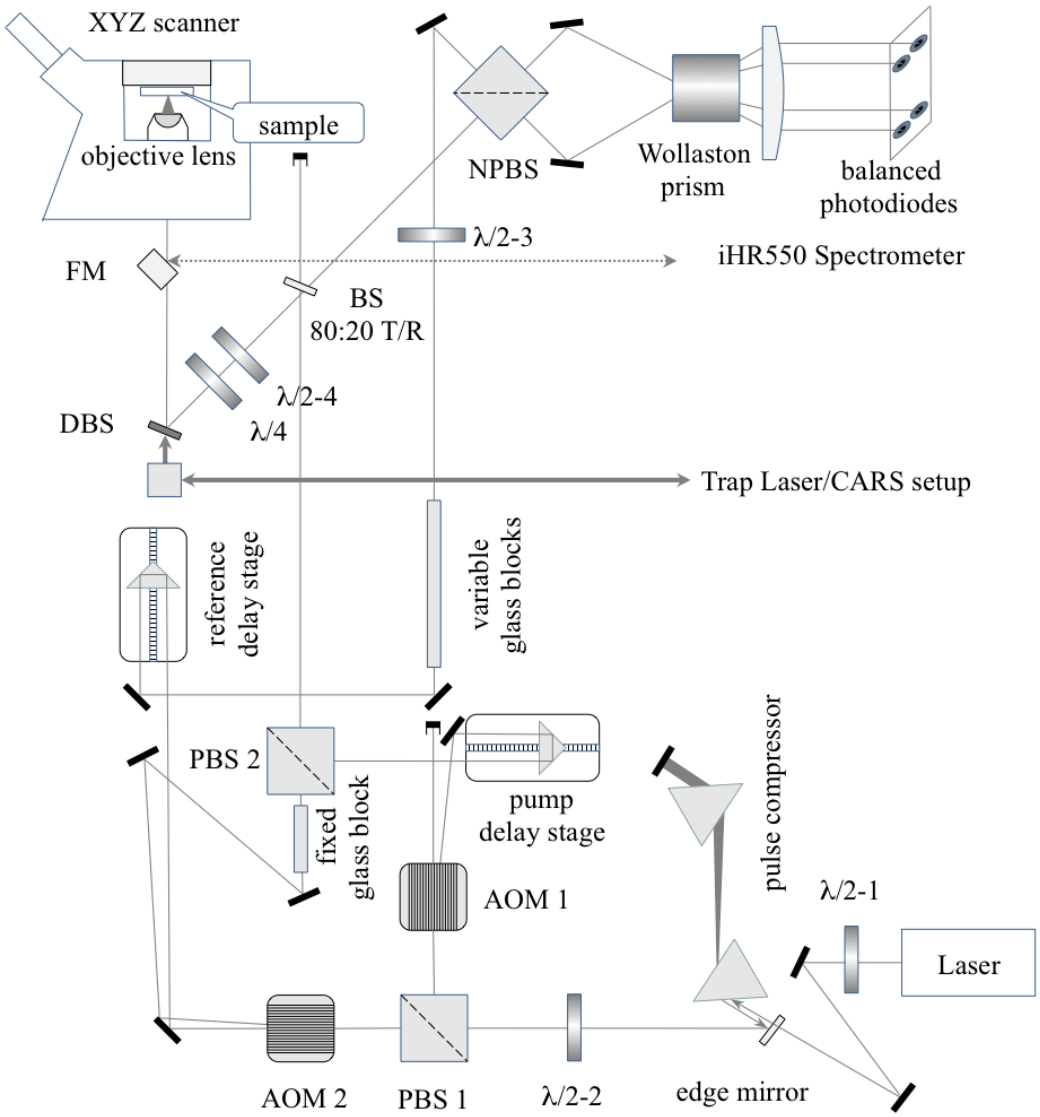

Fig. 2.10: A schematic of the FWM setup coupled into Nikon Ti-U inverted microscope, via the right port. This drawing was adapted from Ref. 61. All abbreviations are explained in the text.

pass through various optics they are chirped; that is, a temporal broadening of the pulses occurs due to group velocity dispersion (GVD). For best time resolution we require that the pulses are not chirped when they reach the sample. Thus, the prism-based pulse compressor, shown in Fig. 2.10 is used to negatively chirp the signal to pre-compensate the positive chirp arising from optics in the beam path. Furthermore, when of the pump and probe arrive at the sample, they must have the same chirp. Since, each passes through different optics, glass blocks are added to equalize chirp

between the different beams. In particular, since the reference does not go through the microscope optics, including the objective, and since the objective can be changed, the reference line has variable glass blocks, allowing matching of the GVD for both beam paths for maximum interference. After the pulse compressor, it passes through another $\lambda/2$ waveplate ($\lambda/2-2$ in Fig. 2.10). The waveplate is rotatable and adjusted to pass approximately 45° polarised light to the polarising beam splitter (PBS 1), such that the resulting horizontal polarised transmitted and vertically polarised reflected beams are of approximately equal intensity. The vertically polarised reflection from PBS 1 forms the pump beam, while the horizontally polarised transmission of PBS 1 will be split into the reference and probe beams. The three beams constitute a degenerate FWM scheme. The pump is used to excite the NP, with a field, E_1, whose intensity is temporally modulated by an acousto-optic modulator (AOM_1). AOM_1 is driven at the radiofrequency (RF), $\Omega_1/2\pi = 83\,\text{MHz}$, with a square-wave amplitude modulation of frequency, $\Omega_m/2\pi = 0.4\,\text{MHz}$. The first order diffraction is used so that the frequency of E_1 is upshifted by Ω_1, allowing it to be discriminated from the other fields in the heterodyne detection, described below, and to determine the zero time. The amplitude of the first order diffracted beam is given by the sine square of the amplitude of the RF. In this setup, the pump field contributes to both ω_1 and ω_2 to induce the "density grating" discussed in Sec. 1.2.2, resulting in a change in the dielectric susceptibility of the material. The change is probed by a second beam, called the probe, with field, E_2, a delay time τ after the pump pulse. The probe passes through another AOM (AOM_2), which is driven at constant amplitude at, $\Omega_2/2\pi = 82\,\text{MHz}$. The first order diffraction is used and the probe optical frequency is upshifted by Ω_2. Pump and probe beam intensities are controlled by the RF power in the AOMs. The third beam is the zeroth order diffraction through AOM2, and thus is frequency-unshifted. It acts as reference, with field, E_{ref}, in the heterodyne detection scheme. The cross-linearly polarised, pump and probe fields are recombined using a second polarising beam splitter (PBS2), and then encounter a non-polarising beamsplitter (BS 80:20 T:R), which reflects into a $\lambda/2$ waveplate ($\lambda/2$-4 in Fig. 2.10), immediately followed by a $\lambda/4$ waveplate. The beams are circularly polarised at the sample plane, by the waveplate combination. After passing through the waveplate combination, they are reflected by a dichroic beam split-

ter (DBS) into the microscope. The DBS allows us to couple into the microscope (via the right port), beams at different wavelengths to perform other experiments, such as CARS, and SRS, as well as to use a trap laser. The pump and probe fields are focused onto the sample by either the 0.95 NA, or 1.45 NA, objective. Sample position is controlled via the nanostage described in Sec. 2.1. The pump-probe type of FWM which we detect is the FWM field, $E_{\mathrm{FWM}} \propto E_1 E_1^* E_2$. E_{FWM} is detected in reflection (epi-direction) along with the reflected probe field, $E_{2\mathrm{r}}$. The reflection passes back through the $\lambda/4$ and $\lambda/2$ waveplates, such that they return to linear polarisation in the orthogonal direction for a circular polarization at the sample. At this point, the probe field is vertical (V) with respect to the lab reference frame, for a reflection that does not alter the polarisation state of the probe at the sample. Reflected probe and FWM fields are 80% intensity transmitted by the BS, before interfering with the reference field, via a non-polarising beamsplitter (NPBS). Note that the reference field has initial horizontal polarisation (H), with respect to the lab reference frame, before being reoriented to 45° by a $\lambda/2$ waveplate ($\lambda/2$-3 in Fig. 2.10), to provide equal reference fields of horizontal and vertical polarization. The beams exiting the NPBS, pass through a Wollaston prism, splitting them into horizontal and vertically polarized components. The bottom (top) pair consists of the V (H) components. The 4 beams are focussed onto two balanced pairs of silicon photodiodes, which extract the difference in photo-current between the pairs of equal polarization to reject common-mode noise. The currents are balanced to better than 1%, suppressing common mode noise by more than two orders of magnitude, and achieving shot noise equal to detector noise at reference powers of about 150 μW per diode, at 1.5 MHz, and with $\lambda = 550$ nm. This method allows us to simultaneously detect the co- and cross-circularly polarised components of E_{FWM} and $E_{2\mathrm{r}}$ relative to the incident circularly polarised, E_2.

We now discuss the heterodyne detection scheme. Generally, in heterodyne detection, a signal is detected, via frequency shifting its carrier frequency, resulting in a new frequency ω_{s}, and mixing with a reference, at frequency ω_{R}. In this setup, the photodiodes generate a photo-current, which is proportional to the square of the incident fields. The mathematics describing the effect of squaring the sum of two fields of different frequencies have already been introduced in Sec. 1.2. In this case, however, the higher or-

der terms, such as $2\omega_s$, $2\omega_R$, and $\omega_s+\omega_R$ are filtered out by a low-pass filter. This leaves the difference term, $\omega_s-\omega_R$. If we consider a situation where ω_s is frequency upshifted as $\omega_s=\omega_R+\Delta\omega$, then the difference term becomes $\omega_R+\Delta\omega-\omega_R=\Delta\omega$. In our setup, the interference of the probe and reference, can then be detected at $\Omega_2-\Omega_L=2\pi\times 2\,\mathrm{MHz}$ (i.e. at the shifted probe reference, modulo the laser repetition rate), which provides a direct measure of the probe field. In addition, the intensity modulation of E_1 at Ω_m modulates the susceptibility at Ω_m, which creates sidebands of E_2 at $\Omega_2\pm\Omega_m$. Recall that we wish to detect $E_1E_1^*E_2$. This leads to a description of the pump modulation's effect on the probe field as,

$$U = a\mathrm{e}^{i\Omega_2 t}(1+a_m\cos(\Omega_m+\phi)) \tag{2.5.1}$$

$$= a\mathrm{e}^{i\Omega_2 t}+\frac{aa_m}{2}\mathrm{e}^{i\phi}\mathrm{e}^{i(\Omega_2+\Omega_m)t}+\frac{aa_m}{2}\mathrm{e}^{-i\phi}\mathrm{e}^{i(\Omega_2-\Omega_m)t}, \tag{2.5.2}$$

where U is the signal to be detected, a is the complex amplitude of the reflected probe, a_m is the complex modulation amplitude of the reflection, as a result of the pump intensity modulation, and ϕ is the modulation phase. As well as the probe detected at $\Omega_2-\Omega_L=2\pi\times 2\,\mathrm{MHz}$, via its interference with the reference, the sidebands in U are detected at $\Omega_2\pm\Omega_m-\Omega_L=2\pi\times(2\pm 0.4)\,\mathrm{MHz}$. The complex amplitudes of probe and sidebands are detected by a Zurich Instruments HF2LI digital lock-in amplifier, featuring dual sideband modulation detection. Furthermore, since we detect at both, equivalent sidebands, we can average the dual signal to reduce noise.

All data is recorded, and the setup entirely controlled, by the MultiCARS software, developed in-house. Delay stages for the pump, and reference lines are respectively models M403.6, and M403.8 precision translation stages from Physik Instrumente (PI) GmbH & Co (Karlsruhe, Germany). Translational ranges are 150 mm and 200 mm, with minimum incremental motion 0.2 μm. AOMs are model ASM-802B67, from IntraAction Corp. (Illinois, U.S.A). They are specified to operate with a centre frequency of 80 MHz with frequency shift range ±15 MHz, AR coating (400-600) nm, and diffraction efficiency 85%.

2.6 Miscellaneous materials

Various chemicals, glassware and other items were used during this research. 95% (3-Mercaptopropyl) trimethoxysilane (3MT), and N-Ethylmaleimide (NEM), acetone, toluene, methanol, ethanol, sulphuric acid, 30% hydrogen peroxide, and 2-propanol (isopropanol), silicon-Whacker oil (refractive index, $n = 1.518$), and dimethyl-sulfoxide (DMSO) were all obtained from Sigma-Aldrich® (Zwinjdrecht, the Netherlands). (3MT) and (NEM) were stored at 4C. The other chemicals listed were stored at room temperature in fire safety cabinets. Glass coverslips were, typically, $25 \times 25\,mm^2$, thickness #1.5 from Menzel-Gläser® (Braunschweig, Germany). Glass slides were of size $51 \times 26\,mm^2$ (to fit the nanostage), from Chance Glass Ltd (Malvern, UK). All metallic nanoparticles were obtained from BBI Solutions (Cardiff, UK). 5 ml diameter glass petri dishes, 5 ml and 10 ml glass graduated cylinders, various sizes of borosilicate glass beakers, and 50ml falcon tubes were obtained from Fisher Scientific (Loughborough, UK).

CHAPTER 3

Nanoparticle synthesis and sample preparation

3.1 Introduction

Critical to the work described in this thesis and the work of other group members, was the development of methods to covalently bind metallic NPs to glass, e.g. to coverslips, and to each other, i.e. to form dimers. Binding NPs to glass was performed in order to facilitate laser-based studies on single NPs, by stabilising the NP position. Characterization of the binding was performed via darkfield microscopy. Since, darkfield microscopy detects the scattered light from objects in the sample, high levels of debris can make optical studies on isolated NPs impossible. Glass cleaning is, thus, a key part of sample preparation. In this section we will describe the glass cleaning procedures adopted, as well as the methods used to bind NPs to glass. We also describe several methods, which were investigated to bind NPs together in solution to create dimers. The concept was to covalently bind two spherical NPs together, where one of the spheres was coated by a silica (SiO_2) shell. The SiO_2-shell thickness would control inter-particle distance. The inter-particle distance determines the shift of the LSPR along the long-axis of the dimer. The aim was to study and quantify this effect in the linear and nonlinear regimes, at the single particle level, and in particular with phase-sensitive FWM for development of a proof-of-principle for an in-vitro "plasmon ruler." This segment of the research was a collaborative work involving Cardiff Biophoton-

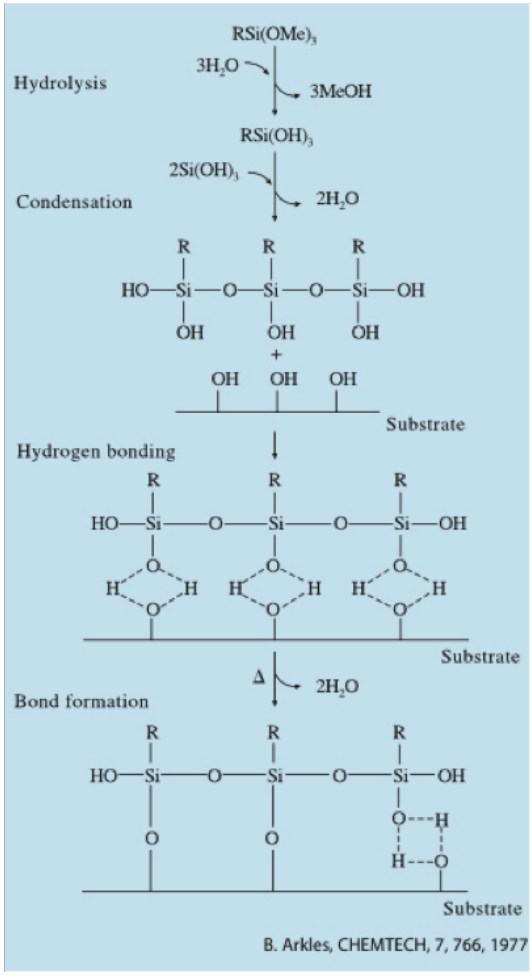

Fig. 3.1: Reaction Pathway for the hydrolytic deposition of silanes on silica.[62] ©Gelest, reprinted with permission.

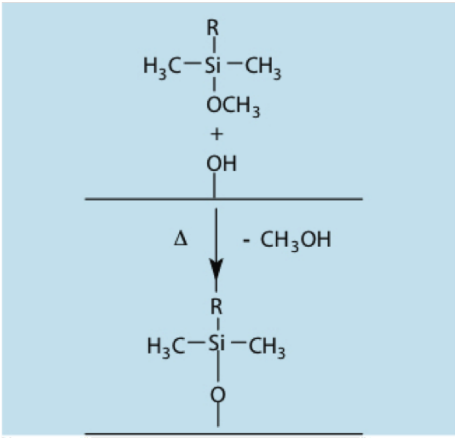

Fig. 3.2: Anhydrous reaction pathway.[62] ©Gelest, reprinted with permission.

ics, Bristol University (Wolfson Bioimaging Facility), and BBI Solutions. BBI supplied the nanoparticles, and optimised methods for growing different thicknesses of SiO_2 around the metallic cores. The Bristol bioimaging facility provided TEM imaging of the samples.

3.2 Glass functionalisation

Deposition of silane-containing compounds is an important method for surface functionalisation or modification with a wide range of applications from alteration of the

hydrophobicity/hydrophilicity of surfaces[62] to biofunctionalisation[63,64]. We benefited from knowledge transfer from another group in the Molecular Biosciences Department who had experience with glass functionalisation. Thus, a simple method, for thiolation of glass coverslips, was inspired largely by the silica surface functionalisation seen in Ref. 63. In that case, the surface was modified with thiolised-DNA and MPTMS (which we call 3MT, see Sec. 2.6). However, this method results in DNA bound via thiol to the glass substrate. We need thiol as the surface functional group, thus we only use 3MT. The functional, "R", group of 3MT is connected, by a silicon atom, to three hydrolyzable methoxyl groups, i.e. OCH_3, represented as $(Me)_3$. For metallic nanoparticles, the concept is that the silane portion of the compound, i.e. $Si(Me)_3$ will bind to the glass, and the thiol group will bind to the metallic nanoparticle. The bond between metal and sulphur is well known, although literature suggests some ambiguity with respect to the direct action of thiols on metallic surfaces[65–67].

The principles of silane deposition are presented in Fig. 3.1, 3.2. Silanes can be deposited on glass and made to react, principally in two ways. These are hydrolytic deposition, or anhydrous deposition, i.e. with, or without, water present during reaction. In the anhydrous case, the hydrolyzable groups react directly with the hydroxyl groups on the surface, or with nearby silane molecules, forming covalent bonds. In the hydrolytic case, there are several steps prior to the formation of the covalent bond. Hydrolysis of the methyl groups and polymerisation of silane molecules, via a condensation reaction lead to available hydroxyl groups on the silane polymers. These hydroxyl groups form hydrogen bonds with silica surface hydroxyl groups. Only during the curing phase, are these converted to covalent Si-O-Si bonds by ejection of water. Note, in Fig. 3.1, the silane molecules are covalently bound to each other as a polymer, prior to the curing step, and are only bound covalently to the silica surface, afterwards. The necessity of this curing step in forming the covalent bond between the glass surface and the silane molecules plays an important role in the discussion of our dimerisation studies.

A detailed procedure for the functionalisation of glass, as well as the subsequent binding of NPs, is given in Appendix C.2. Briefly, the silanes are dissolved in toluene at a concentration of 1%, ready for deposition onto cleaned coverslips. Cleaned coverslips are removed from their storage tubes, and placed on high-grade cleanroom pa-

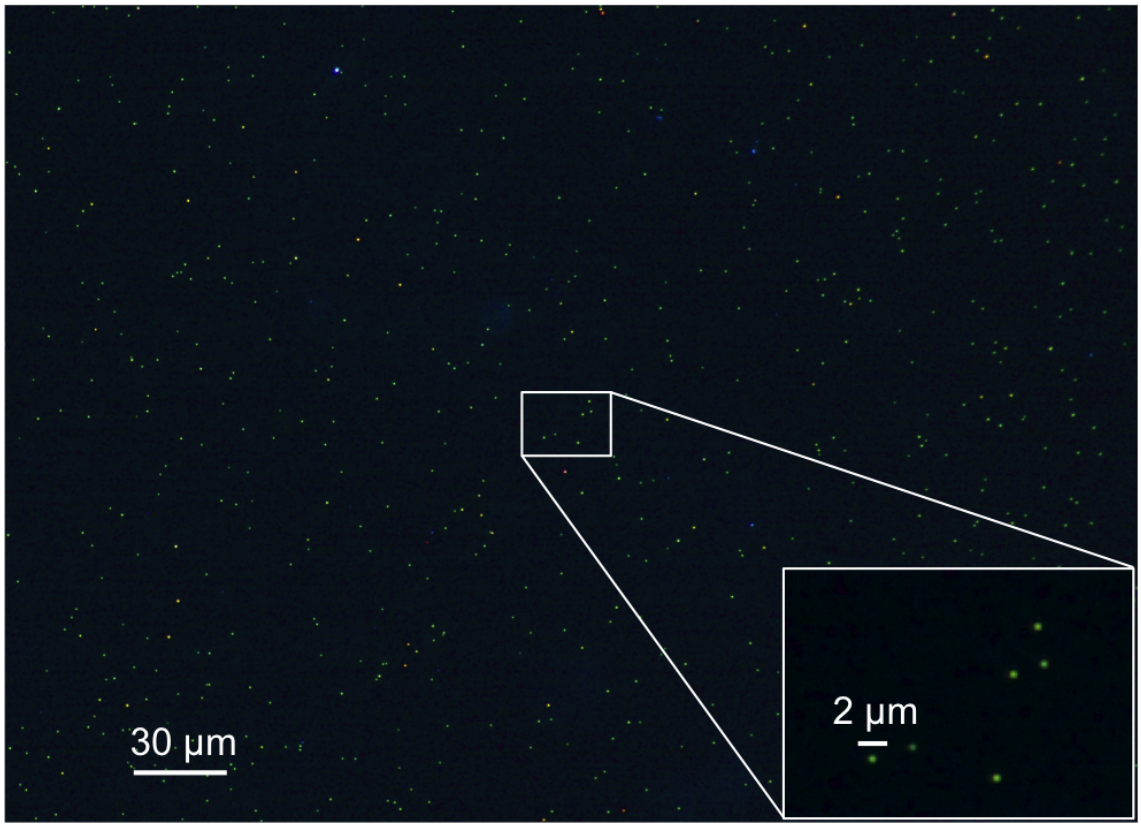

Fig. 3.3: Darkfield image of 50 nm AuNPs covalently bound onto a glass coverslip and immersed in silicone oil ($n = 1.51$). The image is a single exposure of 3 s, captured with the 40D, and using the 0.95 NA 40x objective with 1.5 x tube multiplier.

per. The silane solution is quickly added to one of the coverslips, and the other coverslip is placed on top. The reaction is left to run for 30 minutes at room temperature. The two coverslips are separated and washed with Toluene to remove unbound 3MT. They are then washed with distilled water and dried in N_2. This method provides two coverslips, each with one functionalised side. The coverslips are then placed back in N_2-flushed 50 ml falcon tubes, for storage while the NP dilution is prepared. If the coverslips are not used immediately, they can be left in the tubes for later use. Shelf-life of the thiols once attached to the coverslips has not been investigated, but functionalised coverslips have been used for binding NPs up to a few days later. Either during the 3MT incubation on the coverslips, or after the washing and drying steps, a NP dilution is prepared. NP concentration is based upon areal density requirements for imaging. Particles must be a certain distance apart for our wide-field measurements, which will

be discussed in detail in Sec. 4.2.1. The dilution is prepared in 5 ml of distilled water. A functionalised coverslip is placed with functional side up in a glass petri dish. The dish is placed on a motorized tilt-table. The 5 ml suspension of NPs is poured over the coverslip, in the petri dish. The tilt-table is turned on and the coverslip is left to incubate for one hour. Once finished, the coverslip is removed, and washed several times in distilled water, then dried in N_2. Once dried, the coverslip is placed on a glass slide with desired immersion medium and sealed, as in Sec. 3.2. The particle distribution is generally homogeneous with this preparation method. An example of 50 nm AuNPs bound to glass can be seen in Fig. 3.3.

Controls were performed during initial development of this procedure. In particular, to confirm the binding effect of 3MT, a clean coverslip, *without* functionalisation, was immersed into an NP solution in a glass petri dish. It was incubated on the tilt table for one hour. It was then removed, washed, and finished with a glass slide, as before. The control confirmed little to no presence of NPs after immersion and washing, on coverslips that were *not* functionalised with 3MT. Images are not provided here as they are effectively blank, with the exception of small amounts of debris.

3.3 Nanoparticle dimers

Nanoparticle dimers have been produced, and reported in literature, by methods including using DNA-linkage[8,68,69], substrate-mediated binding or assembly[70], or electron-beam lithography (EBL)[71]. The interparticle distance can be precisely controlled in each of these different techniques. However, within the scope of this work, these are too complex, costly, and would require training. Simpler methods making use of thiol-metal bonds have also been shown[72], and since we gained experience with this chemistry from the glass functionalisation procedure, we decided to form dimers in suspension, based upon the simple thiol-metal and silane-silica chemistry, which had been previously successful. As discussed in the next subsection, we monitored the dimerisation reaction, via absorption spectroscopy, as the reaction progressed. The appearance of an additional peak in the NP suspsension absorption spectrum is attributable to the red-shifted LSPR of any newly formed dimers. At this point, a block-

ing agent was added to stop the reaction, prior to significant formation of larger multimers. We chose NEM as a blocking agent, as it reacts strongly with thiols[73]. In this way, a simple, reproducible method for NP dimerisation was developed, supplying a stock of NP dimers whenever needed. TEM provided absolute confirmation of the formation of dimers.

In practice, three slightly different chemical procedures were investigated to achieve the dimerisation of quasi-spherical AgNP and AuNP monomers in suspension. These three procedures are provided as step-numbered protocols in Appendix D. We were supplied with AgNP samples with core-size 40 nm and SiO_2-shell thicknesses, 6 nm, 10 nm, 12 nm, 17 nm, and 20 nm, and with AuNP samples with core-size 40 nm and SiO_2-shell thickness were 6 nm, 17 nm, and 20 nm, through our collaboration with BBI Solutions. Minimum interparticle distance would be given by dimers formed by two bare NPs (bare-bare). We could then make a range of interparticle distances from combinations of bare-SiO_2-NP and SiO_2-NP - SiO_2-NP from 6 nm to 40 nm. The interparticle distances, below our minimum shell thickness, 6 nm, typically show the greatest effect on the LSPR, as discussed in Sec. 1.1.3. Though, we did not have SiO_2-NPs with shell thicknesses in this range, we did observe these interparticle distances after binding experiments. The origin of the interparticle distances below 6 nm will be discussed. Results concerning silver and dimerisation procedures 1 and 3 are discussed in Appendix E, due to the uncertain nature of the results.

3.3.1 Methods

3.3.1.1 Absorption spectroscopy and Qpod cuvette environment

Spectroscopy was performed using the OO modular spectroscopy setup and SpectraSuite software, as described in Sec. 2.2.2. The 7 W lamp was used with LB200 filter, increasing the relative intensity of the blue part of the spectrum. This was done in particular for silver measurements, to reduce noise in the shorter wavelengths. At the start of an experiment a dark offset was taken with no light to the detector. A reference was taken as close as possible to the corresponding measurement. For the results reported in this work, the sample temperature was typically held at 30°C using the Qpod.

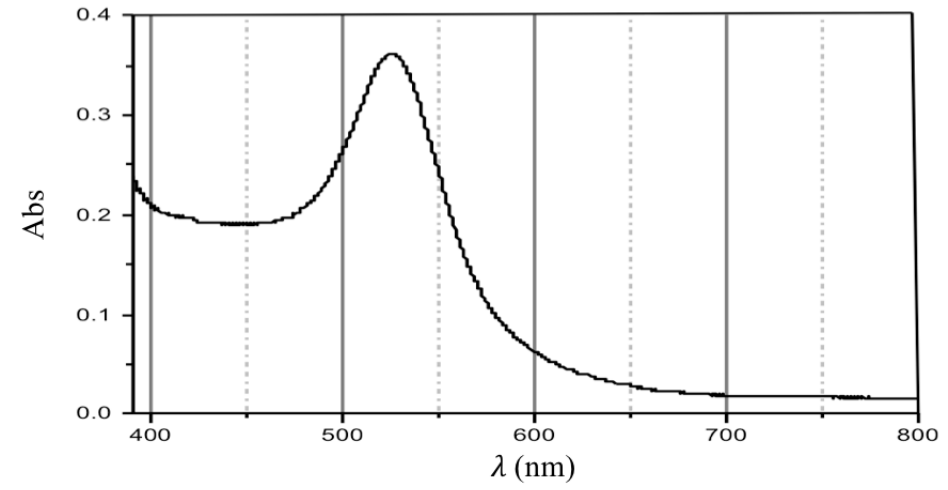

Fig. 3.4: Absorption spectra of bare 40nm AuNPs in water.

Measurements are typically recorded using the preset absorption mode of the acquisition software. SpectraSuite uses the following formulation to calculate absorption,

$$A(\lambda) = -\log_{10}\left(\frac{S(\lambda) - BG(\lambda)}{R(\lambda) - BG(\lambda)}\right) \tag{3.3.1}$$

where S is the signal intensity, BG is the dark offset, and R is the reference intensity, at a given wavelength, λ. This corresponds to the form of the Beer-Lambert law given in Eq. 1.1.8

Since, we frequently look at the change in the absorption spectrum over time, we will rewrite the absorption $A(\lambda)$ as $A(t,\lambda)$, with t the time. Then, we can represent a subtraction of a zero-time absorption spectrum from the absorption spectrum at some later time, t, as

$$A_{\Delta 0}(t,\lambda) = A(t,\lambda) - A(0,\lambda). \tag{3.3.2}$$

3.3.1.2 Dimerisation procedure 2

The major difference between the dimerisation techniques and the glass functionalisation discussed in Sec. 3.2, is that the dimerisation takes place in the liquid phase. The interactions in the previous case, involved 3MT, glass, and metallic NPs. The 3MT was dissolved in toluene, and then allowed to bind to the glass. The toluene was removed, and the sample dried. The NPs were then added, and allowed to bind to the free thiol

groups. Now, we wish to functionalise, either the bare Au samples, or the SiO_2-coated NP samples, with 3MT, directly in suspension. However, toluene is not soluble in water. So we must either transfer the NPs to a new medium, or find another solvent for 3MT. In the second procedure, we simply dissolved 3MT in methanol and added this to a 1:1 mixture of bare- and SiO_2-NPs. In this case, the spectrometer was referenced with the bare-/SiO_2-NP mixture, prior to addition of 3MT. The SpectraSuite software was instructed to save every scan typically for a period of 30 minutes. Scans were begun prior to addition of 3MT, however fast reaction times can be missed, due to the lag of the averaging and file processing which typically took 13 s, as described in Sec. 2.2.2. This was the only procedure used for the observation of gold, due to lack of time, and lack of availability of gold NPs during investigations with procedure 1 (Appendix E).

3.3.2 AuNP dimers

Gold is known to be more stable than silver, and thus, we expected it would present an easier material to work with for these developments. Gold dimers were only investigated with method 2. The absorption spectrum of bare 40 nm AuNP, in H_2O, is shown in Fig. 3.4. Note, the LSPR is at approximately 525 nm. The key results of the dimerisation are summarised in Fig. 3.5, 3.6, and 3.7. Spectra are referenced against the NP colloid, prior to addition of 3MT solution. In general, we do not see stark differences between the bare-bare, bare-6 nm SiO_2-NP, and bare-17 nm SiO_2-NP binding experiments. A strong peak arises around 550 nm in all cases, indicative of a common effect, such as bare-bare binding. Bare-bare binding would be possible due to the polymerisation effect discussed Sec. 3.2. However, from literature[48], we could expect to see a red-shift of ~ 20 nm in water for two nearly-touching 10 nm diameter AuNPs. Furthermore, we expect that this red-shift would increase for an increase in diameter of the particles. This is corroborated by measurements performed with extinction spectroscopy in Sec. 4.8, where we see a ~ 60 nm shift for particles less than 1 nm apart (in oil).

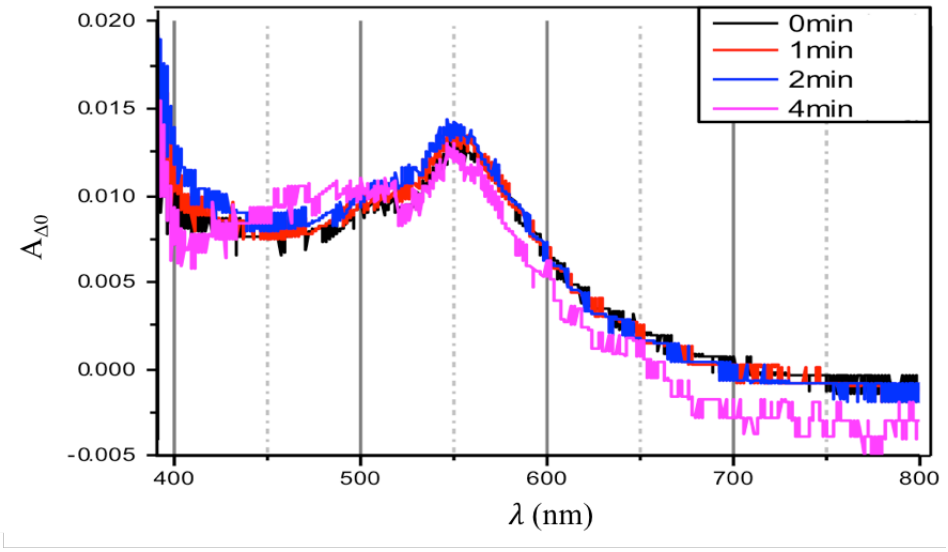

Fig. 3.5: Absorption spectra of bare 40nm AuNPs in water at different times after adding 3MT in methanol.

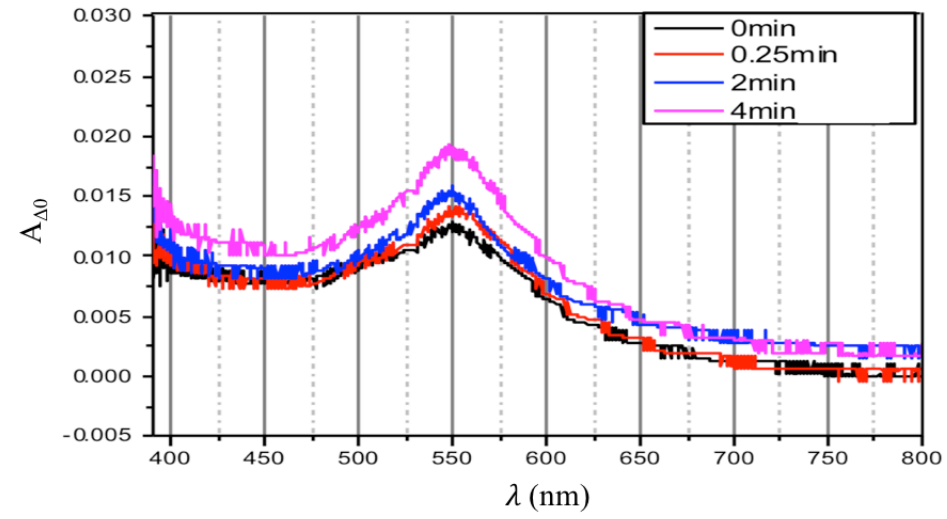

Fig. 3.6: As in Fig. 3.5 for a mixture of bare 40nm AuNPs with 6nm SiO_2-coated AuNPs

It is possible that we see a small range of interparticle distances due to bare-bare binding, since the thickness of the shell will be determined by random, local availability of 3MT. The peaks may ultimately result from a mixture of sources of varying red-shifts, including the addition of a layer of SiO_2 to the bare-NPs by 3MT, bare-bare binding, and bare-SiO_2 binding. Digitization steps can be seen in Fig. 3.5, 3.6, and 3.7, due to an

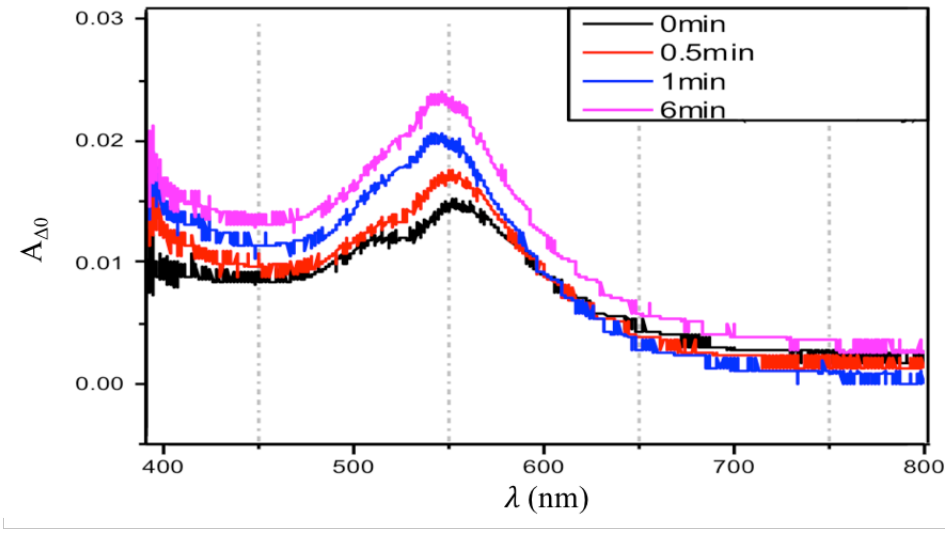

Fig. 3.7: As in Fig. 3.5 for a mixture of bare 40nm AuNPs with 17nm SiO_2-coated AuNPs.

auto-default setting in the SpectraSuite software, which resets the significant digits to 3, every time the program is restarted. Furthermore, the zero-time point was missed during this experiment, due to the speed of the reaction, and little difference in the spectra can be seen in time. The reactions were stopped within a few minutes by addition of NEM at approximately 10^3 times the concentration of 3MT. These samples were stored for use in imaging experiments and TEM. TEM images of the 6 nm shell thickness SiO_2-NPs mixed with bare-NPs and 3MT can be seen in Fig. 3.8, and confirm the presence of dimers of bare-bare and bare-SiO_2-NP types. We saw about 10% dimer yield. One can also clearly see the effect of silane polymerisation and binding via thiol to bare AuNPs. The bare NPs exhibit a thin transparent layer on the surface, distinguishable by mild contrast from the background. We see more significant numbers of bare-bare dimers formed by this method. We attribute this again to the covalent bonds forming between silica and silane molecules only after curing. Samples containing these NPs covalently bound onto glass, were immediately prepared, via the method described in Sec. 3.2, for a study of their linear optical properties, correlatively with FWM, which will be discussed in Sec. 4.3.4 and Sec. 5.3. Small volumes of the samples were also sent to our collaborators at Bristol University (Dr. Paul Verkade's Lab) to be measured by TEM, prior to correlation with FWM.

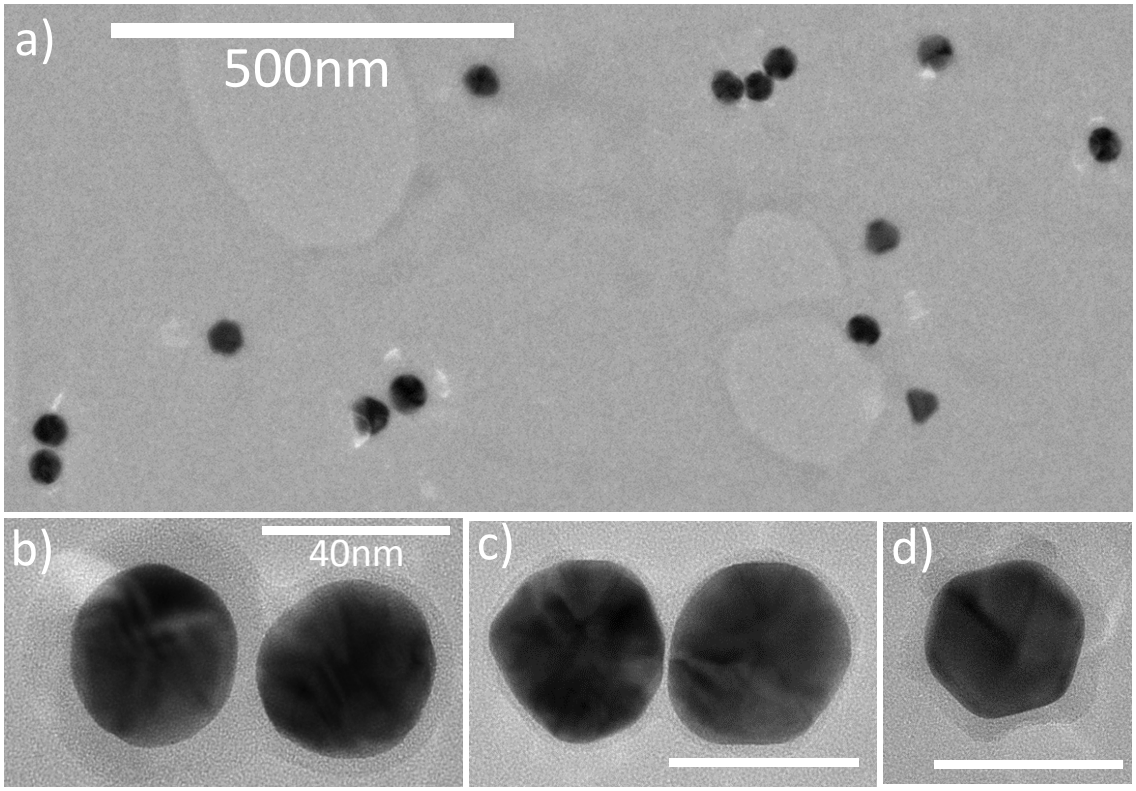

Fig. 3.8: TEM images of gold NPs drop-cast onto a TEM grid, from a solution containing nominal 40 nm NPs coated with a nominal 6 nm thick silica shell, covalently bound to bare 40 nm NPs. a) Overview showing single particles, dimers and trimers. b) Example of a dimer between a silica-coated NP (left) and a bare NP (right). c) Example of a dimer between two bare NPs. d) Example of a single 40 nm NP coated with a 6 nm silica shell. The thin coating visible on the nominally bare NPs is likely due to the (3-mercaptopropyl) trimethoxysilane forming a polymerized structure.

3.4 Conclusions

Reproducible methods for the cleaning of glassware, and covalent binding of NPs to glass, enabling darkfield and extinction imaging of NPs have been presented. Multiple methods to create dimers of metallic NPs in suspension have been investigated. All of these dimerisation methods leave open questions, in terms of yield, reproducibility, and underlying chemistry. The creation of silver dimers remains undetermined, but work on gold NPs produced samples with approximately 10% dimer yield. Thus far, it seems that the main complicating factor in the development of NP dimers in aqueous

suspension is that the silane-silica bond is not covalent until curing, leaving bare-bare binding by silane polymerisation the dominant origin of dimers. Method 3 could potentially sidestep this issue, preparing definitively functionalised SiO_2-NPs. However, one will first need to return these NPs to aqueous suspension after functionalisation. This subject is being pursued by a further collaboration between our group and BBI, and is beyond the scope of this thesis.

CHAPTER 4

Optical exctinction and scattering by nanoparticles

4.1 Introduction

An understanding of the linear optical properties of NPs is critical to any nanosensing concept. Optical properties of individual NPs can significantly differ from the ensemble average, owing to inhomogeneities in NP size and shape. Hence, it is important to quantify the cross-sections at the single NP level, not just with ensemble measurements like absorption spectroscopy. A number of approaches have been developed recently to measure σ_{ext} at the single particle level, so one might ask why we did not implement an already established technique. Quantitative values of σ_{ext}, σ_{abs}, and/or σ_{sca} of single NPs have been reported using dark-field micro-spectroscopy [74], PTI [15,45], and spatial modulation micro-spectroscopy (SMS) [75].

Darkfield microscopy, introduced in Sec. 2.1.1, measures only the scattering of NPs. To provide σ_{sca} values in absolute units, dark-field micro-spectroscopy requires a calibration reference (e.g. by comparison with σ_{ext} known from theory), or calibration of the absolute intensity of illumination, and the absolute detection efficiency. From Eq. 1.1.19, σ_{sca} is roughly proportional to the volume of the NP squared in the Rayleigh regime. Since the scattering intensity scales strongly with the NP size, and the scattering background from the supporting medium is typically similar to NPs of 20 nm size, darkfield microscopy is practically limited to particles larger than $\sim 20\,\text{nm}$. [76].

PTI measures the NP absorption, via the change of the refractive index of the NP environment, due to the resulting heating. It is typically implemented using a laser-based modality, which uses one beam to periodically heat a NP with an amplitude modulated beam, and then another to probe the response. The heating leads to a periodic change in the refractive index of the particle and local environment, and thus a periodic change in the probe beam. The resulting modulation of the probe beam is used to determine σ_{abs}, since the heating of the NP, and thus, the local environment, are due to the absorption of light by the NP[76]. The technique has been demonstrated in different configurations[15,45,77]. Photothermal heterodyne imaging has been used to measure NPs down to 1.4 nm diameter[15]. This technique provides information on σ_{abs}, only. Furthermore, the signal is related to the heating of the local environment, and hence only indirectly to the absorption. Thus, obtaining σ_{abs} in absolute units requires a calibration from reference objects, in the host media of choice.

SMS works by modulating the relative position of a NP with respect to a light beam (either beam position or particle position can be modulated). The movement of the particle in and out of the beam modulates the transmitted power. The modulation amplitude is detectable, and is directly related to σ_{ext}, thus allowing absolute units to be determined. Furthermore, since σ_{ext} is the measured quantity, scattering and absorption can be extracted. This has been shown with special implementations involving phase retrieval, via an interferometric detection[77]. Particles as small as 2 nm have been detected[20]. Another very sensitive technique directly measures the absorption cross-section without the need for modulation[78,79]. This method is capable of measuring absorption of single molecules with cross-sections on the order of 0.1nm^2, which corresponds to gold NPs smaller than 2 nm diameter. In principle this is a transmission experiment, however it is a beam scanning technique with sophisticated detection via balanced photodiodes, etc. All three methods require complex, and potentially costly constructions, typically involving AOMs, lock-in detectors or special other special detector setups. Since, SMS, PTI and the single molecule absorption technique are beam-scanning techniques, they can only be used to measure single NPs at a time. An ideal technique would be one allowing measurement of σ_{abs}, σ_{sca}, and σ_{ext} rapidly, with absolute units, at the single particle level, over a large number of particles simultane-

ously.

In the context of our work, the ability to measure the ensemble optical properties of a given sample, enabled us to compare the statistical distribution of the optical properties to the particle size specifications of the supplier. Individual particle measurements enabled a correlation of the linear optical properties of a NP with, e.g. TEM, SEM, or FWM. In the context of the field of linear optical studies of NPs, the method developed here is easily implementable, low cost, and an effective method for the measurement of the optical cross-sections. We call this method the "wide-field extinction" technique. To enable widespread use, a program called the "Extinction Suite" (ES), was developed to automate measurement and correlation of the data for many NPs, retrieved in a single experiment. We will explore this method in Sec. 4.2.1.

The majority of the results were obtained with single, nominally spherical NPs. Additionally, we investigated dimers. As we will see, the wide field technique provides, in its current form, a coarse spectroscopic resolution given by colour filters. However, when we are particularly interested in the spectral features of NPs, a higher spectroscopic resolution is needed. For instance, the smallest bandpass filter used in this work, is the blue Semrock filter, described in Sec. 2.1.3, with 22 nm bandwidth. For single AuNPs in the dipole limit, the FWHM of typical resonance linewidths is around 50 nm. Hence, our spectral resolution, at best with these filters, is roughly half of the linewidth. In the case of the 40D, the bandwidth of the filters is around 100 nm. Fine resolution of the resonance spectral shape is important for the study of dimers, where in particular, we are interested in the position of the dimer resonance, with respect to the LSPR of a single NP. Hence, we augmented the wide-field technique with a spectrally resolved detection, as described in Sec. 4.8, for analysis of individual particles and dimers. We call this method "extinction spectroscopy."

4.2 Wide-field extinction

4.2.1 Basic technique

The wide-field method is derived directly from the definitions of the optical cross-sections. For example, from Eq. 1.1.14, $\sigma_{\text{ext}} = P_{\text{ext}}/I_{\text{i}}$, with incident intensity I_{i}, and power lost by extinction, P_{ext}. The definition prompts measurement of the extinction cross-section using transmission microscopy. Samples are prepared, either by drop-casting NPs onto the coverslip, as in Sec. 2.4, or by covalent binding of NPs to the coverslip, as in Sec. 3.2. In our inverted microscope setup, the light will enter the sample through the slide first, interact with the NPs on the coverslip, then pass through to the objective. A suitable sample region containing NPs with a mean seperation well above the diffraction limited resolution are chosen, via darkfield microscopy. Then, the illumination is changed to brightfield, as discussed in Sec. 2.1.1, allowing us to capture a brightfield image containing the NPs. In order to obtain I_{i} in Eq. 1.1.14, we defocus the objective or sample, or laterally shift the sample, and then capture the image. We then obtain the normalised transmission image, via a simple division of the image *with* NPs, which we call I_{f}, by the image *without* NPs, which we call I_0. Note, all images are proportional to the detected light intensity, and have been derived from the acquired images by subtraction of the background images taken for blocked illumination, e.g. $I_0 = I_{\text{i}} - I_{\text{B}}$, with I_{B} the image taken for blocked illumination. The extinction is the power lost from the initial field, so we calculate the relative extinction image, with

$$\Delta = 1 - \frac{I_{\text{f}}}{I_0} = \frac{I_0 - I_{\text{f}}}{I_0}. \tag{4.2.1}$$

To obtain the scattering information we can use the darkfield image of the same region. From extinction and scattering we can then calculate the absorption.

The images may each be averages of many images taken in a short interval. Averaging images reduces noise in the image by a factor of $1/\sqrt{N}$, where N is the number of images averaged. If we reference by defocussing, then in the defocused image a NP distributes its effect over a radius of about $r_{\text{d}} = \text{NA}\,\text{d}$, with d the relative displacement of the objective and sample. I_0 is then similar to the intensity I_{f} in the absence of the NP. The extinction cross-section of a NP located within the area A_{i} in the image can

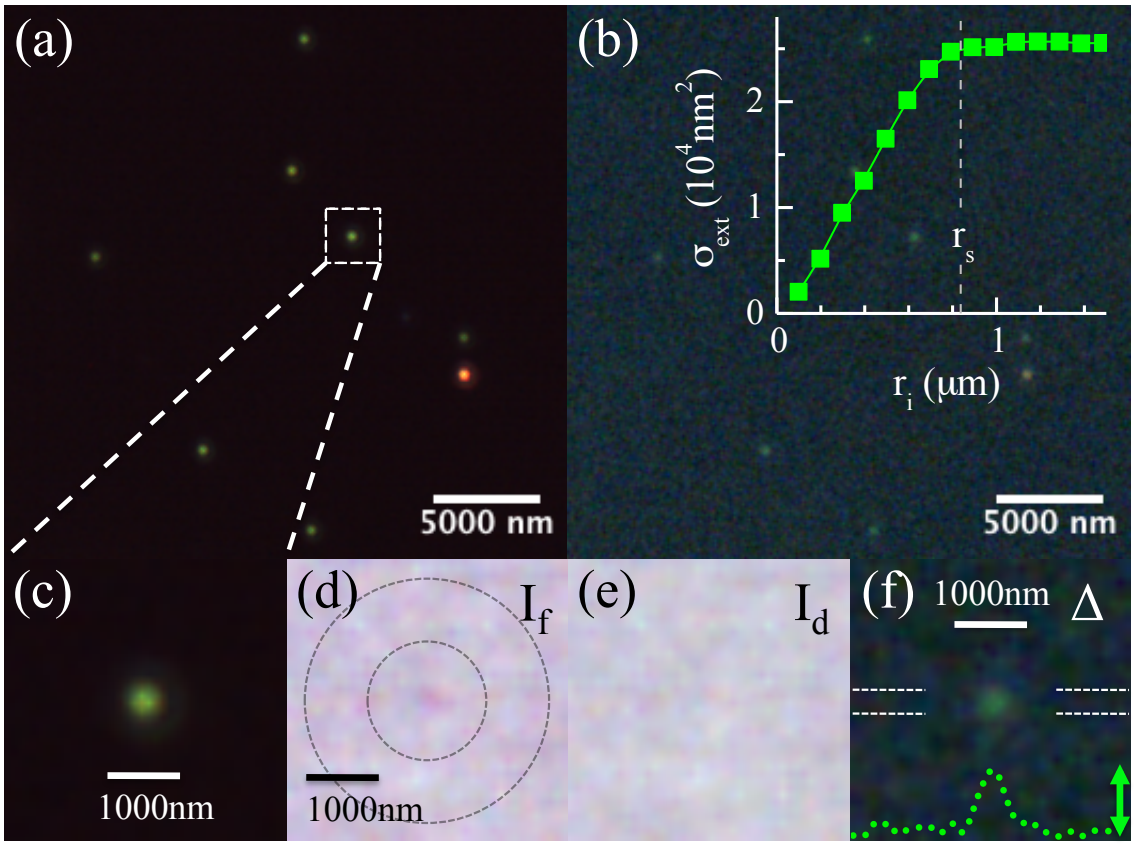

Fig. 4.1: (a) Full Colour (FC) dark-field image of 40 nm diameter gold NPs. (b) Corresponding FC extinction image Δ from 0 (black) to 0.043 (white). (c) Zoom of dark-field image. (d,e) Corresponding zoom of the FC brightfield transmission with NP in focus I_f (d) and out-of-focus I_0 (e). (f) Zoom of FC extinction image. The line cut has vertical scale bar from 0 to 0.017, with background fluctuations on of ±0.0017, and was taken within the band marked by the dotted white lines (3 pixel vertical bin).

then be expressed as

$$\sigma_{\text{ext}} = \int_{A_i} \Delta dA. \tag{4.2.2}$$

An example of a colour dark-field image and the corresponding Δ image for gold NPs of 40 nm diameter is shown in Fig. 4.1. The area, A_i, is taken to be a circular area of radius, r_i. The dependence of the measured σ_{ext} on r_i is shown in the inset of Fig. 4.1b for the G channel of the 40D, using a constant Δ_b from $r_i = 1.5\,\mu$m . A saturation of σ_{ext} is observed for $r_i > 800\,\text{nm} \sim 3\lambda/(2\text{NA})$, approximately at the second Airy ring of the objective point-spread function (PSF). Hence, $r_i \approx 3\lambda/(2\,\text{NA})$ is chosen to be the minimum radius, at which we see saturation of the measured σ_{ext}. This behavior can be

qualitatively understood considering that Δ is the result of the interference between the scattered field of the NP and the illumination field. For a spatially coherent illumination this interference would lead to fringes in σ_{ext} decaying as $1/r$. However, the short spatial coherence length $d_{\text{c}} \sim \lambda/\text{NA}_{\text{c}}$ of the illumination suppresses these fringes for $r > d_{\text{c}}$ [80].

To account for the mismatch between I_0 and I_{f}, due to defocusing or shifting, drift of the illumination intensity, and the residual influence of the NP, we determine a local background extinction $\Delta_{\text{b}} = A_{\text{b}}^{-1} \int_{A_{\text{b}}} \Delta \text{d}A$ in the area A_{b} between the radii r_{i} and $2r_{\text{i}}$, as sketched in Fig. 4.1d, yielding the background-corrected

$$\sigma_{\text{ext}} = \int_{A_{\text{i}}} (\Delta - \Delta_{\text{b}}) dA. \tag{4.2.3}$$

The defocus distance, d, is chosen such the correction area A_{b} is within the defocused image of the NP, i.e. $2r_{\text{i}} < r_{\text{d}}$, ensuring a homogeneous influence of the NP over A_{i} and A_{b}. We typically use a defocus length, $d \approx 15\,\mu m$, yielding $r_{\text{d}} \approx 14.25\,\mu m$, using the 0.95 NA objective. If the shifted-reference method is used, I_{f} and I_0 differ only by the position of the NPs. Hence, we can equally measure σ_{ext} of a particle for $\Delta = 1 - I_{\text{f}}/I_0$, and for $\Delta = 1 - I_0/I_{\text{f}}$, where the measurement position changes by the shift distance. We can obtain two measurements of σ_{ext}, and average the result to decrease the noise by $\sqrt{2}$. Typically, shift-distances are approximately $2r_{\text{i}}$. This is the minimum possible shift, such that, within our measurement sensitivity, the intensity profiles of two NPs do not interfere. By minimising the shift, we also minimise the difference, between I_{f} and I_0. We can determine the noise in the background, $\hat{\sigma}_{\text{noise}}$, by measuring σ_{ext} at random locations in the image where there are no particles (this is discussed in Sec. 4.2.4.7, 4.2.4.9).

As proof of principle, we performed measurements on AuNPs of 40 nm and 100 nm nominal diameter. The results over 104 individual 40 nm diameter AuNPs are summarised in Fig. 4.2. Data was taken with the 40D, averaging over 36 images, and using the 0.95 NA 40x objective with 1.5 x multiplier. The distribution of σ_{ext} in the 40D G channel, whose wavelength range, discussed in Sec. 2.1.2, corresponds to the AuNP plasmon resonance, has a mean, $\bar{\sigma}_{\text{ext}} = 4000\,\text{nm}^2$. This is consistent with experimental and theoretical values found in literature [26,28,32,75]. We find the measured standard deviation of σ_{ext}, $\hat{\sigma}_{\text{total}} = 1300\,\text{nm}^2$, and the standard deviation of the background,

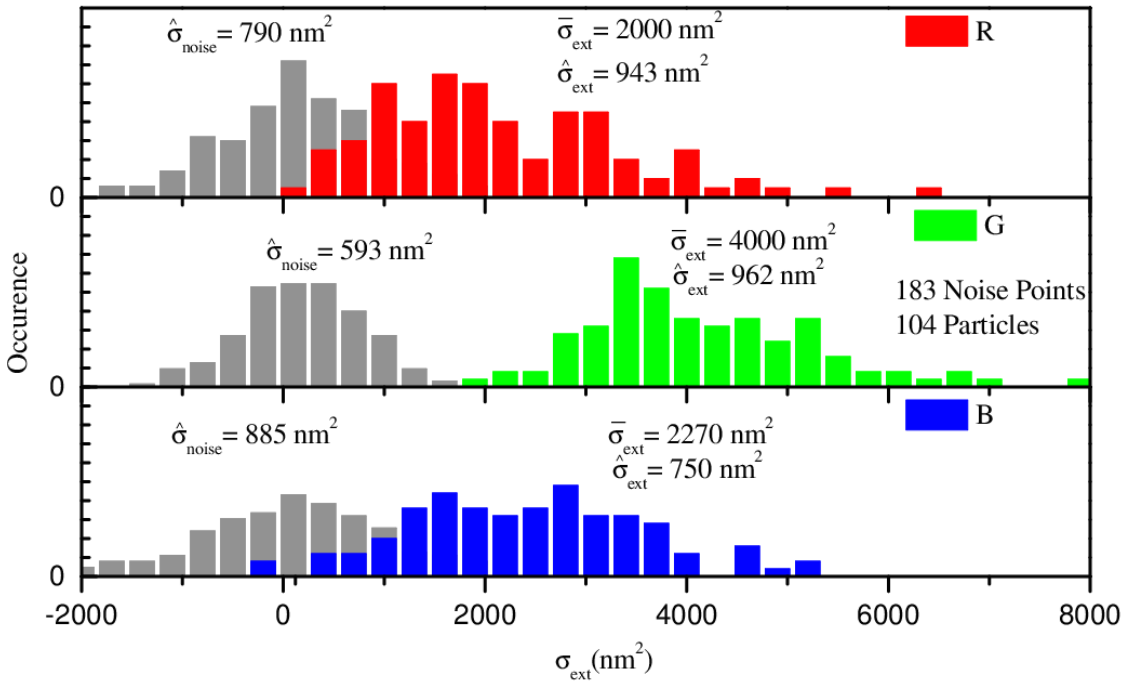

Fig. 4.2: Distributions of σ_{ext} for 104 AuNPs of nominal 40 nm diameter in the R, G, and B colour channels as indicated. The grey histograms show the noise distribution obtained by measuring σ_{ext} in 183 randomly selected regions without NPs. Figure reproduced from Ref. 80

$\hat{\sigma}_{\text{noise}} = 590\,\text{nm}^2$. $\hat{\sigma}_{\text{total}}$ contains a part due to the measurement noise. So, in order to deduce the standard deviation of the NP ensemble arising from the size distribution, $\hat{\sigma}_{\text{ext}}$, we assume independent Gaussian distributions of noise and NP extinction cross-sections, allowing us to use $\hat{\sigma}^2_{\text{ext}} = \hat{\sigma}^2_{\text{total}} - \hat{\sigma}^2_{\text{noise}}$. Thus, the standard deviation due to the size distribution of NPs, is $\hat{\sigma}_{\text{ext}} = 960\,\text{nm}^2$.

We can augment the measurements of σ_{ext}, by measuring σ_{sca}, in a darkfield image. Using the scattered intensity I_{df}, measured in dark-field microscopy and integrated over the same spatial area A_{i} as σ_{ext}, we obtain the detected power scattered by the NP. The scattered power is proportional to the scattering cross-section σ_{sca}. Normalising the scattered intensity to I_0 we can write

$$\sigma_{\text{sca}} = \eta \int_{A_{\text{i}}} \frac{I_{\text{df}}}{I_0} \frac{t_{\text{f}}}{t_{\text{df}}} \text{dA} \tag{4.2.4}$$

with t_{f} the exposure time in brightfield, t_{df} the exposure time in darkfield, and the constant η determined by relative excitation intensities between dark field and bright field illumination. This ratio is determined by the condenser NA_{c} ranges in bright field and

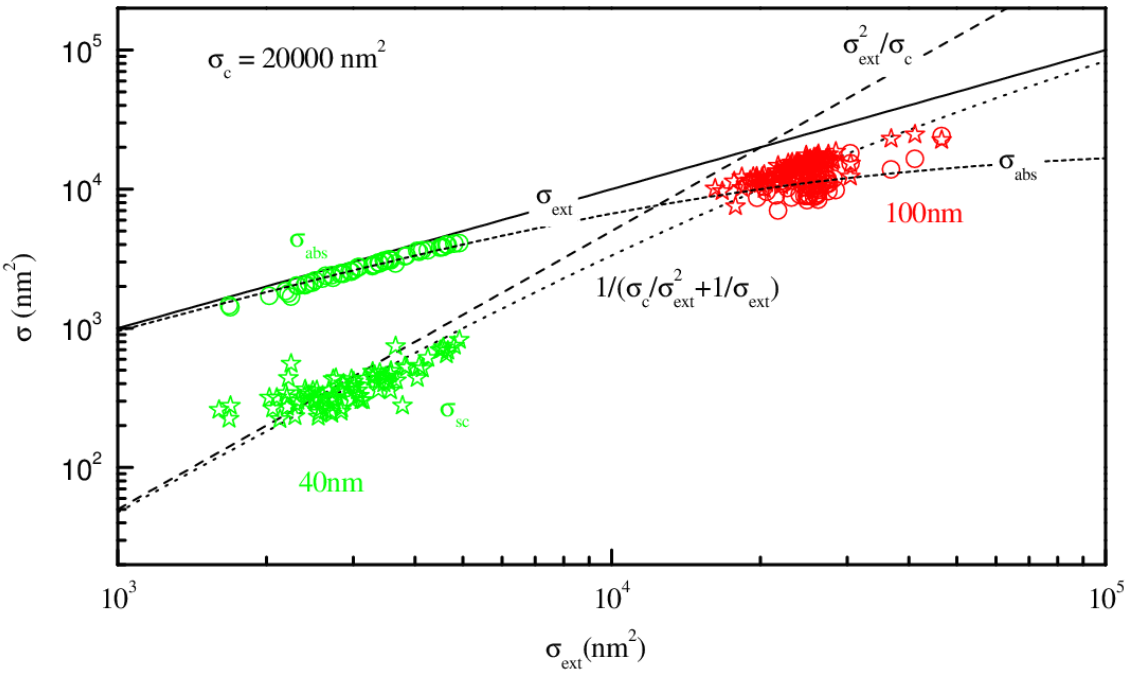

Fig. 4.3: Scattering cross-section σ_{sca} (stars) measured in dark-field images versus σ_{ext} measured in extinction images for 40 nm AuNPs and 100 nm AuNPs. The deduced absorption crossections σ_{abs} are given as circles. The dotted line gives the fitted scaling as labeled. The limiting behaviour for small σ_{ext} (dashed line) and large σ_{ext} (solid line), and the expected absorption cross-section (short-dashed) are also shown.

dark field. If η is known σ_{sca} can be quantified in absolute units. We determined η by comparing σ_{sca} with σ_{ext} on each NP of the ensemble, as shown in Fig. 4.3. AuNPs with σ_{ext} well below a certain cut-off value (σ_c) are dominated by absorption with cross-section σ_{abs} scaling as R^3. Since, σ_{sca} is proportional to R^6 in this regime, we expect $\sigma_{sca}\sigma_c = \sigma_{ext}^2$. Conversely, scattering dominates for larger particles such that $\sigma_{ext} \simeq \sigma_{sca}$. This trend is indeed observed inFig. 4.3, and a fit of the interpolation $1/\sigma_{sca} = \sigma_c/\sigma_{ext}^2 + 1/\sigma_{ext}$ allows us to infer $\sigma_c = 34000\,\mathrm{nm}^2$ and $\eta = 26$, both with about 10% error. The resulting σ_{sca} of the AuNPs is consistent with literature[32]. σ_{abs} is also given in Fig. 4.3. Using the calibrated σ_{sca} we find a detection limit for σ_{sca} of about $100\,\mathrm{nm}^2$, corresponding to an AuNP of 15 nm diameter. Measurements of σ_{sca} are limited by a background scattering contributing to I_{df} in our samples. In the absence of background scattering, increasing the exposure time allows in principle to detect $\sigma_{sca} < 1\,\mathrm{nm}^2$, corresponding to AuNP diameters < 10 nm, considering the camera dark

noise. For the dark-field data shown in Fig. 4.3, we used exposure times on the order of 5 s.

In order to determine σ_{ext}, and σ_{sca} of many particles, from an extinction image we developed the image analysis programme, ES. For a colour camera, such as the 40D, we split the images into RGB channels. With a monochrome camera, such as the PCO, colour information can be obtained by repeating the experiment, using different filters, such as the R,G, or B filter (with ranges described in Sec. 2.1) into the illumination. Multiple acquisitions of I_{f}, I_0, and I_{df} are averaged (see Sec. 4.2.4.2 and 4.2.4.3). Δ is calculated using Eq. 4.2.1. To find potential particle locations to be analyzed, we determine the particle locations as the peak pixels (maxima) of Δ with values in a range adjusted to reject noise and large aggregates (discussed further in Sec. 4.2.4.7). For each particle location, we choose A_{i} given by a centered disk of radius $r_{\text{i}} \approx 3\lambda/(2\text{NA})$ and calculate σ_{ext} and σ_{sca}. The measurement radius, r_{i} depends on the wavelength, and the objective NA. For the 0.95NA, 40x objective $r_{\text{i}} = 837$ nm, and for the 1.45NA, 100x objective, $r_{\text{i}} = 569$ nm, for $\lambda = 550$ nm. Once all particles of interest have been measured, the ES determines the mean, $\bar{\sigma}_{\text{ext}}$, and the measured standard deviation, $\hat{\sigma}_{\text{total}}$, of the NP ensemble, as well as a measurement of the noise in units of cross-section, $\hat{\sigma}_{\text{noise}}$.

In case data for different wavelengths are available, we can select individual NPs using their extinction colour, retaining particles with σ_{ext} largest in the colour channel corresponding to the expected plasmon resonance, e.g. G (R) for 40 nm (100 nm) spherical AuNPs having a LSPR at 540 nm (590 nm) in a surrounding medium of 1.5 refractive index. Particles which correspond to aggregates, debris, or largely non-spherical AuNPs are typically excluded in this way.

This technique has been extended to include polarisation-resolution by the addition of a linear polarizer in the excitation, as discussed in Sec. 2.1.1. We measure σ_{ext} and σ_{sca} as a function of polariser angle, θ. The polarization dependence provides information on the NP asphericity. Analysis of the dependence of σ_{ext} and σ_{sca} on θ is performed by fitting the experimental data with the function,

$$\sigma(\theta) = \sigma_0(1 + \alpha\cos(2(\theta - \theta_0))) \tag{4.2.5}$$

where σ_0 is the polarization-averaged cross-section σ, $\alpha \geq 0$ is the amplitude of the polarization dependence, and $0 \geq \theta_0 \geq \pi$ is an angular offset, indicating the direction

of the NP asymmetry. To estimate the influence of the measurement noise on the fit parameters we calculated their distribution over Gaussian random fluctuations of the fitted $\sigma(\theta)$ with a standard deviation $\hat{\sigma}_{\text{noise}}$. In more detail, for every angle, θ_{n}, there is a corresponding measurement of $\sigma^{\text{n}}_{\text{ext}}$ (or $\sigma^{\text{n}}_{\text{sca}}$), with an associated $\hat{\sigma}^{\text{n}}_{\text{noise}}$. For the cross-section measurements at each angle, a random number with Gaussian distribution and variance $\hat{\sigma}_{\text{noise}}$ is added and a fit with Eq. 4.2.5 to this data is made. The resulting parameters are statistically analyzed over many realizations of the random numbers, providing their distributions, mean, and RMS due to noise. Typically, the data is fitted 100 times.

4.2.2 Considerations for finite solid angle optics

We discuss here the impact of the finite solid angle of excitation, and collection, in the determination of the cross-section. The finite angular range of an objective implies that it also collects a fraction of the scattered light (see Sec. 1.1.1), leading to an underestimate of the extinction. This effect is represented in Fig. 2.3 (see Sec. 2.1.1). The green rays indicate scattering in (A) and (B). θ is the angle between the forward direction of the incident light, $\theta = 0$, and the scattered ray, i.e. θ is the zenith direction in spherical coordinates. Importantly, in Fig. 2.3, scattered rays are visible, for $\theta > 0$, within the NA of the objective. In (A) and (B), the angular dependence of the intensity is depicted by the length of the dotted (solid) green rays, for isotropic (dipolar) scattering. In the case of unpolarised excitation, the angular dependence of dipolar scattering is described below by Eq. 4.2.8. Isotropic scattering is not angularly dependent, and hence is represented by dotted line rays of equal length, for all θ, in Fig. 2.3(A). Generally, $P = \int I \cdot \mathrm{d}A$, with the infinitesimal area in spherical coordinates given by

$$\mathrm{dA} = r^2 \,\mathrm{d}\Omega = r^2 \sin\theta \,\mathrm{d}\theta \,\mathrm{d}\phi. \tag{4.2.6}$$

For isotropic scattering, we calculate the radiated power P, over a given angle θ, and the azimuth angle ϕ from zero to 2π, as

$$P = Cr^2 \int_{\Omega_{\text{sph}}} = Cr^2 \int_0^{2\pi} \int_0^{\theta} \sin\theta \,\mathrm{d}\theta \,\mathrm{d}\phi = -2\pi C r^2 \, cos(\theta)\Big|_0^{\pi} = 2\pi C r^2 (1 - \cos\theta), \tag{4.2.7}$$

with C a constant. If we collect all of the scattered light over a sphere, then θ is taken from zero to π, and Eq. 4.2.7 gives $P = 4\pi C r^2$. We call the acceptance half-angle of our

objective, θ_o, given by $n\sin\theta_o = \mathrm{NA}$, and the associated solid angle, Ω_o. Ω_o in a sample of refractive index $n = 1.5$, collected by an objective of NA = 0.95, is 1.38 steradians. For *isotropic* scattering this is $(1.38/4\pi) = 11\%$ of the total scattered light. We could correct for this, by adding 11% of the measured σ_{sca} to σ_{ext}. However, *dipolar* scattering is angularly dependent. For an unpolarized beam of light, of intensity I_0, incident on a spherical particle, the scattered intensity at observation distance R is given by[81],

$$I_{\mathrm{scat}} = I_0 \frac{\mathrm{k}^4 \alpha^2}{2\mathrm{R}^2}(1+\cos^2\theta) \tag{4.2.8}$$

where α is the polarizability. I_{scat} is independent of the azimuth angle, for unpolarized excitation and spherical particles. In this case, the collected scattered power is $P = \int_{\Omega_{\mathrm{obj}}} I_{\mathrm{scat}}\, r^2\, \mathrm{d}\Omega$. With $r = R$, we find

$$P^{\mathrm{col}} = \int_0^{2\pi}\int_0^{\theta_{\mathrm{obj}}} I_{\mathrm{scat}} \sin\theta \,\mathrm{d}\theta\,\mathrm{d}\phi \qquad P^{\mathrm{tot}} = \int_0^{2\pi}\int_0^{\pi} I_{\mathrm{scat}} \sin\theta \,\mathrm{d}\theta\,\mathrm{d}\phi, \tag{4.2.9}$$

where P_Ω^{col} is the scattered power collected by the objective, and P_Ω^{tot} is the total scattered power. If we assume the incident light is only in the forward direction, then I_{scat} and the objective collection are co-axial in our spherical coordinate system. So, using $P_\Omega^{\mathrm{col}}/P_\Omega^{\mathrm{tot}}$, we find that the objective collects 14.82% of the total scattered power for particles in the dipole regime. 14.82% is an upper limit in the dipolar case, because we have made an assumption about the excitation. We now take into account the NA range of the excitation light from the condenser.

We first consider Eq. 4.2.9, where I_{scat} now depends on $\theta, \phi, \theta_i, \phi_i$, with the scattered ray at angles θ and ϕ and the incident ray at angles θ_i and ϕ_i. We use a spherical coordinate system with the azimuthal axis given by the collection objective axis. Since I_{scat} only depends on $\cos(\alpha)$, with α the angle between incident direction $\mathbf{v}$ and scattered direction $\mathbf{u}$ (see Eq. 4.2.8), we can determine $\cos\alpha = \mathbf{u}\cdot\mathbf{v}$, with the dot product, where $\mathbf{u}$ and $\mathbf{v}$ presented in cartesian coordinates as

$$\mathbf{u} = \begin{pmatrix} \cos\phi\sin\theta \\ \sin\phi\sin\theta \\ \cos\theta \end{pmatrix} \qquad \mathbf{v} = \begin{pmatrix} \cos\phi_i\sin\theta_i \\ \sin\phi_i\sin\theta_i \\ \cos\theta_i \end{pmatrix}.$$

Thus,

$$\cos\alpha = \cos\phi\cos\phi_i\sin\theta\sin\theta_i + \sin\phi\sin\phi_i\sin\theta\sin\theta_i + \cos\theta\cos\theta_i \tag{4.2.10}$$

Using the trigonometric identity, $\cos(\alpha-\beta) = \cos\alpha\cos\beta + \sin\alpha\sin\beta$, Eq. 4.2.10 becomes

$$\cos\alpha = \cos(\phi')\sin\theta\sin\theta_\mathrm{i} + \cos\theta\cos\theta_\mathrm{i}, \tag{4.2.11}$$

with $\phi' = \phi - \phi_\mathrm{i}$. We can transform I_scat in terms of this new angle, α, and by collecting the constants into a single variable, C, with

$$I_\mathrm{scat} = C\left(1+\cos^2\alpha\right) \tag{4.2.12}$$

Substituting this into Eq. 4.2.9, we obtain

$$P_\mathrm{scat}^\mathrm{col} = C\cdot\int_{\phi_\mathrm{i}}\int_{\theta_\mathrm{i}}\int_{\phi}\int_{\theta}\left(1+\cos^2\alpha\right)\sin\theta\sin\theta_\mathrm{i}\mathrm{d}\theta\,\mathrm{d}\phi\mathrm{d}\theta_\mathrm{i}\mathrm{d}\phi_\mathrm{i}. \tag{4.2.13}$$

However, with $\cos\alpha$ in the form of Eq. 4.2.11 we can change the limits of integration from ϕ_i and ϕ to ϕ' and $\phi'' = \phi' + \phi_\mathrm{i}$, to get

$$P_\mathrm{scat}^\mathrm{col} = C\cdot\int_{\phi''}\int_{\theta_\mathrm{i}}\int_{\phi'}\int_{\theta}\left(\cos(\phi')\sin\theta\sin\theta_\mathrm{i} + \cos\theta\cos\theta_\mathrm{i}\right)\sin\theta\sin\theta_\mathrm{i}\mathrm{d}\theta\,\mathrm{d}\phi'\mathrm{d}\theta_\mathrm{i}\mathrm{d}\phi''. \tag{4.2.14}$$

Now, since the azimuth angles are taken from 0 to 2π, and the limits integration of θ_i and θ are based on the condenser and objective NAs, respectively, we find

$$P_\mathrm{scat}^\mathrm{col} = 2\pi C\cdot\int_{\theta_\mathrm{c,min}}^{\theta_\mathrm{c,max}}\int_{\theta_\mathrm{o,min}}^{\theta_\mathrm{o,max}}\sin\theta_\mathrm{i}\sin\theta\left(1+\left(\cos\phi'\sin\theta\sin\theta_\mathrm{i}+\cos\theta\cos\theta_\mathrm{i}\right)^2\right)\mathrm{d}\theta\,\mathrm{d}\phi'\mathrm{d}\theta_\mathrm{i}. \tag{4.2.15}$$

This leads to

$$P_\mathrm{scat}^\mathrm{col} = \frac{2\pi^2 C}{8}\Big(\cos\theta\cos\theta_\mathrm{i}\left(22+2\cos^2\theta\cos^2\theta_\mathrm{i}+\right.$$
$$\left.\sin^2\theta\sin^2\theta_\mathrm{i}+2\sin^2\theta+2\sin^2\theta_\mathrm{i}\right)\Big)\Big|_{\theta_\mathrm{o,min}}^{\theta_\mathrm{o,max}}\Big|_{\theta_\mathrm{c,min}}^{\theta_\mathrm{c,max}} \tag{4.2.16}$$

If one wanted to calculate the absolute collected power, one would need to take into account that I_0 is spread over all angles of the condenser. Hence, Eq. 4.2.15 must be normalised by the solid angle of the condenser, Ω_cond. We are not concerned with the absolute power scattered here, because we look only at $P_\mathrm{scat}^\mathrm{col}/P_\mathrm{scat}^\mathrm{tot}$. To determine, $P_\mathrm{scat}^\mathrm{tot}$, we use Eq. 4.2.15 integrating θ from 0 to π, and keeping all other limits the same. For the case of condenser NA matched to objective NA (i.e. extinction measurement conditions), with NA = 0.95 for the 40 x objective, and immersion medium of refractive

index 1.5, then from $P^{\text{col}}_{\text{scat}}/P^{\text{tot}}_{\text{scat}}$ we find the collected fraction of scattered light to be 13.6%. This difference increases for immersion media of decreasing refractive index, e.g. water, due to the change in collection angles. This analytic solution allows for calculation of the collected scattering fraction for *any* configuration of condenser and objective, e.g. dark-field. In the case of our darkfield setup with NA range (1.1-1.4), with objective and immersion oil as before, the fraction of scattered light is 10.8%.

If we call the collected fraction of scattered light in *brightfield*, ζ_{col}, then the measured extinction is, $\sigma_{\text{meas}} = \sigma_{\text{abs}} + (1-\zeta_{\text{col}})\sigma_{\text{sca}}$. So, from measured values of σ_{ext} and σ_{sca}, the corrected absorption is, $\sigma_{\text{abs}} = \sigma_{\text{ext}} - (1-\zeta_{\text{col}})\sigma_{\text{sca}}$. For particles in the Mie regime ($R \geq \lambda$), the forward scatter becomes dominant. For our setup, this would result in the objective collecting, an increasing fraction of the total scattered power, i.e. ζ_{col} increases in the Mie regime.

4.2.3 Shot-noise and systematic noise

In order to estimate the minimum possible noise for the PCO, we consider the following, as in Ref. 80. The relative shot noise is given by $1/\sqrt{N_{\text{ph}}}$ with the detected number of photons N_{ph} which is determined by the number of acquisitions N_{a}, the full-well capacity N_{fw} of the camera pixels, the number of pixels N_{px} in the area A_{i}, and the fraction ν of pixels used for the colour channel (for the Bayer colour filter of our camera $\nu = 1/2$ for G and $\nu = 1/4$ for R, B), yielding $\hat{\sigma}_{\text{noise}} = A_{\text{i}}/\sqrt{N_{\text{a}}N_{\text{fw}}\nu N_{\text{px}}}$. With the pixel size d_{px}, the area $A_{\text{i}} = \pi r_{\text{i}}^2$ with $r_{\text{i}} = 3\lambda/(2\text{NA})$, and the magnification M onto the camera, we find

$$\hat{\sigma}_{\text{noise}} = \frac{3\lambda d_{\text{px}}}{2M\text{NA}}\sqrt{\frac{\pi}{N_{\text{a}}N_{\text{fw}}\nu}} \tag{4.2.17}$$

For the green channel of the 40D, we have $N_{\text{fw}} = 4\times10^4$ electrons, $N_{\text{a}} = 36$, $M = 60$, $d_{\text{px}} = 5.7\,\mu$m, NA = 0.95, $\lambda = 0.53\,\mu$m, and $\nu = 1/2$, yielding $\hat{\sigma}_{\text{noise}} = 589\,\text{nm}^2$, in agreement with the measured noise in Fig. 4.2. The blue and red channels have a factor of $\sqrt{2}$ larger noise due to the smaller ν. We will now discuss measurement of the noise in the PCO image, before applying Eq. 4.2.17 to extrapolate a limiting value for the measurable extinction cross-section. Significant effort was dedicated to decreasing the detection limit of the wide-field technique. Characterisation of several sCMOS cameras, as

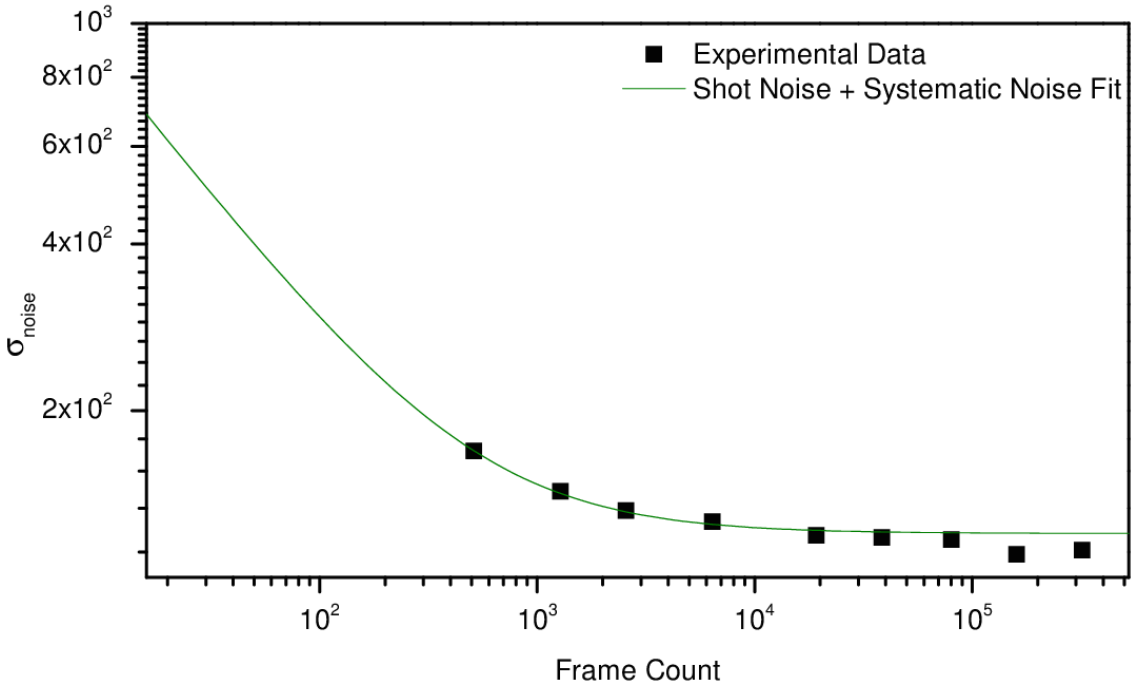

Fig. 4.4: The dependence of measured $\hat{\sigma}_{\text{noise}}$ on the number of averaged I_{f}, I_0, and I_{B} frames used to construct the extinction image. The plot was fitted with $\left(\frac{b^2}{x}+a^2\right)^{-1/2}$, where $b = 2700\,\text{nm}^2$ is the shot noise for a single frame, and $a = 120\,\text{nm}^2$ is the systematic noise.

well as the Canon 40D and 70D, were important in determining the lowest achievable shot-noise, and thus the ultimate limiting factor in the extinction measurement. The PCO Edge 5.5 sCMOS camera was eventually chosen over several competitors, considering cost, specifications and supplied software. Reports on noise and saturation, for the two cameras used in this work, the Canon 40D and the PCO.edge 5.5 RS, are given in Appendix B. Briefly, for two identical images, I_1 and I_2, differing only by noise, we call the noise image, $I_{\text{noise}} = I_1 - I_2$. For N_{a} images taken, we have two methods of analysing the effect of averaging on the noise. The first method is to separately average the first half of N_{a} images and the latter half of N_{a} images, and then perform the subtraction to get the averaged, I_{noise}. This means that the average time, between subtracted images is $\tau_{\text{sub}} = N_{\text{a}}\,t_{\text{ex}}$, with t_{ex} the exposure time. However, this method is prone to long-term drift in the sensor. Instead, a better method is to subtract adjacent image pairs, that is,

$$\bar{I} = \frac{(I_1 - I_2) + (I_3 - I_4) + \ldots + (I_{N_{\text{a}}-1} - I_{N_{\text{a}}})}{N_{\text{a}}}. \tag{4.2.18}$$

In this case, τ_{sub} reduces to t_{ex}, which eliminates long-term effects. We can see from Appendix B that image averaging decreases the noise as $1/\sqrt{N_{\text{a}}}$, as expected in both the 40D and PCO, up to the final measurement point of 8192 noise images (16384 images acquired). Hence, we can use Eq. 4.2.17 to estimate noise at large values of N_{a}, to obtain limiting practical values of the measurable extinction. For $N_{\text{a}} = 320512$ images, using the 40 x objective, with 1.45 NA and 1.5x multiplier giving $M = 60$, and the PCO, with $d_{\text{px}} = 6.5\,\mu$m, $\nu = 1$, and $N_{\text{fw}} = 30000$ electrons, we expect a noise in the extinction of $\hat{\sigma}_{\text{noise}} = 6\,\text{nm}^2$. We test this experimentally, by performing extinction measurements on a clean sample and measuring background points. We took up to 320512 images, averaging 256 prior to saving frames, hence, reducing the number of saved frames to 1252, per focus, reference, and background sets. Frame size was 400 x 400, allowing a framerate of 534 FPS, and thus a measurement time per image set of ~ 10 minutes. $\hat{\sigma}_{\text{noise}}$ was then measured for extinction images developed by averaging over increasing numbers of the captured images. The dependence of extinction noise on averaged frames can be seen in Fig. 4.4, where a systematic offset can be seen around $120\,\text{nm}^2$. We fitted this noise trend, assuming a Gaussian addition of the shot noise and systematic noise. If we drop the systematic offset, assuming this can be dealt with in the experimentation, this fit leads to the conclusion that at 320512 frames, with the 0.95 NA objective and effective 60x magnification, we can achieve $\hat{\sigma}_{\text{noise}}$ of $4.8\,\text{nm}^2$. This is in reasonable agreement with our expectation.

To reduce the influence of the drift on the results, we developed a time-symmetric referencing technique. Assuming a measurement time t for all frames averaged into I_{f} and I_0, we measure I_0 for $t/2$, then measure I_{f} for full time, t, and then measure I_0 for the remaining $t/2$. Furthermore, referencing via defocus, versus lateral sample shift, produces different systematic errors. When defocusing the objective, the light path significantly changes, and results in the large systematic errors. Since, we have an xyz-controllable nanostage, we are instead able to defocus the sample, by moving it away from the objective. However, both defocus methods suffer from the need to move the sample far enough away from the objective, that the defocused NP does not measurably influence the reference field. We defocus by up to $15\,\mu$m. The shift-reference method only requires the movement of the particle by $2r_{\text{i}}$, which can be on the order

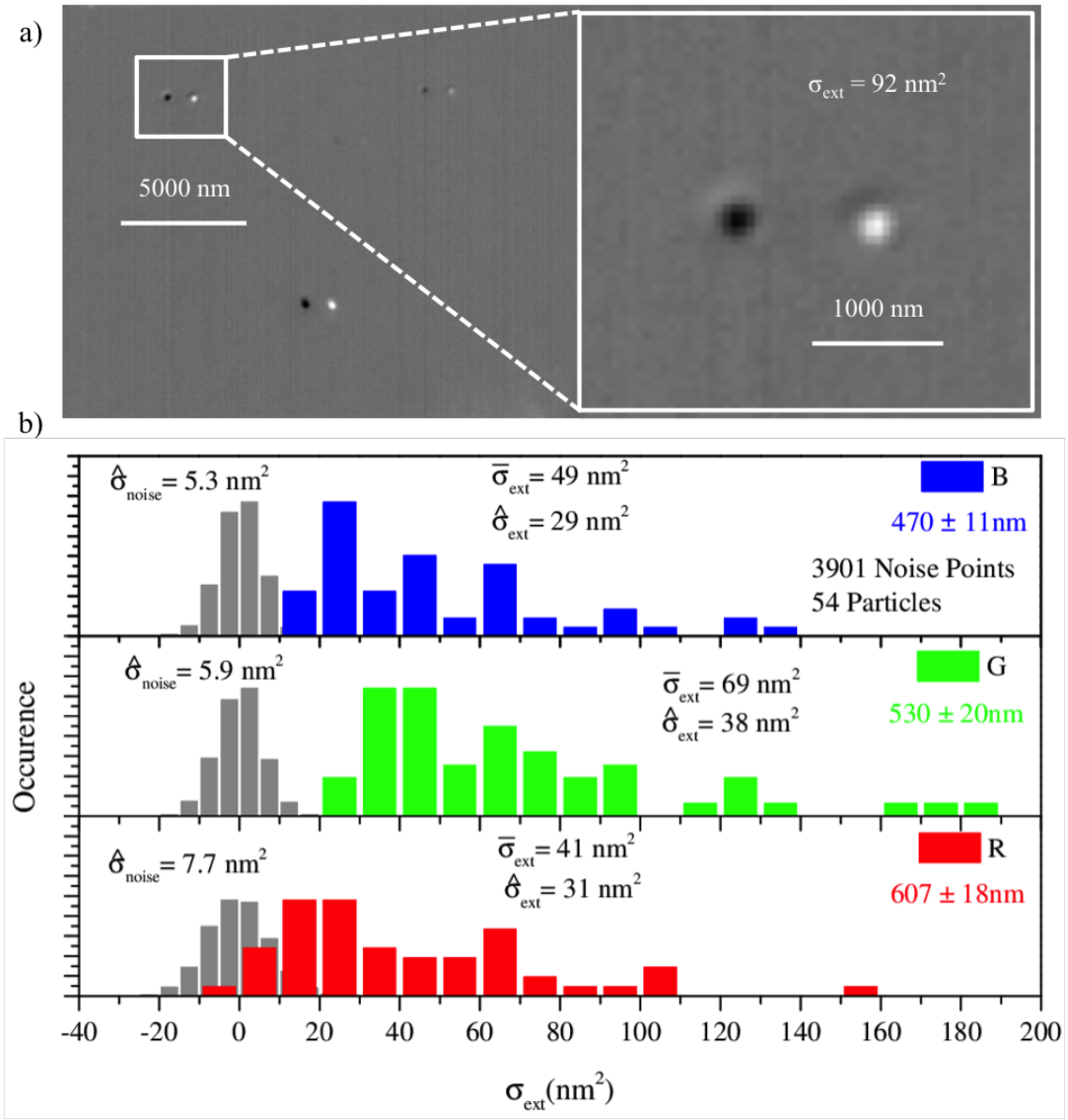

Fig. 4.5: a) Wide-field extinction image of single AuNPs of nominal 10 nm diameter in the G channel, using a 100x 1.45 NA oil objective and a sCMOS camera (see text). The right panel is a zoom over the region indicated by the white frame. Grey scale min =-0.005, max = 0.00055. b) Distributions of σ_{ext} for 54 AuNPs of nominal 10 nm diameter in the R, G, and B colour channels as indicated. The grey histograms show the noise distribution obtained by measuring σ_{ext} in 3901 randomly selected regions without NPs.

of a micron, and is the best possible reference.

After, characterisation of the cameras was completed, and experimental method were optimised, drop cast samples of 10 nm AuNPs were made. The 10 nm samples were imaged with the PCO acquiring 100 images, each averaged over 256 frames, to give a total framecount = 2.56×10^4 over 64.48 second integration time, with 397 FPS, and a 640 x 540 frame size. This measurement time was chosen as the setup began to drift in the z-direction, which we cannot account for in the analysis. Using Eq. 4.2.17, given the PCO parameters, and the 100x 1.45 NA objective, the expected value of the noise for $N_a = 2.56 \times 10^4$ frames is $\hat{\sigma}_{\text{noise}} = 2.37\,\text{nm}^2$. The particles were measured with each of the R, G, and B, Semrock filters. The results are shown in Fig. 4.5. The measured $\hat{\sigma}_{\text{noise}}$, was 5.9nm^2 in the green channel, and as low as 5.3nm^2 in the blue channel, and are approximately a factor of 2 larger than expected. However, we must take into account systematic contributions could still be present. $\hat{\sigma}_{\text{noise}}$ below $6\,\text{nm}^2$ allows measurement of AuNPs down to 5 nm diameter for a total experiment time of ~ 3 minutes. This is a significant improvement over our previous results with the 40D.

4.2.4 Extinction suite plugin for ImageJ

4.2.4.1 Introduction

The wide-field extinction technique, discussed in Sec. 4.2.1, can produce extinction images containing data for hundreds of particles. Manual analysis of each of these particles would be inefficient. We have therefore developed a programme for automated data analysis, the ES, to analyse the data, including ensemble statistics. The experimental technique is applicable to any nanoparticles and on any microscope system equipped with a camera. The analysis plugin was written to meet the standards of the experimental technique's wide applicability, serving as a direct analytical companion. This section describes the ES and exemplifies the analysis procedure. Results, obtained using the ES, have contributed to the data shown in Ref. 17,80,82.

The ES was written in ImageJ's macro language (IML). IML was chosen to leverage the features of ImageJ. ImageJ is a free, widely used program for image handling, developed by the NIH. It has a large stock of image analysis functions built-in, and with IML, these

functions could be used in a simplified (C-like) language construct. IML has many built-in functions useful for programming, for instance for curve fitting and plotting, and array functions, etc. It also allows use of ImageJ's GUI.

ES consists of four main modules - Image Conversion, Image Averaging, Extinction Image Development, and Particle Analysis. All modules may be used individually, or in particular combinations so long as the requested modules have the necessary data available. In general, options will change depending on the modules chosen, the input format, and the kind of experiment, e.g. whether it was polarization-resolved, or included darkfield images.

4.2.4.2 Image conversion

In order to be widely applicable, the ES accepts a variety of input image formats, including proprietary RAW format images from consumer cameras, such as the Canon EOS 40D with ".CR2" format, using the DCRAW Reader plugin[83]. The DCRAW reader has a number of useful conversion options. In order to obtain quantitative measurements, the true raw readout of the camera must be used.

40D The Canon ".CR2" format natively outputs as 8-bit, with non-linear intensity response, in colour. Note that the true digitizer range of the camera is 14-bit. The colour image is made up of units of four pixels according to the Bayer filter pattern; one blue pixel, two green pixels, and one red pixel[84]. For the remainder of this discussion, the units of four pixels will be called a Bayer pixel, and individual pixels making up the Bayer pixel will be called colour pixels. For the Canon EOS 40D, which has a sensor with 10.1 megapixels (MP), there are actually 2.525 MP with the blue filter, 2.525 MP with the red filter, and 5.05 MP with the green filter. For the entire 10.1 MP image to be rendered in full colour, the filter pattern requires that the camera interpolate the other colour pixels in each of the Bayer pixels. Using DCRAW, the 14-bit range, linear in the number of electrons per pixel, can be retrieved by choosing options "16-bit" and "linear." To remove interpolation, which does not provide more information, but increases the data size by a factor of 4, the "half size" option can be applied, returning images in colour pixels. The two green colour pixels per Bayer pixel, are averaged. Hence, the

40D raw output image, of 2592 x 3888 pixels, is converted to a three channel 16-bit Tiff image of 1301 x 1954 pixels. Note the apparent increase in available pixels from the "half size option", i.e. $2592/2 < 1301$. This is most likely due to edge pixels removed by the native output processing. The DCRAW half-size option means that interpolation is no longer necessary, and hence, can make direct use of the edge pixels. To make sure further scaling or processing, such as colour balancing, is removed, the "Document mode, no scaling" option is selected. The output range of the images is 14-bit, corresponding to the digitizer range.

BW Some cameras output colour images, which do not need conversion. For further analysis, the resulting three-channel tiff is split into three one channel Tiffs. Typically Tiff format is used for ES image analysis. Many scientific cameras can output directly to, e.g., Tiff format and present the raw readout of the camera needed for a valid quantitative analysis.

4.2.4.3 Image averaging

The next module of ES is the image averaging module, which is used to average the multiple images taken for each of the analysed image sets, i.e. focus, reference, and background, as well as darkfield and background with darkfield exposure times, if taken. Assuming the user has specified their inputs correctly, the software will move through the folders, averaging each of the image sets. Colour images have their individual colour channels averaged, after the splitting mentioned above.

4.2.4.4 Extinction image development

The extinction image development module creates the extinction images using Eq. 4.2.1, discussed in Sec. 4.2.1. Actual implementation of the mathematics to manipulate the images is performed using ImageJ's math functions, and ImageJ's process function, Image Calculator, for division and subtraction of images. The background is subtracted from the defocus image and the darkfield image. Note, darkfield images and brightfield images are typically captured with different exposure times. Hence, if darkfield images are captured, a second set of background images should be captured

with matched exposure time. The developed images are saved in 32-bit float tiff format.

4.2.4.5 Particle analysis

The particle analysis module is more complicated from both coding and user perspectives. The user is required to work with the images. They must choose intensity limits, noise tolerances, and image regions. These inputs allow the plugin to automate finding valid particles, suitable background points, and performing image registration. The analysis module also features a number of user options to increase the selectivity, reliability, and convenience of the measurements. For example, when colour information is obtained, the user may input the expected dominant colour channel, e.g. the green channel of the Canon EOS 40D for spherical gold NPs, or the blue channel for spherical silver NPs. The plugin supports simultaneous measurement of up to two distinct NP sizes in a single image, assuming either all NPs are of the same material, or that colour information is not utilised. If the experiment was polarisation-resolved, the user can specify how many times the polarisation-dependent fit data is simulated to determine the fit error (this concept is discussed in Sec. 4.2.1).

Processing can take anywhere from 30 seconds to > 10 minutes depending on the computer, the number of particles in the image, the number of background points to be sampled, whether or not the experiment was polarisation-resolved, and if so, the number of angles, etc. An online manual can be found in Ref. 85, so details into how a user should operate the program will not be given here. However, it is worth discussing how some of the automations are implemented.

To avoid confusion in this section, the nomenclature regarding “particle”, “background points” and intensity “maxima” is as follows: the word “particle” refers to a physical object in the image, e.g. a diffraction-limited spot, which can cover an area of many pixels, the phrase “background points” is analogous to “particle” in that it refers to an area of the image containing many pixels without a particle, and the word “maximum” is the individual pixel with the highest intensity in a particle.

4.2.4.6 Image registration

Image registration is used to compensate for spatial drift, and is typically required, for a polarisation-resolved measurements, or for darkfield images, generally due to elongated experiment time and increased manual mechanical interference with the setup. For example, the microscope shows thermal drift, or can be moved, e.g. when inserting/removing the dark field ring, or when switching polariser angle. These small movements manifest as a different sample position relative to the light path, and hence, to the detector. So, the particles are shifted, within images taken at different experimental stages. Registration determines these shifts and corrects them. The image registration uses the particle positions to track a pattern of particles across the images. The particles are located via their intensity maxima, with ImageJ's Find Maxima function. A pixel is considered a local maximum, if it is more intense than its surrounding pixels, by a user-chosen level. This level is called the "noise tolerance," in the Find Maxima function, and should be chosen so that only one maximum per particle is found.

At this point one should elucidate why a pattern recognition operation was chosen to perform the registration. A natural choice would be image cross-correlation, however implementation through IML was not straightforward, and could be time-consuming for large datasets. One could think to use an intensity metric; for instance a particle has its mean intensity measured in the initial image, and then all particles in a small region of the subsequent images are measured, until a corresponding intensity is found. However, this is not effective for a number of reasons. It would only be reasonable if the shift was very small, otherwise a large search area would be needed, in an image with potentially hundreds of particles. Next, the intensity scales are relative in the extinction (0-1), and absolute in darkfield (0-65536 max), so it would only work when the images are of the same type. Furthermore, measurement noise requires that the particle's mean intensity falls within a range. This means that there is a chance of finding another particle, whose mean intensity is within the range of the target. If instead a pattern recognition operation is adopted, it is the relative positions of the particles which is tracked. This relationship should be fixed regardless of intensity variations or scaling.

Patterns are recognized by the plugin, first by choice of a primary particle, within a

user-selected region containing a group of N particles, then by measurement of the difference between the primary particle maximum's xy coordinates and the xy coordinates of the maxima of the other N−1 particles. The length N array of absolute maxima x and y coordinates is recorded. The length N − 1 array of relative x and y coordinate-differences determines the pattern. The plugin then searches for the pattern by comparing xy coordinate-differences from the original image to those in the new image(s). Please note, that the groups in the new images may contain more, or less, particles than the group in the original. This can be due, for instance, to the fact that darkfield images are not limited by shot noise, like extinction images, but rather by the absolute amount of light available. Hence, in most cases, there will be scatterers which are detected in darkfield, but do not have a large enough total extinction to appear above the (shot) noise in the extinction images. The appearance of new particles has no affect on the relative positions of the original particles. When xy coordinate-differences are matched, the particles are known to be those of the original image. The new absolute positions of their maxima are recorded. The shifts are subsequently calculated. The final calculated x and y shifts are the means of all of the measured shifts of all matched particles in the pattern. This further increases the reliability of the shift value. To reduce registration time, it is generally advisable that the user-selected region is small, and that a high noise tolerance is selected, so that not too may maxima make up the pattern, e.g. 10 particles is sufficient. The plugin accommodates small changes to the pattern, via the "Pattern Recognition Tolerance" (PRT). The PRT is just a constant, γ_{p}, chosen by the user. It can be changed to allow for the possibility that, between image sets, particle maxima may deviate by a few pixels, e.g. due to image noise, even if the particle has not physically moved relative to the sample. The PRT works as follows. Two particles have coordinate differences, δx_1 and δx_2, in the initial image and in the image to be registered, respectively. In order to match the pattern, the programme will not look exactly for $\delta x_2 = \delta x_1$, but rather for $\delta x_2 \in [\delta x_1 - \gamma_{\mathrm{p}}, \delta x_1 + \gamma_{\mathrm{p}}]$. Typically, the PRT is kept small, e.g. less than three pixels.

4.2.4.7 Particle and background identification

After registration, particle analysis begins by using the Find Maxima function as described in the previous section, but generally in a larger user-defined region, and at a lower noise tolerance, increasing the number of identified points. The noise tolerance is chosen as a compromise, between maximizing the number of recognized particles and minimizing the number of recognized background. It is typically 4-5 RMS above the background. Once a noise tolerance is specified, the plugin records the locations of the points the image. A "proximity filter" excludes any pairs of points within a distance, $2r_\mathrm{i}$ from the analysis. Next, a user-specified number of random points, in regions of the image *without NPs* is analysed, i.e. in regions further than $2r_\mathrm{i}$ away from of a particle. The background points are measured in the same way as the particles, as described in Sec. 4.2.1. This gives a direct measure of the noise, in the extinction cross-section, for that particular experiment. Proximity-filtered particles are further filtered by the user-defined, intensity range(s). Again, the program can accept up to two intensity ranges, for analysis of two nominal particle sizes. The particle mean intensities are measured within the area defined by r_i. A particle is considered acceptable, if its mean measured intensity falls within the specified range(s). It is determined to be a representative NP of one size, or the other, depending on which intensity range it falls into.

4.2.4.8 Gaussian fitting of particle peak coordinates

The actual location of the maximum of a particle within r_i is determined both by the particle's intensity profile and by image noise. Hence, the center of the particle's spatial intensity profile may not be at the local pixel maximum, as determined by ImageJ. To improve the accuracy of a particle's xy coordinate location, Gaussian fitting of the particle's intensity profile is performed within $[-r_\mathrm{i}, r_\mathrm{i}]$, along the x,y, and two xy diagonal directions. The diagonals account for potentially diagonally asymmetric point spread functions, which we have noted in darkfield, with the 40 x 0.95 NA objective. Note, this is only a subtle effect. The mean location of the peak, extracted from the Gaussians fitted along the four directions, yields sub-pixel location accuracy. This fit assumes a particle's intensity profile has a peak, which is suited for a diffraction-limited spot. Thus,

the fit is only performed *after* proximity and intensity-filtering of particles, avoiding bad fits resulting from irregular intensity profiles of unfiltered objects.

4.2.4.9 Cross-section measurement methods

Once the coordinates of the particles in an extinction image have been recorded, the extinction cross-sections are calculated. The method we used for published results, is the "double radius method," described in Sec. 4.2.1. It makes use of several custom algorithms to increase usability in dense samples. In its final form, it is the most reliable and accommodating measurement method developed within the ES. Before describing it, we will consider the other, earlier developed measurement methods available in the ES. There are three methods available for the measurement of cross sections, and the determination of background offsets and measurement noise. Two methods make use of a single radius. The differences lie in the locality of the background measurement, and the required distance between particles. Note, when using either of the two single radius techniques, $2r_\mathrm{i}$ is the smallest separation, between two particles, before rejection by the proximity filter. If two particles were closer than $2r_\mathrm{i}$, the detectable parts of their intensities would overlap significantly (see Sec. 4.2.1), distorting the measurements. We call $2r_\mathrm{i}$ the proximity limit, regardless of measurement technique, and it gives the upper limit for analysable sample densities.

In all methods a user selects a region of an image, in which to locate particles and background points. In the original method of the earliest versions of ES, the plugin measures the mean intensities of each of the particles and random background points inside of the large region, with a ROI of radius, r_i. For the moment, let us redefine the variables concerning measured intensities. The mean intensity measurement of a single random background point is δ_b. The mean of l random background intensity measurements is

$$\Delta_\mathrm{b} = \frac{1}{l}\sum_{\mathrm{k}=1}^{l}\delta_{\mathrm{b,k}}, \tag{4.2.19}$$

with $\delta_{\mathrm{b,k}}$ the mean intensity measurement of the k^{th} background point. In this case, Δ_b is the same for all particles, regardless of their location, as it was deduced from values measured across the entire large region. For this reason, we will call it the "single region

reduction method." The error in the extinction measurements is determined with

$$\hat{\sigma}_{\text{noise}} = \int_{A_\text{i}} \hat{\delta}_\text{b}\, \text{dA}, \tag{4.2.20}$$

with

$$\hat{\delta}_\text{b} = \sqrt{\frac{1}{l-1}\sum_{\text{k}=1}^{l}(\delta_{\text{b,k}} - \bar{\delta}_\text{b})^2}. \tag{4.2.21}$$

The single region method has the advantage that particles need only be $2r_\text{i}$ apart. The disadvantage is that in this method, Δ_b is not local to each particle, but is an offset measured across the entire selected image range.

The second method is the same as the first, but also uses a second ROI, of user-defined radius, centered at each particle position, in which the background points are found. This second ROI should be as small as possible, while leaving enough space to measure a user-chosen number of random background points using the ROI, of radius r_i. Nearby particles may be present inside the second ROI. If so, they are taken into account by the Find Maxima function, as described in Sec. 4.2.4.6, 4.2.4.7. This technique is considerably slower than the first. Every particle has its own local region, in which the Find Maxima function is run, and valid background points are found and measured. For every particle, k, $\Delta_{\text{b,k}}$ and $\hat{\delta}_{\text{b,k}}$ are deduced as Δ_b and $\hat{\delta}_\text{b}$ were for the single large region of the previous method. As such, this method is referred to as the "regional reduction method." The regional reduction method is superior to the single region method, because every particle has a unique, nearly-local background offset. The limit for inter-particle distance is again at $2r_\text{i}$.

In earlier versions of the plugin, the double radius method appears to effectively be a mixture of the first and second methods mentioned. Inside a large single region, a number of particles and valid background points are located. All of these are measured in the same fashion. A ROI of radius r_i takes the mean intensity of the particle or background point. Then, a second ROI, of radius $r_\text{j} = 2r_\text{i}$, takes the combined mean intensity of the first region, $[0, r_\text{i}]$, plus the mean local background intensity of the outer region, $[r_\text{i}, r_\text{j}]$. Note for a given particle, k, the mean intensity in the region $[0, r_\text{i}]$ is δ_k, with local background, $\delta_{\text{b,k}}$, in the outer region, $[r_\text{i}, r_\text{j}]$, around the particle. Since, we measure the combined mean intensity of the inner and outer regions with the second ROI in $[0, r_\text{j}]$, $\delta_{\text{b,k}}$ had to be deduced in this early version. For l random background

points, we calculate the mean and standard deviation over all l of $\delta_l - \delta_{b,l}$. The mean is approximately zero. The integration over A_i of the standard deviation directly yields the noise in the measured cross-section associated with this local background reduction method. Determination of a local background offset should give the most accurate measure of the extinction for a given particle. The disadvantage is that particles must be at least $r_j + r_i$ apart, so the local background region is not influenced by the intensities of the neighboring NPs. Note, r_j need not be $2r_i$, but in practice this has been found to be an effective and reliable radius for this technique. The larger the radius, the more pixels can be included when measuring the mean intensity, decreasing the noise of the measurement. However, the point is to be local, so the radius should not be very large, due to increasing systematic errors. As such, in practice, this results in the requirement of inter-particle distances of at least $3r_i$. Hence, sample density must be lower than in either of the previous two examples. In order to develop a local reduction method capable of the $2r_i$ inter-particle limit, the final version of the double radius method implements custom ROI functions, as well as the $N\hat{\delta}_b$ recursion technique.

4.2.4.10 Custom ROI coordinate functions and $N\hat{\delta}_b$ recursion

The $N\hat{\delta}_b$ recursion technique is an algorithm developed to remove pixels affected by other particles in the outer ring of the double radius method, and hence, to reduce the inter-particle distance limit to $2r_i$, regardless of r_j. We accomplish this as follows, again choosing new variable names to avoid confusion. A given particle has mean, Δ_b, and standard deviation, $\hat{\delta}_b$, of the pixels in it's outer measurement region, $[r_i, r_j]$. A given pixel, $P \in [r_i, r_j]$, has intensity, I. We exclude any pixel, P, for $I \notin [\Delta_b - N\hat{\delta}_b, \Delta_b + N\hat{\delta}_b]$. We then remeasure the mean and standard deviation, performing this recursively, until the magnitude of the standard deviation converges. N is a simple factor indicating the number of standard deviations to be accepted. By default, N is 2. In this way, we can exclude outliers in the background area, due to, e.g., nearby particles. The spacing limit is now reduced to $2r_i$. Any particle which loses more than 50% of the pixels in its background, via the $N\hat{\delta}_b$ recursion loop is discarded.

The $N\hat{\delta}_b$ recursion technique, requires direct access to individual pixel coordinates and intensity values within the ROIs. While ImageJ has many functions available for

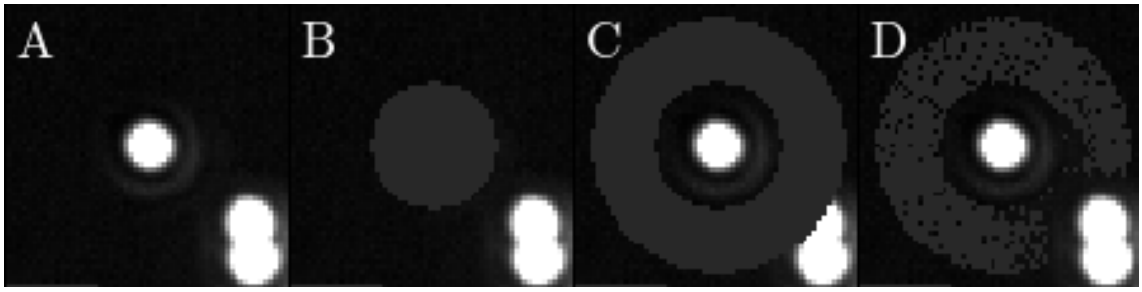

Fig. 4.6: A) Extinction Image of a 60nm AuNP taken with a 1.45NA100x objective, and a 1.5x tube multiplier for total 150x magnification. Images are approximately 2.4μm in width. Value range has been scaled to allow observation of first Airy ring (linear grayscale from, black:-0.01 to white:0.03). B) Pixels found by custom function have been coloured gray for a ROI with $r \in [0, r_\mathrm{i}]$, and $r_\mathrm{i} \approx 570\,\mathrm{nm}$, corresponding to 13.13 pixels. C) ROI with $r \in (r_\mathrm{i}, 2r_\mathrm{i}]$. D) ROI of (C) after $N\hat{\delta}_\mathrm{b}$ recursion loop. The width of each image is approximately 2.5 μm.

measurements with ROIs, it is not straight forward to obtain individual pixel data from them. Accordingly, custom ROI functions were developed to support the $N\hat{\delta}_\mathrm{b}$ recursion operation. The ROI functions are circular ROIs used to calculate the pixel positions in an ROI centered on the origin, for given inner and outer radii. Now, say we want to measure a particle with the double radius method, so we need two ROIs. The function determines the pixel locations in a ROI for arguments (inner radius, outer radius). ROI 1 would be called with arguments $(0, r_\mathrm{i})$ and ROI 2 with arguments $(r_\mathrm{i}, r_\mathrm{j})$. The coordinates for ROI 1 and ROI 2 are then output as arrays. Because the ROI is always taken at the origin, the function only needs to be run one time for a ROI of a given size. The coordinates of a particle can then simply be added to the position arrays of the ROI function, in order to make them unique. A further function performs this particle location addition, and then tells ImageJ to measure the intensity of the pixel values at each of the coordinates. A new array is created, for each of the two ROI, containing the intensity values of the pixels for a given particle. The mean and standard deviation can then be easily calculated. Since, individual pixel locations are tied directly to intensity values via array indexing, the $N\hat{\delta}_\mathrm{b}$ recursion method is made possible. In the latest release of ES, these ROI functions supersede those of ImageJ, for measurement of particle and background data. Not only do they allow for the pixel identification necessary in the $N\hat{\delta}_\mathrm{b}$ loop, but they allow for direct measurement of the mean intensity

in the outer region. Thus, the local background no longer needs to be calculated. Furthermore, the author has noted that ImageJ ROIs can be off-center, when the radius is an even number of pixels. The custom ROI functions ensure that ROIs are always centered regardless of odd or even radius. On top of this the functions produce measurement areas, which when scaled to physical units, match very closely the expected area for a radius, r_i, assuming πr_i^2. The ImageJ ROIs produce areas which can be off the expected value by a few percent. The author does not know the method by which ImageJ determines pixels to be inside or outside of an ROI. However, in the custom functions, ROIs are constructed as follows. A pixel at position $[x, y]$, with $x, y \in \mathbb{Z}$, sits a distance $r = \sqrt{x^2 + y^2}$ from the origin, $[0,0]$. For a given inner radius, r_i, and outer radius, r_j, the pixel is considered to be a constituent of the ROI, if $r \in (r_\mathrm{i}, r_\mathrm{j}]$, or in the special case where $r_\mathrm{i} = 0$, if $r \in [r_\mathrm{i}, r_\mathrm{j}]$. Radii should never be rounded by the user prior to entry into the plugin. An example of ROIs that might be used for the double radius method can be seen in Fig. 4.6 B and C. Note in Fig. 4.6 C that the outer region overlaps some nearby particles. The $N\hat{\delta}_\mathrm{b}$ recursion loop is used to remove these overlapping pixels, and the effect can be seen in Fig. 4.6 D.

4.2.4.11 Further features and outputs

The ES provides a set of further options and fucntionality. For instance, polarisation-dependent extinction data can be easily correlated, and printed to ImageJ's results table. They can subsequently be saved as .xls files and opened in Excel, Origin, etc. IML functions can also fit the data with custom equations. Plotting can be performed directly with IML. Many of the plots in ES are custom built, however. Histograms directly from ImageJ cannot display more than one set of data, and are not very aesthetic. Thus, new histogram plotting has been written, but within the construct of the plotting functions of IML, i.e. the histogram max, min, bin, and count values are calculated by ES, and subsequently, drawn onto a plot via IML's functions. If the experiment was performed with a colour camera, plots are colour-coded accordingly. The plots are saved as PNG files.

ES outputs the following contents for a standard experiment using unpolarised excitation:

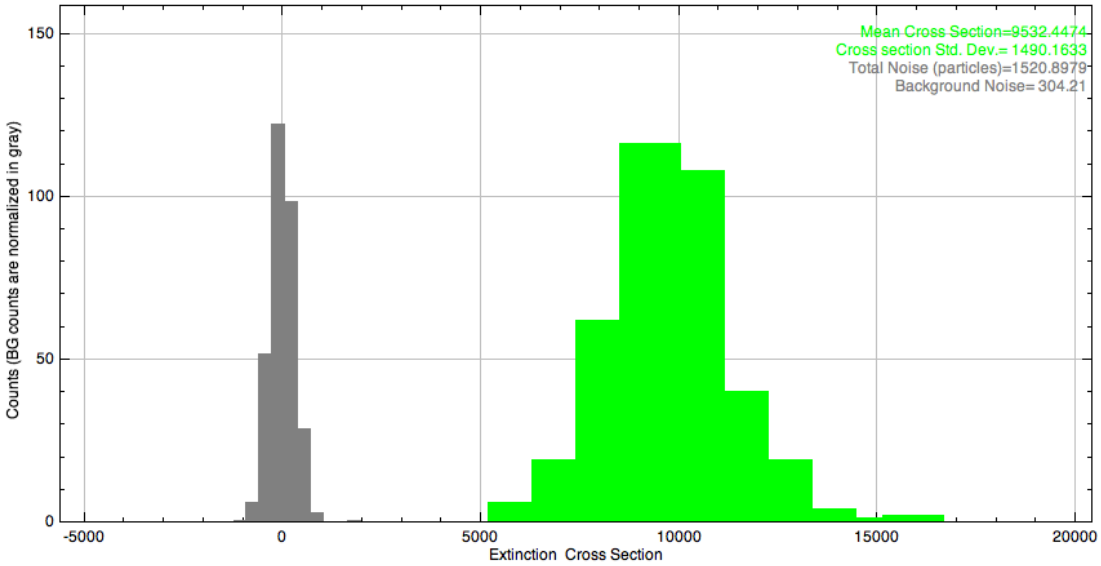

Fig. 4.7: A plot output of ES, representing the distributions of σ_{ext} for 60 nm AuNPs (green) and of background datapoints (gray), for the green channel extinction image. In the plot, the "Mean Cross Section" is $\bar{\sigma}_{\text{ext}}$, "Cross section Std. Dev." is $\hat{\sigma}_{\text{ext}}$, "Total Noise(particles)" is $\hat{\sigma}_{\text{total}}$, and "Background Noise" is $\hat{\sigma}_{\text{noise}}$.

1. a spreadsheet containing the x and y coordinates, extinction, and (if applicable) scattering cross-sections for every particle, in each available colour channel.

2. a similar spreadsheet for background data.

3. the extinction image, in which every particle accepted for measurement is marked with a number corresponding to its index on the spreadsheet.

4. a plot displaying the distributions of both background and particle data for each available colour channel. An example of a histogram, is shown in Fig. 4.7.

For a typical polarisation-resolved experiment, the ES creates the standard outputs, for every polarizer angle. The ES then correlates all the extinction and scattering (if present) data across all of the polarisation steps. It outputs a spreadsheet with:

1. extinction and scattering cross-sections as a function of polariser angle, in each available colour channel, along with the fitted parameters σ_0, α, and θ_0, determined with Eq. 4.2.5.

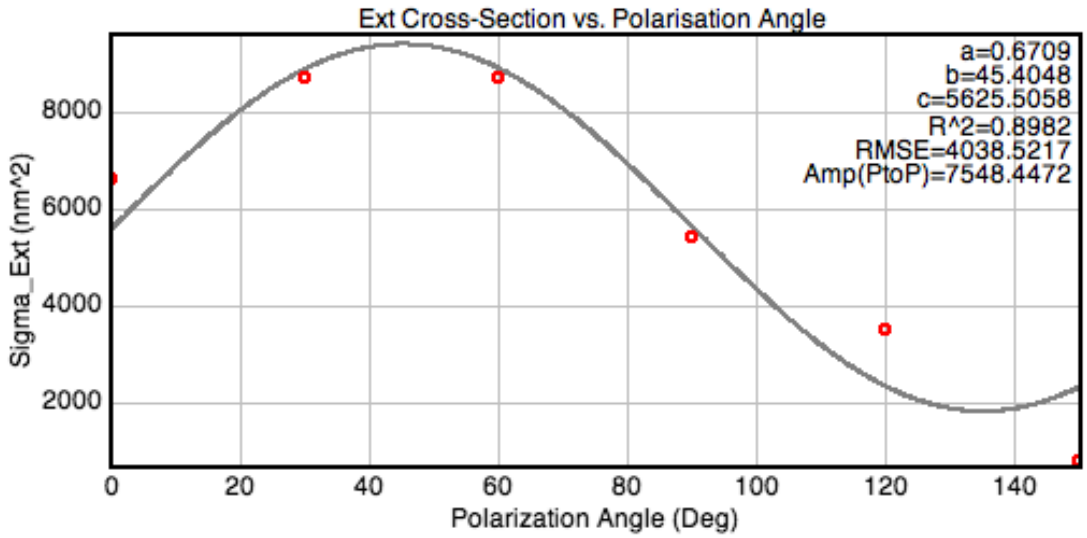

Fig. 4.8: A plot from the ES showing the dependence of σ_{ext} on polariser angle in the red channel. Red datapoints are experimental values taken every 30°, from 0° to 150°. The solid line is the fit of Eq. 4.2.5, using parameters shown in the plot. α, θ_0, and the σ_0 are given by a, b, and c, respectively.

2. Every particle has its measured cross-sections plotted as a function of polarisation angle.

3. The polarisation data is also fitted a number of times using simulated noise as described in Sec. 4.2.1, spreadsheets are provided giving the fit parameters for each simulated fit, as well as the resulting mean and standard deviation for every particle.

4. Histograms of the simulated fit parameters for every particle are provided.

5. The histogram of all simulations for fit parameters for all particles is provided, i.e. the histogram of histograms for each fit parameter.

These data are given for extinction and scattering, if darkfield images were taken. An example of the dependence σ_{ext} on polariser angle can be seen in Fig. 4.8, for a strongly anisotropic particle.

4.2.4.12 Planned extensions

The Extinction Suite has proved very useful in the analysis of large amounts of data. To further enhance the efficiency and functionality, the following extensions are planned:

1. N-channel capability, allowing for more flexible selection of the number of spectral ranges in an experiment.

2. The code in some places could be improved to increase efficiency and readiness for future expansions.

3. A possible way forward is to convert the code to Python, which can be natively implemented in ImageJ, and offers better support for customisation and higher level mathematics.

4.3 Gold

Gold is a commonly used, and extensively studied material, in a wide range of optical, chemical, and biological research, both in the form of NPs, or as extended structures[5,6,86,86,87]. Amongst metals it is the most chemically inert, making it particularly attractive for application in biological settings, as other metallic compounds can have toxic effects on cells. As such, it is a widely studied metallic NP material, and AuNPs are well suited to test the effectiveness of the wide-field technique.

4.3.1 Unpolarised extinction and scattering

AuNPs have a LSPR resulting in a peak of the cross-sections, around 550 nm for $n = 1.5$ environment in the electrostatic approximation, as discussed in Sec. 1.1.3. For particles larger than 50 nm, propagation effects become important, leading to a shift of the peak to the red, reaching 575 nm for 80 nm diameter particles. The measured σ_{ext} is shown in Fig. 4.9 for AuNPs as function of diameter. To select these particles from debris, we accordingly set the colour filtering in the analysis program. For example, 30 nm and 40 nm AuNPs have a LSPR around 550 nm, meaning we can set the requirement that the measured cross section be largest in the G channel. However, for particles larger

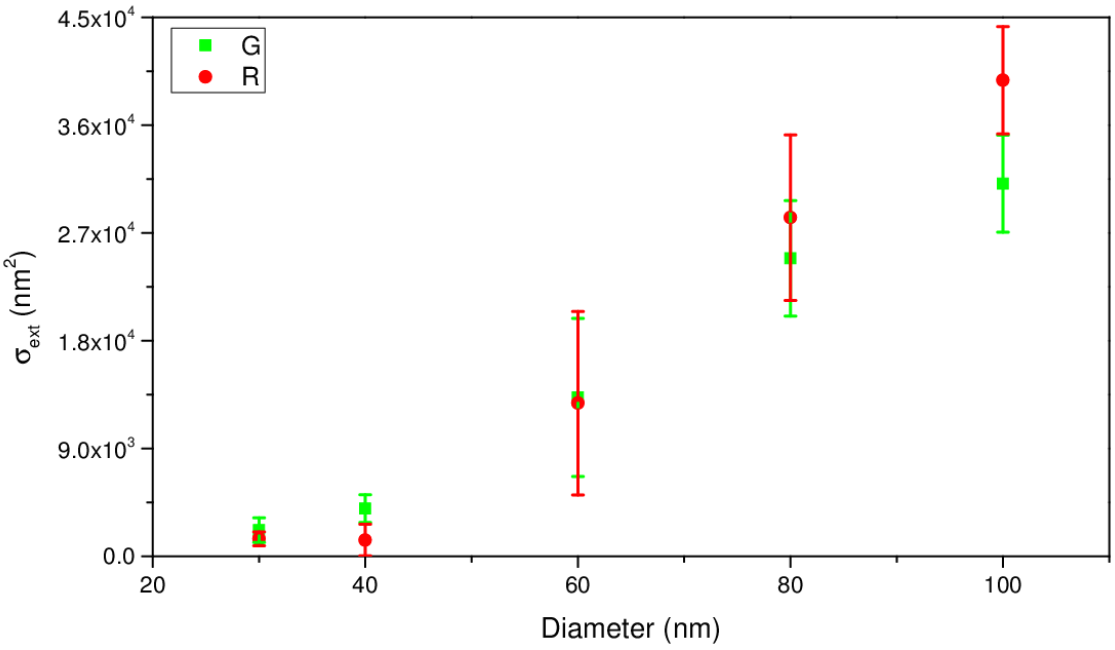

Fig. 4.9: Extinction cross-section, σ_{ext}, in the G and R channels as a function of nominal particle diameter for gold particles. The data shown are $\bar{\sigma}_{\text{ext}}$ with error bars given by $\hat{\sigma}_{\text{ext}}$, for each channel and each nominal diameter.

than 50 nm, the LSPR is sufficiently red-shifted, such that the measured cross section may be largest in either the R *or* G channels. Hence, for 60 nm and 80 nm NPs, we accept the data of particles whose σ_{ext} is largest in either channel. For 100 nm particles, we require that the cross-section be largest in the R channel.

In Fig. 4.10, we present the σ_{sca} and corrected σ_{abs} data of the colour channel of largest $\bar{\sigma}_{\text{ext}}$. However, problematically, because we now accept the data of particles whose cross-section could be largest in either of two channels, we also artificially increase the standard deviation of whichever channel is presented, i.e. G for 60 nm NPs and R for 80 nm NPs. Note the comparatively wide distributions of σ_{ext} for 60 nm and 80 nm nominal diameter samples in Fig. 4.9. This highlights a disadvantage of this technique, as currently implemented, namely coarse spectral resolution. We could improve upon this by using the sCMOS camera with a larger number of colour filters, each having a narrower bandwidth (seen in Fig. 4.5 for 10 nm particles), or implementing a Fourier transform spectroscopy.

Fig. 4.10 provides a direct comparison of the measured and theoretical σ_{sca} and σ_{abs} to

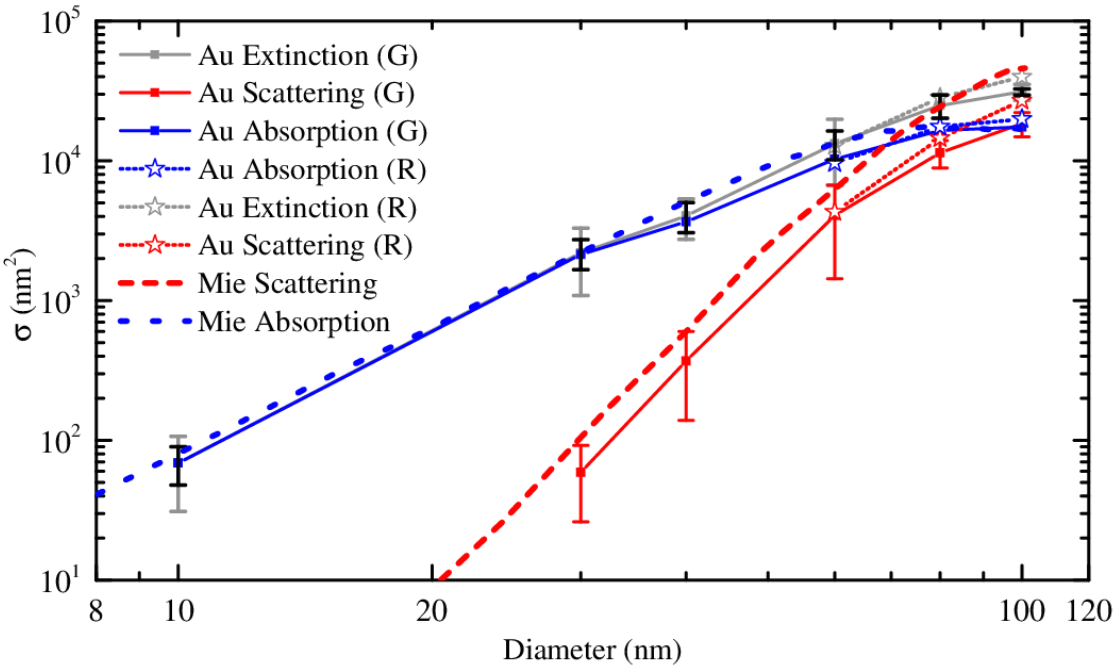

Fig. 4.10: Extinction, scattering and absorption cross section measured in the G channel on a series of nominally spherical AuNPs with nominal diameter from 10 nm to 100 nm (solid squares). For 60 nm, 80 nm and 100 nm diameter the values measured in the R channel are also given (empty stars). The thick blue dashed (red dotted) line is the calculated absorption (scattering) cross section from Mie theory at the LSPR. Symbols (connected by thin lines as guide to the eye) give the experimental cross-sections as average over > 50 individually measured NPs in the wide-field image, and bars give the standard deviation due to NP size/shape/environment distribution. Black bars are calculated from the manufacturer specified size distributions (see text). Note that 10 nm AuNPs have a σ_{sca} below the measurements noise.

Mie and Rayleigh theory taken from Ref. 32. Measured values of σ_{sca} were obtained using η from Sec. 4.4. Theoretical data is given at the resonance wavelength of each size, *not* fixed at one wavelength. For AuNPs larger than 50 nm, both the G and R channel data are presented. Note, that the R channel measurements clearly dominate scattering for particle diameters larger than 60 nm, and only dominate absorption above 80 nm. This is due to the interband absorption in gold increasing the absorption towards lower wavelengths, discussed in Sec. 1.1.2, 1.1.3. We find agreement with theory within error. We note the measured scattering is systematically lower than theory, showing an increasing deviation above 60 nm. We have to consider that, while the the-

ory values are the peak values across the spectral range, the measured quantities are spectral averages over the wide ranges, namely 80 nm, 100 nm, and 90 nm bandwidths for the 40D R, G, and B channels, respectively. We can approximate the effect of the averaging by evaluating

$$\int_{\lambda_1}^{\lambda_2} \frac{\sigma(\lambda)\,\mathrm{d}\lambda}{\lambda_2 - \lambda_1}, \tag{4.3.1}$$

with σ being σ_{ext}, σ_{sca}, or σ_{abs} from Eq. 1.1.19, as desired, and using data for ϵ_{r} from Ref. 35. For the 10 nm particles, the wavelength range of the Semrock green filter (530 ± 20 nm) was used in the calculation. For all others, the FWHM range of the G filter of the 40D (530 ± 50 nm) was used. The resulting spectrally averaged values of σ_{sca}=(0.11, 62, 349, 3974) nm^2, and σ_{ext}=(71, 1485, 3723, 15361) nm^2, for (10, 30, 40, and 60) nm diameter particles, respectively, are in excellent agreement with our measured values in Fig. 4.10. If we perform this same calculation for 80 nm and 100 nm particles, we obtain σ_{sca}=(22326, 85167) nm^2, and σ_{ext}=(49318, 137886) nm^2, respectively. These values are too high compared to the measured values, indicating that these particles are too large to be considered in the Rayleigh limit.

We can further consider the η factor. From our discussion of the scattered power in Sec. 4.2.2, the measured extinction is $\sigma_{\mathrm{meas}} = \sigma_{\mathrm{abs}} + (1 - \zeta_{\mathrm{col}})\sigma_{\mathrm{sca}}$. We note that an increasing discrepancy appears for particles greater than 60 nm in Fig. 4.10. This discrepancy increases as nominal particle size increases. We attribute this to the increased collection of scattered light by our objective as the particles enter the Mie regime. Since, forward scatter begins to dominate we collect an increasing portion of the total scattered light, hence ζ_{col} increases. Thus, η should also increase. Since, we held η fixed at 10 for all particle sizes, those particles (80 nm and 100 nm) which are in the Mie regime, show scattering cross-sections deviating increasingly from theory. Scattering begins to dominate later than we would expect (compare crossing point of thin dotted blue and red lines, to crossing point of thick dotted blue and red lines) as a combination of the systematic offset and the increased offset at larger sizes. Nonetheless, this suggests that, *within the dipole limit*, we have a calibrated value which can be used for any nominally spherical particle type. We need only to correct the systematic offset, perhaps by using filters with narrower ranges.

The gray error bars in Fig. 4.10 represent $\hat{\sigma}_{\mathrm{ext}}$, which can be attributed to a size dis-

tribution of the AuNPs as follows. The scaling of $\sigma_{\text{ext}} \propto D^{\gamma}$ for spherical particles of diameter D is known from Mie theory [88]. Qualitatively, in the dipole approximation, $\gamma \approx 3$ for small particles where the extinction is dominated by absorption and increases towards $\gamma = 6$ for larger particles where the extinction is dominated by scattering. But, if we consider Fig. 1.5, then the scattering is never dominant in a regime where $\gamma = 6$, and indeed the effects of retardation are clear as the particles grow larger than $\sim$ 80nm. The slope of the absorption diminishes to ~ 0, shortly followed by the scattering. To deduce γ quantitatively, the absorption and scattering curves in Fig. 1.5 were digitized, and summed to find the Mie extinction versus diameter, at resonance wavelength. The derivative of the curve in log-log scale was taken to deduce γ for any size. We found $\gamma \approx 3$ for 40 nm diameter NPs and $\gamma \approx 0.65$ for 100 nm diameter NPs. This scaling allows us to estimate the relative standard deviation of the diameter $\delta D/D = \hat{\sigma}_{\text{ext}}/(\bar{\sigma}_{\text{ext}}\gamma)$. The manufacturer specifies $\delta D/D < 0.08$ for 40 nm and 100 nm particles determined by electron microscopy. Measurements of σ_{ext} for 40 nm AuNPs in the G channel, give $\bar{\sigma}_{\text{ext}} = 4040\,\text{nm}^2$ and $\hat{\sigma}_{\text{ext}} = 1303\,\text{nm}^2$, resulting in $\delta D/D = 0.106$ with $\gamma = 3$. While measurements on 100 nm AuNPs in the R channel yield $\bar{\sigma}_{\text{ext}} = 39755\,\text{nm}^2$ and $\hat{\sigma}_{\text{ext}} = 4474\,\text{nm}^2$, resulting in $\delta D/D = 0.172$ with $\gamma = 0.65$. These values are consistent with literature [26,28,32,75] for spherical 100 nm AuNPs, but do not meet the manufacturers size specifications. Thus $\hat{\sigma}_{\text{ext}}$ is on the upper limit of what would be expected from the size distribution of spherical particles in a constant dielectric environment. It has been shown in the literature that additional factors influencing $\hat{\sigma}_{\text{ext}}$ might be the NP imperfect sphericity [45], as well as fluctuations in the local dielectric environment and the electron-surface scattering damping parameter [75].

4.3.2 Polarisation-resolved extinction

Furthermore, we measured the dependence of σ_{ext} on the linear polarization angle θ of the excitation and analyse the data as described in Sec. 4.2.1. The resulting $\sigma_{\text{ext}}(\theta)$ is shown in Fig. 4.11(top and middle right) for θ between 0° to 180° in steps of 10° for two selected AuNPs in the red channel. AuNP1 has a fitted $\alpha = 0.07$, and its distribution, given the experimental noise, is shown, having a mean value $\bar{\alpha} = 0.15$ and a standard deviation $\hat{\alpha} = 0.08$. AuNP2 instead is significantly non-spherical with a fitted $\alpha = 0.75$

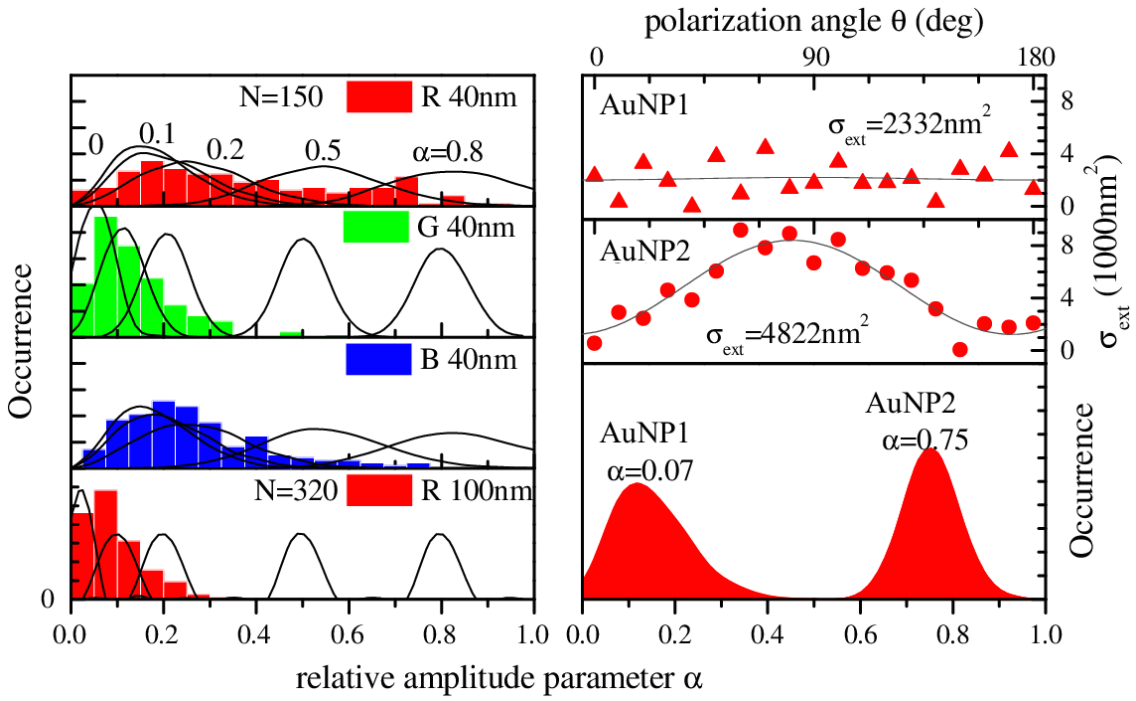

Fig. 4.11: Left Column: Distributions of the relative amplitude α, for 150 AuNPs of 40 nm diameter in the R, G, and B colour channel, and 320 AuNPs of 100 nm diameter in the R channel. The distributions due to $\hat{\sigma}_{\text{noise}}$ for AuNPs of $\alpha = 0, 0.1, 0.2, 0.5, 0.8$ are given as black lines using $\bar{\sigma}_{\text{ext}}$ as given in Fig. 4.2. Right Column: $\sigma_{\text{ext}}(\theta)$ in the R channel with fits for two 40 nm AuNPs, and distribution of the deduced amplitude parameter α by the measurement noise $\hat{\sigma}_{\text{noise}}$.

and a distribution with $\bar{\alpha} = 0.75$ well above $\hat{\alpha} = 0.06$. The red channel is used here as it is most sensitive to LSPR shifts due to asphericity. The distribution of α over the NP ensemble is shown in Fig. 4.11 (left) for 40 nm and 100 nm AuNPs for different colour channels. For comparison, the simulated distribution of α for AuNPs having $\sigma_{\text{ext}}(\theta)$ given by the fit function are shown for $\alpha = 0, 0.1, 0.2, 0.5, 0.8$ in Fig. 4.11 as black lines using $\sigma_0 = \bar{\sigma}_{\text{ext}}$ of the colour channel. The comparison shows that the polarization dependence can identify non-spherical AuNPs through the distinct values of α. To further infer the NP geometrical aspect ratio from these data a comparison with theory is needed which we reported in Ref. 82.

4.3.3 Nanostars

A sample of gold nanostars was also measured. Gold nanostars are a new product under development at BBI. The aim of the project is to extend the LSPR wavelength to the near infrared. In turn, this would extend the wavelength range of BBI's lateral flow colourimetric assays for in-vitro diagnostics. The sample consisted of 30 nm nominal core diameter nanostars, whose tip-to-tip nominal diameter was 70 nm. UV-Vis-IR spectroscopy data was provided, which allows a rough comparison. This can be seen in Fig. 4.12 along with the σ_{ext} data. We find very large σ_{ext} distributions for gold nanostars. The gold nanostars are a complex shape, as can be seen in Fig. 4.13, with sharp tips giving rise to red-shifted LSPRs. Furthermore, the particles can differ, via a set of parameters, such as core size, point-to-point size, and the number of points per star.

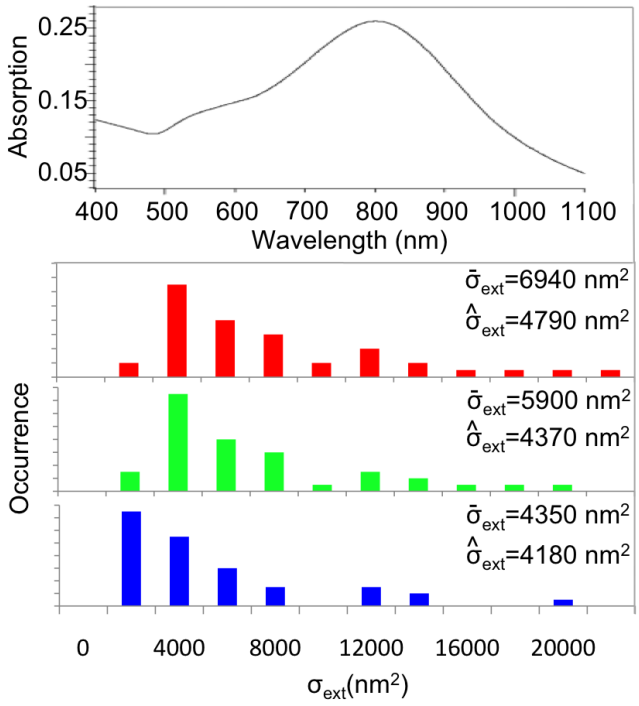

Fig. 4.12: Upper: UV-Vis-IR spectral absorbance data of Au nanostars, courtesy of Jemma Theobald with BBI Solutions. Lower: Distributions of σ_{ext} in the red, green, and blue channels for gold nanostars of 30 nm nominal core diameter, and 70 nm nominal point-to-point diameter.

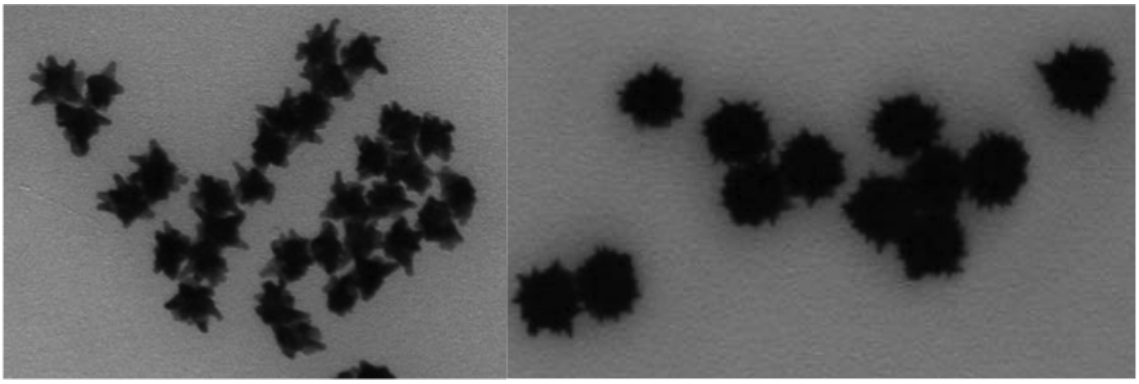

Fig. 4.13: Top left: TEM image of 37.3 nm core diameter nano stars. Top right: 133.7nm core diameter nanostars.

4.3.4 40 nm AuNP dimers

A dimer sample was investigated, containing SiO_2-coated AuNPs, nominally of shell thickness 6 nm and 40 nm core diameter, bound covalently to bare AuNPs, also of 40 nm nominal diameter. Pairs of bare-bare NPs are also present in this sample, along with unbound single particles. The development of this sample was described in Sec. 3.3.2. The silica shell, with $n \approx 1.46$, is nearly index-matched to the silicone oil, $n \approx 1.51$. Measurements were performed for darkfield and extinction, with the 40D, as the PCO was not available at the time. As discussed the fitted parameters are subject to error based upon the measurement noise. In the case of the 40D, we can achieve a lower noise limit in darkfield than we can in brightfield for "clean" samples. The measured noise, in units of cross-section, for scattering is obtained similarly to that of extinction, with random measurements of background-subtracted σ_{sca}, in image points without NPs. So, in this experiment, with an exposure time of 10 s and averaging over two frames , $\hat{\sigma}^{\text{scat}}_{\text{noise}}$ was on the order of $10\,\text{nm}^2$, $5\,\text{nm}^2$, and $5\,\text{nm}^2$ in the B, G, and R colour channels, respectively, slightly depending on the polariser angle. The measured noise in the scattering was lower than that in the extinction, and led to decreased error in the polarization-resolved measurements, and the associated fitted parameters. Fig. 4.14 summarises the measurements on this sample of dimers. Three quantities are presented, namely the sum of σ_{ext} in the G and R channels, the cross-section colour $(\sigma_{\text{G}} - \sigma_{\text{R}})/(\sigma_{\text{G}} + \sigma_{\text{R}})$, and the asymmetry ratio, $\alpha_{\text{PR}}/\alpha_{\text{PG}}$, with the asym-

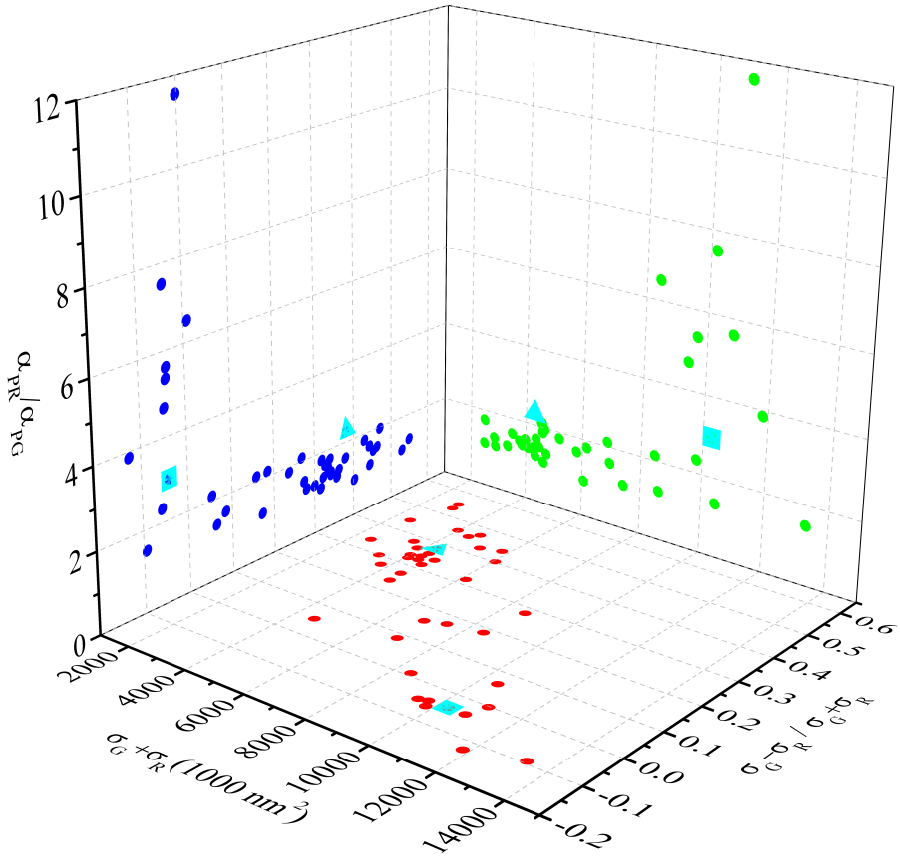

Fig. 4.14: Optical properties measured on individual NPs covalently bound onto glass, from a solution containing nominal 40 nm NPs coated with a 6 nm thick silica shell and covalently bound to bare 40 nm NPs (same as in Fig. 3.8). Measurements are shown as a trivariate distribution using the cross-section $\sigma_R + \sigma_G$, the contrast $(\sigma_G - \sigma_R)/(\sigma_G + \sigma_R)$, and the asymmetry parameter ratio α_{PR}/α_{PG} (see text). Black symbols indicate the two particles shown in Fig. 4.20.

metry parameters α_R, and α_G, given by α in the fit of Eq. 4.2.5, to the measurements in the R and G channels. This choice is motivated as follows: (1) the sum cross-section is approximately proportional to the number of 40 nm AuNPs are contained in the analysed particle, (2) the cross-section colour is indicative of the LSPR wavelength, with single spherical particles having $\sigma_G > \sigma_R$, and dimers having $\sigma_R > \sigma_G$, and (3) the ratio asymmetry parameter is used to emphasize the asymmetry, where with single quasi-spherical particles $\alpha_{PR}/\alpha_{PG} \sim 1$, with single slightly elliptical particles $\alpha_{PR}/\alpha_{PG} \geq 1$, and with dimers or highly elliptical particles $\alpha_{PR}/\alpha_{PG} \gg 1$. Inspecting Fig. 4.14, the data shows that an increasing ratio asymmetry parameter corresponds to an increas-

ingly red differential cross-section, and an increasing sum cross-section. We expect that the larger the asymmetry of the particle, the further red-shifted the LSPR, as discussed in Sec. 1.1.1. Furthermore, the long axis of an elliptical particle, or of a dimer, should have a larger cross-section than that of a single quasi-spherical NP. Thus, the correlation between the variables in Fig. 4.14 indicates the suitability of the wide-field technique to distinguish single, dimer, or multimer NPs. Particle grouping is apparent with three groups represented in the sum-differential plane. The collection of points in the small sum cross-section regime are attributed to single quasi-spherical particles. The few scattered points around 8000 nm^2 are likely dimers with a large gap size or elliptical single particles. The grouping around $10000-12000\,nm^2$ is attributed to dimers of small gap, or trimers. Two datapoints, one representing a single NP (triangle), and one representing what we expect is a dimer (square), shown in Fig. 4.14, were measured with the extinction spectroscopy technique (seen in Fig. 4.20). Their spectra correspond to that of a single NP, and a dimer, which we modeled[82] using COMSOL Multiphysics. The modeling was consistent with the experiment for a heterodimer of 5.5 nm gap, consisting of two single NPs of 32 nm diameter, and 33 nm diameter. Assuming a single NP with $\sigma_{ext} \approx 4000\,nm^2$, we would anticipate an uncoupled dimer would have $\sigma_{ext} \approx 8000\,nm^2$. This dimer exhibits $\sigma_{ext} \approx 11000\,nm^2$ suggesting a strongly coupled dimer, i.e. small gap size. This way of visualising the sample data makes it possible to identify NPs as singles, dimers, or multimers. TEM or SEM can confirm the exact interparticle distances, particle shapes, and morphologies, but these techniques are more complex and do not directly measure the plasmonic properties.

4.4 Nanodiamond

A brief aside will be made at this point to discuss nanodiamonds (ND), because they were an important part of the optimizations of the wide-field technique. One use for these ND measurements was in the correlation of CARS, electron microscopy, quantitative DIC, and extinction cross sections for proof of principle of unlabeled CARS bioimaging of single NDs. This is summarized in a paper we published in 2014[17]. NDs also offered an interesting opportunity to determine η without size-scaling of the ex-

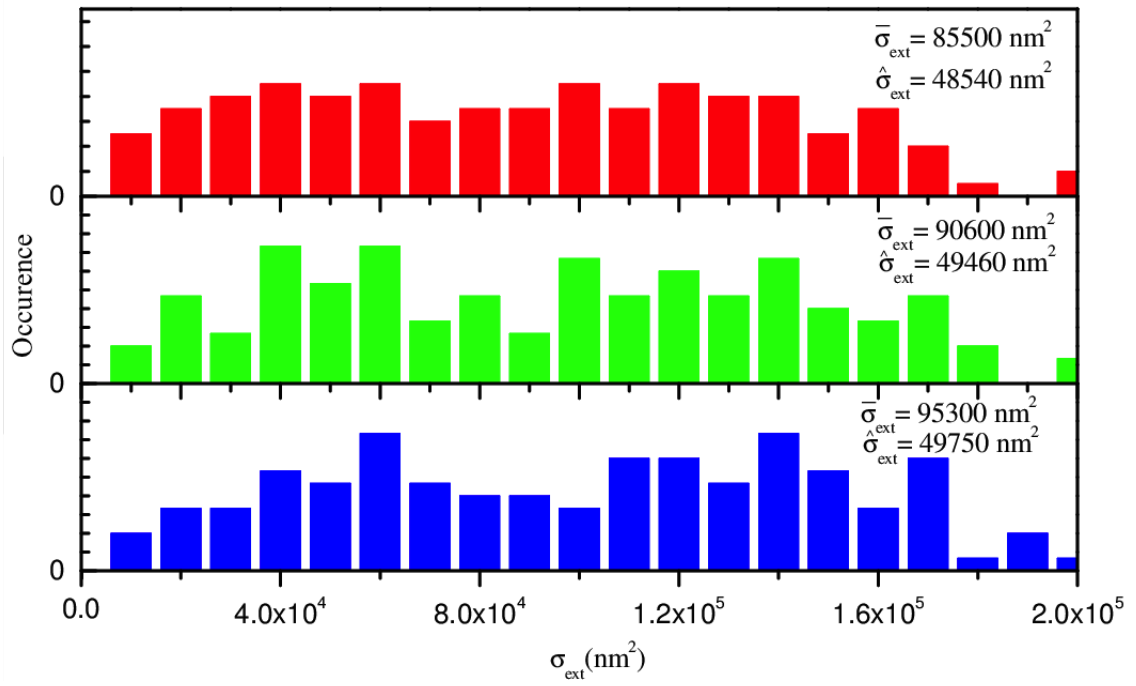

Fig. 4.15: Distributions of σ_{ext} in the red, green, and blue channels for NDs whose upper size limit is nominally 250nm diameter.

tinction cross-section based on a particular material. NDs are scattering-only particles, thus, $\sigma_{\text{ext}} = \sigma_{\text{sca}}$. Hence Eq. 4.2.4 becomes

$$\sigma_{\text{ext}} = \eta \int_{A_i} \frac{I_{\text{df}}}{I_0} \text{dA}. \tag{4.4.1}$$

So, η can be found if we measure the extinction and scattering on NDs. This is directly written into ES, and is calculated if requested. We find $\eta \sim 10$ with about 10% error. This is consistent with our modeling of the collected scattering fraction using darkfield condenser ranges, discussed in Sec. 4.2.2. The method of η determination described previously, and relating to Fig. 4.3, requires measurements for more than one nominal particle size in order to fit a simplified model (resembling theory). Both η and σ_c are then fitted parameters, each with a certain error, however they are only applicable to the material in question, due to specific plasmonic properties. Hence, the ND method is preferred as it should be an absolute calibration of the condenser ranges in bright and darkfield. Broad σ_{ext} distributions are observed for NDs seen in Fig. 4.15. The data is consistent with our knowledge of the samples. The NDs are produced by explosion of grown crystals, providing a wide distribution of physical sizes who are only nom-

inally upper-limited to 250 nm. A noteworthy complication of measuring a material like diamond is that it has no plasmon resonance, like we would see with the metallic NPs. Based on the LSPR wavelength, and in turn the colour of the scattered light, metallic NPs allow us to place quite specific restrictions on the particles whose data we collect. Since, NDs do not afford us this opportunity, we also collect data from debris. Even after cleaning, debris can find a way onto the glass at later stages of the binding experiments. Hence, the distributions in this case may be affected by material other than desired. Indeed, the accuracy of the η factor, via ND measurement is potentially affected by particles which are not ND, but cannot be excluded based upon colour or intensity. We could investigate this by calculation of η from measurements of scattering and extinction on several samples, prepared in the usual way, but with no added NPs, i.e. find η for debris. The measurable ND particles are generally considerably larger than 100 nm diameter, and thus already present a problem, since they are not within the dipole regime. Additionally, the particles, observed under scanning electron microscopy, are not close to spherical, increasing the deviation from dipolar scattering for a spherical particle. In the future, we hope to measure NDs of diameter smaller than 100nm, or other more spherical non-absorbing particles, like barium-titanate. This should help improve the accuracy of the η factor.

4.5 Silver

Silver NPs in the Rayleigh regime have LSPRs in the deep blue around 400 nm. However, for larger particles, like those measured here, in a surrounding medium of refractive index, $n_m = 1.51$, the resonance is shifted[89] to about 430 nm, within the detectable range of the 40D. Silver is a relevant material, because of its LSPR in the visible range, and because of the increased strength of its plasmic response compared to, e.g., gold (see discussion in Sec. 1.1.2). We have measured AgNPs of different nominal diameters, using the wide-field technique to determine σ_{ext}, σ_{sca}, and σ_{abs}. The results are presented in Fig. 4.16, we show the dependence of σ_{ext}, σ_{sca}, and σ_{abs}, on nominal diameter. The values are smaller than literature values[90] at the LSPR peak. We would expect that for a given diameter, silver would present larger cross sections

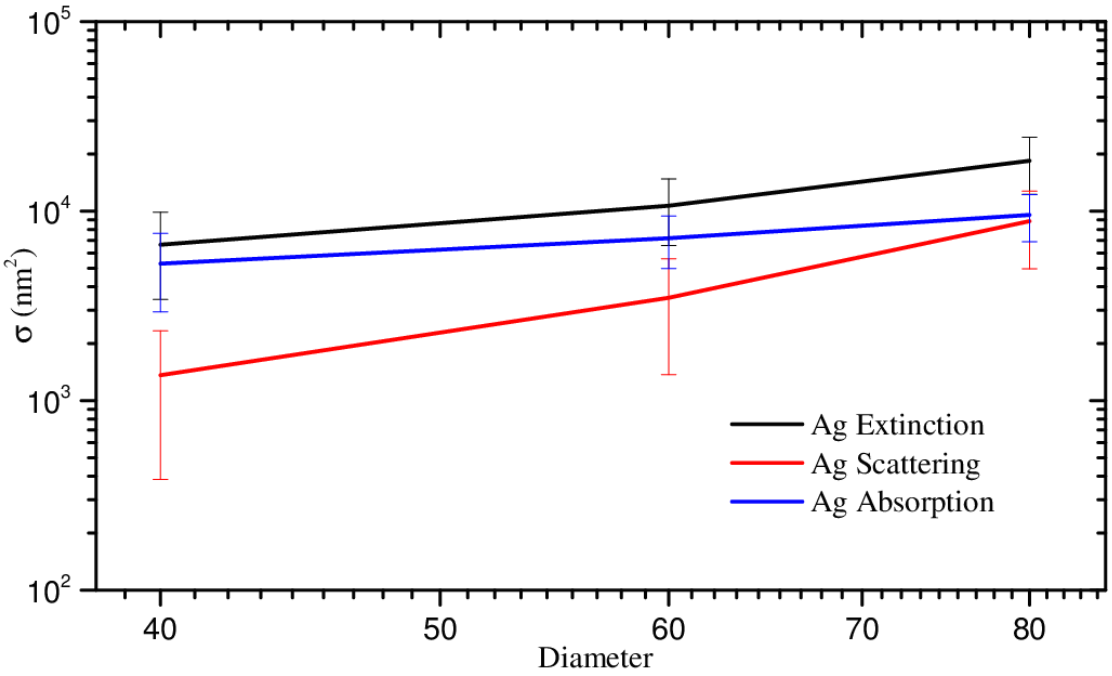

Fig. 4.16: Dependence of silver nanoparticle σ_{ext} on nominal particle diameter. $\bar{\sigma}_{\text{ext}}$ and $\hat{\sigma}_{\text{ext}}$ are provided for particle distributions of nominal diameter 40 nm, 60 nm, and 80 nm. The 40D B channel was used for all measurements shown.

than gold. Comparison of Fig. 4.10 and Fig. 4.16 shows that the silver has systematically smaller values. If we calculate the spectrally averaged cross-sections, as in Sec. 4.3, we find that $\sigma_{\text{sca}} = (1661, 18915, 106277)\,\text{nm}^2$, and $\sigma_{\text{ext}} = (2261, 20941, 111080)\,\text{nm}^2$. These values do not correspond well to the measured values in Fig. 4.16. Unfortunately, it is hard to determine the source of this error. First, our spectral averaging is an approximation, which assumes that the spectral intensity is constant over the averaged range. We could improve this by taking the filter curves and lamp spectral intensities into account. We can also assess the individual cases. The 80 nm particle is beyond the Rayleigh regime, and can be discounted. The calculated σ_{ext} for a 40 nm diameter is nearly 4 times smaller than measured values, and that for a 60 nm particle is nearly twice as large as measured. Generally, the large cross-sections expected from the dipole approximations for silver, are not realised practically, due to oxidation of AgNPs. However, we have seen that silver samples can differ in suspension, with some losing their plasmonic properties after a certain shelf life. The relative age of the samples affects the relative level of surface oxidation, and thus the decrease of plasmonic

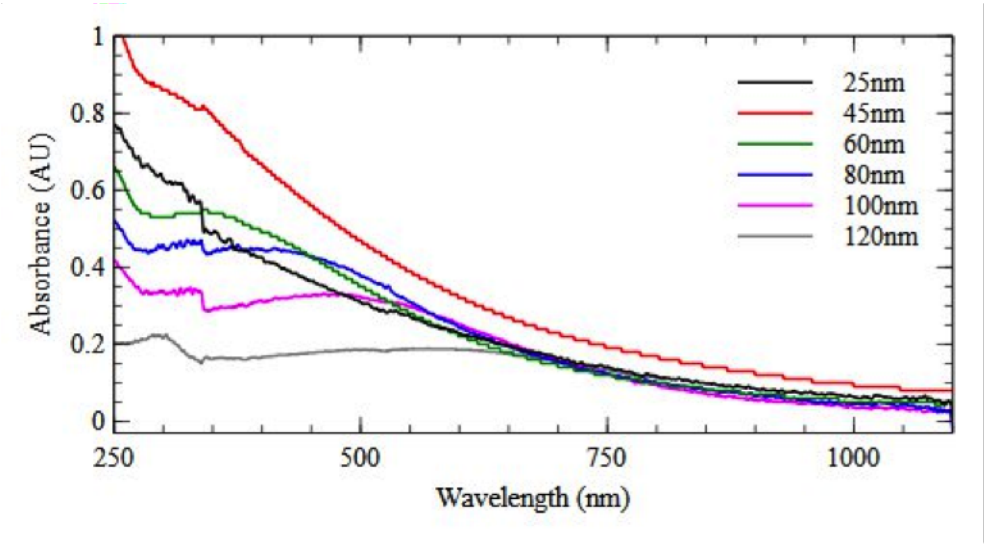

Fig. 4.17: UV/Vis absorbance data of Pt nanosphere ensembles. Figure and caption reproduced from Master's thesis by Jemma Theobald.

properties of the NPs. Hence, the results may be due to a mix of quality or age amongst the samples of different sizes.

4.6 Platinum

Platinum nanoparticles were obtained from BBI Solutions, in connection with the Master's project of Jemma Theobald. Quantitative measurements on platinum are sparse in literature[91,92]. Pt is of general interest, because it is a noble metal and the LSPR is widely tunable, using different shapes and sizes[46], as can be seen in Fig. 4.17. We note in Fig. 4.17 that the LSPR is not well defined, compared to the LSPR for gold and silver NPs, in agreement with the discussion of the dielectric function in Sec. 1.1.2 and the calculated cross-section in Fig. 1.3. The imaginary part of epsilon, which can be seen in Fig. 1.2, is larger than the real part, where $\epsilon_1 = -2\epsilon_m$, so that the LSPR is not realised in the visible wavelengths. This also explains why we never see scattering dominate absorption, within our measured size range of PtNPs. In Fig. 4.18 we present our measured σ_{ext}, σ_{sca}, and σ_{abs}, as a function of nominal particle diameter. We note that $\bar{\sigma}_{ext}$ was largest in the B channel for particles of diameter up to, and including, 80 nm. Above 80 nm $\bar{\sigma}_{ext}$ was largest in the R channel. This is in agreement with Fig. 4.17.

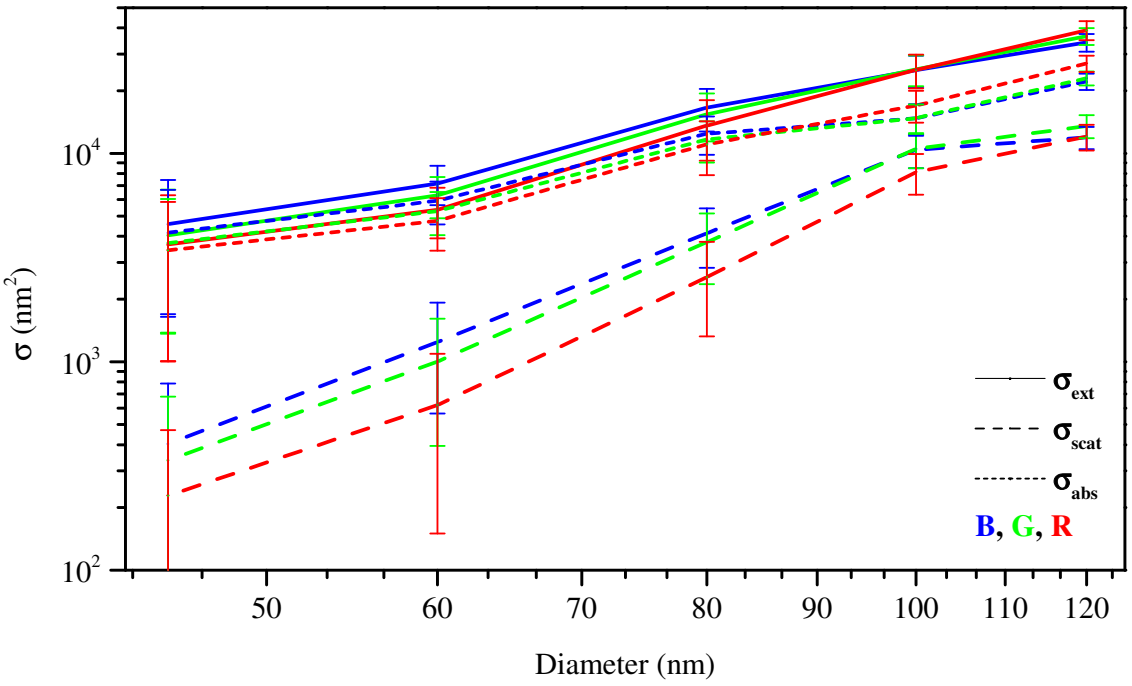

Fig. 4.18: Dependence of platinum nanoparticle σ_{ext}, σ_{sca}, and σ_{abs} on nominal particle diameter. $\bar{\sigma}$ and $\hat{\sigma}$ are provided for particle distributions of nominal diameter 45 nm, 60 nm, 80 nm, 100 nm, and 120 nm. Cross sections are shown in each of the B,G, and R channels of the 40D.

4.7 Material comparisons

In this section we compare data from the Au, Ag and Pt nanoparticles. We first reconsider Fig. 4.10, Fig. 4.16, and Fig. 4.18. The most obvious feature is the size above which scattering begins to dominate the extinction. Recall from Sec. 4.3, that scattering values are systematically too low (likely due to an underestimate of eta). This means, generally, that scattering should dominate for all samples, earlier than it appears to in this data. However, in agreement with literature[89,90] for Ag scattering, this size is smallest, around 52 nm. This is a consequence of the small ϵ_2, close to zero in the region where $\epsilon_1 = -2\epsilon_{\text{med}}$ for Ag. Hence, radiative decay (scattering) dominates plasmon damping in Ag at an earlier stage than in Au. For Pt in our size range, scattering never exceeds absorption. For a given nominal size, and at resonance, we would expect Au and AgNP cross sections to be larger than Pt[46]. However, we see cross-sections for various sizes of the three metals to be of comparable size. We can attribute this to the spectral averaging. Let us consider Fig. 4.19, which shows the differences in the LSPR peak position,

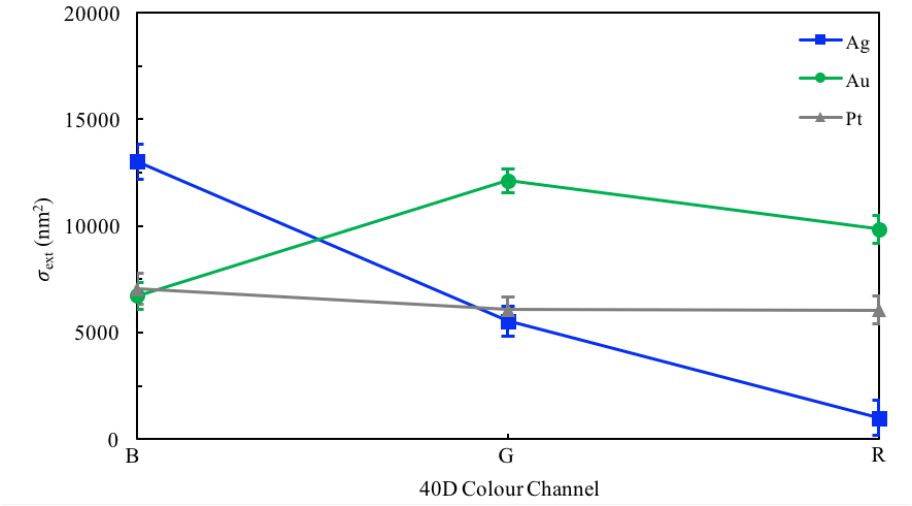

Fig. 4.19: Extinction cross-section of single Ag, Au and Pt NPs, in R,G, and B colour channels. σ_{ext} and $\hat{\sigma}_{\text{noise}}$ are provided for a single particle of nominally 60 nm diameter, whose σ_{ext} was close to $\bar{\sigma}_{\text{ext}}$ of its associated sample distribution.

between the three materials, via the dependence of σ_{ext} on the 40D colour channel. Data is shown for a single particle, of nominally 60 nm diameter, for each of the three materials. The particles were chosen to have their σ_{ext} close to $\bar{\sigma}_{\text{ext}}$ of the associated sample distributions. We can see the green peak for the gold, the blue peak for the silver, and close to wavelength independence of the platinum. This is consistent with findings by Johnson et al[93]. Since the absorption of Pt is very broad, and hence the dependence on wavelength weak, the effect of spectral averaging is mitigated, compared to that of gold and silver.

4.8 Extinction spectroscopy

Extinction Spectroscopy was developed to determine the resonance shape and peak position of the LSPR for dimers. While, the wide-field technique in its present implementation can provide spectral information, as defined by the filters used, it is of interest to be able to study individual NPs, with a high spectral resolution. In context, our correlative TEM imaging required the use of pioloform/copper grids. It was found that the TEM grids were warped to a certain extent, due to the distortion of the copper

grid. The wide-field extinction technique requires a planar distribution of the particles of interest. Samples based on pioloform, where particle z position varies considerably, within a field of view, meant that we could not obtain data on many particles simultaneously. The extinction spectroscopy provided a convenient way to measure individual particles, as well as obtain comprehensive spectral information.

The extinction spectroscopy technique is similar to the wide-field technique, in that it is a transmission measurement. Unlike the wide-field method, the transmission is imaged onto the iHR550 spectrometer, discussed in Sec. 2.2.1. The spectrometer is equipped with an imaging camera, and thus finding particles is made simple. Once, the particle is reasonably centered, in the field of view, we close the slit down to make sure the particle is within the open range. The particle position is adjusted first by eye, then is optimised in spectroscopy mode, observing the effect on the lamp spectrum. The spectrometer settings are controlled by Horiba Jobin-Yvon, proprietary software, USBSpectrometer V3. Relevant settings are wavelength position, grating selection, and slit-width. In this work, we always use the 100 lines /mm grating. Since, the slit has 1:1 magnification with the intermediate image plane, we find that the magnification of the slit at the sample is simply the width divided by the magnification, i.e. for 100x objective, 60 μm slit gives 600 nm width at the sample. This was sufficient to remove excess background from the spectroscopy, and allow enough light to the spectrometer for measurement.

The Andor Solis software was used to analyse the data. Spectra were averaged over 200 takes, with exposure time 0.1s, obtaining intensity counts around 4×10^4 of each take. Background spectra were taken for blocked illumination at the same settings. Referencing is similar to that of the wide-field method. We shift to an area nearby, without any NPs, and capture spectra with the same settings. Local background subtraction was performed by using vertical bins. Typically 7 bins were used, with the particle centered in the middle bin. The three bins, above and below the particle, were then able used to as Δ_b. However, generally each bin was tested as Δ_b, and only the one recovering the best spectral lineshape and zero-extinction tails, was chosen. Vertical pixels and binning can be experimentally dependent, and will be discussed for each of the cases below. 800 horizontal bins were used, binning the 1600 pixel range by 2. Ab-

solute units are recovered similarly to the wide-field technique, by using scaled pixels and calculating the area over which the NP power was measured. A measurement area in the spectroscopy is 1 vertical bin $\times W_s$. The vertical binning is sample-dependent, so we have either 4, or 2, pixels in the vertical bins for the glass, or pioloform, sample respectively (discussed below). Pixel scaling was found to be ~ 149.2 nm/pixel, in the image, via movement of a fixed object a known distance in the image, using the nanostage. Two kinds of samples were investigated with this spectroscopy. One kind was 40 nm Au dimers on glass, immersed in silicon oil, as discussed in Sec. 3.3.2, 4.3.4, and the other was 40 nm Au dimers mounted on pioloform, suspended over a copper grip.

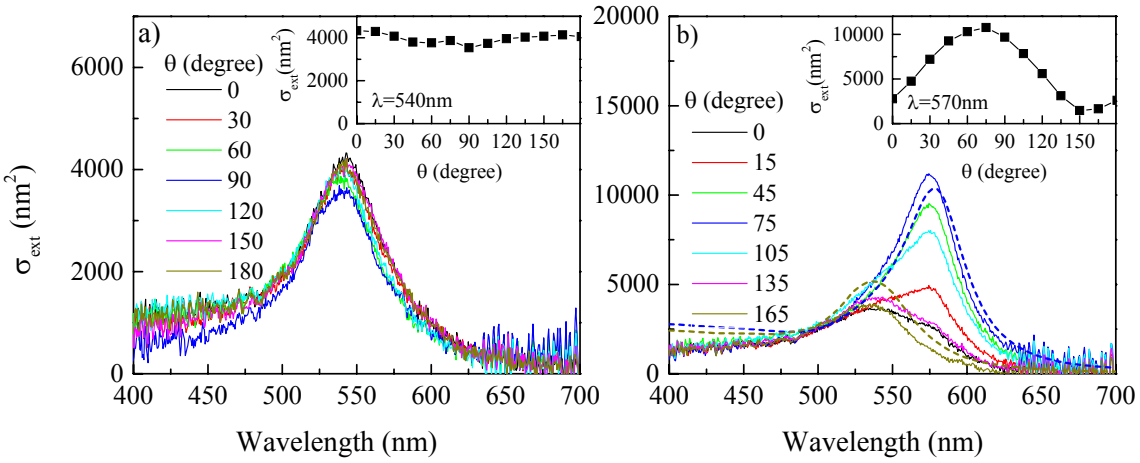

Fig. 4.20: Extinction spectra on the particles indicated as black symbols in Fig. 4.14 for various in-plane linear polarisation angles θ of the white-light illumination as indicated. The insets show the extinction versus polarizer angle at the indicated wavelength. a) Spectra on the particle indicated by the black triangle in Fig. 4.14. b) Spectra on the particle indicated by the black square in Fig. 4.14. Dotted lines are numerical simulations of the extinction spectra of a dimer consisting of a spherical NP of 32 nm diameter with a gap distance of 5.5 nm from a second particle of 33 nm diameter, calculated using COMSOL Multiphysics for the two in-plane polarisations along and perpendicular to the interparticle axis. Measured spectra were acquired using an exposure time of 0.1 s, and 200 frames average.

4.8.1 AuNP dimers on glass

For the dimers on glass vertical binning was 7 bins of 4 pixels each. Examples of a single NP, and a dimer, on the glass sample can be seen in Fig. 4.20. The single NP

exhibits a spectral shape, and peak σ_{ext}, in agreement with our wide-field results and the literature. However, since, we do not have TEM images of these particles, we do not know their morphology, or gap size. Thus, the dimer was modeled by a colleague, as discussed in Ref. 82, and seen in Fig. 4.20.

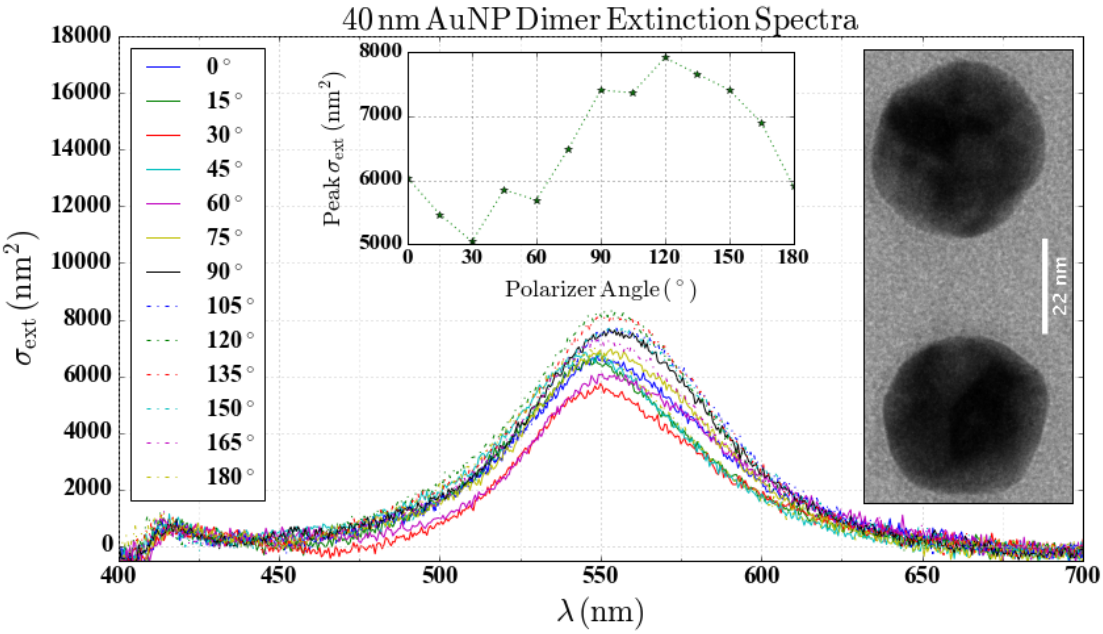

Fig. 4.21: Extinction spectra of a dimer with gap size of 22.3 nm for various in-plane linear polarisation angles, θ, of the white-light illumination as indicated. The insets show the extinction versus polarizer angle at the approximate dimer peak spectral position, and a TEM micrograph of the dimer. The orientation of the long axis of the dimer is taken from the maximum of the polarisation dependence, hence here $\theta_0 \approx 120°$

4.8.2 AuNP dimers on pioloform

Samples of AuNP dimers mounted on pioloform were prepared as follows. A small volume, e.g. $(10-20\,\mu\text{l})$ of the dimer suspension was drop cast onto pioloform-copper grids and imaged with TEM. They were then sent back to our lab in this form. Coverslips and slides were cleaned as usual. A 13 mm diameter sticky-gasket was fixed to a glass slide. A drop of silicon oil was added to the well of the gasket. The pioloform-copper grid was placed NP-side-up into the oil. In order to ensure immersion, a very small drop of oil was added to the NP-side of the grid, and then coverslip was added.

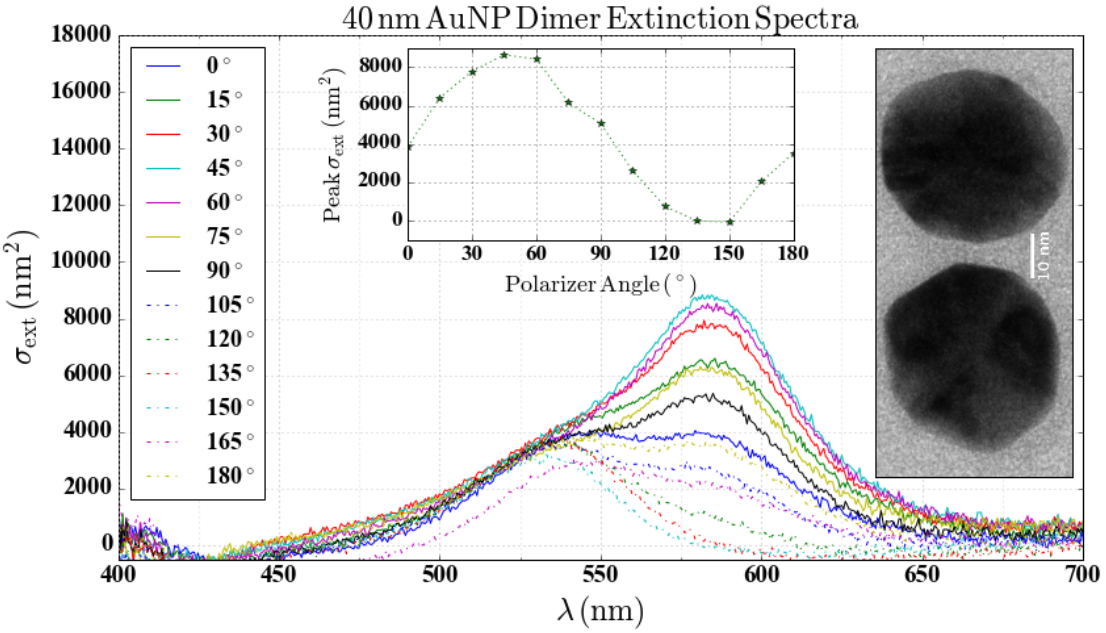

Fig. 4.22: As in Fig. 4.21 for a dimer with gap size ~ 5 nm, with $\theta_0 \approx 45°$.

The gasket sealed the sample and provided a spacer for the grid. In this format, the NPs would be closest to the coverslip and thus the objective. For the dimers mounted on pioloform, it was found that the TEM beam caused a "burn" in the imaged region. We attribute this to graphetisation of the pioloform by the beam. These regions can be smaller than the optical resolution, which means that NPs could not be measured with the widefield extinction or extinction spectroscopy. As such, special care was taken that the aperture of electron beam was at least the size of several r_i, about 3 μm diameter. In this way, the graphetisation was homogeneous over the particle position, and larger than the optical resolution. This ensured, that a local background, due to the graphetisation can be deducted from the measurements. Even with this TEM exposure, the graphetisation was inhomogeneous, and 4-pixel bins were not resulting in spectra with sufficiently low background. Vertical binning was modified to 7 bins of 2 pixels each. This meant less light was available, but that Δ_b was more local to the particle. Examples of dimers of different gap-size are shown in Fig. 4.21, 4.22, and 4.23 with gap sizes of $s \sim 22.3$ nm, $s \sim 5$ nm, and $s \sim 0.5$ nm, respectively. As expected from discussion in Sec. 1.1.3, we see a gap-size dependent red-shift in the peak for in-plane polarisation along the dimer axis. Due to time constraints, further measurements on

dimers, using the extinction spectroscopy technique were not taken. We hope to examine the remainder of the sample in the near future. As expected from the discussion in Sec. 1.1.3, there is a significant red-shift as the gap size decreases, with a peak position moving from around 555 nm in the most distant case to about 615 nm in the closest case.

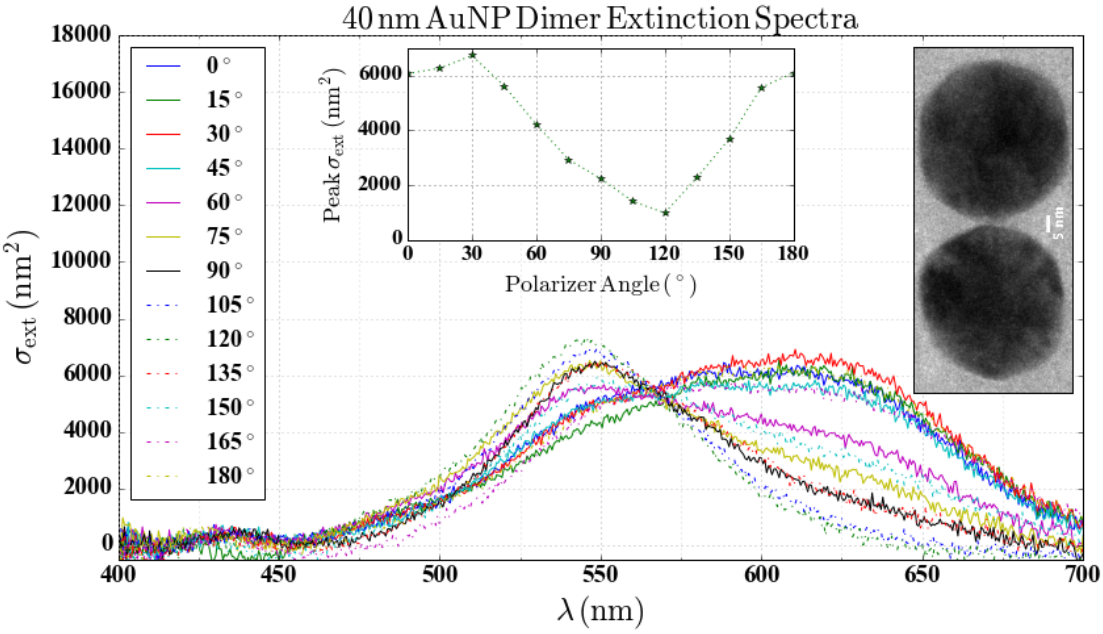

Fig. 4.23: As in Fig. 4.21 and Fig. 4.22 for a dimer with gap size ~ 0.5 nm, with $\theta_0 \approx 30°$.

4.8.3 Summary

In this section, we have presented a novel, to our knowledge, technique for the measurement of σ_{ext}, σ_{abs}, and σ_{sca} in absolute units, using a wide-field technique, and requiring only a brightfield/darkfield transmission microscope and a camera, and a computer for data analysis. With cameras and lenses of suitable specifications, we have shown that single gold nanoparticles with diameter, as small as, 5 nm can be detected. Of great advantage, is the speed with which we can measure and analyse hundreds of NPs. With a single experiment taking around 20-40 minutes (including microscope setup, camera setup, finding suitable sample regions, etc.), and analysis in less than 10 minutes, a stock sample can be effectively characterised in less than an hour. The

actual measurement time can be as low as a few minutes in total, so that with suited automation, this technique is capable of high throughput analysis. While only coarse spectral resolution is currently available for this method, we hope to improve upon the spectral aspect of the technique with the addition of Fourier transform spectroscopy. In the future, we plan to work closely with BBI Solutions, in order to study new particles of different material, shape and size. Some group members are already starting to use the technique to look at carbon nanotubes.

The extinction spectroscopy technique proved useful for the case of isolated particles of interest. With its fine spectral resolution, it allowed observation of the polarisation-dependent changes in NP dimer spectra. This study is critical to our work in FWM on dimers. We hope to expand upon, and improve, our results using this technique, with more experience, better monitoring of particle-slit alignment, and measurement of more dimerised NPs.

CHAPTER 5

Four-wave mixing measurements on AuNP monomers and dimers

5.1 Motivation

The majority of techniques available for bioimaging rely on fluorescent labels, which are used as markers for various cellular structures, and functional molecules. Within the field of fluorescence microscopy a range of techniques exist to achieve super-resolution, including, for example, far-field modalities[94] like confocal microscopy with/without stimulated emission depletion (STED)[95], photoactivated localisation microscopy (PALM)[96], stochastic optical reconstruction microscopy (STORM)[97], and ground state depletion followed by individual molecule return microscopy (GSDIM)[98], or near-field techniques like total internal reflection fluorescence microscopy (TIRF)[99], etc.[100–102]. Near-field techniques can achieve resolution on the order of 10 nm, but require that the imaging target is sufficiently close to a near field probe, such as a surface to a high index material, or field-enhancing metallic antenna, etc., restricting the usefulness of the techniques in terms of imaging within the volume of, e.g., a cell. The far-field technique, STED, is a form of confocal fluorescence microscopy, that uses two coincident laser beams to excite fluorescence in a sub-diffraction-limited spot. This is generally achieved in two phases. First the fluorophores are excited with a Gaussian (transverse mode) laser beam, tuned to the absorption wavelength of the labels. Then, a second laser, shaped to have a transverse mode with a zero-intensity

center (ring shaped), quenches the fluorophores in an outer ring. The secondary beam is red-shifted (tuned to the emission of the label) to stimulate the emission into the depletion laser photon modes, leaving only those fluorophores in the central spot excited for detection in other photon modes. These are selected typically using their spectral properties, i.e. the STED laser and the detection have no spectral overlap. The other far-field techniques mentioned are typically implemented with wide-field, rather than beam-scanning, excitation. PALM, STORM, and GSDIM all rely on stochastic excitation, imaging, and then photoswitching, of a sparse set of active fluorophores, spaced farther apart than one diffraction-limited resolution. The point spread functions of the individual fluorescing molecules can be fitted, e.g. with a gaussian function, to determine the center position with an accuracy better than the size of the PSF itself. This process of activation, imaging, location determination, and then quenching, can be repeated many times to obtain the location information for many different random subsets of fluorophores. The locations of the fluorophores, collected over all of the cycles, are plotted to produce an image, whose resolution is now given by the accuracy of the position determination, and by the labeling density. The above methods can achieve resolutions on the order of $10-20\,\mathrm{nm}$. However, the stochastic methods can be slow, due to the number of cycles needed, and because the error is determined effectively by the number of photons collected from the fluorophores. Förster resonance energy transfer is a conceptually different fluorescence technique, based upon energy transfer between donor and acceptor fluorophores. The efficiency of the energy transfer scales as the inverse 6^{th} power of the distance, between the fluorophores, and hence is very sensitive to small changes in separation. It has been used for some time, as a molecular ruler with nanometric sensitivity (limited to below $10\,\mathrm{nm}$) [8,103]. In this case, the signal can be low, or fluctuating, due to photoblinking. Indeed, generally, fluorescent techniques can result in unwanted photobleaching and phototoxicity. An excellent tool would therefore be an imaging method based on a non-fluorescing label, achieving similar resolution, and without the limitations of photobleaching, phototoxicity, or long acquisition times. To date, the use of non-fluorescing NPs as sensitive markers for nanoscopy has been less rigourously examined. The ideal imaging modality would be chemically sensitive, and achieve similar or better resolution, without the

need for a chemically-bound label. In fact, this is the core concept of the CARS/FWM nanoscopy project, which endeavours to use optical trapping to localise a nanoparticle to the microscopy target. However, bioimaging with bound, non-fluorescing NP labels holds significant fundamental interest, as well as potentially different functionalities.

As discussed in Sec. , 4.1, studies based upon imaging of non-fluorescing NPs are hampered by the robustness of available techniques for the detection of single particles; particularly techniques which could be compatible with live-cell imaging. Darkfield microscopy can only practically be used to image metallic NPs down to around 20 nm, as the scattering by non-target particles becomes comparable. DIC is a phase-sensitive technique, and so is non-specific. PTI is a pump-probe microscopy, which can be very sensitive, detecting particles as small as 1-5 nm. It is noteworthy, that this is, in part, due to the use of a probe beam whose wavelength is far from the LSPR, such that it is not strongly absorbed[15]. This allows high probe powers resulting in a lower relative shot noise, and thus higher sensitivity. However, PTI suffers from background, due to the fact that it is detecting the thermally-mediated refractive index change of the particle and local dielectric environment, such that any absorbing structure is imaged.

FWM imaging of metallic NPs is an imaging modality developed within the Cardiff Biophotonics group, capable of imaging individual AuNPs down to 5 nm[5]. FWM has a higher selectivity and thus a lower background than pti owing to the doubly resonant nature of the excitation. In the context of super-resolution microscopy, lateral and axial intensity resolutions of 140 nm and 470 nm (FWHM), have been achieved[5]. Furthermore, our group has shown that the phase difference, between the generated FWM field and the probe, is sensitive to shifts of the LSPR peak position relative to the probe wavelength[34]. As mentioned in Sec. 1, metallic NP-dimers have been proposed as a novel nanoscale-sensing tool, due to the gap-dependent shift of the symmetric longitudinal dimer LSPR peak from that of the single particle[8]. Thus far, "plasmon rulers" have been demonstrated using DNA linkage to control interparticle distance, and observed using darkfield scattering spectroscopy[8]. Long observation times were possible (>3000s), and distance sensitivity is limited to below, approximately, the size of the individual NPs of the dimer. However, darkfield scattering spectroscopy has a significant non-specific background, as previously mentioned. Furthermore, it is complex to de-

termine the exact size of the gap in absolute units, so the conversion of LSPR shift to interparticle distance was estimated using theoretical predictions[104]. A version of the "plasmon ruler" has also been shown in 3D, using complex nanostructures, fabricated via multiple phases of e-beam lithography and gold deposition[105]. In a recent publication[82], we presented a preliminary investigation of a novel combination of FWM and metallic NP-dimers. We used the wide-field extinction technique to measure the polarisation-resolved extinction of a sample containing single 40 nm diameter AuNPs and dimers, as described in Sec. 4.3.4. In the same field of view, we performed FWM measurements on individual particles. We then correlated the FWM phase to the relative amplitude parameter, α from Eq. 4.2.5, since α corresponds to the relative asymmetry of NPs or NP-combinations, and in-turn to a more shifted LSPR. This chapter will cover further work on this subject, including new correlative TEM/FWM data of individual 40 nm monomers and dimers.

5.2 Experimental details

Pump-probe type measurements of the ultrafast dynamics of metallic NPs have been of increasing interest recently, as NPs have become more commonly used in applications. Pump-probe setups can take many different configurations, including PTI and FWM[29,34,76,106,107]. We provide a brief summary of the underlying physics of the NP response.

The following discussion is based on Ref. 29,34,108. The short pulse duration, large peak intensities, and pulse energies, available in ultrafast pulsed laser excitation, make it possible to excite optical nonlinearities in certain materials, and probe NP ultrafast dynamics. In $\chi^{(3)}$ materials, the intense pulses can result in modification of the material's dielectric susceptibility. Time-resolved ultrafast pump-probe spectroscopies are used to investigate the dynamics of this effect. The time-resolution of these spectroscopies comes from the ability to control the relative arrival time of the pump and probe pulses at the sample. Typically, the pump arrives first, to excite the NP electron distribution, and the probe interrogates the changes caused by the pump. The pump pulse resonantly excites the LSPR, which then dephases, within about 10 fs[27,29,34], ei-

ther by radiative decay through scattering, or by non-radiative decay through absorption. The absorption leads to single electron excitations. The excited electrons thermalise with other electrons, via electron-electron scattering establishing a hot electron gas on the 100 fs timescale. The hot distribution then thermalises with the lattice, via electron-phonon coupling, on a timescale of the order of a few picoseconds. The particle eventually thermalises with its surroundings by heat conduction on a 100ps to nanosecond timescale, depending on the NP size. The transiently heated system effects a change in the dielectric function, hence a change in the LSPR, which is probed by the second pulse. An example of the dynamics of the change in the real and imaginary parts of the polarisability of Au, for a nominally spherical NPs, is shown in Fig. 5.1(a).

In our setup, the heterodyne detection scheme and dual channel lock-ins allow measurement of the real and imaginary parts of the probe and FWM fields. In particular, the lock-ins detect the real part, X, as the component of a signal in-phase with the reference, and the imaginary part, Y, as the in-quadrature component ($\pi/2$ out-of-phase). From X and Y, and by projecting E_{F} onto E_2, we determine the amplitude, A_{rel}, and phase, Φ, components of E_{F} *relative* to E_2, with Φ taken as the orthogonal component, such that[34]

$$A_{\mathrm{rel}} = \frac{X_2 X_{\mathrm{FWM}} + Y_2 Y_{\mathrm{FWM}}}{|E_2|^2} \qquad \text{and} \qquad \Phi = \frac{X_2 Y_{\mathrm{FWM}} + Y_2 X_{\mathrm{FWM}}}{|E_2|^2}. \tag{5.2.1}$$

In a previous work by the group[34], it was established that the changes in the real and imaginary parts of the dielectric function can be related directly to the measured A and P of the FWM and probe fields. We begin by expressing the pump-induced change in the polarisability, $\widehat{\alpha}$, as $\widehat{\alpha}_\Delta$, such that $E_{\mathrm{F}} \propto \widehat{\alpha}_\Delta E_2$. $\widehat{\alpha}_\Delta$ and E_2 can be put in terms of amplitude and phase as,

$$\widehat{\alpha}_\Delta = |\widehat{\alpha}_\Delta|\,\mathrm{e}^{i\phi} = \widehat{\alpha}_{\Delta\mathrm{R}} + \mathrm{i}\widehat{\alpha}_{\Delta\mathrm{I}} \qquad \text{and} \qquad \mathrm{E}_2 = |\mathrm{E}_2|\mathrm{e}^{i\varphi}. \tag{5.2.2}$$

Hence,

$$E_{\mathrm{F}} \propto |\widehat{\alpha}_\Delta||E_2|\mathrm{e}^{i(\varphi+\phi)}, \tag{5.2.3}$$

with ϕ the phase difference, between the FWM and probe fields at the particle position. The experimental design in Ref. 34, was such that the detection was in the forward

direction. The transmitted probe acquires a phase shift in the far field compared to the spherical wave of the FWM field, which is called the Gouy phase shift. From focus to infinity the phase shift is $-\pi/2$, so that the phase difference between the FWM and probe field is $\phi+\pi/2$. Hence,

$$A_{\text{rel}} \propto |\widehat{\alpha}_{\Delta}| \cos\left(\phi+\frac{\pi}{2}\right) = -|\widehat{\alpha}_{\Delta}| \sin(\phi) = -\widehat{\alpha}_{\Delta I} \tag{5.2.4}$$

$$\Phi \propto |\widehat{\alpha}_{\Delta}| \sin\left(\phi+\frac{\pi}{2}\right) = |\widehat{\alpha}_{\Delta}| \cos(\phi) = \widehat{\alpha}_{\Delta R} \tag{5.2.5}$$

The FWM phase, ϕ can be determined via the ratio of $\widehat{\alpha}_{\Delta I}$ and $\widehat{\alpha}_{\Delta R}$. In Fig. 5.1(b), we can see the dependence of measured ϕ on excitation energy. Within a range of $2.2\pm0.2\,\text{eV}$ ($\sim 565\pm25\,\text{nm}$), the phase changes by $\sim 3\pi/4$, quantifying the sensitivity of the phase to displacement of the probe wavelength from the LSPR. Note, the $\sim\pi$ phase in the case where the excitation is near the resonance ($\sim 2.2-2.3\,\text{eV}$), and that the phase increases, as the excitation wavelength decreases compared to the resonance. Significantly, this phase sensitivity is ratiometric, independent of signal strength, and absolute phase stability. We will investigate this for NP dimers later in this chapter. An important difference in the two setups is that the detection in *Ettore* is in the epi-direction. As a result, the phase shift of $E_{2\text{r}}$ in the far field, with respect to E_{F}, is different. There is no Gouy phase shift because both detected fields are scattered by the particle. So instead of obtaining ϕ, via a ratio of $\widehat{\alpha}_{\Delta I}/\widehat{\alpha}_{\Delta R}$, we deduce it from $E_{\text{F}}/E_{2\text{r}}$. Further discussion of this is made in Sec. 5.3.2.

It's also important to consider how asymmetry in NPs influence the measured FWM field. In the experimental setup of Ref. 109, the reference (pump) field is (cross) polarised along the x(y)-axis, of the laboratory xy basis, where the z-axis is the axial direction. The probe is linearly polarised at an adjustable angle, θ, with respect to the reference direction, forming the basis of a polarisation-resolved FWM setup. The FWM setup of *Ettore*, used in this work uses cross-circularly polarised pump and probe beams at the sample, and simultaneous dual polarisation detection of co and cross/circularly polarized fields. This enables to measure the complete polarisation-resolved field simultaneously. However, for purposes of illustration, we will first explore the linear polarisation setup and how it can be used to obtain information on NP shape. We begin by including the polarisability tensor (described in Eq. 1.1.11) in the

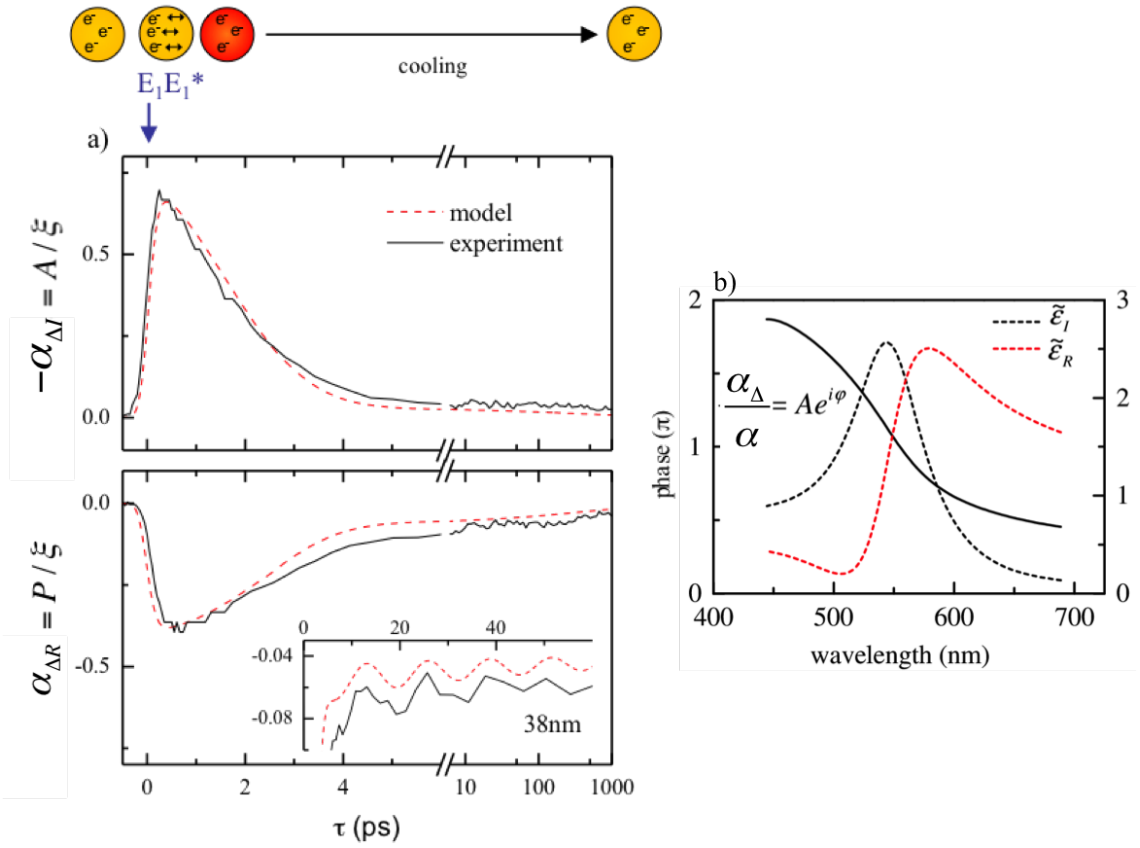

Fig. 5.1: a) Transient changes of the real ($\widehat{\alpha}_{\Delta R}$) and imaginary ($\widehat{\alpha}_{\Delta I}$) part of the polarisability of a single 38 nm diameter AuNP excited and probed at 550 nm. Pump (probe) fluence is 0.65 J/m^2 (0.05 J/m^2). Acquisition time per point is 200 ms. Dashed lines are corresponding calculations. The top sketch illustrates the LSPR excitation by the pump (E_1) and the subsequent heating and cooling dynamics monitored by the probe pulse. The inset shows coherent phonon oscillations from which the 38 nm diameter is deduced (see Ref. 34). b) Spectrally resolved real and imaginary parts of the dielectric constant $\widehat{\alpha}$ (dotted lines) simulated for the 38 nm NP in a) prior to the arrival of the pump, together with the phase φ (solid line) of the complex quantity $\widehat{\alpha}_\Delta/\widehat{\alpha}$ with the pump-induced change $\widehat{\alpha}_\Delta$ calculated at $\tau = 0.5$ ps. ξ is a constant related to properties of the detection. Figure and caption reproduced from Ref. 34

probe-induced dipole moment, such that

$$\mathbf{p}_2 = \epsilon_\mathrm{m} \widehat{\alpha}_\mathrm{M} \mathbf{E}_2, \quad \text{with} \quad \widehat{\alpha}_\mathrm{M} = \mathbf{R}_{\beta,\mathbf{u}} \, \widehat{\alpha} \, \mathbf{R}^\mathrm{T}_{\beta,\mathbf{u}}, \tag{5.2.6}$$

with the three-dimensional rotation matrix, $\mathbf{R}_{\beta,\mathbf{u}}$, defined by the NP angle, β, around the axis, $\mathbf{u}$. The rotation matrix transforms the NP basis into that of the laboratory. The particle is assumed to be an oblate spheroid, with two semi-minor axes and one semi-major axis, which lies in the xy plane. Hence, $\mathbf{u}$ is the z axis of the laboratory. The angle β is the between the particle's semi-major axis and the x-axis. The probe field is given by $\mathbf{E}_2 = E_2 \hat{\mathbf{e}}_2$, with unit vector $\hat{\mathbf{e}}_2 = (\cos(\theta), \sin(\theta), 0)$. E_F is projected along the reference field with a polariser, and the signal is given by ,

$$E_\mathrm{F} \propto \hat{\mathbf{e}}_\mathrm{x} \cdot \widehat{\alpha}_\Delta \, \hat{\mathbf{e}}_2 E_2, \tag{5.2.7}$$

with $\hat{\mathbf{e}}_\mathrm{x}$ the unit vector along the reference polarisation direction. From Eq. 5.2.7 it is clear that, either for a perfectly spherical particle, or for a particle with axes aligned along the x or y directions of the laboratory frame, the polarisation-dependent FWM field will have a maximum at $\theta = 0$, and will be zero at $\theta = \pi/2$. In the case of an asymmetric particle, with axes not aligned along x or y, then the polarizability tensor yields a component to $\mathbf{E}_2$ along $\hat{\mathbf{e}}_\mathrm{x}$, even when the probe and reference are cross-polarised. This effect is dependent upon the eccentricity of the particle. Overall, the polarisation-resolved technique provides information, both on the asymmetry of the particle, as well as its orientation within the laboratory frame. It should be noted, that the linear polarisation-resolved technique has been shown to be sensitive to eccentricities as small as 0.97. Real NPs are always non-spherical to some extent. We note that for a 40nm AuNP, 0.03 eccentricity corresponds to 1.2nm, corresponding to only 3 gold lattice constants. The dependence of the signal on θ, in this case, makes it possible to determine the orientation of the particle, i.e. via fit to models described in Ref. 34,109. However, the circular polarisation-resolved setup of *Ettore*, in combination with Epi-detection, simplifies this calculation, as the orientation can be directly taken from the relative phase, between co and cross-polarized signal. The relative phase is orientation angle divided by 2, with respect to a reference system given by the setup. In this work, we do not use the polarisation-resolved technique to explicitly determine particle orientation. This will be presented in a forthcoming publication[61].

5.3 FWM measurements

5.3.1 Alignment and settings

The setup is aligned using a gold film sample. In order to calibrate the polarisation states at the sample, the $\lambda/2-4$ and $\lambda/4$ waveplates of Fig. 2.10, were manually rotated, such that the detected cross-polarised signal was minimised in an flat section of the gold film. The laser power into the microscope was controlled by adjusting the AOM RF power. $20\,\mu$W pump and $10\,\mu$W probe powers are measured immediately prior to entry of the beams into the right port of the microscope. These powers are used for all measurements in this work. Two kinds of measurements were taken: xy-τ delay scans and xy-z scans. The xy indicates a 2-dimensional transverse spatial scan. $-\tau$ indicates that the 3rd scan dimension is a scan of the pump delay time τ. -z indicates that the 3rd dimension is a spatial scan in the axial direction. Typically, particles were brought roughly into focus, and a preliminary xy-z scan allowed fine location of the z-position yielding the peak FWM signal. At this point a τ delay scan was performed from -0.5 ps to 6.0 ps. The delay yielding the strongest FWM signal, in the range (0.3-0.5 ps), was then fixed for a final xy-z scan of $1.0\times1.0\times1.0\,\mu\text{m}^3$ for sample 1 (see Sec. 3.3.2), or $1.0\times1.0\times1.5\,\mu\text{m}^3$ for TEM-correlated samples (samples 2a-2d, see Sec. 3.3.2). The 40x 0.95 NA lens was used to investigate sample 1, with a resolution given by $\lambda/(2\text{NA}) = 289$ nm. The 100x 1.45 NA lens was used for samples 2a-2d, with a resolution of 190 nm. For sample 1, sampling occurred at 3 points per resolution (ppr), and for samples 2a-2d, at 6 or 9 ppr. For sample 1 xyz scans, this resulted in $15\times15\times11$ points, with 3 ms per point. For samples 2a-2d, this leads to $49\times49\times15$ points, with 2 ms per point.

5.3.2 AuNP dimers on glass

In a region of Sample 1 (see Sec. 3.3.2, 4.3.4), a set of nominally 40 nm AuNPs was characterised with wide-field extinction and extinction spectroscopy, as described in Sec. 4.3.4 and Sec. 4.8. A preliminary analysis of correlated FWM measurements was presented in Ref. 82. We introduce the following convention for the polarisations of the fields. For a given field, $\mathbf{E}^{\pm}$, + indicates a left-circular polarization, co-polarised to

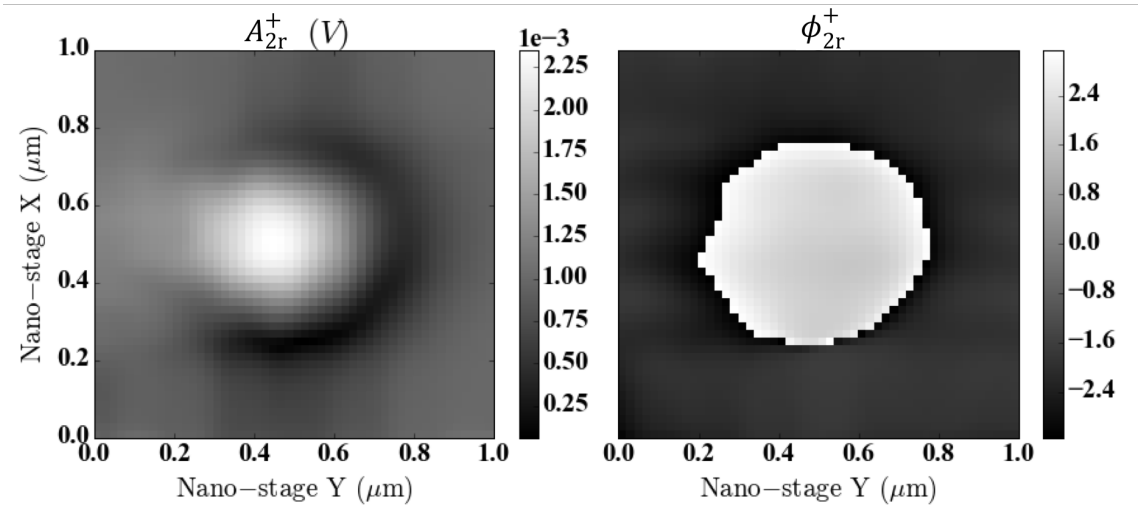

Fig. 5.2: Co-polarised probe amplitude, A^{+}_{2r}, and phase, ϕ^{+}_{2r}, measured on a dimer from sample 1.

the probe, and − indicates a right-circular polarisation, cross-polarised to the probe. We express the dipole moment induced in the NP by the incident probe, $\mathbf{E}^{+}_{2}$, as

$$\mathbf{p}_2 = \epsilon_m \widehat{\alpha}_M \mathbf{E}^{+}_{2}. \tag{5.3.1}$$

We can then write E_{2r} and E_F in terms of $\mathbf{p}_2$ and $\mathbf{E}^{\pm}_{R}$ with,

$$E^{\pm}_{2r} = (\mathbf{E}^{\pm}_{R})^{*} \cdot (\epsilon_m \widehat{\alpha}_M \mathbf{E}^{+}_{2}) \qquad E^{\pm}_{F} = (\mathbf{E}^{\pm}_{R})^{*} \cdot (\epsilon_m \widehat{\alpha}_\Delta \mathbf{E}^{+}_{2}), \tag{5.3.2}$$

where $\mathbf{E}^{\pm}_{R}$ are reference field components, with the complex conjugate and scalar product describing the detected interference of the fields. We will use the convention that A indicates $|E|$ for a complex amplitude E, and ϕ is the phase.

In the case of all probe measurements, a background was noticed in the region around the particle. This can be seen in Fig. 5.2. We attribute the background to the reflection by the refractive index mismatch of the oil-glass interface, at which the particles sit. The background in the amplitude and phase can be related to the thickness of, or height variation in, the material. As discussed in Sec. 1.1.1, the real part of the refractive index is related to the phase velocity of the EM wave in the medium. Hence, two rays propagating through different lengths of the same material will experience a phase difference, as a result of the difference in optical path length. We do not expect to see variation in background amplitude for this sample, since the refractive indices

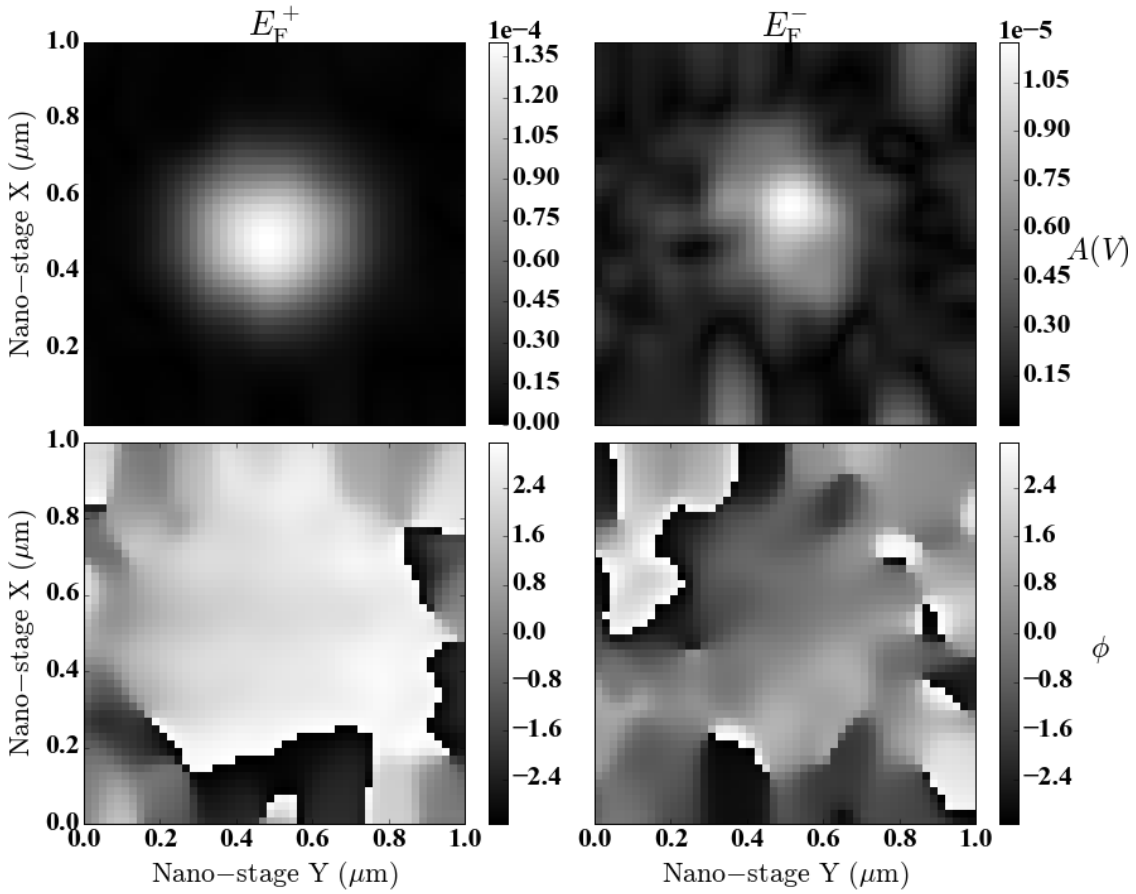

Fig. 5.3: The background-subtracted amplitudes (phases) are presented in the top (bottom) row for the co (cross) fields, E_F^+, E_F^- in the left (right) column, measured on the single, nominally 40 nm AuNP, represented by the triangle in Fig. 4.20. Acquisition time 2 ms per point, for 15×15 points giving a $1 \times 1\,\mu m^2$ measurement area. Measurement sampling was 3 ppr, with resolution of the 0.95NA objective equal to 289 nm. Data was interpolated to 50×50 points during analysis for presentation of the images.

of glass and oil are real, homogeneous, and constant. From Fig. 5.2, the background in both amplitude and phase is reasonably homogeneous, with maximum variation within $1\,\mu$m of $< 10\,\%$ and $< \pi/5$, respectively. This suggests little thickness or height variation, which is expected for the glass substrate. To remove the background, the average pixel value was taken in the region outside the particle, and was subtracted as a complex number from the whole image.

Examples of the background-subtracted amplitudes and phases of $E_F^{\pm}$ are shown in

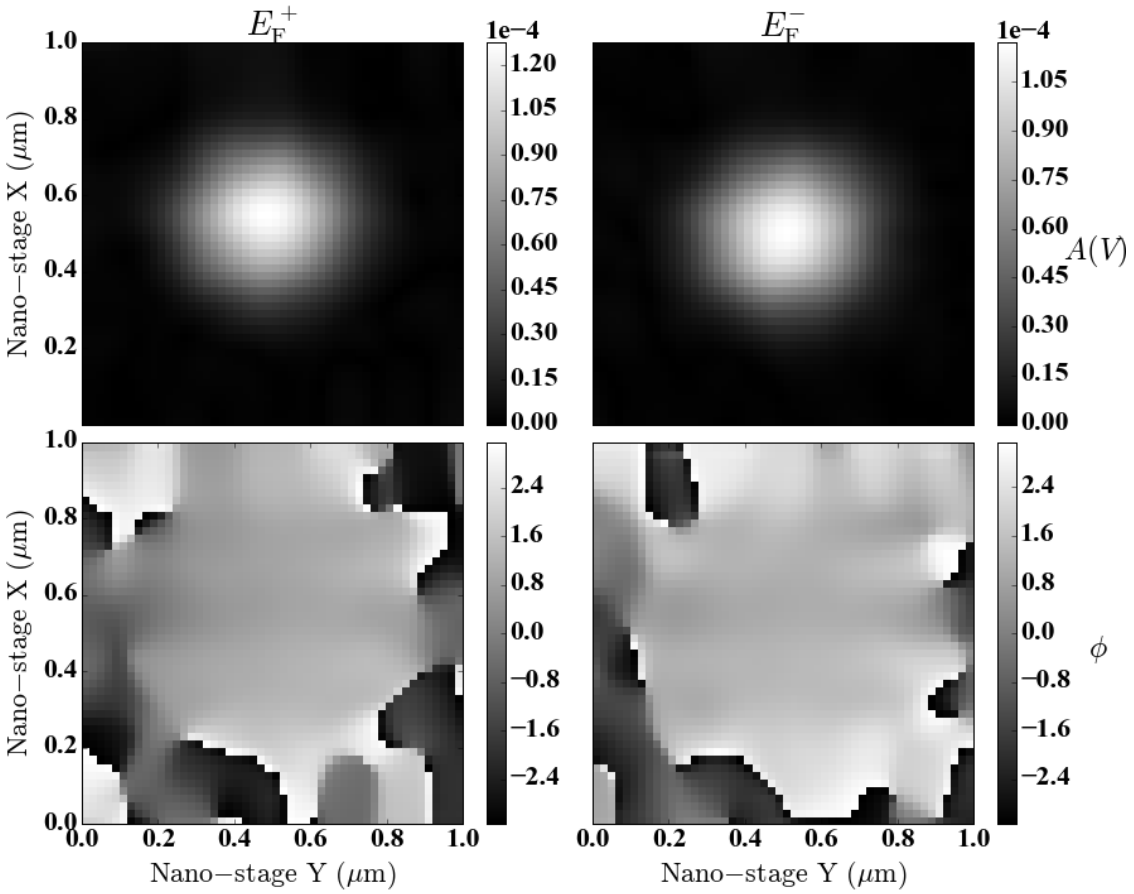

Fig. 5.4: As Fig. 5.3, but for the dimer, represented by the square in Fig. 4.20

Fig. 5.3 and Fig. 5.4 for the single NP and dimer seen in Fig. 4.20. A_F^- is approximately an order of magnitude lower than A_F^+ for the single particle, while it is of similar amplitude for the dimer. An example of the ultrafast dynamics of these two particles, with respect to pump delay, τ, can be seen in Fig. 5.5. We see the characteristic rise time of a few hundred femtoseconds, with a peak around 0.5 ps. Note, this plot merely serves as confirmation that we are indeed measuring AuNPs, and is not intended to exemplify any differences between single NP and dimer NP ultrafast dynamics.

To obtain the FWM phase, we consider the ratio of the co-polarised FWM and reflected probe, E_F^+ / E_{2r}^+, which gives

$$\frac{E_F^+}{E_{2r}^+} = \frac{\widehat{\alpha}_\Delta}{\widehat{\alpha}_M} = \left|\frac{\widehat{\alpha}_\Delta}{\widehat{\alpha}_M}\right| e^{i\phi^+} \tag{5.3.3}$$

We calculated the phase, ϕ^+, from the complex ratio by taking the average value of the fields, within a few pixels of the peak amplitude position. The number of pixels to

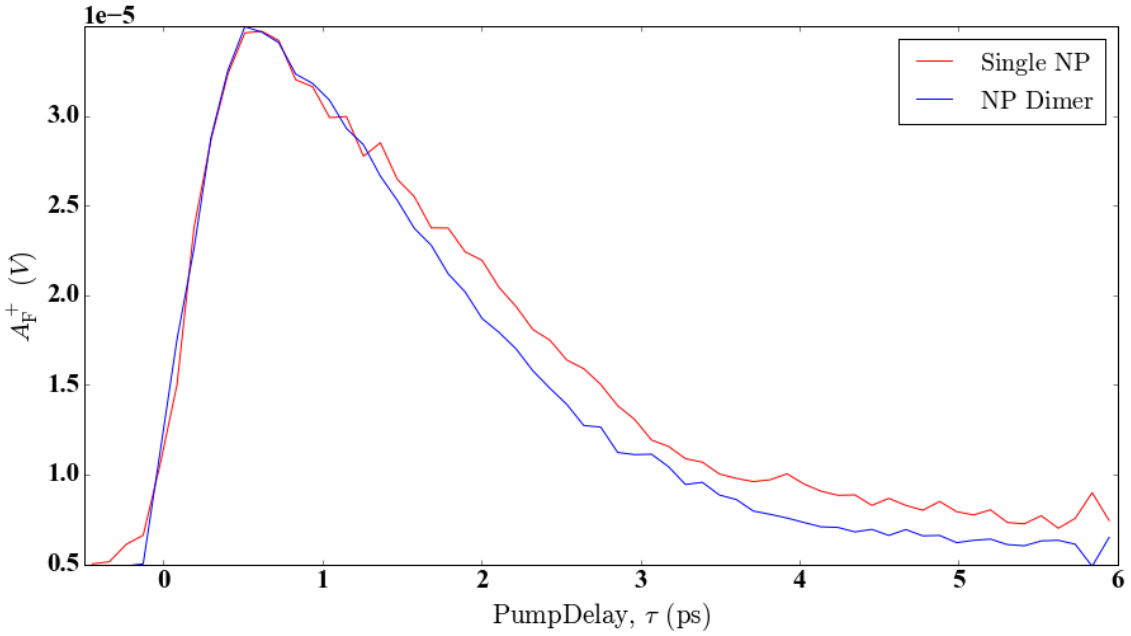

Fig. 5.5: Co-polarised FWM amplitude, A_F^+, measured on the single NP (triangle) and dimer (square) from Fig. 4.20, as a function of pump delay, τ.

average was determined as the peak position $\pm 1/3$ of the resolution. So, in this case, due to the low sampling (3 points per resolution), the average was taken for the peak position ± 1 pixels in x and y. Note, that the averaging is done on the fields to avoid systematic errors due to the non-linear transformation of Eq.1.3.3 from the fields to the phase ϕ^+.

The FWM phase measurements of particles in sample 1, were correlated to the relative amplitude parameter, α_R, which is an indicator of NP asymmetry. The data is presented in Fig. 5.6. Recalling Fig. 5.1(b), as the probe wavelength becomes further blue-shifted from the resonance, the phase increases. Here, we expect that the LSPR along the long axis will red-shift, as discussed in Sec. 1.1.1 & 1.1.3, relative to the probe wavelength, for increasing values of α_R. Thus, for larger α_R, we expect to see the phase increasing from that of the single particle, which is expected to have $\phi^+ \sim \pi$. The data show a phase of 0.99π with a standard deviation 0.12π, without a significant dependence on α_R. The linear fit, with parameters given in the caption of Fig. 5.6, has a slope of $(-0.081 \pm 0.15)\pi$. The standard deviation is significant, and the slope is close to zero within this error. This is unexpected, but is likely due to the large outliers at small

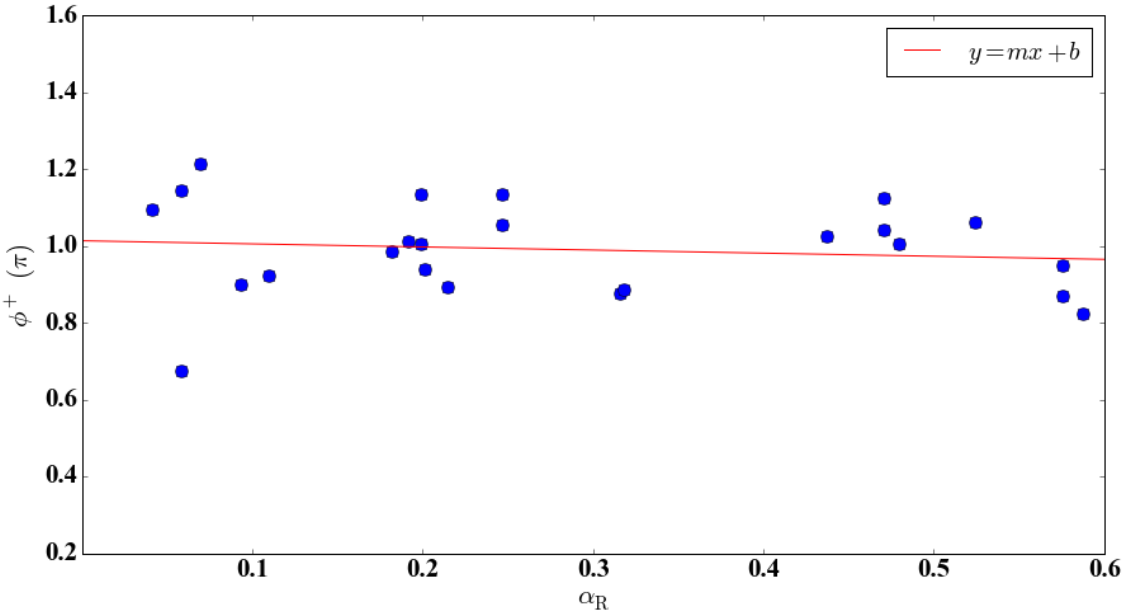

Fig. 5.6: ϕ^+ as a function of α_R for particles in Sample 1. Note the y-axis values displayed are divided by π. A linear fit is given with slope, $m = (-0.081 \pm 0.15)\pi$ and intercept, $b = (1.014 \pm 0.05)\pi$.

α_R. The phase of the co-polarised ratio is reporting the average resonance shift of the LSPRs, weighted with their polarisabilities. Since, only the LSPR polarised along the long axis is red-shifting, the overall effect is reduced in this phase. It would be better to select the polarisation along the red-shifting LSPR only, to observe the largest change. Since, we measure both co- and cross-polarized fields, we can determine the field polarized along an arbitrary direction by choosing the corresponding superposition. We start by expressing the complex amplitudes of the fields explicitly, as

$$E^+_{2r} = A^+_{2r}\, e^{-i\phi^+_{2r}} \qquad E^+_F = A^+_F\, e^{-i\phi^+_F} \tag{5.3.4}$$

$$E^-_{2r} = A^-_{2r}\, e^{-i\phi^-_{2r}} \qquad E^-_F = A^-_F\, e^{-i\phi^-_F}, \tag{5.3.5}$$

where A indicates $|E|$ for a complex amplitude E, and ϕ is the phase. Let us consider the sum of the co- and cross-circularly polarized fields of amplitudes C and D. We need not know the absolute phase, so we choose C to be real, and D to be complex, resulting in an elliptical polarisation, with

$$G = C\begin{pmatrix}1\\-i\end{pmatrix} + D\begin{pmatrix}1\\i\end{pmatrix} = \begin{pmatrix}C+D\\-i(C-D)\end{pmatrix}. \tag{5.3.6}$$

If we assume D is real, the ellipse is characterised by semi-major and semi-minor axes of lengths, $C+D$ aligned along the x-direction, and $C-D$ aligned along the y-direction, respectively. The subtraction of the two waves yields the same ellipse rotated by $\pi/2$. If one of the circularly polarised waves is offset from the other, by an arbitrary phase offset, $e^{-i\phi_{off}}$, then the semi-major axis will lie at an angle relative to the positive x-axis. We assume that the polarization is along the major(minor) semi-axis, when it is of maximum(minimum) amplitude. This is not quite correct considering the different phase of the response along the individual axes, due to the different resonance frequencies. However, for strongly asymmetric particles, the response is dominated by one LSPR, and the assumption is reasonable for the co-polarized result. In this case, we can determine the in-phase and out of phase superpositions, with

$$E_{2r}^{\parallel} = \left(A_{2r}^{+} e^{-i\phi_{2r}^{+}}\right) + e^{i\phi_{2r}^{\Delta}} \left(A_{2r}^{-} e^{-i\phi_{2r}^{-}}\right) \qquad E_{F}^{\parallel} = \left(A_{F}^{+} e^{-i\phi_{F}^{+}}\right) + e^{i\phi_{2r}^{\Delta}} \left(A_{F}^{-} e^{-i\phi_{F}^{-}}\right) \quad (5.3.7)$$

$$E_{2r}^{\perp} = \left(A_{2r}^{+} e^{-i\phi_{2r}^{+}}\right) - e^{i\phi_{2r}^{\Delta}} \left(A_{2r}^{-} e^{-i\phi_{2r}^{-}}\right) \qquad E_{F}^{\perp} = \left(A_{F}^{+} e^{-i\phi_{F}^{+}}\right) - e^{i\phi_{2r}^{\Delta}} \left(A_{F}^{-} e^{-i\phi_{F}^{-}}\right), \quad (5.3.8)$$

where $E_{2r}^{\parallel}$ is the field taken along the long axis of the asymmetry (parallel), $E_{2r}^{\perp}$ is the field taken along the short axis (perpendicular), and $\phi_{2r}^{\Delta} = \phi_{2r}^{-} - \phi_{2r}^{+}$ is the phase difference between the co- and cross-polarised reflected probe fields. ϕ_{2r}^{Δ} is the phase offset in the polarisation ellipse described above. We use only the probe phase difference in all cases, as the signal can be compared with the extinction data. ϕ_{2r}^{Δ} can be directly calculated from the measured cross- and co-polarised fields, by taking the phase from the ratio of $E_{2r}^{-}/E_{2r}^{+}$and E_{F}^{-}/E_{F}^{+}. Note, typically these ratios are measured directly by MultiCARS, so there is no need for secondary analysis. Also, ϕ_{2r}^{Δ} is directly related to the orientation of the particle. This is beyond the scope of this report, but will be discussed in detail in Ref. 61. We can now obtain the FWM phase from the ratios of $E_{F}^{\parallel}/E_{2r}^{\parallel}$ and $E_{F}^{\perp}/E_{2r}^{\perp}$. The expectation is that the phase of $E_{F}^{\parallel}/E_{2r}^{\parallel}$, called $\phi^{\parallel}$, will exhibit a strong dependence on α_R, and the phase of $E_{F}^{\perp}/E_{2r}^{\perp}$, called $\phi^{\perp}$, will show weak dependence on α_R. The results of these calculations can be seen in Fig. 5.7. As expected there is no discernible dependence of the phase on α_R for the perpendicular case. There is small enhancement in the parallel case, as seen by the fitted slope increasing to $(-0.0379 \pm 0.133)\pi$, however the error again dominates the value. Due to significant outliers at small α_R, the expected trend is not clearly realised. Discounting the three outliers of large $\phi^{\parallel}$ for α_R<0.1, we can see that the linear fit would yield a pos-

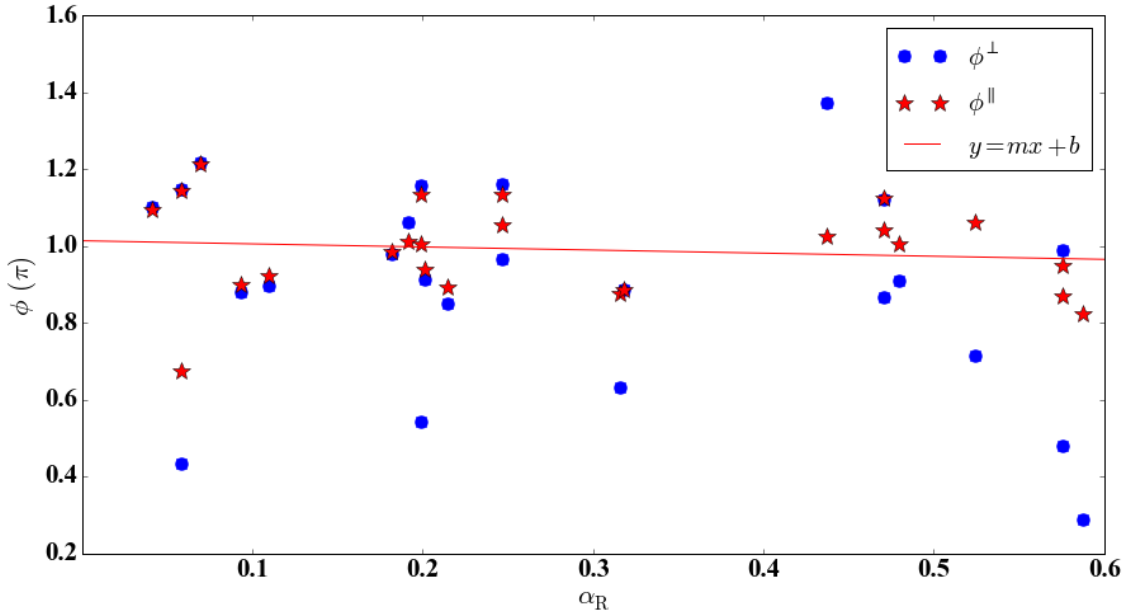

Fig. 5.7: As in Fig. 5.6, for $\phi^{\parallel}$. A linear fit is given with slope, $m = (-0.0397 \pm 0.133)\pi$, and intercept, $b = (1.036 \pm 0.045)\pi$.

itive slope, as expected. Since, we do not know the exact geometries of the particles in this case, we cannot draw any conclusion from these datasets, but this establishes an analytical procedure, which we can use on the TEM correlated data sets.

5.3.3 AuNP monomers and dimers on pioloform

The samples, discussed in this section, allowed for correlative TEM and optical measurements. Samples 2a-2d are AuNPs drop-cast on pioloform TEM grids, as described in Sec. 4.8.2. We will call samples 2a & 2b, set 1, and 2c & 2d, set 2, corresponding to the two separate FWM measurement days. We found that the pioloform caused significant background in the detected probe, which was enhanced in the graphetised regions induced by the preceding TEM characterisation. This is exemplified in Fig. 5.8, showing the measured field amplitudes A^{+}_{2r} and A^{+}_{F} over an area of $15\text{x}15\,\mu\text{m}^2$. The wide overlapping circles are graphetised regions of the pioloform, indicating TEM measurements on each of the particles. Pioloform has a refractive index[110] of $n = 1.485$, which is significantly different from the embedding oil ($n \sim 1.518$). Hence, even in the absence of TEM damage, the index mismatch leads to a reflected probe. Furthermore,

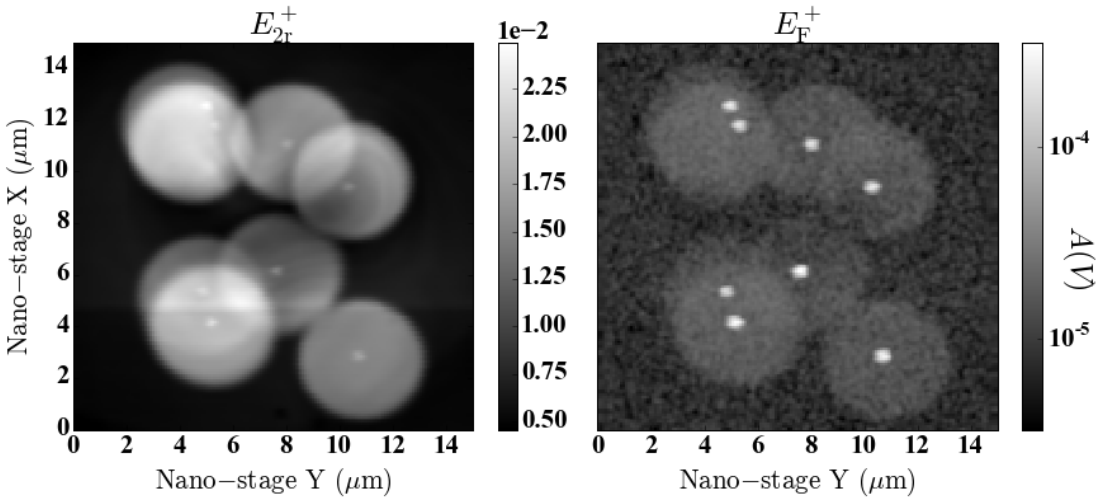

Fig. 5.8: A_{2r}^{+}(left) and A_{F}^{+} (right) in a region of nearby single AuNPs in sample 2b.

the pioloform has height and thickness variations across the imaged region, resulting in variations in the phase and amplitude of the reflection. This can be seen in Fig. 5.8. The FWM signal is less affected by the pioloform background. In regions which have not been imaged by TEM, no FWM signal from the pioloform was observed within the dynamic range of the experiment. This is expected, since pioloform is non-absorbing, and thus no non-instantaneous, non-linear response should occur. The regions damaged by the TEM imaging, however create an observable FWM signal, visible in Fig. 5.8. This FWM signal is nearly independent of the pump-probe delay. Hence, we can distinguish it from that of AuNPs, via the dynamics, e.g. we measure at the delay time $\tau = 0.4\,\text{ps}$ giving the strongest Au FWM signal. This background is of photothermal origin, created by the absorption in the damaged pioloform due to graphitization. Fig. 5.9 presents a zoomed region ($x, y \in [0,2]\,\mu\text{m}$) of Fig. 5.8, where there is no TEM damage. We can see that phase differs by nearly π across the image, suggesting significant height variation within $2\,\mu$m. On the other hand, amplitude variations are small, i.e. less than 10%, suggesting little variation in thickness. An example of A_{2r}^{+} and ϕ_{2r}^{+} can be seen in Fig. 5.10, for a dimer imaged also with TEM. Outside of the peak, A_{2r}^{+} is an order of magnitude larger than that of the region without TEM damage, and exhibits an approximately linear gradient in the x-direction. ϕ_{2r}^{+} shows a nearly π change in the x-direction, this time over only $1\,\mu$m. We note that comparison of Fig. 5.2 and Fig. 5.10, shows that the background in glass is more homogeneous around the parti-

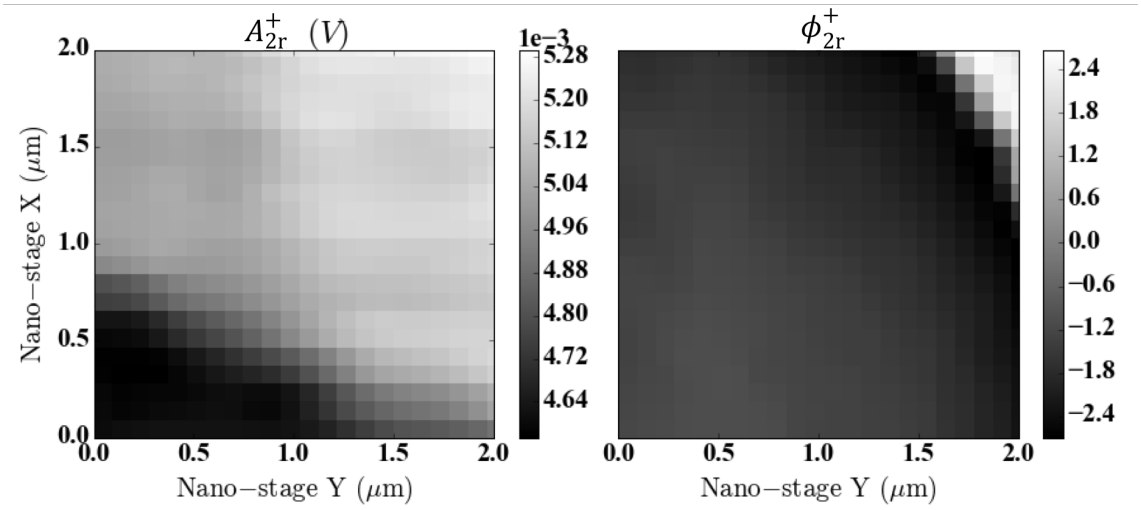

Fig. 5.9: A^+_{2r}(left) and ϕ^+_{2r} (right) in in the region with $x, y \in (0,2)$ of the region presented in Fig. 5.8.

cle, but of similar *relative* magnitude compared to the particle signal, i.e. particle signal is approximately twice as large as the background. In order to subtract the background here, the average pixel value of E_2 was taken only above and below the particle in the y-direction, and approximately at the position of the particle peak amplitude in the x-direction.

The resulting $\phi^{\parallel}$ and $\phi^{\perp}$ are shown in Fig. 5.11. We see a systematic dependence of $\phi^{\parallel}$ on gap size for both particle sets. In contrast, the $\phi^{\perp}$ dataset shows no correlation to the gap size. A selection of single NPs were also measured in set 1, showing the distribution of $\phi^{\parallel}$, with mean 0.918π and a standard deviation 0.175π. Since, these single NPs act as our reference, it's important to consider why this large phase range might occur. The single NPs discussed here are the NPs imaged in Fig. 5.8. We cannot attribute the phase range of the single particles to background, because a similar phase range is seen in sample 1, for particles of small α_R. Hence, we conclude that the spread of phase measurements for single NPs is not likely due to the measurement method. Instead, we must consider the inhomogeneity of the NPs themselves. The TEM image of the single NP with significant outlying value, $\phi^{\parallel} \approx 1.18$, is shown Fig. 5.12(a). The triangular shape is different from other NPs shown in this work, as well as being slightly larger (45 nm) than the average (40 nm). To develop a reasonable estimate of the single NP $\phi^{\parallel}$, we assume that the triangular NP is artificially increasing the phase range of the

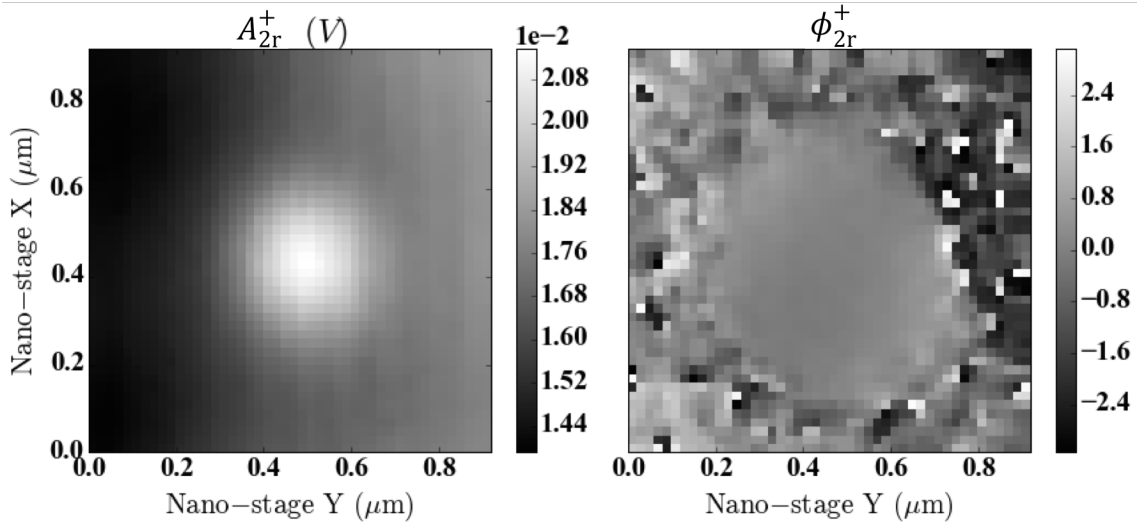

Fig. 5.10: The amplitude and phase of E^+_{2r}, measured on the dimer in sample 2a.

singles. We discount this NP, and take the average $\phi^{\parallel}$ of the remaining singles, giving $\bar{\phi}^{\parallel} = (0.863 \pm 0.135)\pi$. Notably, the values of $\phi^{\perp}$ give $\bar{\phi}^{\perp} = (0.860 \pm 0.087)\pi$. The standard deviation is 55% larger in the phase taken along the asymmetry, which suggests we are sensitive to the anisotropy of individual particles. This is supported by TEM measurements, which we've used to estimate the eccentricity of these particles to be a significant, $e = 0.355 \pm 0.058$. To compare the $\phi^{\parallel}$ data to the FWM phase dependence in Fig. 5.1(b), we use $\bar{\phi}^{\parallel}$ as a single NP baseline, and measure the maximum phase change divided by the expected spectral shift, with

$$\frac{\Delta\phi^{\parallel}}{\Delta\lambda} = \frac{\phi^{\parallel}_{\max} - \bar{\phi}^{\parallel}}{\Delta\lambda}. \tag{5.3.9}$$

From the extinction spectroscopy measurements (see Sec. 4.8), the spectral shifts can be as large as $\sim 65\,\text{nm}$, for a gap size around $0.5 - 1.0\,\text{nm}$. So with $\phi^{\parallel}_{\max} = 1.37\pi$ and $\Delta\lambda = 65\,\text{nm}$, we find $\Delta\phi^{\parallel}/\Delta\lambda \approx 2.46 \cdot 10^{-2}\,\text{rad/nm}$. From the modeled FWM phase dependence in Fig. 5.1(b), we can estimate a value of $\Delta\phi^{\parallel}/\Delta\lambda \approx 2.5 \cdot 10^{-2}\,\text{rad/nm}$, in reasonable agreement. Furthermore, we note the dimer corresponding to a $G = 60\,\text{nm}$ gap size, visible at far right of Fig. 5.11. This gap size yields $G/D \approx 1.5$. For $G/D >\sim 1.5$ we expect $\Delta\lambda/\lambda_0 < 0.0025$[48], corresponding to a shift of less than 1.5 nm assuming a resonance at 550 nm. Accordingly, the $\phi^{\parallel}$ of this dimer is approximately the same as the single NPs. The grouping of 3 dimers with around 20 nm gap size exhibit an increased phase compared to the $G = 60\,\text{nm}$ dimer, as expected. However, they also exhibit a

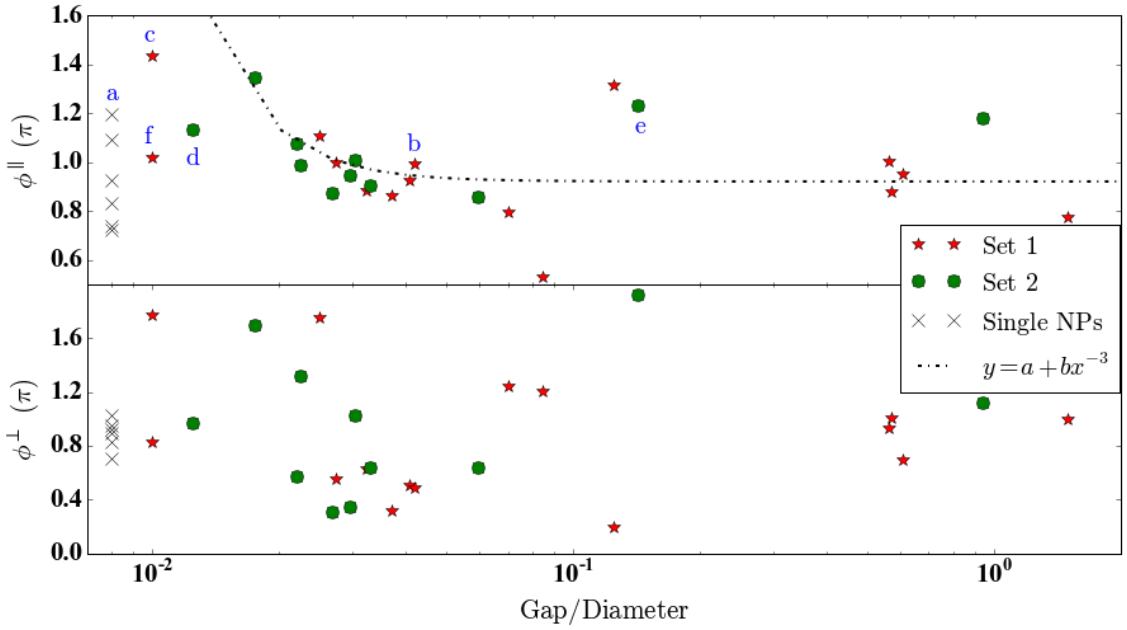

Fig. 5.11: $\phi^{\parallel}(\phi^{\perp})$ versus normalized gap size in top (bottom) frame. Dimers from set 1 are indicated by red stars, dimers from set 2 by green circles, and single NPs from set 1 by blue crosses plotted at a normalised gap size value, $8 \cdot 10^{-3}$. The two red stars at normalised gap size $1 \cdot 10^{-2}$, indicate two dimers from set 1, which have zero gap. Letters indicate particles exhibited in Fig. 5.12. $\phi^{\parallel}$data were fit with $y = a + bx^{-3}$, with $a = (0.921 \pm 0.258)\pi$ and $b = (1.744 \pm 4.818)\pi \times 10^{-6}$.

$\sim \pi/5$ range. We expect variability, due to individual particle inhomogeneity, to dominate $\phi^{\parallel}$ variability for single particles. However, for strongly coupled NPs, the dimer mode will most strongly affect the LSPR shift, and therefore $\phi^{\parallel}$. As the dimer becomes more weakly coupled, the individual particle variability will become more important. This could explain the spread of the three $G \approx 20$ nm dimers.

NP dimers may themselves exhibit varying coupling, due to particle inhomogeneities. Fig. 5.12 presents several examples of dimers, with letters corresponding to measured values of the phase in Fig. 5.11. We can see the faceted surfaces of the constituent NPs. It is well known that the fields of metallic NPs focus at sharp points, as discussed in Sec. 1.1.3. Looking closely at the particle (b), with gap size 1.64 nm, we see that the "points" of the two particles are adjacent to each other, not directly opposite. This could potentially affect the strength of NP coupling, as we would expect the strongest

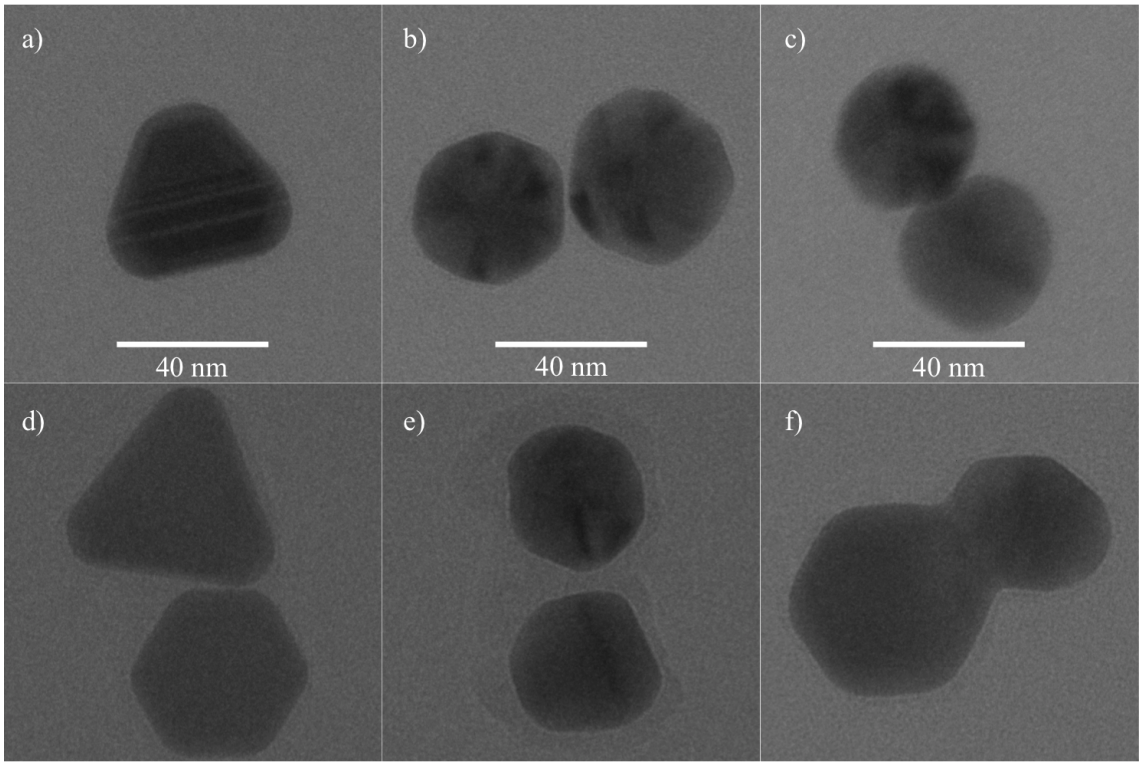

Fig. 5.12: TEM images of the single and dimer NPs, discussed in the text.

coupled field to depend on the arrangement of the strongest parts of the fields of both constituent NPs. We can address some of the outliers in the plot with geometry arguments based on the TEM images. The two red stars aligned at $G/D = 1 \times 10^{-2}$ and indicated by "c" and "f" in Fig. 5.11, correspond to dimers, which seemingly have zero gap, as seen in Fig. 5.12. (c) appears to be a touching dimer, while (f) appears to be a fused single metallic NP, with the constituent single NPs of different size in (c) and (f). Both of these cases deviate from the gap-dependent dimer model. Indeed, we still see a significant phase shift, as expected, but we cannot translate them into the rest of the dataset. The green circle datapoint in Fig. 5.11 corresponds to the dimer in Fig. 5.12(d). Similarly, the odd combination of these shapes, means we must treat this point as an individual case. Four outlying values of $\phi^{\parallel}$, in Fig. 5.11 are not related to outlying shapes as observed by TEM. Excluding the particles discussed, we fit the data using $y = a + bx^{-3}$, assuming the potential due to dipole-dipole interaction to scale as $(G/D)^{-3}$, as discussed in Sec. 1.1.3. The fit parameters with standard errors are given in the caption of Fig. 5.11. The errors are large, but we see the fit provides a $\phi^{\parallel} = 0.921\pi$, at large G/D,

in reasonable agreement with $\bar{\phi} = 0.86\pi$ for the single NPs. The fitted $\phi^{\parallel} = 1.28$ at the smallest measured $G/D = 0.017$ is ~ 5% lower than the phase value for smallest measured gap distance, $\phi^{\parallel} = 1.35$. From $G = 0.68\,\text{nm}$ to $G = 2.4\,\text{nm}$, measured $\phi^{\parallel}$ changes by a significant $\Delta\phi^{\parallel} = 0.58\pi\,\text{rad}$, while the fit $\phi^{\parallel}$ changes by $\Delta\phi^{\parallel} = 0.35\pi\,\text{rad}$. The trend is not observed for $\phi^{\perp}$, suggesting we are probing the particle asymmetry. The considerable error can be attributed to the variability of the measurement at a given gap size. The fit is, however, sufficient to suggest that we are sensitive to the gap change, and that the scaling can be described by the dipole-dipole interaction. Hence, we can conclude that the intrinsic FWM phase measurement, which is sensitive to LSPR shift, can be used to investigate interparticle distances, with a sensitivity approximately given, by $\Delta\phi^{\parallel}/\Delta\lambda \approx 2.46 \cdot 10^{-2}\,\text{rad/nm}$. More correlative extinction and FWM imaging needs to be performed to understand the origin of the spread of the results. It is likely due to the spread in individual NP geometries.

5.4 Summary

We have shown that there is a correlation between FWM phase and dimer gap distances, measured with TEM. Furthermore, our dual phase ($\phi^{\parallel}$, $\phi^{\perp}$) method of analysis has suggested we can be uniquely sensitive to the dimer symmetric longitudinal mode. We found that single NP variability is a complicating factor in practical measurements. In the future, we hope to perform more extinction spectroscopy measurements on the particles in these samples. We could then correlate the known gap size to LSPR shift and FWM phase for all measurements. In this work, comparison has been made between the observed $\phi^{\parallel}$ relation and that of the single particle model from Ref. 34,109. We will develop a fitting model in the future publication, for a quantitative understanding of the results, in terms of NP size and shape.

Conclusions

In this work, several imaging techniques and chemistry protocols have been presented which focus on the study of NPs and the development of NP-based methods. In Sec. 3, we presented techniques for the covalent binding of NPs to glass, or to each other to facilitate formation of NP dimers in suspension. Sec. 4 exhibited our wide-field imaging technique, capable of simultaneous acquisition of data from potentially hundreds of individual NPs, as well as an extinction spectroscopy technique for obtaining higher resolution spectra from single NPs. Finally, in Sec. 5.3 we discussed an initial work towards an in-vitro plasmon ruler using phase-sensitive FWM imaging.

The covalent bindings described in Sec. 3, were critical to the development of our imaging techniques. Drop casting provides suitable stability, when using low intensity illumination, such as the (30-100) W lamp. However, in the presence of high intensity pulsed lasers, the possibility exists that the particles can be moved, due directly to optical pressure, or to heating. Thus, covalent binding to glass (coverslips), using 3MT, provided a very stable platform, with which we could image NPs, without fear of mobility. The silane and thiol-metal chemistry employed to bind nanoparticles to glass, was also used to form AuNP dimers in suspension. Interparticle distance was controlled, via the thickness of silica shells on the outside of the NPs, provided by BBI Solutions. Due to silane polymerisation, we also obtained bound dimers of very small interparticle distance, resulting from bare-bare binding. Occurrence of dimers was confirmed by TEM imaging performed in collaboration with Bristol University.

We have presented a novel, to our knowledge, wide-field extinction technique in Sec. 4.2.1, which we have shown to be sensitive to AuNPs down to 5 nm diameter. It is possible to collect data on potentially hundreds of NPs simultaneously, in a single

field of view, meaning we can also obtain ensemble statistics from a single imaging experiment. The technique can be polarisation-, and/or coarsely spectrally-resolved in its current implementation. Conveniently, the wide-field extinction can be put into practice on any microscope, with any (digital) camera, in a cost-effective way. Analysis can be performed easily with the Extinction Suite on any PC capable of running ImageJ. We have used this method to study a range of particle sizes and materials, including Au, Ag, Pt, and diamond NPs. Comparison of our measured Au cross-sections, with theory and literature values, show them to be in good agreement. In the future, we would like to perform studies on nanorods, on an increased size range of AgNPs, on dimers of an increased range of interparticle distances, on carbon nanotubes, and more. We also expect to implement Fourier transform spectroscopy to increase the spectral resolution possible with this technique. Due to the rapidity of this technique, and thus its potential for high throughput, the wide-field extinction technique could find a place in for example, the nanoparticle fabrication industry. Nanoparticles fabricated in large batches are often characterised only with TEM or DLS, which provides size and shape information, but at extreme cost to the companies. These methods do not provide easily obtainable information on the optical properties of the NPs. Since, our technique can be polarisation-resolved, we are able to estimate both the size distribution, as well as the distribution of relative sphericity of particles, while directly providing information on NP optical properties. All of this is achieved at a fraction of the cost of a transmission electron microscope or DLS device.

The work presented in Sec. 5.3 served as a proof-of-concept for the in-vitro plasmon ruler, based upon phase-sensitive FWM of the frequency shift of the LSPR of metallic (Au) NPs. We used TEM imaging to measure the interparticle distances of various AuNP dimers. We then performed FWM imaging on each of these dimers, to correlate the phase shift with the interparticle distance. In addition, we measured the extinction spectra on several of these dimers, to determine the shift of the longitudinal mode LSPR relative to the single NP case. The study revealed, that we are indeed sensitive to the gap distance in FWM. However NP inhomogeneity strongly affects dimer optical properties. Since, the NPs vary individually in both size and shape, the dimer gap is not the only factor defining the resonance position. Our method will have to take this

into account, if we hope to use it practically in the future. If we can better characterise the phase shift, the proposed in-vitro plasmon ruler could be used to study cellular processes at the single molecule level. For example, our future goals include the study of AuNPs and AgNPs conjugated with different ligands. Different cellular receptors interact differently with their associated ligands. For instance the transferrin receptor is known to accept two transferrin ligands simultaneously, while others may only interact with single ligands at a time. Since, FWM can distinguish, between monomers and dimers via the phase shift, our technique potentially offers an opportunity for differential studies of cellular receptors, without the need for fluorescent markers and associated drawbacks. Additionally, we expect that we will be able to monitor interparticle distances and therefore trafficking of various cellular molecules.

CHAPTER 6

List of Acronyms

3MT (3-Mercaptopropyl) trimethoxysilane

40D Canon 40D camera

Ag Silver

Al Aluminium

AOM Acousto-optic modulator

APM Adjacent Pair Method

ASM Adjacent Set Method

Au Gold

BG Background

BI Bright images

CARS Coherent anti-Stokes Raman scattering

CO_2 Carbon dioxide

DI Dark images

DIC Differential interference contrast

DFG Difference-frequency generation

DMSO Dimethyl sulfoxide

DSLR Digital single lens reflex

EM Electron Microscopy (Introduction only)

EM Electromagnetic (Sec. 1 onwards)

ES Extinction Suite

FC Full color

FM Flip mirror

FPS Frames per second

FWHM Full width at half maximum

FWM Four-wave mixing

GQE Geometric Quantum Efficiency

GSDIM Ground state depletion followed by individual molecule return microscopy

GVD Group velocity dispersion

H_2O Water

H_2O_2 Hydrogen peroxide

HWHM Full width at half maximum

IML ImageJ macro language

LSPR Localised surface plasmon ruler

MP Megapixel

NA Numerical aperture

NCB Neutral Color Balance

ND Nanodiamond

NEM N-Ethylmaleimide

NP Nanoparticle

NPBS Non-polarising beam splitter

NSP Newport/Spectra-Physics

OO Ocean Optics

OPO Opto parametric oscillator

PALM Photoactivated localisation microscopy

PBS Polarising beam splitter

PCO PCO Edge 5.5 sCMOS camera

PI Physik Instrumente GmbH & Co

PRT Pattern recognition tolerance

Pt platinum

PTI Photothermal imaging

QE Quantum efficiency

RF Radio Frequency

ROI Region of interest

sCMOS scientific-CMOS

SEM Scanning electron microscopy

SFG Sum-frequency generation

SHG Second harmonic generation

SiO_2 Silicon dioxide (silica)

SMS Spatial modulation microscopy

STED Stimulated emission depletion

STORM Stochastic optical reconstruction microscopy

TEM Transmission electron microscopy

THG Third harmonic generation

TIRF Total internal reflection fluorescence

Ti:Sa Titanium Sapphire

APPENDIX A

Filters

A.1 LB200 filter

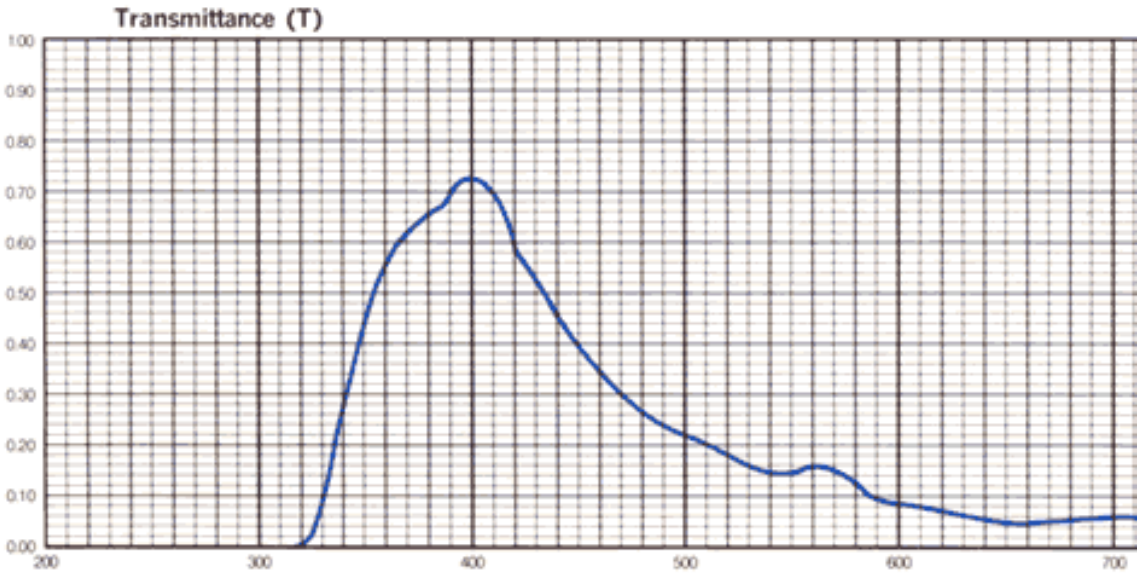

Transmission spectrum of the LB200 Hoya filter. x-axis is wavelength, in nm.

A.2 Nikon NCB filter

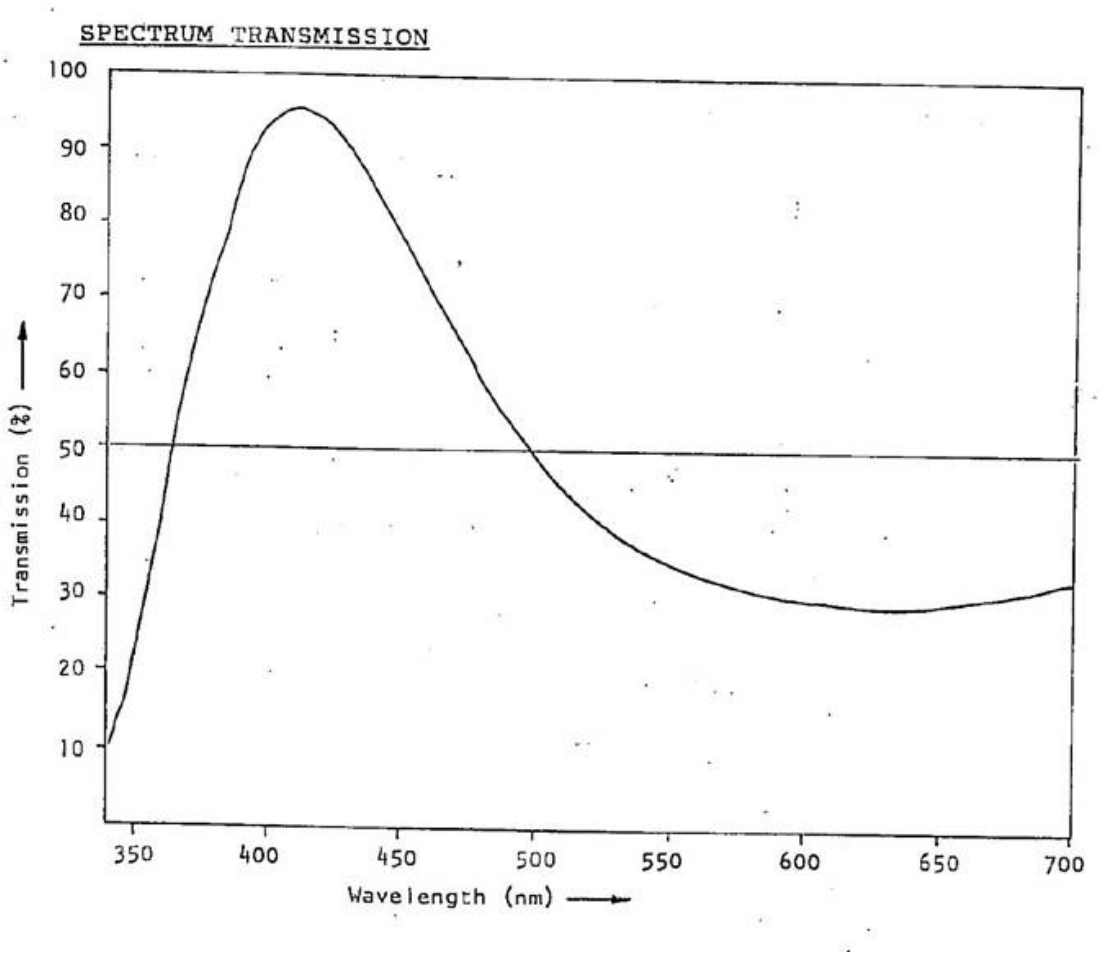

Transmission spectrum of the Nikon NCB filter

A.3 Semrock filters

A.3.1 Blue filter

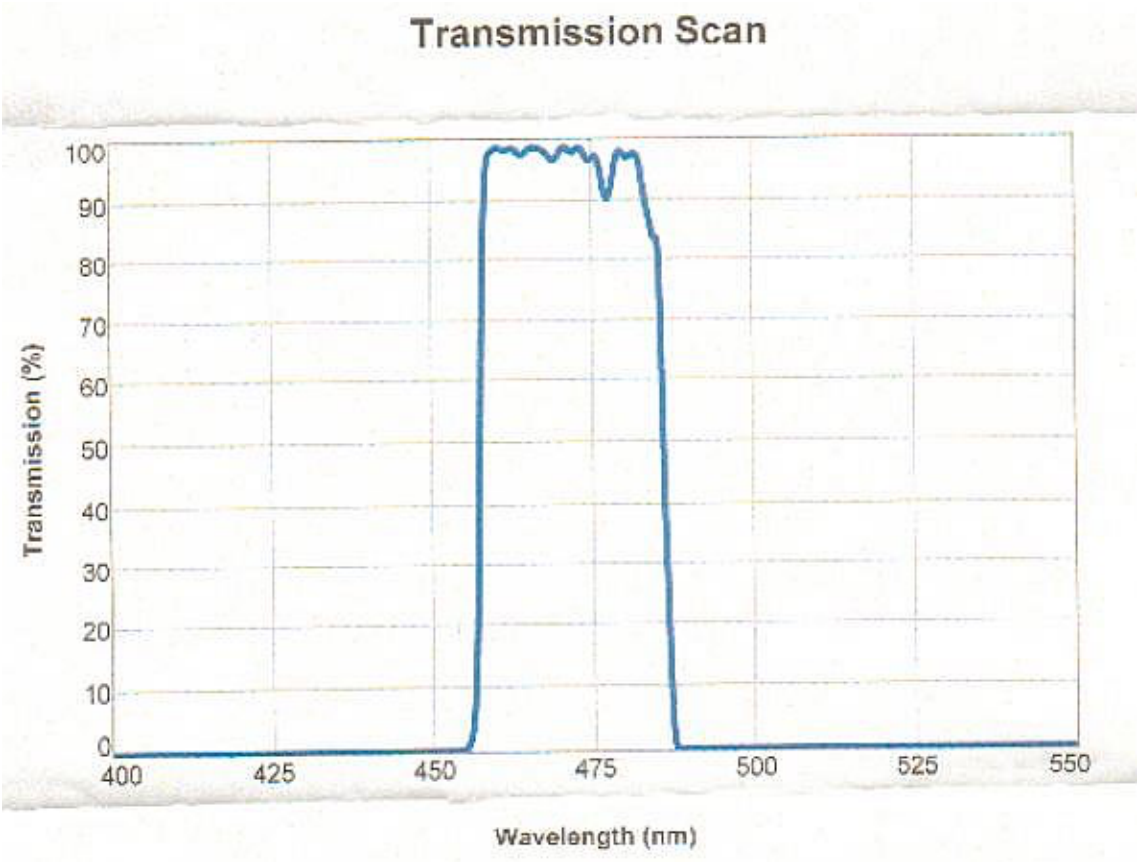

Transmission spectrum of the Semrock FF01-470/22 blue filter (470 ± 11 nm)

A.3.2 Green filter

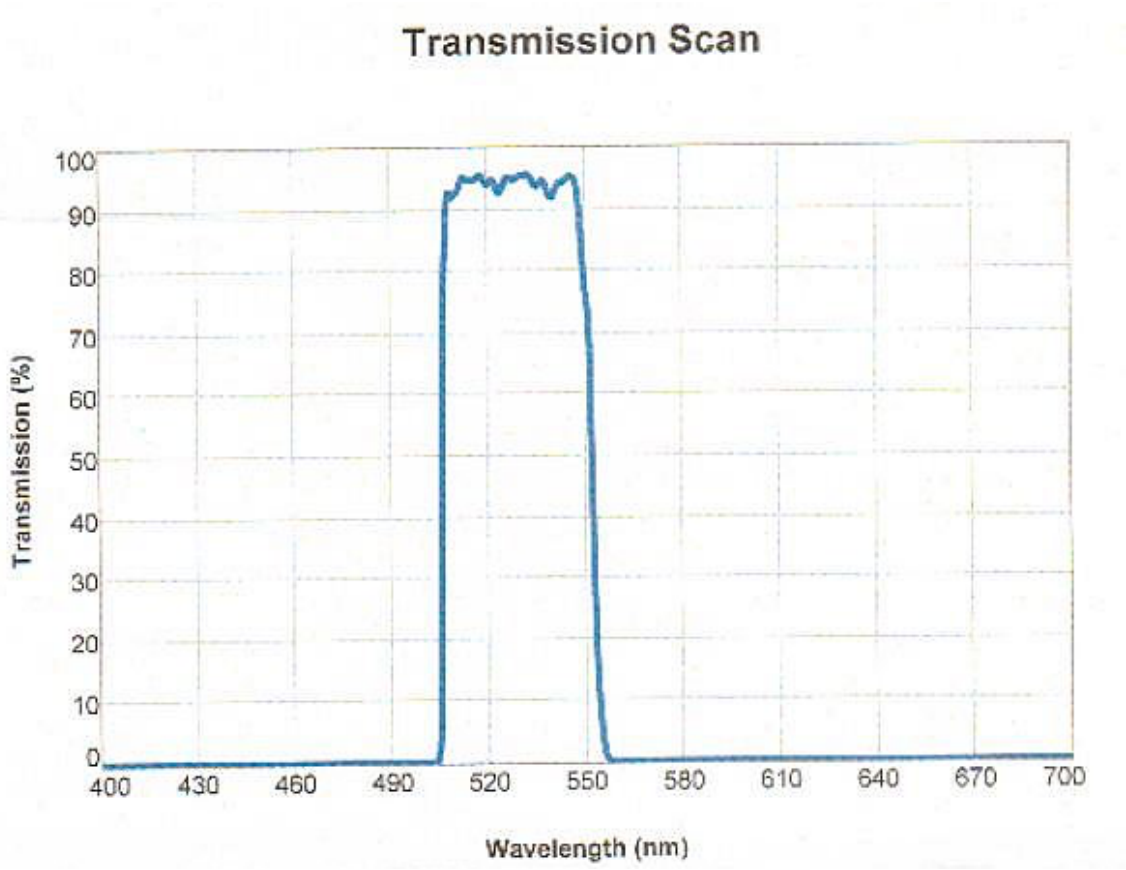

Transmission spectrum of the Semrock FF01-530/43 green filter (530 ± 20 nm)

A.3.3 Red filter

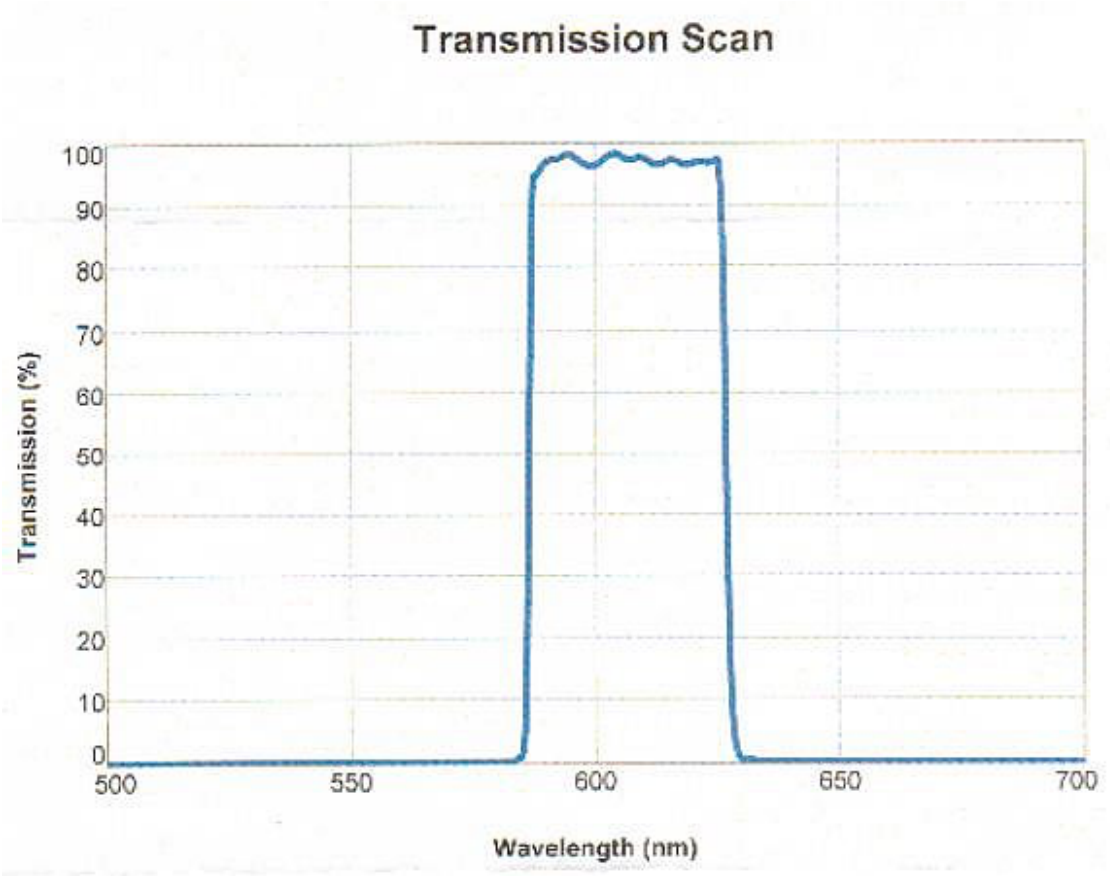

Transmission spectrum of the Semrock FF01-607/18 red filter (607 ± 18 nm)

APPENDIX B

Camera information

In this work it was particularly important to determine the effect of averaging an increasing number of images on the noise using different cameras. In this appendix, we examine this averaging effect, as well as the camera gain and linearity. In general, a camera image is made up of a 2-dimensional array of pixels, each obtaining a value related to the intensity at its specified location. The distribution of pixel values within the image result from a combination of the detected signal, systematic noise, and random noise. In our representation, we forgo an explicit description of the intensity and pixel values and coordinates, and represent the image and image components as,

$$I_0 = I_{\text{signal}} + I_{\text{syst.noise}} + I_{\text{rand.noise}}. \tag{B.0.1}$$

Two identical camera images, I_1 and I_2, differ only by random noise. It follows that we can construct an image displaying only random noise by subtracting I_2 from I_1 with,

$$\hat{I} = I_1 - I_2 = I_{(1)\text{rand.noise}} - I_{(2)\text{rand.noise}}. \tag{B.0.2}$$

B.1 PCO.edge 5.5

B.1.1 Noise

The PCO camera software can average up to 256 frames into a single image, so one could take into account both an "adjacent pair method (APM)" of averaging and an "adjacent set method (ASM)" of averaging. For a set of K captured images the APM

develops $L = K/2$ "noise images," denoted by $\hat{I}$, and each derived from the difference between one image and the subsequent image, such that $\hat{I} = I_{2K-1} - I_{2K}$. The average noise image, $\langle \hat{I} \rangle_L$, is then calculated from the L image-pair differences. Hence, the APM should be relatively insensitive to long term sensor drift. However, if there are any changes to the camera system during the time frame of image acquisition, we should be able to better observe their effect using the ASM. For a set of $K = 2L$ images, the ASM averages the first half of the images and relates this to the average of the second half by, $\langle \hat{I} \rangle_L = \langle I \rangle_{1...L} - \langle I \rangle_{L+1...K}$. I first set out how the noise is calculated for a pair of images, then will expand on the procedure for increasing numbers of images using both the APM and ASM. Additionally, I perform these measurements for both pixel readout speeds available on the PCO camera, namely 95 MHz, and 286 MHz.

For a single pair of images, the "noise image," $\hat{I}$, is calculated. The standard deviation, $\hat{\sigma}_1$, of the 2560 x 2160 pixels of $\hat{I}$, is then calculated. From $\hat{\sigma}_1$, the standard deviation, σ_1, of pixel values attributable to each of the image components $I_{(1)\,\text{rand.noise}}$ and $I_{(2)\,\text{rand.noise}}$ can be deduced as

$$\sigma_1 = \frac{\hat{\sigma}_1}{\sqrt{2}}. \tag{B.1.1}$$

Here, the subscript 1 indicates that the standard deviation is calculated over the difference of one pair of images. The read noise associated with the camera sensor was characterised using Eq. B.1.1, by capturing images after blocking the source of light to the camera. We refer to these images as dark images (DI). For a single pair of DI, we represent σ_1 with σ_R, with R indicating that this is the read noise of the sensor. We call images taken with light provided to the camera, bright images (BI). For a single pair of BI, the noise, $\bar{\sigma}_1$, is calculated as % fractional error, using σ_1 divided by μ_1, the average pixel value of the *background-subtracted* and *averaged* image, as

$$\bar{\sigma}_1 = 100 \cdot \frac{\hat{\sigma}_1}{\sqrt{2}\,\mu_1}, \tag{B.1.2}$$

where

$$\mu_1 = \frac{(I_1 + I_2) - (I_{BG1} + I_{BG2})}{2}. \tag{B.1.3}$$

Note, for DI we do not calculate the read noise as the % fractional error, since there is no signal by which to normalise the data.

The image noise was obtained via three methods: (1) APM and (2) ASM, both using captured images *without pre-averaging* by the PCO camera/software, and (3) APM using images generated by *pre-averaging* over 256 captured frames. For the available datasets, in (1) and (2) $L = 2^{\mathrm{N}}$, with N= 0…10, and in (3) $L = 2^{\mathrm{N}}$, with N= 0…5 when using BI, or N= 0…6 when using DI. Note in (3), as a result of pre-averaging over 256 frames prior to subtraction of adjacent images, a single "noise image" in (3) is equivalent to ASM at $L = 256$. Using the APM, the average noise image was calculated as,

$$\langle \hat{I} \rangle_{\mathrm{L}} = \frac{1}{L} \sum_{\mathrm{i}=1}^{L} (I_{2\mathrm{i}-1} - I_{2\mathrm{i}}), \tag{B.1.4}$$

and the standard deviation as in Eq. B.1.2 with,

$$\bar{\sigma}_{\mathrm{L}} = 100 \cdot \frac{\hat{\sigma}_{\mathrm{L}}}{\sqrt{2}\,\mu_{2\mathrm{L}}}. \tag{B.1.5}$$

The subscript L indicates that the standard deviation is calculated from $\langle \hat{I} \rangle_{\mathrm{L}}$, with $\langle \hat{I} \rangle_{\mathrm{L}}$ averaged over L image-pair differences. Using the ASM, the average "noise image" was calculated as,

$$\langle \hat{I} \rangle_{\mathrm{L}} = \sum_{\mathrm{i}=1}^{L} \frac{I_{\mathrm{i}}}{L} - \sum_{\mathrm{j}=\mathrm{L}+1}^{2\mathrm{L}} \frac{(I_{\mathrm{j}})}{L}, \tag{B.1.6}$$

and the standard deviation as in Eq. B.1.5.

For DI, $\langle \hat{I} \rangle_{\mathrm{L}}$ was calculated for APM and ASM as in Eq. B.1.4 and B.1.6. However, the read noise, σ_{R}, is calculated, as in Eq. B.1.1 using $\hat{\sigma}_{\mathrm{L}}$ with

$$\sigma_{\mathrm{R}} = \frac{\hat{\sigma}_{\mathrm{L}}}{\sqrt{2}}. \tag{B.1.7}$$

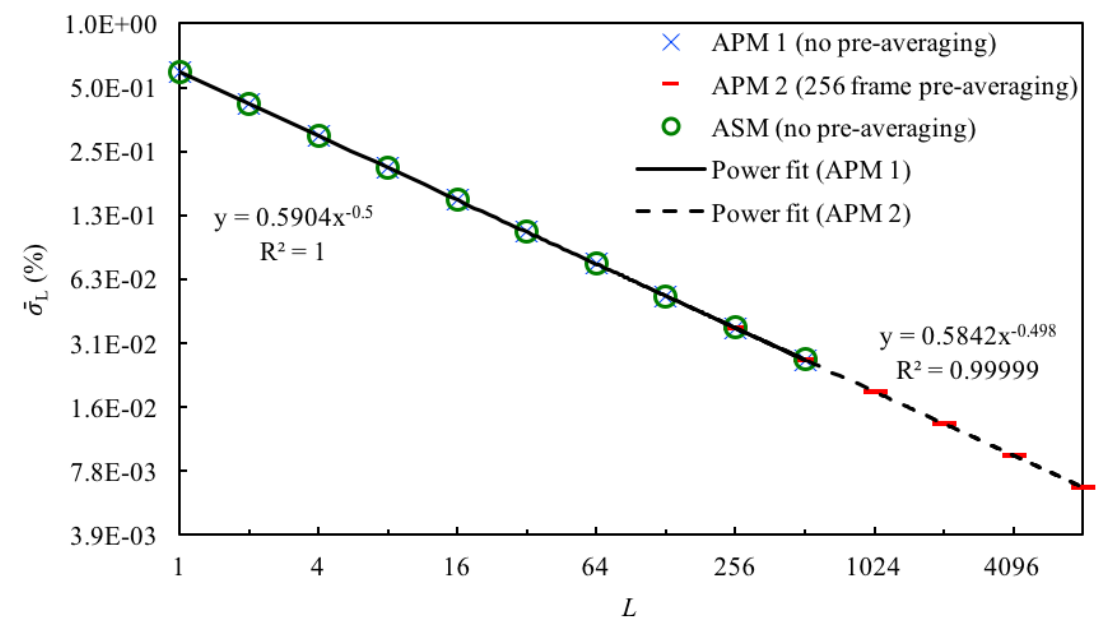

Fig. B.1: $\bar{\sigma}_L$ versus L, for the 286 MHz readout speed. Power law fits are given for the APM using (1) with and (2) without frame pre-averaging. Note: in the APM L corresponds to the number of "noise images" averaged, as in Eq. B.1.4, and in the ASM L corresponds to the number of images averaged per set before construction of the "noise image," as in Eq. B.1.6. Axes are Log_2-Log_2 format.

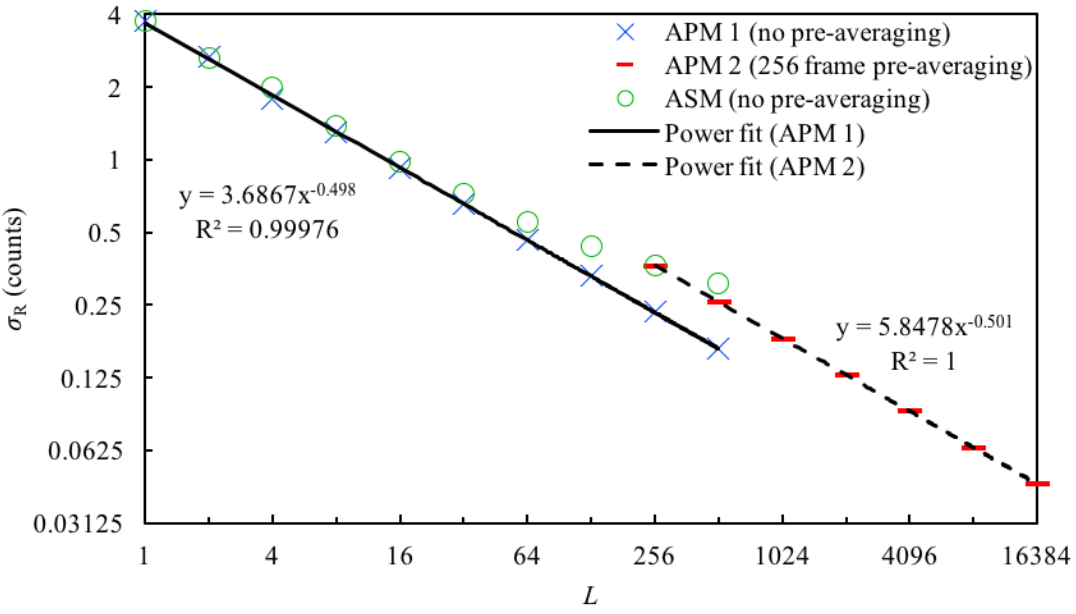

Fig. B.2: σ_R versus L. All else is as in Fig. B.1.

Fig. B.1 shows $\bar{\sigma}_{\mathrm{L}}$ for increasing L, using the 286 MHz readout speed. The frame rate was ~ 95 FPS (exposure time ~ 10.5 ms). Hence, 1024 images (512 "noise images") required a total acquisition time of ~ 10.75 seconds, and 16384 images (32 pre-averaged "noise images"), an acquisition time of ~ 172 seconds (not including the time to write the files to hard-disk). No significant difference between the three methods was apparent for BI (mean image intensity count was 53,146). Furthermore, via the power law fits, there was good agreement in all cases to the expected effect of averaging on standard deviation, i.e. that for an average over N images, the noise decreases as $\mathrm{N}^{-1/2}$.

σ_{R} associated with the PCO, was also characterised, as seen in Fig. B.2. The framerate, and hence acquisition times, were the same as those of the data in Fig. B.1. The APM without pre-averaging and APM with 256 frame pre-averaging both show power fits, which correspond to a $\mathrm{N}^{-1/2}$ decrease in the noise. However, there is a visible offset comparing the single acquisition APM to the 256 pre-averaged APM. The discrepancy between the APM and ASM data grows with an increasing number of averaged images. The origin of this discrepancy needs to be investigated further. It may be attributable to discretisation resulting from the averaging when σ_{R} is smaller than 1, as with σ_{R} by $L = 32$. However, it could be systematic, since the two sets in the ASM are not randomly selected, but chronological. Hence, as the set-size in the ASM grows, a disparity may develop between the first set and the second set. This would be a result of averaging over increasing numbers of images, which necessarily implies increased acquisition time per set. The 256 pre-averaging in the APM should exhibit a similar effect at the $L = 256$ datapoint. Note that the ASM data indeed overlaps the 256 pre-averaged APM data at the 256 image data point, as expected for either explanation of the offset. Given the power fit to the APM data *without* pre-averaging, $\sigma_{\mathrm{R}} = 0.0414$, can be expected for $L = 8192$, or $\sigma_{\mathrm{R}} = 0.0294$, for $L = 16384$. Note that for $L = 16384$, the 256 *pre-averaged* APM data gave $\sigma_{\mathrm{R}} = 0.0454$.

The noise analysis for the 95 MHz readout speed shows, generally, decreased shot noise and read noise, compared to the 286 MHz speed. In Fig. B.4, at $L = 8192$, $\sigma_{\mathrm{R}} = 0.054$ counts. This is ~ 8.5% lower than with the 286 MHz readout speed. Extrapolating the single acquisition APM data, a read noise as low as 0.0307 counts using $L = 8192$ could be expected. A similar offset, between the single acquisition data and pre-averaged

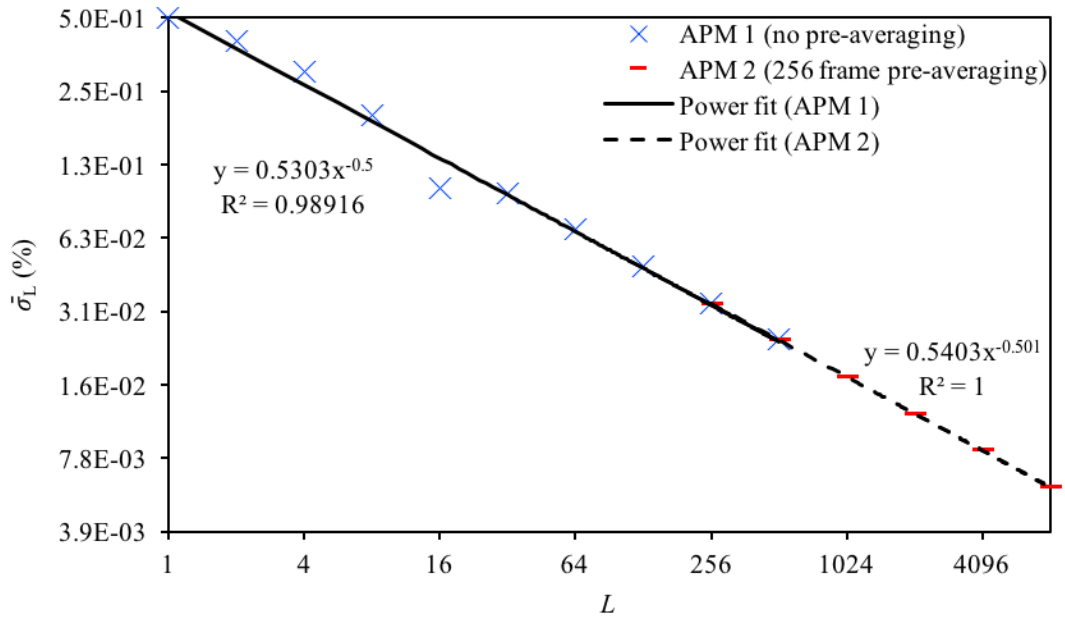

Fig. B.3: As in Fig. B.1 for the 95 MHz readout speed.

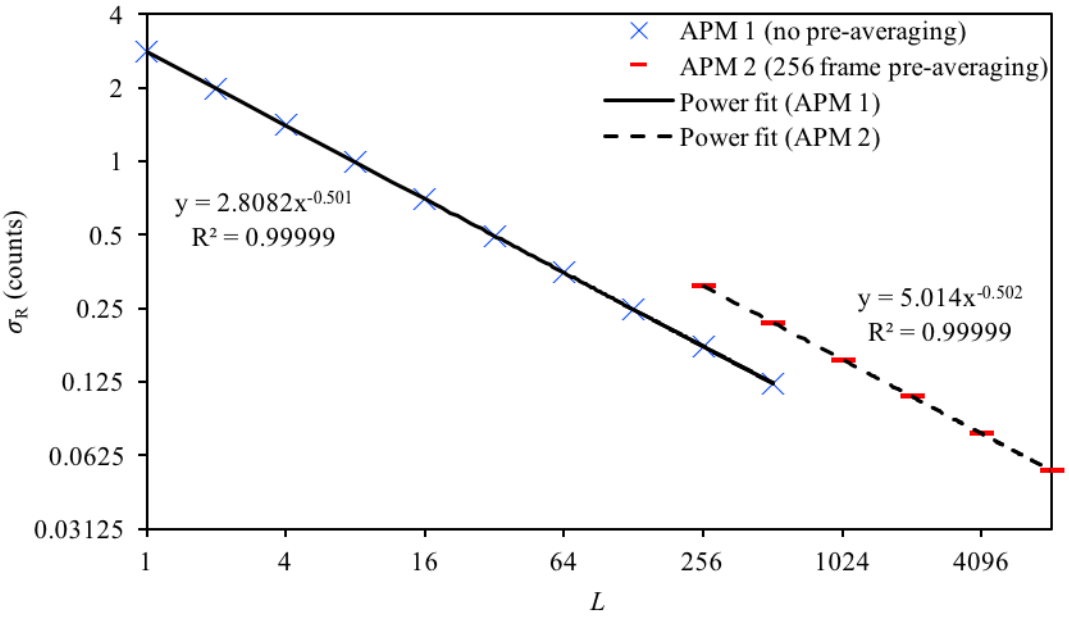

Fig. B.4: As in Fig. B.2 for the 95MHz readout speed.

data seen in Fig. B.2, is visible in Fig. B.4. In this case, the offset is slightly larger. This may support the hypothesis that the discrepancy is due to increased acquisition time of the sets in the ASM for large L, since the 95 MHz readout speed increases image

acquisition time by a factor of $286/95 \approx 3$.

B.1.2 Gain

In order to deduce the number of photoelectrons per count of the PCO sensor, one considers that the number of photoelectrons, N, is proportional to the number of counts P, times the gain, G. Hence, $N = P \cdot G$. Note that P includes a background offset, I will call B_{avg}. The standard deviation, $\bar{\sigma}_1$, of the pixel value of some image $(I_1 - I_2)$ is some combination of the shot noise (in pixel value count), σ_{S}, and the read-noise, σ_{R}. However, since the shot noise and read noise are independent of each other, they can be added in quadrature, hence

$$\bar{\sigma}_1^2 = \sigma_{\text{S}}^2 + \sigma_{\text{R}}^2 \tag{B.1.8}$$

Importantly, σ_{S} is related to the standard deviation of detected photoelectrons, σ_{E}, as N to P, so

$$\sigma_{\text{S}}\, G = \sigma_{\text{E}} \tag{B.1.9}$$

Since, shot noise follows a Poissonian distribution, we use $\sigma_{\text{E}} = \sqrt{N}$, and relate σ_{S} to N, by

$$\sigma_{\text{S}} = \frac{\sqrt{N}}{G} \tag{B.1.10}$$

Substituting Eq. B.1.10 into Eq. B.1.8 and rearranging, we find,

$$G^2\,(\bar{\sigma}_1^2 - \sigma_{\text{R}}^2) = \text{N} \tag{B.1.11}$$

Using μ_1 from above, i.e. the average pixel value of the background-subtracted and averaged image, and $N = P \cdot G$, we finally obtain,

$$G = \frac{\mu_1}{\bar{\sigma}_1^2 - \sigma_{\text{R}}^2} \tag{B.1.12}$$

The above is calculated using a single pair of BI and a single pair of DI. The gain, G, then has units of "per count", or photoelectron/count as needed.

The resulting value for the PCO sensor using the 286 MHz readout speed is, $G = 0.5421 \pm 0.02$ e^-/count, yielding the read noise in electrons of a single frame, $\sigma_{\text{R}} = 2.04\,\text{e}^-$. The software quoted value for this conversion factor is $G = 0.45\,\text{e}^-$/count, with $\sigma_{\text{R}} = 1.69\,\text{e}^-$. Using the 95 MHz readout speed, $G = 0.5754 \pm 0.02\,\text{e}^-$/count, yielding the

read noise in electrons of a single frame, $\sigma_R = 1.62\,e^-$. The software quoted value for this conversion factor is $G = 0.45\,e^-/\text{count}$, with $\sigma_R = 1.27\,e^-$.

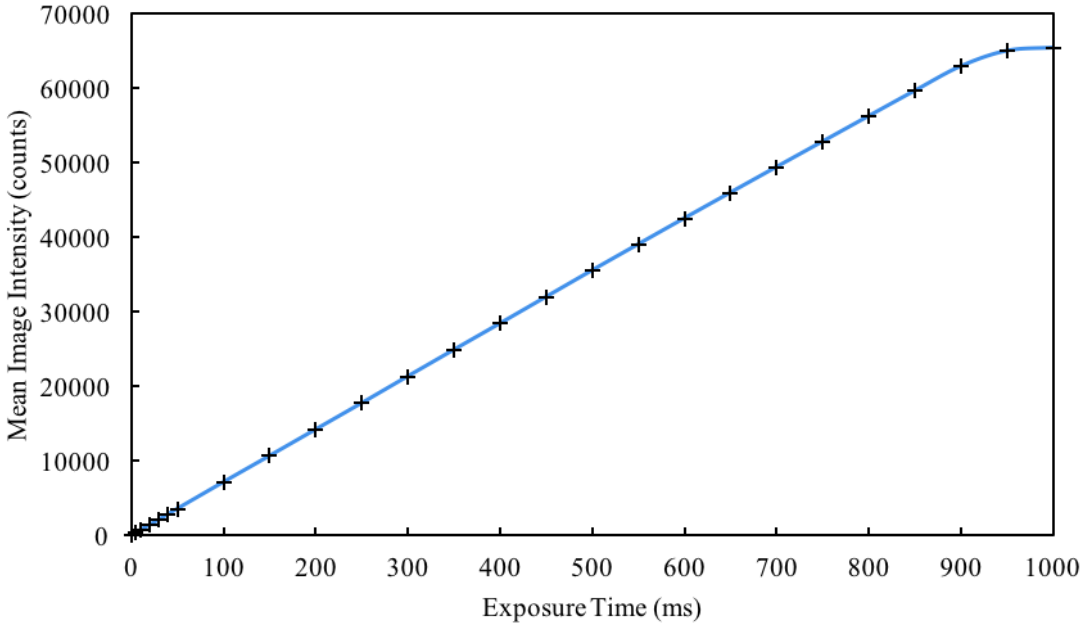

Fig. B.5: The mean image intensity is given as a function of exposure time at a given lamp setting, for the PCO. Axes scales are linear.

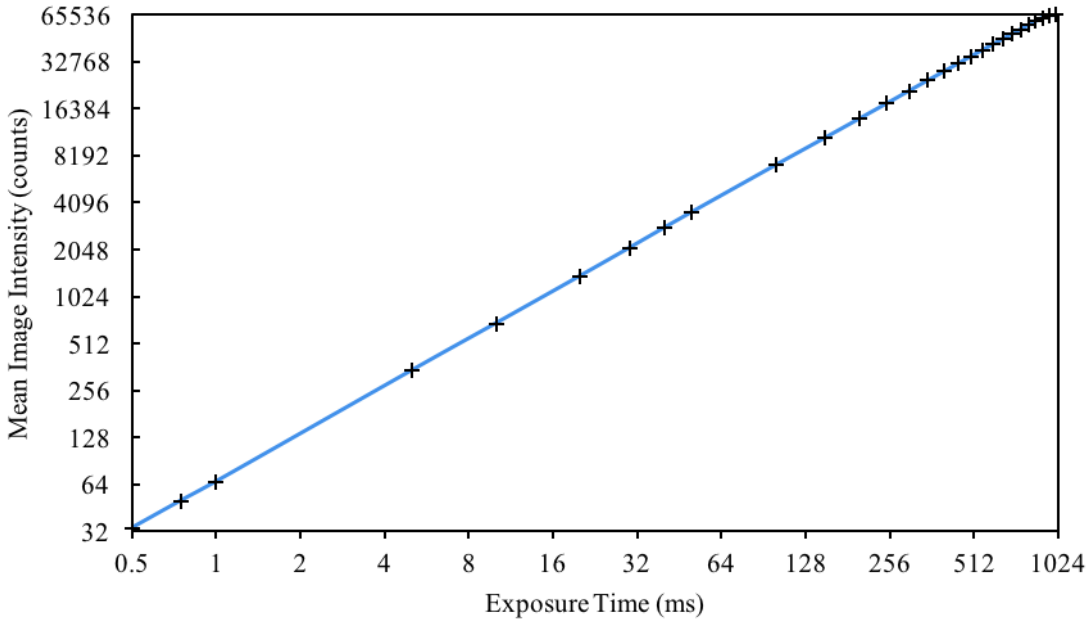

Fig. B.6: As in Fig. B.5, with Log_2-Log_2 axes.

B.1.3 Linearity

Fig. B.5 and Fig. B.6 show the camera response at different exposure times for a given lamp setting. Fig. B.5 uses linear axes and Fig. B.6 uses Log_2-Log_2 axes.

B.2 Canon 40D

The APM described in Sec. B.1.1, was also used to characterise the noise, and hence the gain, of the 40D, for ISO 100. The images are converted to 16-bit Tiffs using the half-size option of DCRAW Reader, as described in Sec. 4.2.4.2, recovering their 14-bit raw linear format. “Bright images" were taken using the LB200 filter at the 30 W lamp setting, which achieves similar intensity, and thus noise, in the R and B channels. Note, there are two green pixels, one red pixel, and one blue pixel, within the Bayer pixel of the camera, as described in Sec. 2.1.2. The 30 W lamp intensity was adjusted to obtain about $2^{13.45} \approx 11,200$ counts of the 2^{14} bit range, using 1/160 s shutterspeed.

B.2.1 Noise

Using BI, we obtain $\bar{\sigma}_{\text{L}} = (0.6652, 0.3488, 0.6497)\%$ for a single “noise image”, in the (R,G,B) channels. Averaging over 64 “noise images”, these values can be reduced to $\bar{\sigma}_{\text{L}} = (0.0834, 0.0437, 0.0813)\%$. Practically speaking, one could take up to 128 images with the 40D, leading to the best obtainable noise of $\bar{\sigma}_{\text{L}} = (0.0586, 0.0311, 0.0575)\%$.

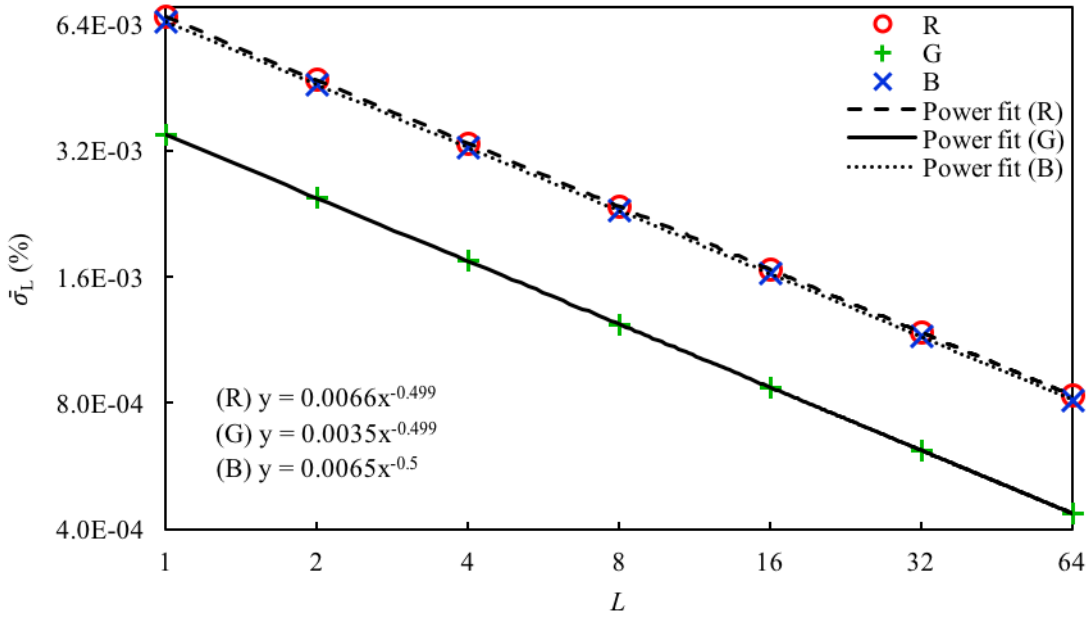

Fig. B.7: $\bar{\sigma}_L$ versus L, for the 40D. All data and fits are given for the APM. Axes are Log_2-Log_2 format.

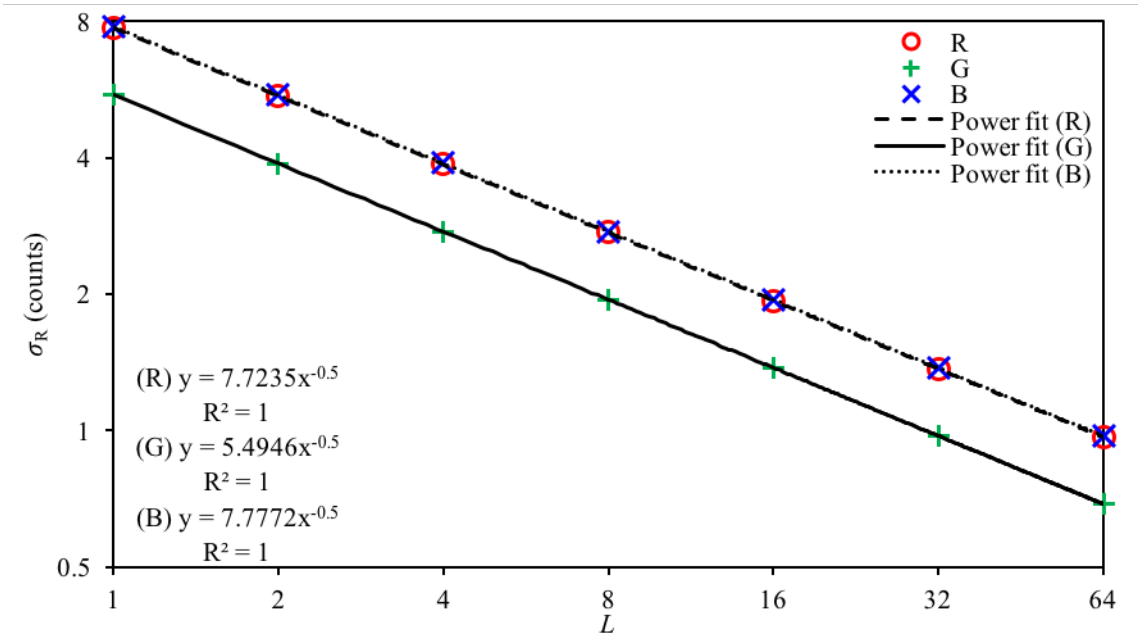

Fig. B.8: σ_R versus L, for the 40D. All else as in Fig. B.7.

For DI, we obtain $\sigma_R = (7.72, 5.49, 7.78)$ counts for a single image pair difference. Averaging over 64 image pair differences, these values can be reduced to $\sigma_R =$

(0.967, 0.688, 0.972) counts. Extrapolating to 128 images, leads to the best practically obtainable read noise with $\sigma_R = (0.683, 0.483, 0.687)$ counts.

B.2.2 Gain

The gain was calculated for each of the three channels, as in Sec. B.1.2. We find gain of factors of $G = (3.2623, 6.7256, 3.2006)\,e^-/\text{count}$, for the (R,G,B) colour channels, respectively. The G channel gain is ~ 2x larger than the R or B channel gain factors due to the additional green pixel.

B.2.3 Linearity

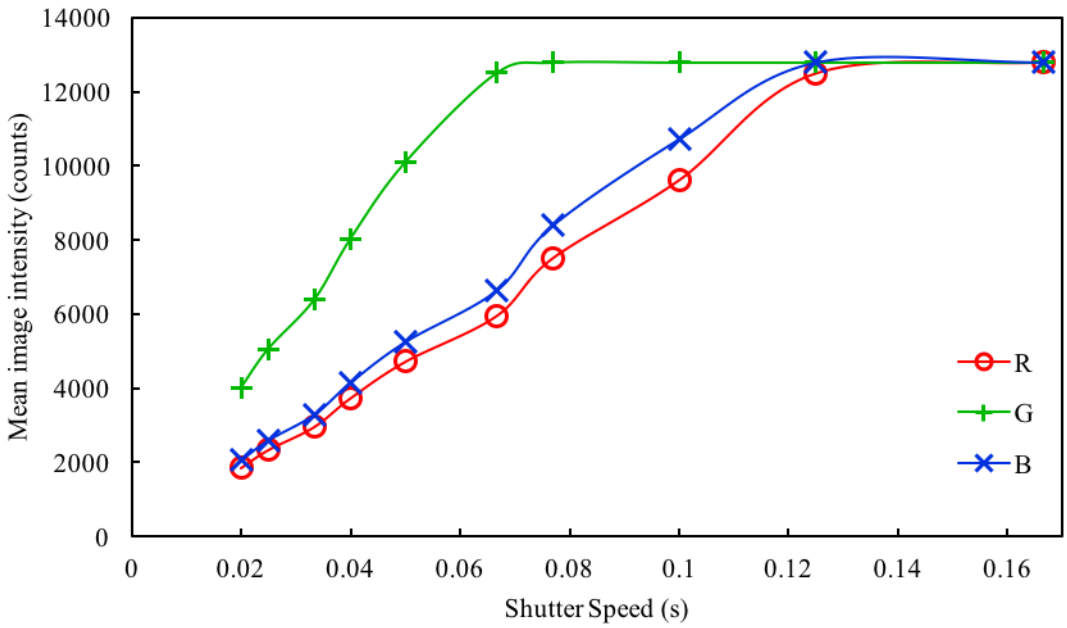

Fig. B.9: Mean image intensity versus exposure time at a given lamp setting, for the 40D. Axes scales are linear.

The background-subtracted sensor intensity (in counts) is shown for different exposure times, using the same lamp setting. The raw saturation occurs at 13824 counts. The DI background offset is approximately 1023 counts, leading to saturation, in Fig. B.9, of about 12800 counts. Note the G channel saturates first as a result of the

specific combination of the LB200 or NCB filters, the lamp output, and the 40D colour filters. The non-linear plot is attributed to inexact shutter speeds.

APPENDIX C

Chemistry protocols

C.1 Piranha (Caro's) etch

The Piranha etch portion of this was developed by Cardiff Biophotonics group member, Craig McPhee. In order to facilitate effective measurements of nanoparticles on standard coverslips and slides, glassware must be cleaned thoroughly to avoid high levels of debris. This cleaning is performed in two main stages, with a preliminary preparation.

C.1.1 Preparation

Before either cleaning stage is performed, the chemical etch is prepared in a fume hood, on a hot plate at ~ 100°C.

1. A large beaker (e.g. 2 L) is filled with ice water and set aside in the hood for emergency spills.

2. A shallow (30-40mm) flat-bottom dish is placed atop the hotplate, and filled about half full with water.

3. A beaker, which will contain the chemical cleaning agent, is placed into this dish for safety. The beaker most commonly used is a 100ml borosilicate glass beaker. The total reaction volume should be enough to cover a coverslip standing on-end (25mm), or enough to cover half of a microscope slide.

The chemical etch is called Caro's etch, or commonly Piranha etch, and is a mixture of sulphuric acid (H_2SO_4) and hydrogen peroxide (H_2O_2). We use a 1:3 or 1:4 mixture, where 1 part H_2O_2 is added to 3 (or 4) parts H_2SO_4. The hydrogen peroxide is a 30% solution, as purchased. It is a dangerous solution and this procedure should be followed with all necessary caution. Prior to the first stage of cleaning, the amount of sulphuric acid desired is added to the beaker in the safety dish on the hotplate. The hydrogen peroxide will be added after the first stage of cleaning, for safety purposes. 3 smaller beakers (e.g. 100ml or 200ml) should be kept to the side and filled with distilled water (we use Millipore 18M¡ de-ionized water). These beakers will be used to wash the coverslips and slides once removed from the piranha etch. Once all preparations have been made, the following steps are followed.

C.1.2 Stage 1

The slides are cleaned with acetone and high-quality cleanroom wipes. The wipe is dampened with acetone, and then both sides of any coverslips and slides are wiped, with pressure, several times. This is done to remove any large physical debris which may not be removed by the following chemical etch. The slides and coverslips are left aside on cleanroom wipe, on a flat surface. If they will be left for some time they are covered.

C.1.3 Stage 2

1. The pre-cleaned coverslips and slides from stage 1 are placed into a beaker (we find that about 5 will fit into the above beaker standing on-end and resting against the sidewalls of the beaker. They are left to stand on end so that both sides are cleaned.

2. At this point, the appropriate amount of hydrogen peroxide is added to the beaker. The solution may be delicately agitated by use of PTFE tweezers, in order to evenly distribute the hydrogen peroxide throughout the beaker.

3. The tweezers are removed, and immediately stirred in the large beaker of water,

to remove residual piranha etch.

4. The slides and coverslips are left in the beaker for ~ 10 minutes.

5. After this, each slide/coverslip is taken out and rinsed several times in each of the 3 beakers of distilled water.

6. The item is then dried with dry nitrogen and stored individually in a 50ml falcon tube. The process is repeated for each of the slides/coverslips.

If more than one batch is needed, the 1st stage of the cleaning can be performed on the subsequent batches while the 2nd stage is running on the previous one. Only one overall preparation need be done if the batches will all be cleaned in the same sitting.

Once finished, the piranha etch should be emptied in small volumes into the large beaker of water. For each volume of piranha solution emptied into the beaker, a large portion of the water in the beaker is poured down the sink (with faucet running). The large beaker should then be partially refilled with water. This process is repeated, until the piranha etch is poured away. All glassware should be rinsed several times with DI water to remove any residual piranha etch.

C.2 Glass functionalisation

C.2.1 Cleaning and Preparation

1. Clean all necessary glassware if not already done. This is preferably performed with sulphuric acid. Wash several times with water. Air dry in hood, or dry manually with N2.

   (a) 3 Beakers

   (b) 1 graduated cylinder PER nanoparticle sample (e.g. one for each different nominal size sample)

   (c) 1 small beaker (5ml) or graduated cylinder for silane-containing chemical dilution

(d) 1 glass petri dish PER prepared coverslip

(e) Coverslips should be cleaned via the Caro's etch method as outlined in Appendix C.1

2. Prepare 1 beaker or conical flask with water, 1 with toluene, and leave 1 empty for waste.

C.2.2 Glass Functionalisation

1. Make 1% solution of desired silane-containing compound, e.g. for bare metallic nanoparticles, use 3MT (stock 95%). 10 μl in 940 μl should be sufficient.

2. Perform the glass functionalization in coverslip-pairs. Mark one side of each glass coverslip with indelible ink. This side should NOT be functionalized. If the slide must be put down, e.g. on a clean piece of optics paper, place the marked side down.

3. Place a piece of clean optics paper on the tabletop. Place the marked side of one coverslip down on the paper. Put $\sim 15-20\,\mu$l of the diluted silane solution on the center of the slide. Move onto step 6) quickly.

4. Gently place the unmarked side of a second coverslip down onto the 1st. If necessary realign the sides of the two slides so that they are flush. Your solution should now be in between the slides and coating both unmarked sides simultaneously. Place a glass petri lid (need not be a cleaned dish) over the pair of slides. Add weight to help seal. Repeat for as many slides as you need.

5. Leave for 30 minutes at room temperature.

6. Once finished transfer any and all slides on optics paper into fume hood. Place toluene, water, and empty (waste) beaker into fume hood. Uncover slide pair. Take pair apart. Place one marked side down back onto the paper and recover. Hold free slide with Teflon tweezers.

7. Wash free slide several times with toluene (run-off should go into waste beaker).

8. Wash free slide several times with water (run-off should go into waste beaker).

9. Dry slide with N_2.

10. Place into falcon tube and fill tube with N_2.

11. Repeat for all slides. Empty waste beaker into fume hood sink as appropriate.

C.2.3 Nanoparticle binding

1. Prepare dilution of stock nanoparticle solution as necessary in graduated cylinder. Final volume should be 5ml or greater.

2. Place cleaned glass petri dish onto motorised tilt-table.

3. Remove a functionalized coverslip from the falcon tube and place in center of glass petri marked-side down.

4. Empty 5ml of diluted nanoparticle solution into petri dish. If necessary, push slide back down with Teflon tweezers. Cover petri dish with lid.

5. Turn on tilt-table to move slowly enough that water does not spill over the sides of the dish.

6. Leave for 1 hour, checking occasionally to make sure slide is still submerged.

7. Remove slide from dish with Teflon tweezers.

8. Wash both sides several times with water (run-off into waste beaker).

9. Dry in N_2, place back in falcon tube.

10. Place a glass slide (pre-cleaned via Caro's etch), onto support, such as a falcon tube cap so that the middle of slide is not in contact with any surface on either side. Place one drop ($\sim 10-20\,\mu$l) of immersion medium (e.g. silicone oil, or water), onto center of glass slide.

11. Remove nanoparticle-prepared coverslip from falcon tube. Gently place coated-side (unmarked- side) of the coverslip down onto the center of glass slide, being careful not to get bubbles.

12. Seal with clear nail varnish.

13. Empty wastes and excess chemicals into sink. Run tap briefly. Wash all glassware with DI water. Leave to air dry in hood.

APPENDIX D

Dimerisation protocols

D.1 Dimerisation procedure 1

The following protocols are written as a guide. The experimenter may determine which reaction volumes or dilutions he/she would prefer.

D.1.1 Materials

1. Cuvette for reference
2. Cuvette(s) for sample(s)
3. A few 1.5 ml Eppendorf tubes, as necessary, for dilutions and sample centrifugations.
4. 1 small beaker for 3-MT stock solution (unnecessary if not using toluene)
5. 1 flask/beaker for distilled (Millipore) water
6. 1 beaker for methanol
7. Solution are metallic nanoparticles (e.g. silver)
8. Solution/aliquots of silica-coated nanoparticles (e.g. coated silver NPs)
9. (1-10) μl pipette and tips

10. 100 μl or 200 μl (max) pipette and tips

11. 1000 μl (max) pipette and tips

D.1.2 Method

Main steps:

A Exchange solvents (water -> methanol)

B Thiolate Silica-coated silver nanoparticles (Si-AgNPs)

C Mix bare AgNPs and thiolated Si-AgNPs

1. Pipette desired volume of stock Si-AgNP solution into 1.5 ml Eppendorf tube.

   (a) 125 μl was chosen for many of my experiments. 125 μl is a half of an aliquot as provided by BBI.

2. Choose Concentration of (3-Mercaptopropyl)trimethoxysilane (3-MT) and prepare dilutions of 3-MT in methanol, which will be used to thiolate silica-coated particles. A suitable reaction volume must also be chosen at this point. 1000 μl or higher is suitable, although larger volumes lead to higher losses during centrifugation steps.

   (a) Stock 3-MT is given as 95%. With molecular weight 196.34 g/mol this gives molar concentration $4.84 \cdot 10^{-3}$ mol/ml.

   (b) The reaction volume for the thiolation step of this procedure, should have concentration of 3-MT on the order of 10^{-14} mol/ml, for NP concentrations on the order 10^{8} NP/ml. In this "thiolation" step, we do not wish to see a peak indicating dimerization (secondary right-shifted peaks), between Si-AgNPs. Hence, this concentration was chosen, because no dimer peak was observed, in contrast to higher concentrations. The experiment was performed at 30 C. For higher concentrations, peaks were observed within 10 minutes.

3. Centrifuge Eppendorf for 5min at 12000rcf (remember to balance centrifuge with blank Eppendorf if only making one sample.

4. Carefully, pipette supernatant (H2O) away and discard.

5. For 125 μl sample, $\sim$ 100 μl of supernatant could be safely removed without significantly effecting NP pellet.

6. Resuspend immediately in methanol to a volume equivalent to the desired reaction volume minus the volume of 3-MT solution which will be added, e.g. Final volume=1000 μl=25 μl (NP pellet) + 10 μl (3-MT)+965 μl (Methanol).

7. Sonicate for 5 minutes.

8. Add required volume of 3-MT dilution to reach desired reaction volume. Mix well and allow reaction to run for 30 minutes at room temp.

9. When the reaction is complete centrifuge sample at 12000 relative centrifugal force (rcf) for 5 minutes.

10. Immediately, and carefully, extract $\sim$ (975 – 980) μl supernatant and discard.

11. Immediately resuspend pellet in Millipore H2O.

12. Repeat steps 8-10 at least once to reduce presence of unbound 3-MT in sample. Final volume can be 500 μl. Repeating too many times will lead to losses in available Si-AgNP for dimerization.

13. Prepare a bare AgNP sample by adding 125 μl of stock bare AgNP solution to an Eppendorf tube. Then wash and resuspend in water as many times as was performed for the Si-AgNP sample to simulate the same losses due to washing. Final volume can be 500 μl.

14. Sonicate for 5 minutes.

15. Prepare cuvette with 500 μl Millipore H2O.

16. Add 500 μl thiolated Si-AgNP solution from step 11 to cuvette.

17. Prepare reference cuvette with water up to 1.5ml.

18. Follow guidelines of Qpod and spectrasuite procedure as recently outlined, and reference the water control cuvette in spectrometer.

19. Remove water control cuvette, and place the cuvette with Si-AgNPs from step 14 in cuvette holder.

20. Running in Absorption mode, instruct SpectraSuite to save every scan (each averaged over 1000) for an extended period, e.g. 30 minutes.

21. Quickly, add the bare AgNP sample from step 12 to the cuvette in the holder. Mix well (you can use the magnetic stirrer here to continue mixing over duration of observation).

22. During the observation period (or before step 16) prepare a solution of N-ethylmaleimide, (N-EM). This solution should lead to final concentration of N-ethylmaleimide on the order of 10^2 times (or more) that of 3-MT used in the thiolation reaction.

    (a) N-ethylmaleimide is stored as a powder and so must be aliquoted by the experimenter at his/her discretion.

23. Once, a dimer peak is seen, one should be prepared to act quickly and add the N-EM to the cuvette to prevent further aggregation. Continue recording scans until no change is seen in the absorption.

D.2 Dimerisation Procedure 2

D.2.1 Materials

1. Cuvette for reference

2. Cuvette(s) for sample(s)

3. A few 1.5 ml Eppendorf tubes, as necessary, for dilutions and sample centrifugations.

4. 1 small beaker for 3-MT stock solution if desired (unnecessary if not using toluene)
5. 1 flask/beaker for distilled (Millipore) water
6. 1 beaker for methanol
7. Solution of metallic nanoparticles (e.g. silver)
8. Solution/aliquots of silica-coated nanoparticles (e.g. coated silver NPs)
9. (1-10) μl pipette and tips
10. 100 μl or 200 μl (max) pipette and tips
11. 1000 μl (max) pipette and tips

D.2.2 Method

Main Steps:

A Prepare reference cuvette and sample cuvette

B Prepare methanol + 3-MT solution

C Add 3-MT preparation to sample cuvette and observe via spectrometer

1. Pipette desired volume of stock Si-AgNP solution into cuvette.
   (a) 250 μl was chosen for many of my experiments. 250 μl is a full aliquot as provided by BBI.
2. Pipette desired volume of stock bare AgNP solution into cuvette.
   (a) A matching volume was chosen here as concentrations should be on the same order for particles of the same metallic-core size and material.
3. Add at least 1.5ml of Millipore H2O to fresh cuvette to act as reference.

4. Prepare methanol solution of 3-MT. Remember that the final reaction volume must be at least 1.5ml.

    (a) Concentration here was considerably higher than in protocol 1, on the order of 10^{-8} or 10^{-9} mol/ml. Positive results were only seen for gold NP and the secondary peak appeared within 3-10 minutes.

    (b) Silver NP showed a continually broadening and right-shifting peak, indicating mass aggregation or perhaps degradation of the silver by the higher levels of 3-MT. Perhaps lower levels may be used with silver, with longer reaction times.

5. Add necessary volume of H2O to bring cuvette reaction volume to desired amount, minus that of 3-MT solution, which will be added during observation. From steps 1, 2, and 4, one will now be able to calculate the volume of water needed, and that of 3-MT solution, to bring the reaction volume to the desired amount in the cuvette.

6. Reference the water control cuvette in spectrometer.

7. Begin absorption mode and place sample cuvette in chamber.

8. Begin continuous save mode of SpectraSuite, for an extended period.

9. While measuring absorption, add necessary volume of 3-MT solution, mix well. Use magnetic stirrer for continuous mixing.

10. During the observation period (or before step 6) prepare a solution of N-ethylmaleimide, (N-EM). This solution should lead to final concentration of (N-EM) on the order of 10^2 times (or more) that of 3-MT used in the thiolation reaction.

    (a) N-EM is stored as a powder and so must be aliquoted by the experimenter at his/her discretion.

11. Once, a dimer peak is seen, you should be prepared to act quickly and add the N-EM to the cuvette to prevent further aggregation. Continue recording scans until no change is seen in the absorption.

D.3 Dimerisation Procedure 3

Note: This procedure is technically unfinished, so the following will require further work in understanding how to get the functionalised particles back into solution in water. Observation of dimerisation has at this point produced no results. There could be several advantages to this technique. Since, toluene is highly anhydrous, vortexing/sonication of the H2O suspended particles, with toluene-dissolved 3-MT, should allow an anhydrous micro-environments (micro-droplets) for silane-binding to silica shells. Furthermore, the 3-MT will remain in solution in toluene, potentially preventing unbound 3-MT from occurring in final water-based suspension of functionalised particles. The toluene can then be easily extracted since it remains separate from the water after sonication/vortexing ends.

D.3.1 Materials

1. Cuvette for reference
2. Cuvette(s) for sample(s)
3. A few 1.5 ml Eppendorf tubes, as necessary, for dilutions and sample centrifugations.
4. 1 small beaker for 3-MT stock solution if desired
5. One, glass, 5 ml or 10ml graduated cylinder.
6. 1 flask/beaker for distilled (Millipore) water
7. 1 glass beaker for toluene
8. Solution of metallic nanoparticles (e.g. silver)
9. Solution/aliquots of silica-coated nanoparticles (e.g. coated silver NPs)
10. $(1-10)\,\mu$l pipette and tips
11. $100\,\mu$l or $200\,\mu$l (max) pipette and tips
12. $1000\,\mu$l (max) pipette and tips

D.3.2 Method

Main Steps:

A Prepare toluene + 3-MT solution

B Thiolate Si-AgNPs

C Extract Toluene solution

1. Pipette desired volume of stock Si-AgNP solution into graduated cylinder.
    (a) 250 μl was chosen for many of my experiments. 250 μl is a full aliquot as provided by BBI.
2. Add some volume of Millpore H2O to increase the reaction volume.
3. Prepare toluene solution of 3-MT.
    (a) The concentration here should be high, since a high proportion of the toluene-dissolved 3-MT will bind directly to the sides of the glass graduated cylinder. A 1% solution was chosen for my experiments, where the volume to be added was about 1/4 of the volume of water in the cylinder.
4. Add volume of toluene/3-MT solution to graduated cylinder.
    (a) A 1/4 volume of toluene/3-MT solution to Si-AgNP/H2O solution was used here.
5. Close graduated cylinder with parafilm.
6. Vortex 1 minute and observe; check for remaining color in H2O. Repeat until H2O is clear.
7. Sonicate for 5 minutes.

At this point in the procedure, the particles will be functionalized. Many will have stuck to the surface of the graduated cylinder via silane-silane interaction. However, in experiments thus far, the functionalized particles appear to have developed a semi-non-polar nature, and thus, sit at the boundary of the H2O/toluene suspension. Solving this problem is the next step for this procedure at this time.

APPENDIX E

AgNP dimerisation

E.1 Dimerisation procedure 1 comments

The major difference between the dimerisation techniques and the glass functionalisation discussed in Sec. 3.2, is that the dimerisation takes place in the liquid phase. The interactions in the previous case, involved 3MT, glass and metallic NPs. The 3MT was dissolved in toluene, and then allowed to bind to the glass. The toluene was removed, and the sample dried. The NPs were then added, and allowed to bind to the free thiol groups. In this case, we wish to functionalise, either the bare Au samples, or the SiO_2-coated NP samples, with 3MT, directly in suspension. However, toluene is not soluble in water. So we must either transfer the NPs to a new medium, or find another solvent for 3MT. The main logic of the first procedure is then as follows: exchange SiO_2-coated NP solvent, functionalise SiO_2-shells with 3MT, add bare particles to mixture and observe reaction progress with the spectrometer.

In order to facilitate solvent exchange, the NPs were centrifuged, and the water-supernatant discarded. Initially, toluene was tested as possible resuspension medium for the pelleted NPs. However, both bare and SiO_2-coated NPs remained in the water fraction, and did not fall into suspension in toluene, regardless of agitation by vortexing or sonication. Thus, toluene was not viable. DMSO was also tested, since it can dissolve 3MT, and is miscible in water. However, DMSO was observed to have a destructive, or oxidative effect on the NPs. This is most likely due to the presence of a high concentration of sulphur in the medium. Silver is well known to tarnish as a result of

oxidation by sulphur. Furthermore, both DMSO and toluene dissolved to some extent the plastic cuvettes used for the spectroscopy experiments. As a result, methanol was settled upon, as it is miscible in water and can dissolve 3MT. It showed no damaging effects on the NPs, and caused no noticeable damage to the cuvettes.

Once solvent exchange was accomplished, a 3MT dilution, prepared in methanol, was added to the NP-methanol suspension, and allowed to incubate for about 30 minutes. The mixture was centrifuged and the solvent re-exchanged for water, to make sure excess 3MT was removed. The newly water-resuspended, and functionalised SiO_2-NPs were first sonicated for 5 minutes, and then moved to a cuvette, ready for observation. Separately, a dilution of bare-NPs was prepared. Typically, this bare-NP dilution would be put through the same centrifugation and washing steps as the functionalised SiO_2-NPs to simulate the losses experienced in those steps. Thus, in principle the mixture should involve roughly equivalent concentrations of bare- and SiO_2-coated NPs. Prior to mixing the two suspensions and observing the reaction, we must acquire a proper reference spectrum. In this case, the reference spectrum was that of distilled water. As close as possible to the time the referencing was finished, the cuvette containing the functionalised NPs was placed in the holder. The SpectraSuite software was instructed to save every scan for an extended period, e.g. 30 minutes, and then the bare-NPs were added. The reaction was then monitored. Initial experiments did not involve the blocking agent, as we wanted simply to confirm the appearance of a dimer peak.

E.2 Dimerisation procedure 3 comments

This method is an incomplete method, and only relevant to silver-based samples. It is presented only as a promising technique for future dimerisation studies. In this method, 3MT is dissolved in toluene and added directly to a suspension of SiO_2-NPs in water. As stated in Sec. 3.3.1.1, toluene and water do not mix. However by vortexing the mixture, the NPs can become functionalised, when they pass through the 3MT-toluene solution.

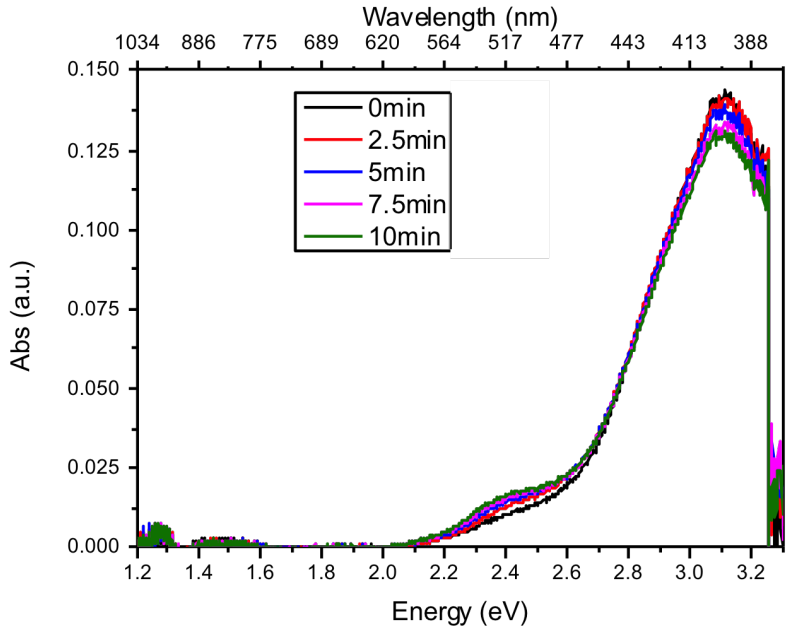

Fig. E.1: Absorption spectra resulting from dimerisation reaction using method 1. Mixture is bare AgNPs plus 6 nm shell SiO_2-NPs.

E.3 AgNP Dimers

E.3.0.1 Method 1 results

Method 1 was only used with AgNPs, due to time limitations and lack of AuNP availability early on. It produced potentially promising results, summarised in Fig. E.1-E.7. We first present the absorption spectra of the mixture of bare-NPs with 6 nm shell SiO_2-NPs as measured by the OO setup in Fig. E.1. As discussed in Sec. 1.1.3[8], the formation of a silver NP dimer manifests as a coupled longitudinal plasmon, more red shifted compared to the isolated particle LSPR. With a 6 nm interparticle gap distance and a 40 nm Ag core diameter the shifted LSPR is expected to be greater than 70 nm. To emphasize the observation of a second red-shifted peak, Fig. E.2 presents $A_{\Delta 0}(t,\lambda)$ for various times t, after the addition of bare particles to the solution containing functionalised silica-coated NPs. Notice the growth of the second peak around 520 nm, and the corresponding loss of the single particle signal around 390 nm. Furthermore, that there is a third contribution to the spectrum, around (435-440) nm, masked by the depleted single particles. In order to expose this peak, we performed a subtraction with a

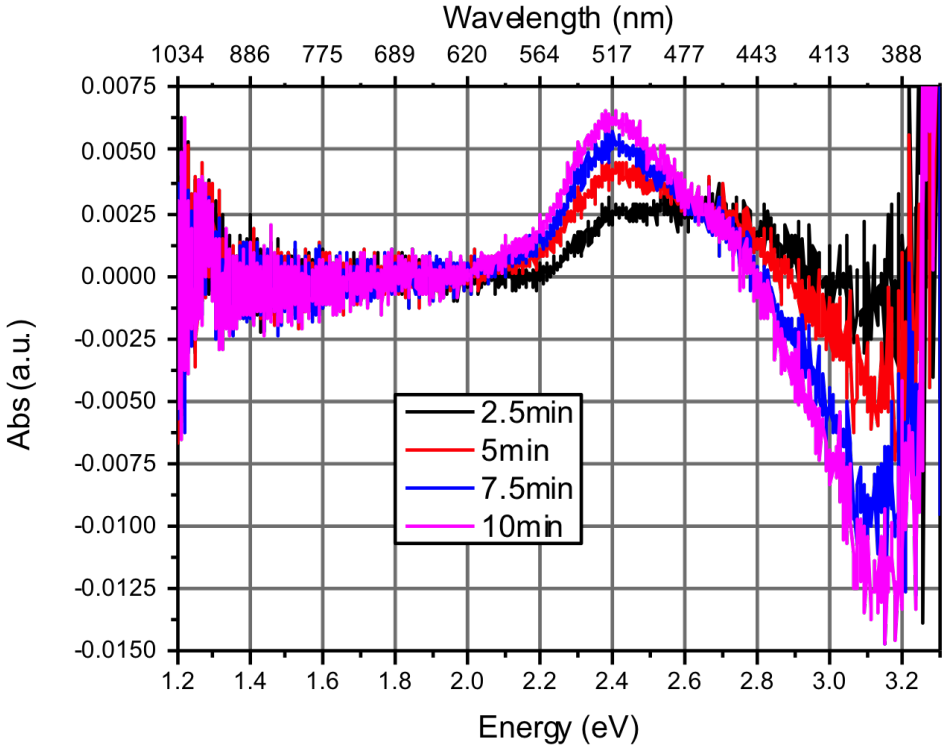

Fig. E.2: $A_{\Delta 0}(t,\lambda)$ for various times t for bare-NPs dimerised with 6 nm shell SiO_2-NPs using method 1.

multiplicative factor compensating for the single particle losses. We represent this as,

$$A_\Delta(t,\lambda) = A(t,\lambda) - \frac{A(0,\lambda)\,A(t,\lambda_a v)}{A(0,\lambda_a v)}, \tag{E.3.1}$$

with $A(t,\lambda_a v)$ an average over a small range of λ, around the position of the single particle LSPR peak. For bare 40 nm AgNPs in water, this average was taken over (390-410) nm. Fig. E.3-E.7 present A_Δ for binding experiments using different SiO_2 shell thicknesses, at various times, t. The multiple peaks were fitted with the function, $\cosh^{-2}$, to determine peak positions. $\cosh^{-2}$ was chosen as a compromise between the sharper peak and broader tails of a Lorentz lineshape, and the broader peak and fast decaying tails of a Gaussian. Using this fit, we determined that the strong secondary peak, occurring around 520 nm, differed by only a few nanometers for the different shell-size experiments. The smaller secondary peak, originally masked by the single particle depletion, moved from ~ 434 nm with ~ 20 nm shell thickness to ~ 443 nm with ~ 6 nm shell thickness. Thus, we see an increasing red-shift for decreasing shell thickness (gap size) as expected[48]. We attribute the peak around 520 nm, to binding of bare

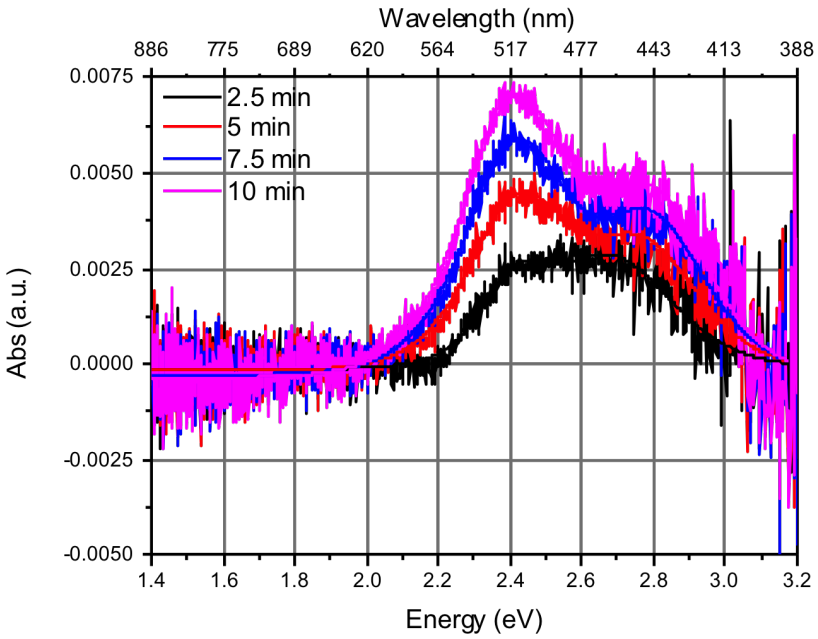

Fig. E.3: $A_\Delta(t,\lambda)$ for various times t for bare-NPs dimerised with 6 nm shell SiO_2-NPs using method 1.

particles to bare particles. Any free 3MT still left in solution can bind via thiol to the bare particles, and the silanes can polymerise as described in Sec. 3.1, allowing nearby bare particles to bind.

Though promising, these results were not reproducible in later attempts. We have no clear explanation for this. One possibility is that the bare-SiO_2-coated dimers represent only a weakly bound state, present due to hydrogen bonding. There is no "curing" step allowing the permanent binding of the silanes to the SiO_2-coating of the NPs in suspension. Conversely, it is possible that the bare-bare binding is permanent, because covalent polymerisation is possible in solution, as well as the thiol-metal bond.

E.3.0.2 Method 2 results

The first method was discontinued, as we were unable to replicate the positive early results. Method 2 was adopted, with the view of more efficiently using the NP material available, by avoiding the multiple time consuming, and lossy steps, of solvent exchange. It was used for both silver and gold NPs. The results of this method were

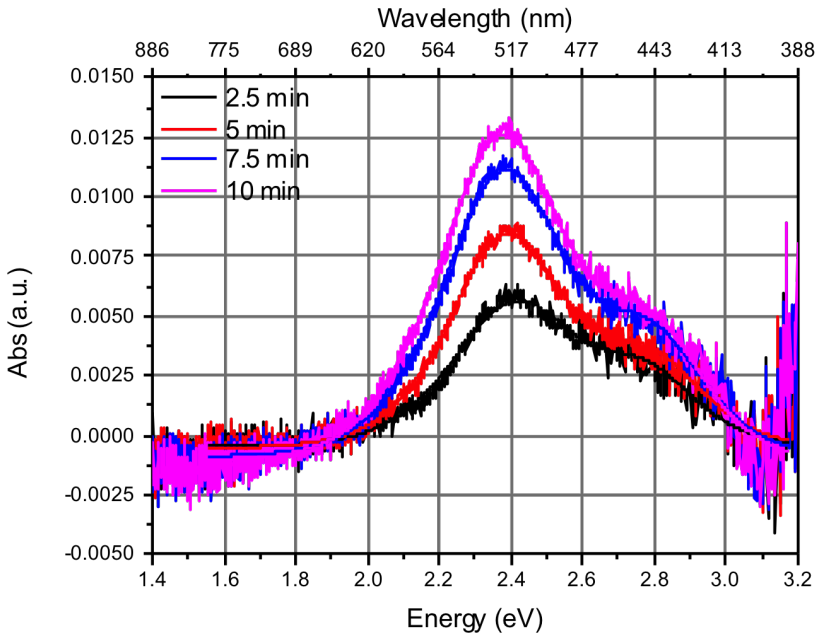

Fig. E.4: $A_\Delta(t,\lambda)$ for various times t for bare-NPs dimerised with 10 nm shell SiO_2-NPs using method 1.

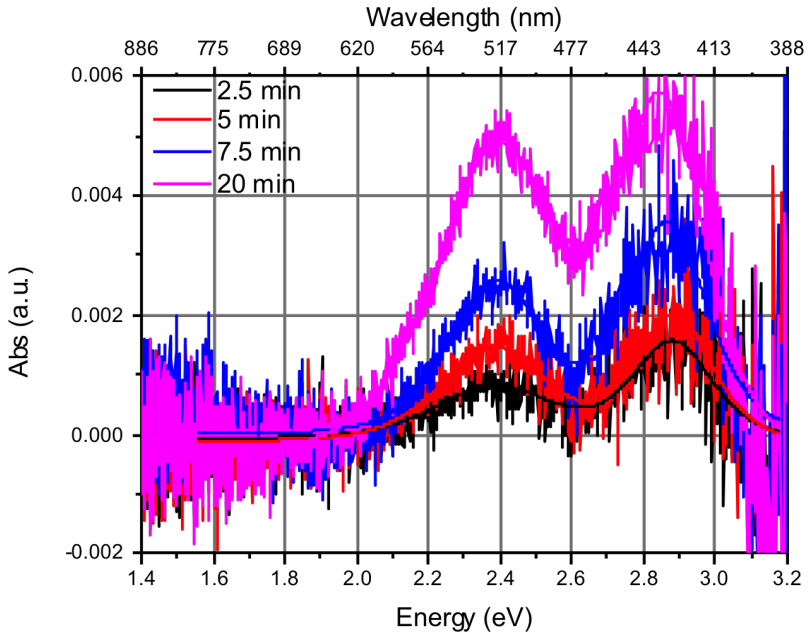

Fig. E.5: $A_\Delta(t,\lambda)$ for various times t for bare-NPs dimerised with 12 nm shell SiO_2-NPs using method 1.

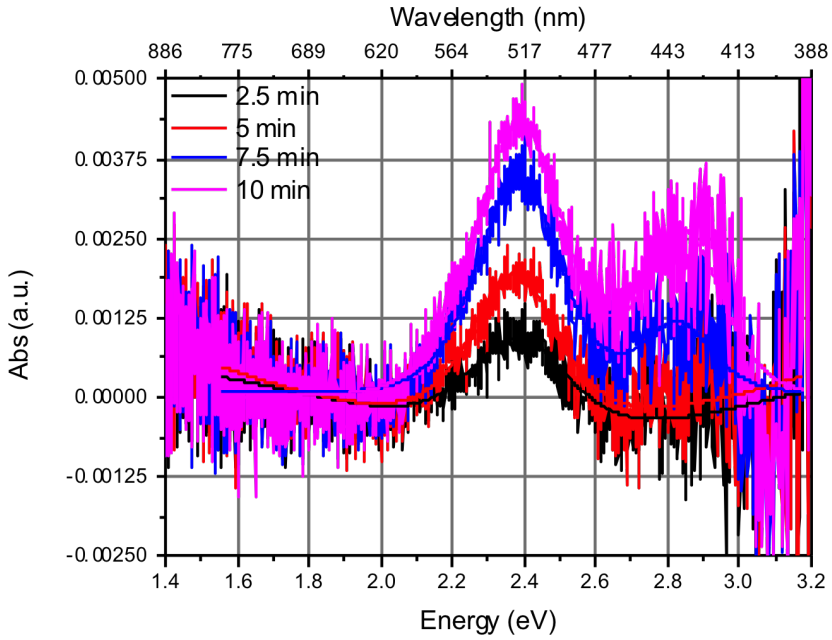

Fig. E.6: $A_\Delta(t,\lambda)$ for various times t for bare-NPs dimerised with 17 nm shell SiO_2-NPs using method 1.

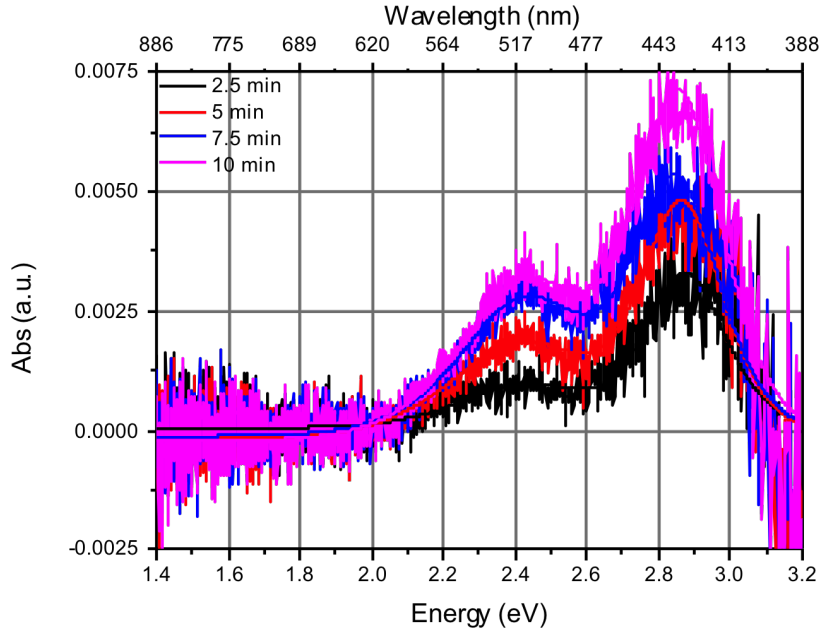

Fig. E.7: $A_\Delta(t,\lambda)$ for various times t for bare-NPs dimerised with 20 nm shell SiO_2-NPs using method 1.

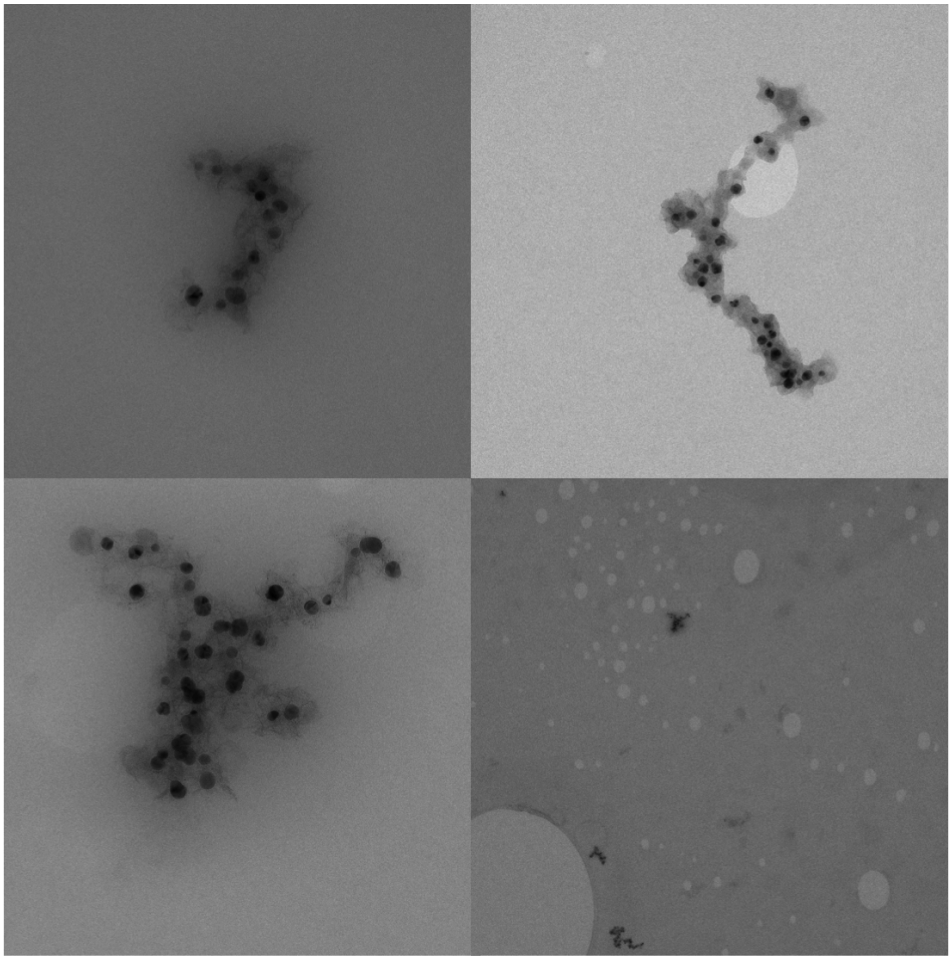

Fig. E.8: TEM images of aggregates of SiO_2-AgNPs formed using method 2.

unclear for silver NPs. Absorption spectroscopy indicated development of dimers, but TEM studies on these samples indicated mass aggregation. Furthermore, almost no single NPs, or small aggregates, appeared to be left in the sample. We attribute this to possible oxidation of Ag by excessive thiols in solution. TEM images of the silver NP samples developed using this method can be seen in Fig. E.8. Notice that only SiO_2-coated NPs are left, and they seem to have aggregated by polymerisation, as the silica surrounding them seems to be continuous. TEM samples are prepared using a small, copper grid, over which is laid a layer of pioloform. A drop of NP solution is added to this pioloform and allowed to dry. The clear aggregation of SiO_2-coated NPs could be due to the solidification of silane-silica bonds during the drying step of the TEM preparation. It does not explain why only large aggregates are left, however. Due to

complications with silver NPs, focus was shifted more strongly to gold NPs.

E.3.0.3 Method 3 results

This method was conceived after obtaining the information in Fig. 3.1 and Fig. 3.2. The assumption had been that the silane-silica bond would form even in solution. The glass functionalisation procedure side-stepped this issue, since the 3MT solvent was toluene, which is very (a) hydrophobic, and (b) volatile. So, even if atmospheric water was available to the coverslips for hydrolytic deposition, the toluene dried out quickly, providing the necessary "curing" step to form covalent bonds. That is to say, whether or not the glass functionalisation procedure was hydrolytic or anhydrous was irrelevant, because the coverslips had the opportunity to dry. If we apply this thinking to the functionalisation of SiO_2-NPs in suspension, then it becomes necessary for the NPs to be functionalised in a non-aqueous environment. This is possible with toluene.

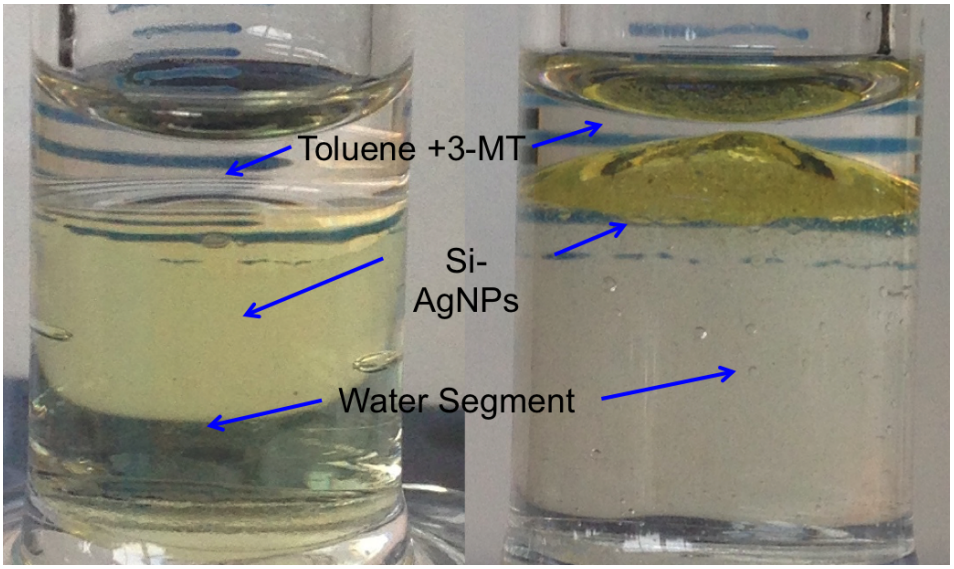

Fig. E.9: Images of SiO_2-coated AgNPs before (left) and after (right) mixing with 3MT, dissolved in toluene. After mixing, the SiO_2 coated AgNPs appear along a boundary between H_2O and toluene.

Fig. E.9 shows the effect of mixing two suspensions; one of SiO_2-NPs in water, and one of 3MT dissolved in toluene. The idea here is that if we agitate this mixture enough, the NPs will physically encounter the 3MT/toluene solution even if they do not remain in

that phase. During this time, an NP will experience a hyrdophobic micro-environment in which it can be functionalised by 3MT. This effect is seen clearly in Fig. E.9. Furthermore, when emptied, the graduated cylinder has a permanent yellow-ish ring indicating that the cylinder itself had been functionalised, and had NPs bound to it during vortexing. Unfortunately, this method was not carried beyond this point, because it was unclear how to get the functionalised SiO_2-NPs back into suspension in water. Notice how the yellow color is condensed at the boundary between the toluene and water after reaction. The advantage of this method is that the 3MT remains dissolved only in toluene, thus if the NPs could be forced back into water-suspension, there would be no excess 3MT causing unwanted binding, oxidation, or aggregation of AgNPs. Method 3 could be a promising start for future attempts at dimerisation of AgNPs.

References

[1] W.L. Barnes, A. Deraux, and T.W. Ebbesen. Surface plasmon subwavelength optics. *Nature*, 424:824–830, 2003.

[2] K. Awazu, M. Fujimaki, C. Rockstuhl, J. Tominaga, H. Murakami, Y. Ohki, N. Yoshida, and T. Watanabe. A plasmonic photocatalyst consisting of silver nanoparticles embedded in titanium dioxide. *J. Am. Chem. Soc.*, 130:1676–1680, 2008.

[3] H.A. Atwater and A. Polman. Plasmonics for improved photovoltaic devices. *Nat. Mater.*, 9:205–213, 2010.

[4] L. Cognet, S. Berciaud, D. Lasne, and B. Lounis. Photothermal methods for single nonluminescent nano-objects. *Analytical Chemistry*, 80:2288–2294, 2008.

[5] F. Masia, W. Langbein, P. Watson, and P. Borri. Resonant four-wave mixing of gold nanoparticles for three-dimensional cell microscopy. *Opt. Lett.*, 34:1816–1818, 2009.

[6] K. Kneipp, H. Kneipp, I. Itzkan, R.R. Dasari, and M.S. Feld. Surface-enhanced raman scattering and biophysics. *J. Phys.: Condens. Matter*, 14:R597–R624, 2002.

[7] A.D. McFarland and R.P. Van Duyne. Single silver nanoparticles as real-time optical sensors with zeptomole sensitivity. *Nano Lett.*, 3:1057–1062, 2003.

[8] C. Sönnichsen, B.M. Reinhard, J. Liphardt, and A.P. Alivisatos. A molecular ruler based on plasmon coupling of single gold and silver nanoparticles. *Nature Biotech.*, 23:741–745, 2005.

[9] L. Moore, E.K. Chow, E. Osawa, Bishop J.M., and D. Ho. Diamond-lipid hybrids enhance chemotherapeutic tolerance and mediate tumor regression. *Advanced Materials*, 25(26):3532–3541, 2013.

[10] A.N. Hegyi and E. Yablonovitch. Nanodiamond imaging: a new molecular imaging approach. *Conf Proc IEEE Eng Med Biol Soc.*, 2012.

[11] N. de Jonge and F.M. Ross. Electron microscopy of specimens in liquid. *Nature Nanotech.*, 6(11):695–704, 2011.

[12] B.R. Smitha, M. Niebertc, T. Plakhotnika, and A.V. Zvyagin. Transfection and imaging of diamond nanocrystals as scattering optical labels. *J. Lumin.*, 127:260–263, 2007.

[13] E. Perevedentseva *et al.* The interaction of the protein lysozyme with bacteria *E. coli* observed using nanodiamond labelling. *Nanotechnology*, 18(315102), 2007.

[14] L. Cognet, C. Tardin, D. Boyer, D. Choquet, P. Tamarat, and B. Lounis. Single metallic nanoparticle imaging for protein detection in cells. *Proceedings of the National Academy of Sciences of the United States of America*, 100(20):11350–11355, 2003.

[15] S. Berciaud, D. Lasne, G.A. Blab, L. Cognet, and B. Lounis. Photothermal heterodyne imaging of individual metallic nanoparticles: Theory versus experiment. *Phys. Rev. B*, 73(045424):1–8, 2006.

[16] D. Lasne, G.A. Blab, F.D. Giorgi, F. Giorgi, F. Ichas, B. Lounis, and L. Cognet. Label-free optical imaging of mitochondria in live cells. *Optics Express*, 15(21):14184–14193, 2007.

[17] I. Pope, L. Payne, G. Zoriniants, E. Thomas, O. Williams, P. Watson, W. Langbein, and P. Borri. Coherent anti-stokes raman scattering microscopy of single nanodiamonds. *Nat Nano*, 9(11):940–946, 2014.

[18] F. Masia, W. Langbein, P. Watson, and P. Borri. Triply surface-plasmon resonant four-wave mixing imaging of gold nanoparticles. *Proc. of SPIE*, 7911(79910Y):1–7, 2011.

[19] M. Hu, C. Novo, A. Funston, H. Wang, H. Staleva, S. Zou, P. Mulvaney, Y. Xia, and G.V. Hartland. Dark-field microscopy studies of single metal nanoparticles: understanding the factors that influence the linewidth of the localized surface plasmon resonance. *J. Mater. Chem.*, 18(17):1949–1960, 2008.

[20] A. Arbouet, D. Christofilos, N. Del Fatti, F. Vallée, J.R. Huntzinger, L. Arnaud, P. Billaud, and M. Broyer. Direct measurement of the single-metal-cluster optical absorption. *Physical Review Letters*, 93(127401), 2004.

[21] David J. Griffiths. *Introduction to Electrodynamics*. Prentice Hall, Upper Saddle River, New Jersey, U.S.A, 3 edition, 1999.

[22] E. Hecht. *Optics*. Addison Wesley, 1301 Sansome St., San Francisco, CA 94111, U.S.A, 4 edition, 2002.

[23] M. Pelton and G.W. Bryant. *Introduction to Metal-Nanoparticle Plasmonics*. A Wiley-Science Wise Co-Publication. Wiley, 2013.

[24] M. Dienerowitz, M. Mazilu, and K. Dholakia. Optical manipulation of nanoparticles: a review. *Journal of Nanophotonics*, 2:021875, 2008.

[25] K.L. Kelly, E. Coronado, L.L. Zhao, and G.C. Schatz. The optical properties of metal nanoparticles: the influence of size, shape, and dielectric environment. *The Journal of Physical Chemistry B*, 107(3):668–677, 2003.

[26] C. Noguez. Optical properties of isolated and supported metal nanoparticles. *Optical Materials*, 27:1204–1211, 2005.

[27] C. Sönnichsen. *Plasmons in metal nanostructures*. PhD thesis, Ludwig-Maximilians-University of Munich, 2001.

[28] M.A. van Dijk, A.L. Tchebotareva, M. Orrit, M. Lippitz, S. Berciaud, D. Lasne, L. Cognet, and B. Lounis. Absorption and scattering microscopy of single metal nanoparticles. *Phys. Chem. Chem. Phys.*, 8:2486–3495, 2006.

[29] G.V. Hartland. Optical studies of dynamics in noble metal nanostructures. *Chemical Reviews*, 111:3858–3887, 2011.

[30] J. Olson, S. Dominguez-Medina, A. Hoggard, L-Y. Wang, W-S. Chang, and S. Link. Optical characterization of single pasmonic nanoparticles. *Chem Soc Rev*, 44:40–57, 2014.

[31] C.F. Bohren and D.R. Huffman. *Absorption and scattering of light by small particles*. Wiley Science. John Wiley and Sons, New York, 1982.

[32] M. van Dijk. *Nonlinear-optical studies of single gold nanoparticles*. PhD thesis, Universiteit Leiden, 2007.

[33] N.W. Ashcroft and N.D. Mermin. *Solid State Physics*. Harcourt, Inc., New York, New York, U.S.A, 1976.

[34] F. Masia, W. Langbein, P. Watson, and P. Borri. Measurement of the dynamics of plasmons inside individual gold nanoparticles using a femtosecond phase-resolved microscope. *Phys. Rev. B*, 85(235403):1–11, 2012.

[35] P. Johnson and R. Christy. Optical constants of the noble metals. *Physical Review B*, 6(12):4370–4379, 1972.

[36] M.A. Ordal, L.L. Long, R.J. Bell, S.E. Bell, R.R. Bell, R.W. Jr. Alexander, and C.A. Ward. Opticl properties of the metals al, co, cu, au, fe, pb, ni, pd, pt, ag, ti, and w in the infrared and far infrared. *Applied Optics*, 22(7):1099–1119, 1983.

[37] A.D. Rakić, A.B. Djurišic, J.M. Elazar, and M.L. Majewski. Optical properties of metallic films for vertical-cavity optoelectronic devices. *Applied Optics*, 37:5271–5283, 1998.

[38] C. Sönnichsen, T. Franzl, T. Wilk, G. von Plessen, and J. Feldmann. Drastic reduction of plasmon damping in gold nanorods. *Physical Review Letters*, 88(7):077402–1 to 077402–4, 2002.

[39] S. Thomas, S.K. Nair, E. Muhammad Abdul Jamal, S.H. Al-Harthi, Manoj Raama Varma, and M.R. Anantharaman. Size-dependent surface plasmon resonance in silver silica nanocomposites. *IOP Nanotechnology*, 19(075710):7, 2008.

[40] U. Kreibig and M. Vollmer. *Optical Properties of Metal Clusters*, volume 25 of *Springer Series in Materials Science*. Springer-Verlag Berlin Heidelberg, Berlin, Germany, 1 edition, 1995.

[41] H. Su, Y. Li, X. Li, and K. Wong. Optical and electrical properties of au nanoparticles in two-dimensional networks: an effective cluster model. *Optical Society of America*, 17(24):22223–22234, 2009.

[42] O.A. Yeshchenko, I.M. Dmitruk, A.A. Alexeenko, A.V. Kotko, J. Verdal, and A.O. Pinchuk. Size and temperature dependence of the surface plasmon resonance in silver nanoparticles. *Ukr. J. Phys.*, 57(2):266–277, 2012.

[43] S.K. Mandal, R.K. Roy, and A.K. Pal. Surface plasmon resonance in nanocrystalline silver particles embedded in sio2 matrix. *Journal of Physics D: Applied Physics*, 35:2198–2205, 2002.

[44] A. Moroz. Depolarization field of spheroidal particles. *J. Opt. Soc. Am. B*, 26(3):517–527, 2009.

[45] A. Tcherniak, J.W. Ha, S. Dominguez-Medina, L.S. Slaughter, and S. Link. Probing a century old prediction one plasmonic particle at a time. *Nano Lett.*, 10:1398–1404, 2010.

[46] I. Zoric, M. Zach, B. Kasemo, and C. Langhammer. Gold, platinum, and aluminum nanodisk plasmons: Material independence, subradiance, and damping mechanisms. *Nano Lett.*, 5(4):2535–2546, 2011.

[47] T. Atay, J-H. Song, and A.V. Nurmikko. Strongly interacting plasmon nanoparticle pairs: From dipole-dipole interaction to conductively coupled regime. *Nano Lett.*, 4(9):1627–1631, 2004.

[48] P.K. Jain, W. Huang, and M.A. El-Sayed. On the universal scaling behavior of the distance decay of plasmon coupling in metal nanoparticle pairs: A plasmon ruler equation. *Nano Lett.*, 7(7):2080–088, 2007.

[49] J-W. Liaw, H-Y. Tsai, and C-H. Huang. Size-dependent surface enhanced fluorescence of gold nanorod: Enhancement or quenching. *Plasmonics*, 7(3):543–553, 2011.

[50] M.Y. Tsvetkov, B. Khlebtsov, E. Panfilova, V.N. Bagratashvili, and N.G. Khlebtsov. Gold nanorods as a perspective technology platform for sers analytics. *Russian Journal of General Chemsitry*, 83(11):2203–2211, 2012.

[51] M. Li, S.K. Cushing, J. Zhang, J. Lankford, Z.P. Aguilar, D. Ma, and N. Wu. Shape-dependent surface-enhanced raman scattering in gold–raman- probe–silica sandwiched nanoparticles for biocompatible applications. *Nanotechnology*, 23(115501):10, 2012.

[52] I. Romero, J. Aizpurua, G.W. Bryant, and F. Garcia de Abajo. Plasmons in nearly touching metallic nanoparticles: singular response in the limit of touching dimers. *Optics Express*, 14(21):9988–9999, 2006.

[53] X. Ben and H.S. Park. Size-dependent validity bounds on the universal plasmon ruler for metal nanostructure dimers. *The Journal of Physical Chemistry C*, 116(35):18944–18951, 2012.

[54] Peter E. Powers. *Fundamentals of Nonlinear Optics*. CRC Press, Taylor and Francis Group, LLC, 6000 Broken Sound Parkway NW, Suite 300, Boca Raton, Fl 33487, U.S.A, 2011.

[55] C. Buil. Canon 40d, 50d, 5d, 5d mark ii comparison. http://www.astrosurf.com/buil/50d/test.htm, 2015.

[56] J.J. Brehm and W.J. Mullin. *Introduction to the Structure of Matter*. Wiley, 1989.

[57] G.B. Rybicki and A.P. Lightman. *Radiative processes in astrophysics*. Wiley, 1979.

[58] OceanOptics. How does my choice of spectrometer slit size affect optical resolution? http://oceanoptics.com/faq/choice-slit-size-affect-resolution/, 2015.

[59] Inc. BWTEK. Part 5: Spectral resolution. http://bwtek.com/spectrometer-part-5-spectral-resolution/, 2015.

[60] Department of Chemistry. Procedure on handling and using acid piranha solution. *Cambridge Chemistry SOP*, 2011.

[61] G. Zoriniants, F. Masia, L. Payne, W. Langbein, and P. Borri. Three-dimensional nanometric position accuracy with single-point detection four-wave mixing interferometry. *Nature (awaiting submission)*, 2015.

[62] B. Arkles. Hydrophobicity, hydrophilicity hydrophobicity, hydrophilicity, and silanes. http://www.gelest.com/goods/pdf/Library/advances/ Hydrophobicity-HydrophilicityandSilanes.pdf, 2006.

[63] A. Kasry, P. Borri, P.R. Davies, A. Harwood, N. Thomas, S. Lofas, and T. Dale. Comparison of methods for generating planar dna-modified surfaces for hybridization studies. *Applied Materials and Interfaces*, 1(8):1793–1798, 2009.

[64] R.J. Martin-Palma, M. Manso, J. Perez-Rigueiro, J.P. Garcia-Ruiz, and J.M. Martinez-Duart. Surface biofunctionalization of materials by amine groups'. *Journal of Materials Research*, 19(08):2415–2420, 2004.

[65] D.H. Buckley. Auger analysis of oxygen and sulfur interactions with various metals and the effect of sliding on these interactions. *National Aeronautics and Space Administration*, NASA Technical Note(D-7340):24, 1973.

[66] J.A. Rodriguez and J. Hrbek. Interaction of sulfur with well-defined metal and oxide surfaces: Unraveling the mysteries behind catalyst poisoning and desulfurization. *Accounts of Chemical Research*, 32(9):719–728, 1999.

[67] A. Cozic, E. Viollier, J-F Chiffoleau, J. Knoery, and E. Rozuel. Interactions between volatile reduced sulfur compounds and metals in the seine estuary (france). *Estuaries and Coasts*, 31(6):1063–1071, 2008.

[68] C. Chi, F. Vargas-Lara, A.V. Tkachenko, F.W. Starr, and O. Gang. Internal structure of nanoparticle dimers linked by dna. *ACS Nano*, 6(8):6793–6802, 2012.

[69] L. Piantanida, D. Naumenko, and M. Lazzarino. Highly efficient gold nanoparticle dimer formation via dna hybridization. *RSC Adv.*, 4:15281–15287, 2014.

[70] H. Wang and N.J. Halas. Plasmonic nanoparticle heterodimers in a semiembedded geometry fabricated by stepwise upright assembly. *Nano Lett.*, 6(12):2945–2948, 2007.

[71] G. Zoriniants and W.L. Barnes. Fluorescence enhancement through modified dye molecule absorption associated with the localized surface plasmon resonances of metallic dimers. *New Journal of Physics*, 10(105002):12, 2008.

[72] T-J Yim, Y. Wang, and X. Zhang. Synthesis of a gold nanoparticle dimer plasmonic resonator through two-phase-mediated functionalization. *Nanotechnology*, 19(435605):6, 2008.

[73] Life Technologies. Pierce nem (n-ethylmaleimide). https://www.lifetechnologies.com/order/catalog/product/23030, 2015.

[74] L.J.E Anderson, K.M. Mayer, R.D. Fraleigh, Yi Yang, S. Lee, and J.H. Hafner. Quantitative measurements of individual gold nanoparticle scattering cross sections. *J. Phys. Chem. C*, 114:11127–11132, 2010.

[75] O.L. Muskens. Optical extinction spectrum of a single metal nanoparticle: Quantitative characterization of a particle and of its local environment. *Phys. Rev. B*, 78:205410, 2008.

[76] A. Crut, P. Maioli, N. Del Fatti, and F. Vallée. Optical absorption and scattering spectroscopies of single nano-objects. *Chem Soc Rev*, 43(11):3921–56, 2014.

[77] M. Husnik, S. Linden, R. Diehl, J. Niegemann, K. Busch, and M. Wegener. Quantitative experimental determination of scattering and absorption cross-section spectra of individual optical metallic nanoantennas. *Physical Review Letters*, 109(233902), 2012.

[78] P. Kukura, M. Celebrano, A. Renn, and V. Sandoghdar. Single-molecule sensitivity in optical absorption at room temperature. *J. Phys. Chem. Lett.*, 1(23):3323–3327, 2010.

[79] M. Celebrano, P. Kukura, A. Renn, and V. Sandoghdar. Single-molecule imaging by optical absorption. *Nature Photonics*, 5:95–98, 2011.

[80] L.M. Payne, W. Langbein, and P. Borri. Polarization-resolved extinction and scattering cross-sections of individual gold nanoparticles measured by wide-field microscopy on a large ensemble. *Applied Physics Letters*, 102(13), 2013.

[81] S.K. Friedlander. *Smoke, Dust, and Haze: Fundamentals of Aerosol Dynamics*. Topics in chemical engineering. Oxford University Press, Inc., 2 edition, 2000.

[82] L. Payne, G. Zoriniants, F. Masia, K.P. Arkill, P. Verkade, D. Rowles, W. Langbein, and P. Borri. Fd2015-single molecule microscopy: Optical micro-spectroscopy of single metallic nanoparticles: Quantitative extinction and transient resonant four-wave mixing. *Faraday Discuss.*, 2015.

[83] D. Coffin. Decoding raw digital photos in linux. http://www.cybercom.net/~dcoffin/dcraw/, 2015.

[84] wikipedia. Bayer filter. https://en.wikipedia.org/wiki/Bayer_filter, 2004.

[85] L. Payne. Extinction suite macro (v3.2.4.7) for imagej (2011-2015). http : //langsrv.astro.cf.ac.uk/Crosssection/Extinction_Suite/Extinction_Suite.html, 2013.

[86] R.L. Rich and D.G. Myszka. Higher-throughput, label-free, realt-time molecular interaction analysis. *Analytical Biochemistry*, 361(1):1–6, 2007.

[87] B. Liedberg, C. Nylander, and I. Lundstrom. Surface plasmon resonance for gas detection and biosensing. *Sensors and Actuators*, 4:299–304, 1993.

[88] G. Mie. Beitrage zur optik truber medien, speziell kolloidaler metallosungen. *Annalen der Physik*, 330:377–445, 1908.

[89] D.D. Evanoff Jr. and G. Chumanov. Synthesis and optical properties of silver nanoparticles and arrays. *ChemPhysCem*, 6:1221–1231, 2005.

[90] D.D. Evanoff Jr. and G. Chumanov. Size-controlled synthesis of nanoparticles. 2. measurement of extinction, scattering, and absorption cross sections. *J. Phys. Chem. B*, 108:13957–13962, 2004.

[91] N.C. Bigall, T. Hartling, M. Klose, P. Simon, and L.M. Eng. Monodisperse platinum nanospheres with adjustable diameters from 10 to 100 nm: Synthesis and distinct optical properties. *Nano Lett.*, 8(12):4588–4592, 2008.

[92] C. Langhammer, Z. Yuan, and B. Kasemo. Plasmonic properties of supported pt and pd nanostructures. *NL*, 6(4):833–838, 2006.

[93] R.C. Johnson, J. Li, J.T. Hupp, and G.C. Schatz. Hyper-rayleigh scattering studies of silver, copper, and platinum nanoparticle suspensions. *Chemical Physical Letters*, 356:534–540, 2002.

[94] S.W. Hell. Far-field optical nanoscopy. *Science*, 316:1153–1158, 2007.

[95] S.W. Hell and J. Wichmann. Breaking the diffraction resolution limit by stimulated emission: Stimulated-emission-depletion fluorescence microscopy. *Opt. Lett.*, 19(11):780–782, 1994.

[96] E. et al. Betzig. Imaging intracellular fluorescent proteins at nanometer resolution. *Science*, 313:1642–1645, 2006.

[97] M.J. Rust, M. Bates, and X. Zhuang. Sub-diffraction-limit imaging by stochastic optical reconstruction microscopy (storm). *Nature Methods*, 3:793–795, 2006.

[98] J. Fölling, M. Bossi, H. Bock, R. Medda, C.A. Wurm, B. Hein, S. Jakobs, C. Eggeling, and S.W. Hell. Fluorescence nanoscopy by ground-state depletion and single-molecule return. *Nature Methods*, 5:943–945, 2008.

[99] T. Yanagida, Y. Sako, and S. Minoghchi. Single-molecule imaging of egfr signalling on the surface of living cells. *Nature Cell Biology*, 2(3):168–172, 2000.

[100] E. Betzig and J.K. Trautman. Near-field optics: Microscopy, spectroscopy, and surface modification beyond the diffraction limit. *Science*, 257:189–195, 1992.

[101] E. J. Sánchez, L. Novotny, and X. S. Xie. Near-field fluorescence microscopy based on two- photon excitation with metal tips. *Physical Review Letters*, 82:4014–4017, 1999.

[102] P.J. Schuck, D.P. Fromm, A. Sundaramurthy, G.S. Kino, and W.E. Moerner. Improving the mismatch between light and nanoscale objects with gold bowtie nanoantennas. *Physical Review Letters*, 94(017402), 2005.

[103] S. Weiss. Fluorescence spectroscopy of single biomolecules. *Science*, 283:1676–1683, 1999.

[104] Q.H. Wei, K.H. Su, S. Durant, and X. Zhang. Plasmon resonance of finite one-dimensional au nanoparticle chains. *Nano Lett.*, 4:1067–1071, 2004.

[105] N. Liu, M. Hentschel, T. Weiss, A.P. Alivisatos, and H. Giessen. Three-dimensional plasmon rulers. *Science*, 332(6036):1407–1410, 2011.

[106] M.A. van Dijk, M. Lippitz, D. Stolwijk, and M. Orrit. A common-path interferometer for time-resolved and shot-noise-limited detection of single nanoparticles. *Optics Express*, 15(5):2273–2287, 2007.

[107] O.L. Muskens, N. Del Fatti, and F. Vallée. Femtosecond response of a single metal nanoparticle. *Nano Lett.*, 6(3):552–556, 2006.

[108] N. Del Fatti, C. Voisin, M. Achermann, S. Tzortzakis, D. Christofilos, and F. Vallée. Nonequilibrium electron dynamics in noble metals. *Phys. Rev. B*, 61(24):16956–16966, 2000.

[109] F. Masia, W. Langbein, and P. Borri. Polarization-resolved ultrafast dynamics of the complex polarizability in single gold nanoparticles. *Phys Chem Chem Phys*, 15(12):4226–32, 2013.

[110] GuideChem. Polyvinyl butyral (cas no. 63148-65-2). http://www.guidechem.com/reference/dic-25831.html#id_-460445961, 2015.